Understanding Precipitation Responses to Externally Driven Climate Change

Shipeng Zhang
Brasenose College
University of Oxford

A thesis submitted for the degree of
Doctor of Philosophy

Trinity 2023

Acknowledgements

First of all, I would like to express my sincere gratitude to my supervisor, Philip Stier, for his continuous support and guidance. I have been very much enjoying the freedom to explore and develop my research ideas. All the insightful feedbacks he has given throughout my whole Dphil study remain a treasure in my future life.

Particularly, I would like to thank my post-doctoral supervisors, Guy Dagan and Duncan Watson-Parris, for their invaluable, helpful, and timely support. I would also like to thank the entire Climate Processes group for providing such a friendly and lively working atmosphere. I have been enjoying the insightful discussions with all of you. I would like to thank Laura Wilcox and Myles Allen for examining this thesis, and for an interesting and helpful discussion during the viva.

My special thanks to the Clarendon scholarship and the Natural Environment Research Council project RECAP for funding my Dphil project and living expenses in Oxford. I would also like to thank the support from NERC Oxford Doctoral Training Programme in Environmental Research.

I really appreciated being a part of the wonderful community of Brasenose College, which makes my time in Oxford so enjoyable. Special thanks go to Brasenose HCR, library, and dining hall for providing me with such a pleasant experience of studying at Oxford.

I am grateful to Minghuai Wang for hosting me for a few months at Nanjing University in China. I was overwhelmed by the kindness of the people there and enjoyed the discussions and collaboration on scientific topics. It is very appreciated for providing a nice place for me to stay during the challenging time of the pandemic.

Finally, I would like to thank my parents and sister for their endless love and support. It is never easy to raise a child in a small, remote town in China and support him to go to university. You have made it all possible. Despite all the difficulties I have gone through, you have never doubted me and believed that I could make it through. Your support is my greatest motivation.

Abstract

Precipitation plays a fundamental role in transferring water and energy in the climate system. Human activities significantly impact the hydrological cycle, but the magnitude of global and regional changes remains uncertain due to the complex nature of microphysical-dynamical interactions. This thesis aims to improve the understanding of precipitation responses to climate change through a combination of bottom-up (process-driven) and top-down (energetic) approaches.

The relationship between aerosol-induced changes in atmospheric energetics and precipitation responses across different scales is studied in terms of fast (radiatively or microphysically mediated) and slow (temperature-mediated) responses. This thesis proposes an energetic framework to decompose rainfall changes into contributions from clouds, aerosols, and clear-clean sky (without aerosols and clouds). It provides a way to better interpret and quantify the precipitation changes caused by aerosol perturbations. Further investigations show that the increase rate in global-mean precipitation with temperature (hydrological sensitivity; η) is dependent on the spatial pattern of sea surface temperature (SST) change, which has been overlooked before. Warming in strong tropical ascending regions can produce large η via enhanced global circulation and atmospheric radiative cooling. The warming pattern effect significantly contributes to the spread of η in the current generation of general circulation models (GCMs). After accounting for the pattern effect, the reconstructed global-mean precipitation agrees much better with observations, evidencing the importance of SST patterns on global-mean precipitation changes. Furthermore, we extend the analysis to regional rainfall by showing that anthropogenic aerosols modulate the Sahel rainfall variability through their impacts on regional SST. We show analysis supporting the chain of processes whereby changes in anthropogenic aerosol emissions alter net radiative fluxes and sea surface temperature variability in the North Atlantic Ocean, leading to a shift of the intertropical convergence zone (ITCZ), changes in the West African monsoon, and eventually changes in Sahel rainfall. These findings highlight the importance of accurate representation of regional aerosol radiative effects for the simulation of Sahel rainfall variability.

Contents

List of Figures

List of Tables

Chapter 1

Introduction

1.1 Atmospheric aerosols and greenhouse gases

The current climate system plays a vital role in providing a suitable environment for human existence. In turn, human activities also have significant impacts on the climate system, such as surface temperature, clouds, and precipitation, which has undergone unprecedented changes since industrialization (Boucher et al., 2013; Dai, 2013; Koren et al., 2008; Manabe, 2019; Myhre et al., 2014; Ramanathan et al., 2001; Rosenfeld et al., 2008; Trenberth et al., 2014; Forster et al., 2021).

Human activities affect the climate system mainly through modifications to the Earth's energy budget. The effective radiative forcing (ERF) quantifies the change in net radiative flux (shortwave and longwave) at the top of atmosphere (TOA) in response to the perturbations from climate agents, including the adjustments to the climate system that are independent of surface temperature changes (Forster et al., 2021). The adjustments include changes in the temperature profile in the troposphere and stratosphere, water vapour, clouds, and surface albedo. The Intergovernmental Panel on Climate Change's Fifth Assessment Report 5 (IPCC AR5) considered these adjustments to be 'rapid' (Boucher et al., 2013). However, the latest sixth assessment report (AR6) has removed the timescale definition and emphasised the nature of decoupling from surface temperatures (Forster et al., 2021). ERF has been commonly used to evaluate the ability of a climate forcing agent to warm (positive ERF) or cool (negative ERF) the climate system.

The Earth's climate system will subsequently adjust its surface temperature in response to the imposed ERF from climate forcing agents (Ceppi and Gregory, 2017; Manabe, 2019; Zelinka et al., 2020). There are a number of feedback processes involved with the surface temperature changes, including the Planck response and

changes in lapse rate, water vapour, albedo, and clouds (Forster et al., 2021). Although the sign and magnitude of some feedback processes remain considerably uncertain in existing literatures (Zelinka et al., 2020), there is consensus that the sum of all feedback parameters is negative, which enables the climate system to regain equilibrium. General Circulation Models (GCMs) suggest that it normally takes a long time for the climate system to regain equilibrium due to the complex feedback mechanisms and high heat capacity of oceans (Schwartz, 2007) in response to a given perturbation of a climate agent. The timescale can range from a hundred to a thousand years, depending on the model and the anthropogenic forcing perturbations (Caldeira and Myhrvold, 2013; Forster et al., 2021).

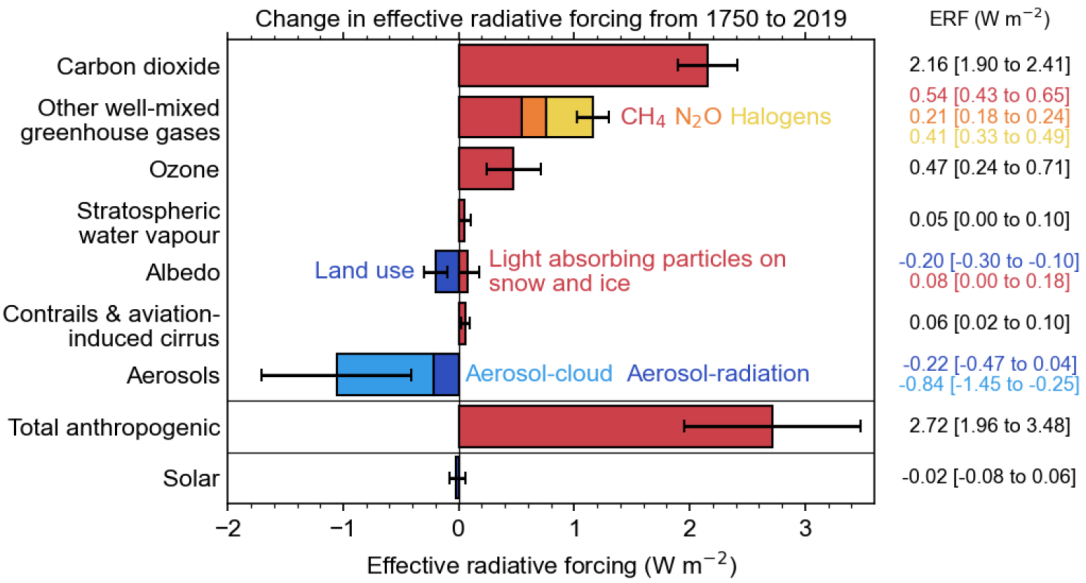

Figure 1.1: The main components of anthropogenic and natural radiative forcing of the climate system between 1750 and 2019. Forcing agents include carbon dioxide, other well-mixed greenhouse gases, ozone, stratospheric water vapour, albedo, contrails and aviation-induced cirrus, aerosols, and solar radiation. Effective radiative forcing from aerosols can be decomposed into contributions aerosol-radiation interactions and aerosol-cloud interactions. Error bars indicate the uncertainty (5-95%) of each estimate. Carbon dioxide contributes the most to the magnitude, whilst anthropogenic aerosols have the largest uncertainty contributed by different pre-industrial aerosol concentrations, emissions, and interactions with radiation and clouds (Forster et al., 2021), see also Sec 1.1.1 for more details).

Amongst all the forcing agents, anthropogenic aerosols and greenhouse gases (GHGs) are of particular interest to climate research. GHGs have the largest ERF; aerosols have the second largest ERF in magnitude, and counteract part of the warm-

ing effect caused by GHGs, but with a large uncertainty (Figure 1.1). Anthropogenic carbon dioxide (CO_2) is the primary driver of recent global warming, which is estimated to be responsible for a 1.01 °C (with 5%-95% confidence interval of 0.74 °C to 1.41 °C) increase in 2019 relative to 1750 (Forster et al., 2021), whilst anthropogenic aerosol effects counteract a certain part of the warming with significant uncertainties (Bellouin et al., 2020). Furthermore, the mechanisms of anthropogenic aerosols and GHGs effects on the Earth's energy budget are different (see Section 1.1.1 and 1.1.2).

Anthropogenic effects on climate are manifested not only in the modification of the Earth's energy budget and global-mean surface temperature but also in changes in the global water cycle (Dai, 2011; Trenberth, 2011; Pendergrass, 2020; Douville et al., 2021). Research shows that climate change can lead to changes in precipitation, glacier melt, surface water runoff and groundwater recharge, which are critical to water supply, food and energy security, and economics (Douville et al., 2021). These impacts are particularly concerning for regions that are vulnerable to changes in water supply, such as Asia, Africa and the Mediterranean region (Mekonnen and Hoekstra, 2016). Climate change could also increase the possibilities of floods and droughts due to the increased variability of precipitation in a warming climate (Dai, 2011; Douville et al., 2021). This thesis aims to improve the understanding of the impact of anthropogenic perturbations on climate, focusing on precipitation changes at different spatial and temporal scales.

1.1.1 Aerosols

Aerosols are defined as solid or liquid particles suspended in the atmosphere, with diameters ranging from approximately 1 nm to 10 μm (Seinfeld and Pandis, 1998). These particles have substantial environmental impacts on atmospheric chemistry, air quality, and human health. Aerosols are also an important climate agent due to their significant effects on the Earth's energy budget and the hydrological cycle through their optical (radiative) and microphysical properties (Boucher et al., 2013; Forster et al., 2021; Douville et al., 2021).

Aerosols can be directly emitted from natural and anthropogenic processes (i.e. primary aerosols), such as sea-spray particles and mineral dust. Some aerosols can also be formed by atmospheric mechanisms and reactions in the atmosphere (i.e. secondary aerosols), such as secondary organic aerosols (SOA), sulphate and nitrate aerosols produced by oxidation of their precursors.

Emissions of aerosols are governed by natural sources and anthropogenic activities, on the basis of which aerosols can be separated into natural and anthropogenic

aerosols. Natural aerosols refer to aerosols or their precursors generated by natural processes such as vegetation, wind, oceans, soil, fire, volcanic activities, and lightning. These aerosols include desert dust (Mahowald et al., 2014), sea salt (Ma et al., 2008), as well as secondary organic aerosols from biogenic sources (Schnell and Vali, 1976). While most aerosols remain in the troposphere, volcanic eruptions can inject aerosols into the stratosphere (Robock, 2000; Malavelle et al., 2017). Anthropogenic aerosols are particles generated by human activities such as agriculture, waste management, industry, and transportation. A majority of them are from fossil fuel combustion, a source of sulphate, black carbon (BC), and nitrate, which have significant climate impacts (Charlson et al., 1992; Bond et al., 2013; Lohmann et al., 2020). It is worth noting that some aerosol species can originate from both natural and anthropogenic sources, such as black carbon and sulphate. Biomass burning, such as wildfires, is a source of both natural and anthropogenic aerosols (Bond et al., 2013; Sophie et al., 2021).

Aerosols are removed from the atmosphere through dry and wet deposition. Dry deposition depends on the particle size and is subject to gravitational sedimentation and Brownian diffusion (Seinfeld and Pandis, 1998). Wet deposition is mainly mediated by atmospheric hydrometeors and can be further divided into in-cloud scavenging and below-cloud scavenging. In-cloud scavenging occurs when the aerosols act as cloud condensation nuclei (CCN) or ice nuclei (IN), or get captured by cloud droplets through collision. Below-cloud scavenging refers to those falling hydrometeors, such as raindrops, snow, hail, and graupel, which capture aerosols and contribute to the removal of aerosols from the atmosphere (Seinfeld and Pandis, 1998). Wet deposition dominates aerosol removal with high efficiency, which gives the lifetime of aerosols usually no more than ten days (Textor et al., 2006). Due to the short atmospheric lifetime of aerosols and the fact that most anthropogenic aerosols sources are located in the Northern hemisphere (Dentener et al., 2006), there is a significant contrast in anthropogenic aerosol concentration between the Northern and Southern hemispheres (Myhre et al., 2013; Wang, 2013), which further leads to distinct clouds, precipitation and radiation responses patterns (Douville et al., 2021; Forster et al., 2021; Kasoar et al., 2016; Undorf et al., 2018). Representation of the aerosol removal is one of the key factors limiting the simulation of aerosols lifetime and distribution in current models (Sophie et al., 2021). For example, an improved size-dependent parameterisation of BC wet scavenging could shorten the BC lifetime and lead to a better agreement with observed profiles (Taylor et al., 2014).

The latest IPCC assessment report (AR6) estimates the ERF from aerosols over 1750-2019 to be -1.1 W m^{-2} with a confidence interval (5% to 95%) of -1.7 to -0.4 W m^{-2}, which is the second largest in magnitude after greenhouse gases (Figure 1.1) (Forster et al., 2021). Despite the large uncertainties, the negative ERF from aerosols is suggested to contribute around -0.51 °C (with 5%-95% confidence interval of -1.05 °C to -0.13 °C) in 2019 relative to 1750 (Forster et al., 2021). Effective radiative forcing from aerosols can be decomposed into contributions aerosol-radiation interactions and aerosol-cloud interactions.

Aerosol-radiation interactions

Aerosols have the ability to scatter and absorb solar radiation directly. Effective Radiative Forcing from aerosol-radiation interactions (ERFari) refers to the direct effect by which aerosols scatter and absorb the solar radiation, combined with subsequent adjustments, involving modifications of humidity, stability of the atmosphere, and consequent adjustments of clouds (Forster et al., 2021; Koch and Del Genio, 2010). Based on their optical (radiative) properties, aerosols can also be categorized into absorbing and non-absorbing aerosols. Aerosols with strong absorbing abilities are called absorbing aerosols, such as BC, while aerosols with weak absorbing abilities are referred to as non-absorbing aerosols, such as sulphate. The adjustments in ERFari are mainly induced by absorbing aerosols, which can modify the atmospheric lapse rate and humidity as well as clouds. A number of models suggest that the adjustments in ERFari lead to increased low-cloud amounts and decreased high-cloud amounts and contribute to a negative ERFari (Smith et al., 2018; Stjern et al., 2017). However, this is not evidenced by some observation-based analyses, which suggest that the discrepancy is due to the deficient atmospheric heating profiles used in models (Allen et al., 2019).

Aerosol-cloud interactions

Aerosols that have the potential to be activated as cloud droplets under certain meteorological conditions are called CCN. Only particles with specific properties can be activated to cloud droplets based on the size and chemical composition. Particles that are larger in size and more hygroscopic are more readily activated (Köhler, 1936). The activation of CCN also requires a critical supersaturation to be reached, which is determined by local conditions such as updraft velocity, temperature, and humidity (Ghan et al., 2011). Other aerosols with low hygroscopicity, such as desert dust and black carbon, can act as IN. They can be lifted to high altitudes and accelerate the

heterogeneous formation of ice droplets. Mixing with hygroscopic aerosols also can make hydrophobic aerosols hygroscopic.

By serving as CCN or IN, aerosols have the ability to strongly affect clouds and radiation (Forster et al., 2021). Effective Radiative Forcing from aerosol-cloud interactions (ERFaci) is the radiative effect in which anthropogenic aerosols interact with clouds through microphysical processes. Increasing the aerosol concentration can increase CCN concentration and thus increase cloud droplet concentration (N_d). Higher N_d leads to a reduction in cloud drop effective radius (r_e), assuming constant liquid water content (Twomey, 1977). The smaller but more numerous cloud droplets lead to more reflection of shortwave radiation back to space, which induces a negative instantaneous radiative forcing (i.e. IRFaci) (Forster et al., 2021). Subsequently, as adjustments, the smaller cloud droplets could slow cloud droplet coalescence processes and suppress or delay precipitation. Since precipitation is thought to decrease cloud water path and/or cloud coverage, the decreased rainfall induced by more aerosols could then increase liquid water path (LWP) and/or cloud coverage (Albrecht, 1989; Rosenfeld et al., 2002). However, the magnitude and sign of these adjustments remain uncertain and dependent on the environmental conditions (Ackerman et al., 2004; Gryspeerdt et al., 2017; Malavelle et al., 2017; Zhang et al., 2016). Some studies show that, when the clouds are non-precipitating, the increase of aerosols could lead to a reduction in LWP and/or cloud fraction because smaller cloud droplets can enhance evaporation and incease the entrainment rate, resulting in cloud dispersal (Ackerman et al., 2004; Christensen and Stephens, 2011; Toll et al., 2019).

ERFaci is estimated to contribute 75-80% to the total aerosol radiative effect in the latest assessment report (AR6) (Forster et al., 2021). Compared with AR5 (Boucher et al., 2013), it is more certain that the total ERF from aerosols is negative (i.e. cooling the climate system) (Forster et al., 2021). However, quantifying aerosol effects on the climate system still remains uncertain and challenging. Uncertainties exist in observations of the anthropogenic forcing agents and climate systems (Adler et al., 2003; Kidd et al., 2017; Koren et al., 2007; Wen et al., 2007). There are various pathways and complex feedbacks involved in anthropogenic effects on the climate system (Bellouin et al., 2020; Haywood and Boucher, 2000; Khain, 2009; Stevens and Feingold, 2009; Toll et al., 2019). Additionally, it is difficult to distinguish aerosols effects from meteorological covariances (Gryspeerdt et al., 2017; Khain, 2009) and internal variabilities (Kay et al., 2015; Monerie et al., 2020) and to identify the causal relationships (Quaas et al., 2010; Gryspeerdt et al., 2017). The range of scales of these effects, from microphysical to large-scale dynamics, significantly contribute to

the uncertainties of representing anthropogenic impacts on the climate system in GCMs, especially the representation of clouds and their interactions (Ghan et al., 2016; Haywood and Boucher, 2000).

1.1.2 Greenhouse gases

The Sun provides energy to the Earth by radiating at short wavelengths and the Earth reflects around one-third of the solar radiation back to space and absorbs the rest of it. On average, the Earth has to radiate the same amount of energy back to space in balance. Since the Earth surface temperature is much lower than the sun, the thermal radiation from the Earth is predominately in the longwave near infrared. Greenhouse gases refer to the gases which are nearly transparent to the shortwave radiation from the sun but absorb infrared radiation emitted from the surface, the atmosphere itself, and clouds. At the same time, the atmosphere emits infrared radiation based on its own temperature at a given altitude. According the Kirkhoff's law which requires the absorption rate to be equal to its emission rate at a given wavelength, the upward infrared radiation by the relatively cold atmosphere is much less than the upward infrared radiation by the relatively warm Earth's surface (Manabe, 2019). For this reason, despite their limited abundance in the atmosphere, GHGs can significantly decrease the upward longwave radiative flux at the top of atmosphere, thereby trapping the terrestrial radiation and warming the surface. This warming effect is also named the greenhouse effect.

Water vapour, CO_2, methane, nitrous oxide, and ozone are the main GHGs in the climate system. GHGs can be emitted from both the natural system and human activities. Natural GHGs, such as CO_2, can be produced by the respiration of animals and plants and the decomposition of organics. Anthropogenic GHGs are mainly generated by fossil fuel combustion, changes in land use, industrial processes, and livestock production. The removal of CO_2 from the atmosphere includes dissolution into the ocean and biological processes such as uptake by plants. Overall the removal of CO_2 is very slow, making the atmospheric residence time of CO_2 hundreds of years (Archer et al., 2009), which is much longer than aerosols and most other short-lived GHGs, for example, methane.

GHGs are essential to providing a habitable environment for human existence. Without GHGs, the global mean temperature might be 33°C lower than now (Manabe, 2019). However, if the concentration of greenhouse gases continues to rise as a result of human activities, the absorption of infrared radiation in the atmosphere increases, leading to what is known as global warming (Manabe and Wetherald, 1975).

As shown in Figure 1.1, the ERF from anthropogenic GHGs is the largest among all forcing agents, which significantly contributed to recent global warming (Forster et al., 2021).

Surface temperature responses

It has been estimated that the concentration of CO_2 has increased by more than 40 percent since industrialization (from 278 ppm to 410 ppm in 2019). This is considered as the main cause of the observed increase in global surface air temperature (GSAT) during the 20th century (Forster et al., 2021), accompanied with a number of impacts on regional climate systems as well (e.g Dai, 2011; Trenberth, 2011; Mekonnen and Hoekstra, 2016; Douville et al., 2021). Climate sensitivity is the typical measure used to quantify how much the Earth's surface will warm after a doubling of atmospheric CO_2. Equilibrium Climate Sensitivity (ECS) refers to the GSAT change in response to a doubling of CO_2 concentration when the TOA energy budget regains balance (neglecting the feedbacks from ice sheets) (Forster et al., 2021). Another metric is the Transient Climate Response (TCR), which measures the GSAT increase when CO_2 concentration is doubled under the scenario of 1% per year increase (i.e. changes in GSAT at year 70). TCR is considered more useful than ECS for short-term climate projections because it provides a more immediate measure of the temperature response to increasing greenhouse gas concentrations within a few decades of CO2 doubling, while ECS measures the long-term temperature response after the climate system has reached a new equilibrium state. ECS and TCR are usually estimated by Earth system models or fully-coupled ocean-atmospheric models and are commonly used to evaluate climate response to external forcing. The latest assessment report (AR6) gives an estimate of 3 °C (5%-95% confidence interval of 2 °C to 5 °C) for ECS and 1.8 °C (5%-95% confidence interval of 1.2 °C to 2.4 °C) for TCR (Forster et al., 2021). The uncertainty is mainly contributed by the complex feedback processes (e.g. temperature-mediated changes associated with lapse rate, water vapour, surface albedo, clouds, and biogeophysical and biogeochemical feedbacks) (Forster et al., 2021). Several studies suggest that the time-evolving surface warming patterns have important effects on climate feedback and subsequently on ECS (Andrews et al., 2015; Andrews and Webb, 2018; Ceppi and Gregory, 2017; Zhou and Penner, 2016; Zhou et al., 2021). For example, Andrews and Webb (2018) found that the cloud and lapse rate feedback are strongly affected by the spatial pattern of surface temperature change in the tropical Pacific, which helps to explain why the climate sensitivity estimated from abrupt4xCO2 simulations differs from those estimated based

on atmosphere-only climate models experiments forced with observed historical SST changes.

In addition, global warming involves not only an increase in global-mean temperature, but also changes in surface warming patterns, as suggested by observations and climate models (e.g. Xie et al., 2010; Held et al., 2010; Armour et al., 2016; Andrews and Webb, 2018). These patterns are determined by multiple factors, including the interactive responses between wind, evaporation, ocean dynamics and thermocline (Xie et al., 2010; Ma et al., 2018). For example, there is a land-sea contrast in terms of surface warming which is much stronger over land compared to the ocean due to the smaller heat capacity and less efficient evaporative cooling over land (Joshi et al., 2008). The weak and delayed warming in the eastern Pacific and Southern Ocean is due to deep mixing layer and oceanic circulation changes (Xie et al., 2010; Armour et al., 2016). There is also a so-called polar amplification (i.e. more warming at high latitudes) caused by ice/snow albedo feedbacks (Manabe et al., 1990; Kashiwase et al., 2017) and enhanced poleward atmospheric energy transport under global warming (Cai, 2005; Cai et al., 2021). The warming pattern effect on the large-scale circulation and regional climate systems have already been well-recognised by previous literature (Palmer, 1986; Barsugli and Sardeshmukh, 2002; Ma et al., 2013, 2018; Zhou et al., 2020b). Recent studies also point out that the warming pattern effects have important implications for changes in global-mean cloud fields, radiation, and climate feedbacks (e.g. Andrews et al., 2015; Zhou et al., 2017; Dong et al., 2019a). For example, a number of fully-coupled climate models suggest that the cloud and lapse rate feedbacks are affected by the evolving sea surface temperature patterns and contribute to the changes and uncertainty in climate sensitivity and feedbacks (Ceppi and Gregory, 2017).

1.2 Precipitation

Precipitation plays an essential role in the Earth's water cycle (Trenberth et al., 2003). Precipitation on land provides water for soil moisture, rivers, and groundwater recharge, while precipitation over the ocean can alter the sea surface salinity, which then changes the density and circulation of the ocean (Douville et al., 2021). Together with clouds, it is also responsible for transporting energy and redistributing water in the climate system.

1.2.1 Clouds and precipitation

The formation of precipitation occurs within clouds, and therefore the global distribution of precipitation is attributable to the distribution of clouds. Briefly, the elevation of a parcel of warm air will usually lead to a decrease in temperature due to adiabatic cooling, and thus the relative humidity increases. If there are available CCN and enough moisture, water vapour will condense onto CCN when the critical supersaturation is reached, and then cloud droplets are formed (Köhler, 1936). The cloud droplets (typically 10 μm in size) can grow through condensation. The condensational growth rate is inversely proportional to droplet size, so this process alone is usually too slow for a droplet to reach a precipitable size of around 1 mm (Lohmann et al., 2007). In warm clouds, the collision-coalescence mechanism is the main pathway of drizzle and rain droplets formation (Lohmann et al., 2007). Droplets can rapidly grow into drizzle droplets through coalescence and collision with other cloud droplets, which is known as autoconversion. The further growing process, during which these drizzle droplets grow by collision with cloud droplets, is known as accretion. The efficiency of the collision-coalescence process increases with the droplet size. Small droplets have a very low collision efficiency, while large droplets can grow rapidly in droplet size. Representation of autoconversion and accretion in numerical models is discussed in section 1.2.2.

If the updraft is strong enough and the air parcel has been lifted above the level where the temperature is below 0 °C, ice processes start to be responsible for the precipitation formation. Since the saturation vapour pressure over ice is lower than over water, ice crystals can grow at the expense of supercooled water droplets, also referred to as the Wegener–Bergeron–Findeisen process (Lohmann et al., 2007). The presence of IN can significantly increase ice crystal formation; without IN, ice crystals can only form by homogeneous nucleation processes. Ice crystals can grow by riming and aggregation processes (the processes of ice crystals colliding with each other or supercooled droplets) until they reach precipitable sizes. Ice crystals may melt into rain during the falling process, depending on the temperature near the ground.

Precipitation rates are usually related to the corresponding cloud types. Based on their vertical motion characteristics and the horizontal extent, clouds can be distinguished into stratiform clouds or convective clouds (Lohmann et al., 2016).

Stratiform clouds, such as cirrus, stratocumulus, nimbostratus, and stratus, have a large horizontal extent (usually from 100 km to 1000 km), much wider than their vertical thickness (Houze Jr, 2014). The precipitation from stratiform clouds is limited due to the weak vertical motions in these clouds (Lohmann et al., 2016). Stratus is

typically formed when the warm air layer has been lifted above the cold air layer as a result of large-scale horizontal wind movements. In contrast, stratocumulus is driven by convective instability with a strong temperature inversion at the cloud top (Wood, 2012). It is noteworthy that stratocumulus extensively covers a wide area of the atmosphere, commonly over subtropical oceans, significantly reflecting incoming solar radiation back to space, increasing the Earth albedo, and leading to a large net negative radiative effect (Forster et al., 2021; Wood, 2012).

Convective clouds, such as cumulus and cumulonimbus, are characterised by buoyancy-driven vertical motions and generally have less horizontal coverage than stratiform clouds. They form as warm and humid air, driven by strong buoyancy, rises through the surrounding colder air. Then water vapour condenses, which releases latent heat at the same time, strengthening the buoyancy and allowing further development of convection. Shallow convective clouds are normally warm (liquid-only) phase clouds. However, if the instability strength is strong enough, the rising humid air parcel could be lifted above the level where temperature is lower than 0 °C, and the additional latent heat released by the freezing process can further enhance buoyancy, leading to the development of deep convective clouds such as cumulonimbus. The vertical motions in deep convective clouds are strong, resulting in intensive precipitation and a relatively short lifetime. Convective clouds are important for the hydrological cycle because the global amount of accumulated rainfall is dominated by precipitation from convective clouds (Yang and Smith, 2008; Yang et al., 2021).

1.2.2 Representation in GCMs

During past decades, climate models have been extensively used as a helpful tool for predicting climate responses and understanding the underlying mechanisms. GCMs, in particular, are widely used for simulating the Earth's climate system. GCMs can reasonably simulate the magnitude of global-mean accumulated rainfall amount due to the fact that it is energetically constrained (see section 1.2.3). However, they still have difficulties in correctly capturing the geographical precipitation pattern, for instance, producing an unrealistic double intertropical convergence zone (ITCZ) (Dai, 2006; Adam et al., 2018; Tian and Dong, 2020) or inaccurate precipitation features, such as too frequent light rainfall compared with observations (Dai, 2006; Stephens et al., 2010; O'Brien et al., 2016; Na et al., 2020).

Limitations in the representation of clouds in global climate models are considered one of the major sources of uncertainty for understanding the climate (Boucher et al., 2013; Forster et al., 2021). The key difficulty is to represent cloud processes, which

range from the microphysical scale to large-scale circulations on the order of tens or hundreds of kilometres (Anderson et al., 2003; Ghan et al., 2016; Forster et al., 2021). For the consideration of computational costs, GCMs used in experiments designed for the Coupled Model Intercomparison Project (CMIP) usually have a spatial resolution of around several hundred kilometres. Given that the scales of many atmospheric processes (e.g., cloud microphysical processes) are too small and computationally expensive to be explicitly resolved in current GCMs, a wide range of parameterisations are employed.

Cloud microphysical processes

Cloud microphysical processes, such as cloud droplet condensational growth, collision-coalescence processes, evaporation, freezing, and melting, are important for the formation and evolution of clouds and precipitation. Additionally, microphysical properties, such as cloud droplet number and size, are important for cloud radiative properties, which further have impacts on the climate system (Forster et al., 2021). Besides the small scales of cloud microphysical processes and complex interactions among various hydrometeors, the high number of hydrometeors ($\sim 10^8$ m^{-3}) within a small cloudy volume (Morrison et al., 2020) makes it impractical to directly simulate the activities of each hydrometeor in a GCM.

There are two most frequently used approaches to parameterise microphysics: bulk schemes and bin schemes (Gettelman and Morrison, 2015; Khain et al., 2015). These two schemes both use particle size distributions (PSDs) to characterise the concentration of particles but differ in their treatments of PSDs.

In bulk schemes, prescribed and semi-empirical PSDs are used to describe the size distributions of different classes of hydrometeors, such as cloud droplets, rain, ice, snow, and graupel. These PSDs typically assume a gamma distribution of particle sizes with prescribed intercept, shape, and slope parameters (Gettelman and Morrison, 2015; Khain et al., 2015). Bulk microphysics schemes describe the different properties of the class of hydrometeor by considering the moments of the PSDs. There are two often-used bulk schemes: single-moment and double-moment schemes. For a given class of hydrometeor, single-moment schemes only represent the mass mixing ratios of the particles, while double-moment schemes consider the number concentrations (as the second moment) as well. Adding number concentration as the second moment can largely improve the simulation of aerosol effects on cloud droplets (Morrison et al., 2020). Additionally, a third moment may also be introduced to provide more information on the properties of hydrometeors, such as radar reflectivity.

In bin schemes, PSDs are explicitly calculated from microphysical equations, so no prior information is required, in contrast to bulk schemes. Given sufficient bins, bin schemes can provide highly detailed representations of microphysical processes since PSDs are allowed to change, with the compensation that this is more computationally expensive. Compared to bulk schemes, bin schemes are typically more than an order of magnitude more computationally expensive (Khain et al., 2015; Morrison et al., 2020). Of current GCMs, most still use bulk schemes to parameterise cloud microphysical processes for long-term simulations, for example, ECHAM6 (Neubauer et al., 2019).

As mentioned in section 1.2.1, the collision-coalescence mechanism in warm clouds is assumed to consist of autoconversion and accretion (Gettelman et al., 2013). Since cloud droplets and raindrops are separated into different hydrometeor classes, bulk schemes describe autoconversion and accretion separately. In contrast, bin schemes have no such separation between cloud droplets and raindrops, thus directly describing the evolution of the PSD due to collision-coalescence processes by solving the stochastic collection equation (Khain et al., 2015). The parameterizations of autoconversion and accretion in bulk schemes are usually derived from the empirical relationships based on explicit calculations in bin schemes. In bulk schemes, the rate of autoconversion is directly dependent on droplet number concentration, which is affected by aerosol concentration (Khairoutdinov and Kogan, 2000). However, accretion is weakly dependent on droplet number concentration and primarily alters rain intensity (Gettelman et al., 2013).

Convective processes

Convective clouds also need to be parameterised due to the low resolutions used in GCMs. They are usually parameterised based on mass flux models (Tiedtke, 1989), which is a computationally efficient approach, but also has limitations in simulating shallow convective cloud amounts, the heterogeneous nature of convective clouds (Christensen and Stephens, 2011; Marinescu et al., 2021), and the effect of aerosol on convective clouds (Tao et al., 2012; Jiang et al., 2018). Some cloud parameterisations alternatively use higher-order closure schemes (Larson and Golaz, 2005; Guo et al., 2015) as well as the so-called super-parameterisation (Grabowski, 2001; Wang et al., 2015). Cloud-resolving models (CRMs) can explicitly resolve many features of deep convective systems but have commonly been performed with a regional domain due to computational limitations (Langhans et al., 2012; Satoh et al., 2019). There have been continuous efforts to employ CRMs in GCMs (Satoh et al., 2019; Stevens et al., 2019; Wang et al., 2015). In super-parameterisations, a CRM (typically 2-D) is embedded

in each column of the GCM and aims to represent many aspects of convective clouds more realistically than the current generation of climate models (Grabowski, 2001; Wang et al., 2015; Satoh et al., 2019), with the compensation of more computational time.

1.2.3 Atmospheric energy budget

Precipitation also plays an essential role in the atmospheric and surface energy budget. The atmosphere exchanges energy with the surface through turbulent fluxes of water vapour and heat. It also exchanges energy with both space and the surface through radiation. The magnitude of global-mean precipitation is strongly governed by the atmospheric energy budget (Allen and Ingram, 2002; Mitchell et al., 1987; O'Gorman, 2015). The atmospheric energy budget can be simplified and described by Equation 1.1.

$$L_c P = \mathrm{ARC} - \mathrm{SH}, \tag{1.1}$$

where L_c refers to the latent heat of condensation (assumed to be constant at 2.25×10^6 J kg^{-1}) and P is the surface precipitation (in the unit of kg m^{-2} s^{-1}, so that the units of the three terms in the equation are W m^{-2}). SH is the surface sensible heat flux. ARC is the atmospheric radiative cooling, defined as the net loss of shortwave (SW) and longwave (LW) radiation in the atmospheric column. ARC can be calculated from the difference between the top of atmosphere and surface radiations, defined as

$$\mathrm{ARC} = \mathrm{LW}_{TOA} + \mathrm{SW}_{TOA} - (\mathrm{LW}_{SUR} + \mathrm{SW}_{SUR}). \tag{1.2}$$

From Equation 1.1, it can be understood that the global average latent heat released by precipitation is energetically balanced by the radiative cooling of the atmosphere and surface energy fluxes. An illustration of global energy flow for the early 21st century is provided in Figure 1.2, which shows globally averaged annual-mean estimates including SH=21 W m^{-2} (with 5%-95% confidence interval of 15-25 W m^{-2}) and $L_c P$=82 W m^{-2} (with 5%-95% confidence interval of 70-85 W m^{-2}). These terms are approximately balanced. This energetic constraint gives the annual global mean precipitation rate of around 2.83 mm d^{-1} (with 5%-95% confidence interval of 2.41-2.93 mm d^{-1}).

1.2.4 Observations

Compared to surface temperature observations, the observational precipitation dataset is much spatially sparser (Adler et al., 2003; Kidd et al., 2017). For global-scale

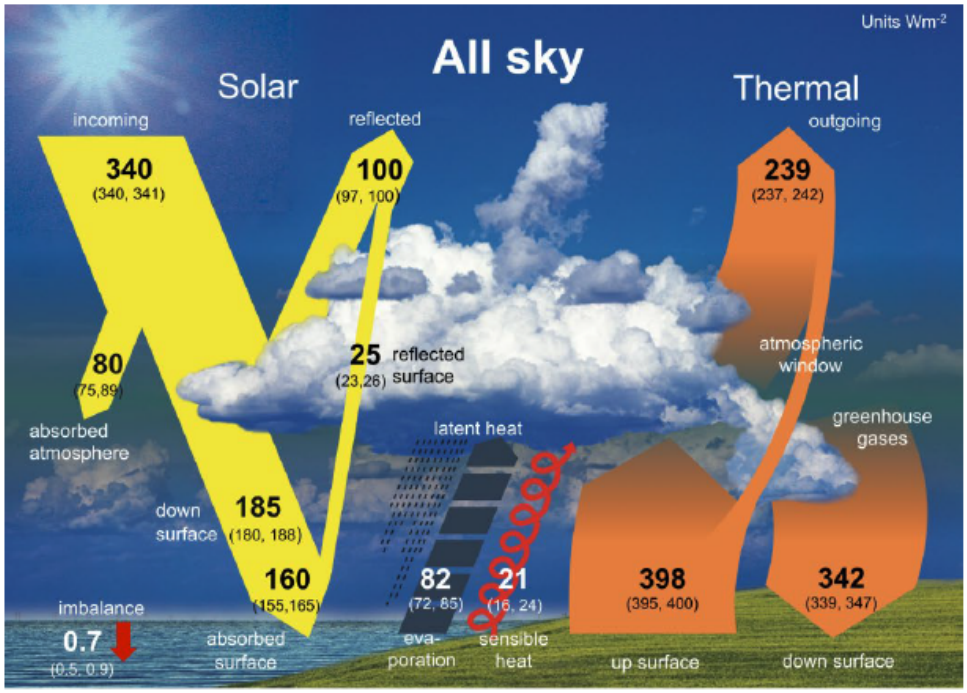

Figure 1.2: Schematic diagram showing the global annual mean Earth's energy budget. Numbers indicates the best estimates of globally averaged values of components in the atmospheric energetic budget with uncertainty ranges (5-95% confidence interval) in parentheses. The arrows indicate the schematic flow of energy in proportion to their values. The magnitudes are obtained by combining satellite-derived estimates and surface observations at the beginning of the 21st century (from Wild et al., 2019).

climate studies, it would be ideal to have long-term precipitation observation data covering the globe. However, given the highly variable and inhomogeneous nature of precipitation, it is almost impossible to get such desirable datasets (Sun et al., 2018).

Ground-based gauge observation is a relatively reliable measurement of surface rainfall, which can cover long periods. The Global Historical Climatology Network (Menne et al., 2012) aggregates precipitation data from thousands of stations, providing a dataset of in situ precipitation observations covering more than 100 years. However, a significant drawback of ground-based datasets is that they are too sparse to provide global coverage. Most stations are located on the land, with very few located on the ocean (Kidd et al., 2017). Another drawback of local rain gauges is their lack of ability to represent the state of a larger region, which is more of interest for precipitation studies and for comparison with model output (Groisman and Legates, 1994).

The satellite system provides an invaluable opportunity to measure and study precipitation with global coverage (Kidd, 2001; Skofronick-Jackson et al., 2017), which is more spatially homogeneous than ground-based observations. Satellite-based precipitation data can be derived from active and passive instruments, with different retrieval algorisms.

Passive microwave (PMW) sensors, such as the Special Sensor Microwave/Imager (SSM/I), can sense through clouds and retrieve particles within raindrop sizes. The early PMW-based retrieval algorithm is based on an empirical relationship between rain rate and brightness temperature. Continuing efforts have been focused on improving this retrieval algorithm by making use of cloud profiles based on cloud models and including more sophisticated probabilistic, physical and iterative algorithms (Bauer et al., 2001; Kummerow et al., 2001; Wentz and Spencer, 1998). It is worth noting that this retrieval method is limited to regions with low surface brightness, such as the ocean. For visible/infrared (VIS/IR) sensors, the retrieval assumption is that the observed IR cloud top temperature can be used to measure rainfall intensity because colder clouds usually correspond to deeper convection, therefore stronger rainfall. An advantage of VIS/IR satellite observations is the extensive coverage of the tropics with fine temporal and spatial resolution. However, it is worth noting that the assumed relationship between cloud top temperature and rainfall intensity is indirect and does not apply to all clouds (Bauer et al., 2001).

Widely used active instruments include the Tropical Rainfall Measuring Mission (TRMM) precipitation radar (PR) (Huffman et al., 2007) and the CloudSat Cloud Profiling Radar (CPR) (Stephens et al., 2009). Active microwave instruments retrieve

rain rates based on the relationship between radar reflectivity and rain droplet radius, which relies on the assumed droplet size distribution (Iguchi and Meneghini, 1994). CloudSat CPR has an advantage over TRMM PR in detecting light rainfall because it uses a higher frequency channel (94 GHz). However, since clouds and precipitation can attenuate the results from active sensors, this could lead to an underestimation of the heavy tropical rainfall retrieved from CloudSat CPR (Ellis et al., 2009).

In addition to the uncertainties in measuring precipitation, another limitation of satellite observations for climate change studies is the relatively short length of their records, only starting in the 1970s, which is shorter than the typical period of interest (from pre-industrial to present day) (Ghan et al., 2016; Penner et al., 2011).

Combining satellite and gauge observations is expected to improve the accuracy and reliability of precipitation products since it merges the advantages of each data type (Huffman et al., 1995).The Global Precipitation Climatology Project (GPCP) monthly precipitation dataset is widely used for precipitation analysis, which collects both the microwave and IR satellite data and ground-based gauge observations across the globe to reproduce global precipitation datasets starting from 1979 (Adler et al., 2003; Xie et al., 2003). Another merged data set is the Climate Prediction Center (CPC) Merged Analysis of Precipitation (CMAP), which uses similar input data sets to GPCP with different merging methodologies (Xie and Arkin, 1998). Comparisons between CMAP and GPCP indicate that the precipitation analyses are generally consistent with each other (Yin et al., 2004). The Global Precipitation Measurement (GPM) mission aims to provide better calibration of space-based observations of rainfall and snow. With the help of the Integrated Multi-satellitE Retrievals for GPM (IMERG) algorithm, GPM uses a constellation of satellites to improve sampling and calibrations, captures the intermittency of precipitation, and provides more accurate and timely precipitation estimates (Hou et al., 2014). It provides a better understanding of precipitation and contributes to the next generation of global precipitation products with more accurate instantaneous precipitation estimates and unified precipitation retrievals from a constellation of satellites (Hou et al., 2014; Sun et al., 2018).

1.3 Precipitation responses to climate change

Although both natural variability and human activities affect the hydrological cycle, there is scientific consensus and observational evidence indicating that anthropogenic

perturbations have increasingly influenced precipitation at various spatial and temporal scales since the last century (Allan et al., 2010; Andreae et al., 2004; Andrews and Forster, 2010; Dai et al., 2004; Douville et al., 2021; Li et al., 2016; Myhre et al., 2017; Pendergrass and Hartmann, 2012; Ramanathan et al., 2001; Trenberth et al., 2014).

In response to increasing GHG concentrations, a number of model simulations suggest that there is a short-term decrease and a subsequent increase in global-mean precipitation (Allen and Ingram, 2002; Bala et al., 2010; Cao et al., 2011; Wu et al., 2010). This can be explained by the initially increased atmospheric stability due to the direct atmospheric warming induced by higher GHG concentration (Baker et al., 2018), followed by increased atmospheric instability as a result of surface warming (Mitchell et al., 1987; Yang et al., 2003). Stronger rainfall intensity is also expected to happen under a warmer climate based on thermodynamic conditions, confirmed by observations and model simulations (Fischer and Knutti, 2016; Neelin et al., 2017; O'Gorman, 2015). However, quantification of the precipitation intensification remains highly uncertain and tends to be largely influenced by the microphysical and dynamical conditions (Pendergrass et al., 2016; Pfahl et al., 2017).

Anthropogenic aerosol effects on precipitation can be even more complicated, as they can modify both global and regional precipitation through impacts on cloud microphysical properties (Section 1.2.2) and the atmospheric energy budget (Section 1.2.3) (Douville et al., 2021). Modelling and observational studies show that the aerosol effect on regional precipitation is not monotonic, which could lead to either an increase or decrease in rainfall depending on the environmental background, aerosol concentration, and cloud regimes (Khain, 2009; Koren et al., 2008, 2012; Liu et al., 2019; Marinescu et al., 2021; Ming et al., 2010; Rosenfeld, 2000; Rosenfeld et al., 2008; Stevens and Feingold, 2009). The changes in clouds and precipitation depend on the aerosol types as well. Some sea salt can act as giant CCN, which is found to accelerate the collision-coalescence process and increase rainfall (Rosenfeld et al., 2002). Absorbing aerosols such as BC are thought to suppress precipitation through convective inhibition, but the magnitude and sign of changes in rainfall rely on the vertical distributions of aerosols (Ming et al., 2010) and their geographical location (Dagan et al., 2019).

Major efforts have been made to understand the response of precipitation to increased GHGs and anthropogenic aerosol emissions, considering its importance and uncertainty (Khain, 2009; Rosenfeld et al., 2008; Stevens and Feingold, 2009). For example, to estimate the effects of anthropogenic aerosol on clouds and precipitation,

many studies focus on the chain of processes from aerosol emission and activation of CCN to cloud microphysics and dynamical regimes (Allan et al., 2020; Ghan et al., 2016; Li et al., 2016). These analyses are known as a 'bottom-up' (process-driven) approach. Bottom-up approaches are important as they have helped to increase our process-level understanding; however, their conclusions remain uncertain due to the complicated nature of aerosol-cloud interactions, which span from microphysical to planetary scales (Boucher et al., 2013; Forster et al., 2021), and the limitations in observational constraints (Hall et al., 2019; Rosenfeld et al., 2002; Wang et al., 2012). An energetic perspective provides an alternative approach for investigating the response of precipitation to anthropogenic perturbations because of the energetic constraints on the changes in latent heat released from precipitation (Allen and Ingram, 2002; Mitchell et al., 1987; Muller and O'Gorman, 2011; O'Gorman et al., 2012). This is also referred to as the 'top-down' approach.

1.3.1 Energetic constraints on precipitation responses

The Clausius-Clapeyron equation provides a strong thermodynamic constraint on the water vapour increase in response to surface warming at approximately 7% K^{-1}. This has also been confirmed by global observations (Trenberth et al., 2003; Wentz and Schabel, 2000). However, modelling results suggest that the rate of increase of global-mean precipitation in response to surface warming is around 2% K^{-1} and so does not follow the Clausius-Clapeyron rate (Allen and Ingram, 2002). Instead, global-mean precipitation and evaporation are strictly determined by the atmospheric and surface energy budgets.

According to the atmospheric energy budget defined in Section 1.2.3, the latent heat released from global-mean precipitation is balanced by the surface latent heat flux and atmospheric radiative cooling. This energetic constraint still applies to the changes in each term in the energy budget. A perturbation of the atmospheric energy budget can be written as follows:

$$L_c \delta P = \delta \mathrm{ARC} - \delta \mathrm{SH}, \tag{1.3}$$

where δ denotes the difference between two climate states (e.g., with and without anthropogenic aerosols). As shown in Equation 1.3, any increase in latent heat released from precipitation should be balanced by a corresponding increase of radiative cooling or a decrease in sensible heat flux from the surface globally. Therefore, factors that affect an energy budget term can modify the hydrological response (Kvalevåg et al., 2013; Stephens and Hu, 2010). Surface sensible heat flux has also been found

to have a non-negligible role in historical precipitation changes despite its relatively small contribution to the total energy budget (Myhre et al., 2018). Understanding precipitation responses from the energetic perspective provides a different approach in addition to the conventional bottom-up approach, which focuses on interpretations from changes in microphysical and cloud processes as well as large-scale circulations.

The energetic constraint explains why the rate of increase of global average precipitation ($\sim$2% K^{-1}) does not keep pace with the specific humidity increase rate suggested by the Clausius-Clapeyron relationship ($\sim$7% K^{-1}) (Allen and Ingram, 2002). The increased rate of precipitation is associated with the increased rate of radiative cooling as a result of the deepening troposphere (Jeevanjee and Romps, 2018). Even though the atmospheric energy budget strongly constrains the precipitation increase in response to warming, it is worth noting that there is still a considerable range in current GCMs, from 2.1% K^{-1} to 3.1% K^{-1} (Allan et al., 2020; Fläschner et al., 2016). Existing literatures suggest that these uncertainties may arise from differences in atmospheric model parametrisation schemes, such as treatments of water vapour shortwave absorption (DeAngelis et al., 2015) and low cloud schemes (Watanabe et al., 2018) in GCMs (see Section 1.3.3).

The energetic approach can also be applied on regional scales by adding the energy transport term (H), which is expected to be zero for the global mean (Muller and O'Gorman, 2011):

$$L_c \delta P = \delta \mathrm{ARC} - \delta \mathrm{SH} + \delta H. \tag{1.4}$$

H is the column-integrated divergence of dry static energy ($\nabla \cdot \overrightarrow{u} s$), where $s = c_p T + gz$ the dry static energy, c_p air specific heat capacity, T temperature, g acceleration due to gravity, z height, and $\overrightarrow{u} = (u, v)$ the horizontal wind velocity. The moist static energy budget is another commonly used approach to study regional rainfall system (e.g. Neelin and Held, 1987; Hill et al., 2017; Wang and Li, 2020), which includes the moisture transport term and surface latent heat as a result from evaporation and examines the factors contributing to changes in the moist static energy $h = s + L_c q$, where q is the specific humidity.

An equally essential constraint on precipitation is the water vapour budget. On a global scale, the evaporation E and precipitation P should be balanced for an equilibrium state. On a regional scale, the imbalance between local precipitation and evaporation is balanced by the moisture flux convergence ($-\nabla \cdot \overrightarrow{u} q$):

$$-\delta(\nabla \cdot \overrightarrow{u} q) = \delta P - \delta E. \tag{1.5}$$

Both the water vapour and energy budgets suggest that the transport term of energy and water vapour is important in determining the geographical pattern of precipitation responses (Muller and O'Gorman, 2011; Richardson et al., 2018b). Further studies demonstrated that the magnitude of the transport term is latitude-dependent, which is linked to the Coriolis force (Dagan et al., 2019). For example, strong adiabatic heating induced by increased absorbing aerosol emission in the extra-tropics is confined to local scales due to strong Coriolis force (thus weak energy transport). However, in the tropics, where the Coriolis force is small, a strong adiabatic heating perturbation can drive strong thermal circulations, which further diverge dry static energy and converge moisture at the same time, resulting in an increase in local precipitation (Dagan et al., 2019). Further study suggests that the horizontal transport term is non-negligible at scales generally smaller than 4000 km. That also means the atmosphere is close to radiative-convective equilibrium when averaged over this scale (Dagan and Stier, 2020).

1.3.2 Fast and slow responses

Changes in precipitation in response to a climate forcing agent can be decomposed into a temperature-independent part and a temperature-dependent part (Andrews et al., 2010; Bala et al., 2010). The temperature-independent component is mediated by near-instantaneous changes in atmospheric diabatic cooling/heating and rapid adjustments associated with changes in the vertical temperature profile, clouds, and water vapour (Sherwood et al., 2015; Stjern et al., 2017). Given its short timescale (from days to weeks), this component is also referred to as the fast response. The temperature-dependent precipitation response is associated with the processes by which the climate system adjusts its surface temperature in response to the TOA radiative flux imbalance. The time scale for this temperature-driven precipitation response can be really long (from years to hundred years) due to the high heat capacity of the ocean and complex feedback mechanisms (Schwartz, 2007; Zelinka et al., 2020). It is therefore referred to as the slow response. The slow response of precipitation and TOA forcing are strongly correlated, as the change in surface temperature is directly related to TOA forcing (Kvalevåg et al., 2013; Suzuki et al., 2017).

The fast and slow responses of precipitation were illustrated by Andrews et al. (2009). They showed the changes in precipitation in response to an instantaneous doubling of CO_2 concentration and an instantaneous increase in solar irradiance respectively in a GCM coupled to a slab ocean (Figure 1.3). In response to the CO_2 forcing, there is an initial decrease in precipitation (the fast response; defined as the

y-intercept in Figure 1.3). This is because the increased CO_2 concentration caused an instantaneous decrease in atmospheric radiative cooling, resulting in an associated decrease in latent heat (and precipitation) as a fast response. It is then followed by a near-linear increase in precipitation as surface temperature rises (a slow response), driven by the enhanced radiative cooling from a warmer atmosphere (O'Gorman et al., 2012). The slow response of precipitation in the solar irradiance experiment (triangles and line of best fit in Figure 1.3) is very similar to the CO_2 experiment. The differences are from fast responses since increased solar irradiance has a much smaller effect on near-instantaneous atmospheric radiative cooling compared to increasing CO_2.

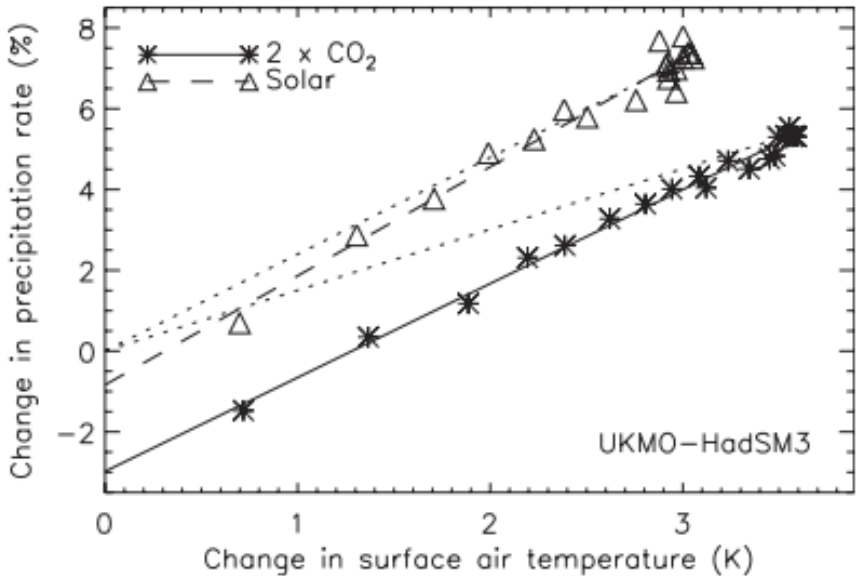

Figure 1.3: Changes in global-mean precipitation as a function of changes in annual global-mean surface air temperature for the Met Office Hadley Centre Slab-Ocean Model version 3 (UKMO-HadSM3) 2xCO_2 and solar increase experiment. Each dot represents the annual mean over individual years (20 years in total) subsequent to an instantaneous increase in CO_2 concentration (asterisks) or solar irradiance (triangles). Dotted lines show the slopes corresponding to the apparent hydrological sensitivities calculated from the final states (from Andrews et al., 2009).

Dividing precipitation changes due to climate agents into fast and slow responses can be very helpful for understanding the mechanisms behind the changes and narrowing their uncertainties in GCMs (e.g. Samset et al., 2016). Previous work has shown that the fast responses of precipitation show more variations among GCMs than the slow responses (Andrews and Forster, 2010; Fläschner et al., 2016). These differences in precipitation responses to various climate drivers are due to the distinct impacts on the near-instantaneous atmospheric adiabatic cooling/heating (Smith et al., 2018).

Climate forcing agents, such as sulphate aerosols and solar irradiance, that have little effect on near-instantaneous radiative cooling/heating, only produce small fast precipitation responses (Liu et al., 2018).

The Precipitation Driver Response Model Intercomparison Project (PDRMIP) (Myhre et al., 2017) used a number of GCMs to evaluate the uncertainties of precipitation responses to different climate forcers such as GHGs, aerosols, and solar radiation change. It is suggested that the response of precipitation is dominated by slow responses rather than fast responses for most climate forcers except BC (Samset et al., 2016; Smith et al., 2018). Among all climate forcing agents, increasing BC emission contributes to the largest uncertainties in estimating changes in precipitation among GCMs (Samset et al., 2016). This is due to the complicated and different parameterisations for physical, chemical, and dynamical processes used in different GCMs to simulate the process chain starting from BC emission to its final climate impact (Stjern et al., 2017).

1.3.3 Hydrological sensitivity

The apparent hydrological sensitivity (η_a) is defined as the sum of fast and slow precipitation responses divided by surface temperature change (Andrews et al., 2010; Bala et al., 2010; Fläschner et al., 2016). It is worth noting that η_a is not solely determined by the climate system or a specific model, as it also affected by the forcing scenario. Samset et al. (2016) found that η_a varies considerably among simulations with different climate forcers perturbations and most of the spread is from fast precipitation response. The hydrological sensitivity (η) refers to the increase rate of global-mean precipitation with respect to surface temperature increase directly, after the fast atmospheric adjustments. The spread of η derived from different climate change scenarios is significantly reduced compared to η_a (DeAngelis et al., 2015; Fläschner et al., 2016). η is a characteristic quantity widely used to evaluate the hydrological intensification under climate change scenarios (Allan et al., 2014; Fläschner et al., 2016; Kvalevåg et al., 2013). Although η is less dependent on the types of forcing agents and therefore has a smaller spread compared to η_a (Andrews et al., 2010; Bala et al., 2010), there is still a non-negligible inter-model spread (a factor of three) of η estimated from current GCMs (DeAngelis et al., 2015; Fläschner et al., 2016).

Much work has been done to study the spread of η among GCMs. Temperature-mediated changes that affect the atmospheric energy budget can eventually impact η. By using the radiative kernel technique (Soden et al., 2008) and applying it to the atmospheric energy budget, O'Gorman et al. (2012) showed how global-mean

precipitation depends on different feedback factors in nine GCMs. Similar to the TOA radiative feedbacks (Bony et al., 2006), the global-mean precipitation feedback factors include water vapour, lapse rate (measures non-uniform warming of the column), Planck (measures uniform warming of the column), clouds, and surface sensible heat flux, as shown in Figure 1.4. A positive feedback indicates a trend to increase the atmospheric column energy and therefore suppress precipitation, and vice versa for a negative feedback (Previdi, 2010). Noteworthy differences might exist when different kernel frameworks and models are used (Fläschner et al., 2016).

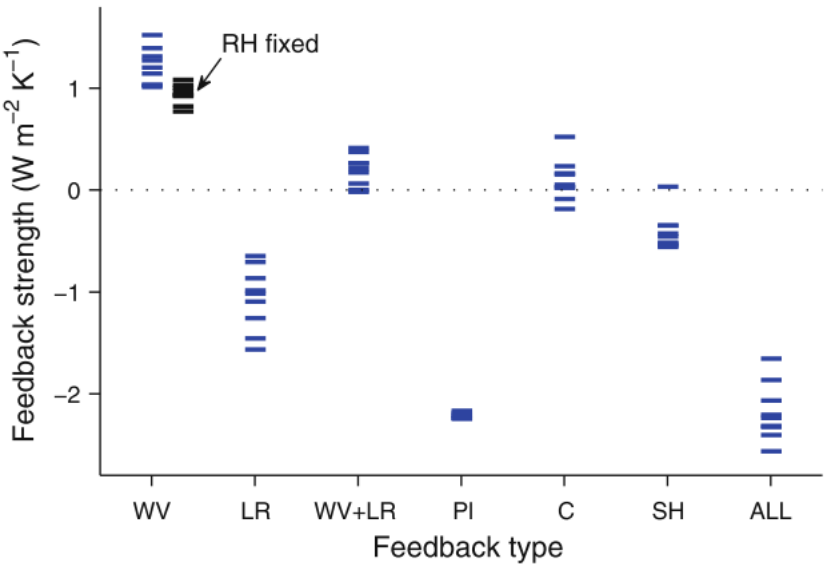

Figure 1.4: Atmospheric energy budget feedbacks (blue dashes) from water vapour (WV), lapse rate (LR), the sum of water vapour and lapse rate (WV+LR), Planck (PI), cloud (C), surface sensible heat flux (SH), and the sum of all (ALL). The albedo feedback is neglectable and not shown. Black dashes indicate the water vapour feedback when relative humidity is fixed. Results are derived from nine global climate models. Positive values indicate a trend to increase the atmospheric column energy and therefore suppress precipitation, and vice versa for negative values (from O'Gorman et al., 2012).

The water vapour feedback tends to decrease precipitation due to increased shortwave absorption and decreased longwave cooling (Previdi, 2010). The magnitude of the water vapour feedback is also dependent on the altitude of increased specific humidity (Previdi, 2010). Fixing the relative humidity can reduce the magnitude and variance of the water feedback (black dashes in Figure 1.4). Although the Clausius-Clapeyron equation constrains water vapour increase rate, variation in model schemes treating shortwave absorbed by water vapour can contribute to much of the spread in the η parameter from GCMs (DeAngelis et al., 2015).

The lapse rate feedback quantifies the changes in the atmosphere energy budget in response to vertically non-uniform warming. It is dominated by the lapse rate changes in the tropics (Held and Soden, 2006), where the vertical temperature profile is close to a moist adiabat. In the tropics, the temperature increase is larger in the upper troposphere than in the lower troposphere in response to surface warming (Bony et al., 2006; Manabe and Wetherald, 1975). This leads to more longwave radiative flux to space and indicates the lapse rate feedback tends to enhance precipitation. Since the water vapour increases with temperature, following the Clausius-Clapeyron equation (Held and Soden, 2006), the lapse rate and water vapour feedback are anticorrelated and usually considered together (Soden et al., 2008). Although the spreads of lapse rate feedback and water vapour are considerably larger on their own, the sum of these two feedbacks has a less inter-model spread (Fläschner et al., 2016; Muller and O'Gorman, 2011).

The Planck feedback enhances precipitation and agrees well in GCMs. It is also the largest magnitude contribution (around 2 W m^{-2} K^{-1}) to the total feedback (Figure 1.4). It is worth mentioning that, unlike the TOA radiative feedback analysis (Bony et al., 2006), the albedo feedback is negligible for the atmospheric energy budget (O'Gorman et al., 2012).

Increasing surface temperature leads to a slight decrease in the surface sensible heating to the atmosphere, which therefore causes an associated increase in precipitation (Previdi, 2010). However, sensible heat flux feedback's magnitude and inter-model spread are relatively small compared to other terms (Figure 1.4).

Cloud feedbacks significantly contribute to the inter-model spread of the total feedback due to the uncertainties in its representation in GCMs (Forster et al., 2021). Clouds, depending on the model, can either increase or decrease precipitation (Figure 1.4), but their multi-model mean tends to suppress precipitation (Fläschner et al., 2016; O'Gorman et al., 2012; Stephens and Ellis, 2008). In particular, low clouds have an essential role in the calculation of TOA cloud feedbacks and can modulate the magnitude of both the equilibrium climate sensitivity and η. Models could potentially underestimate η due to the deficiencies in simulating low-cloud feedbacks (Watanabe et al., 2018). Recent studies find that the SST spatial pattern of warming also has a non-negligible role in determining the magnitude of cloud feedbacks on the TOA energy budget (Andrews and Webb, 2018; Ceppi and Gregory, 2017; Dong et al., 2019b; Zhou et al., 2017). However, this has yet to be examined on the atmospheric energy budget (and global-mean precipitation).

1.3.4 Transient precipitation changes

Global warming will accelerate the hydrological cycle and cause an increase in global-mean precipitation (Trenberth, 2011). However, observations show nearly no trend of increasing precipitation in recent decades, despite an evident trend of increasing surface temperature (Adler et al., 2017; Allan et al., 2020; Morice et al., 2021; Wentz et al., 2007). Figure 1.5 shows the transient changes of temperature, atmospheric moisture, and precipitation from observations and model simulations from 1980 to 2014. There is a statistically significant increase rate of global surface temperature and column integrated water vapour at around 0.15 °C/decade and 1.0 %/decade, respectively. These two rates are translated into a water vapour increase rate of 6.7 %/°C, consistent with the Clausius-Clapeyron thermodynamic expectation (Allan et al., 2020). However, the satellite observations and model simulations indicate that there has been no statistically significant increase in precipitation during the past three decades (Figure 1.5).

The real-world transient precipitation changes are suggested to be a combination of fast and slow components (Andrews and Forster, 2010; Bala et al., 2010).The muted trend of global-mean precipitation during past decades is suggested to be caused by the fast adjustments in atmospheric radiative cooling (Allan et al., 2014; Andrews, 2014; Thorpe and Andrews, 2014) (see also Section 1.3.2). The fast responses from greenhouse gases and absorbing aerosols increase atmospheric radiative absorption and therefore reduce precipitation (Allen and Ingram, 2002; Bala et al., 2010; Ming et al., 2010), which offset much of the increasing trend mediated by surface warming (Allan et al., 2014; Andrews, 2014; Thorpe and Andrews, 2014).

Previous work has tried to use the combination of fast and slow responses to reconstruct historical global-mean precipitation (Allan et al., 2014) and predict future precipitation under different climate scenarios (Thorpe and Andrews, 2014). The reconstruction framework includes a temperature-independent component and a temperature-mediated component, assuming that the contribution of sensible heat flux is small (Fläschner et al., 2016; O'Gorman et al., 2012):

$$L_c \Delta P\,(t) = -\Delta \mathrm{AA}(t) + k \Delta T\,(t)\,, \tag{1.6}$$

where k [W m^{-2} K^{-1}] is the sensitivity of atmospheric radiative (LW+SW) cooling to global temperature change ΔT [K], L_c is the latent heat of condensation, and ΔAA(t) is the transient changes in atmospheric absorption directly induced by aerosols and GHGs through atmospheric-only processes. All terms are in the unit of energy flux

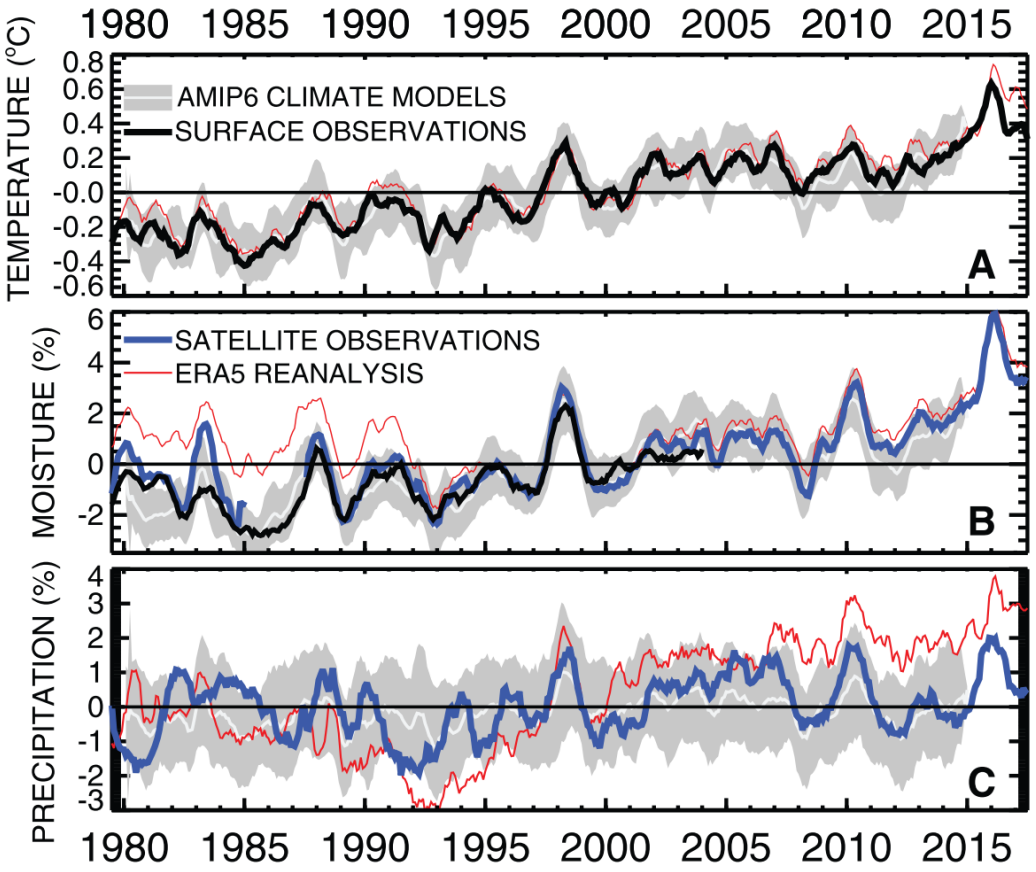

Figure 1.5: Observed and simulated (a) global-mean surface temperature, (b) atmospheric moisture, and (c) precipitation timeseries from 1980 to 2014. The white line indicates the twelve AMIP model ensemble mean, with shading denoting the one standard deviation range. Surface temperature observation is from HadCRUTv4.6 (Morice et al., 2012). Satellite observed column integrated water vapour is from SSM/I and SMMR satellite data (Wentz et al., 2007). Observed precipitation is from GPCPv2.3 (Adler et al., 2017). All timeseries are shown as anomalies (6-month smoothed) relative to the 1994-2000 average (from Allan et al., 2020).

[W m^{-2}]. k can be converted into η (in the unit of % K^{-1}) by dividing by global-mean latent heat released from precipitation (around 82 W m^{-2}; see section 1.2.3). $\Delta AA(t)$ is independent of surface temperature changes and proportional to TOA forcing (Allan et al., 2014; Ming et al., 2010; O'Gorman et al., 2012). $k\Delta T(t)$ scales with transient global mean temperature changes (Allan et al., 2014; Allen and Ingram, 2002; O'Gorman et al., 2012; Samset et al., 2016; Thorpe and Andrews, 2014). The evaluation of reconstructed transient precipitation changes is limited by the availability of global precipitation observations (Adler et al., 2017; Allan et al., 2020) (see also Section 1.2.4), the estimation of near-instantaneous atmospheric radiative cooling (Andrews et al., 2010; Kvalevåg et al., 2013), as well as internal variabilities (e.g. Stephens et al., 2018). However, this approach has demonstrated that different emission scenarios are essential for predicting future precipitation, for their effects on both fast and slow responses. For example, future precipitation projection needs to consider and evaluate the contributions from the cooling effects of anthropogenic aerosols (Wild, 2009) and fast responses mediated by greenhouse gases and absorbing aerosols (Thorpe and Andrews, 2014).

1.3.5 Regional precipitation responses

Precipitation responses to anthropogenic aerosols and GHGs perturbations involves more than just changes in global-mean precipitation. It is well-known that the spatial patterns of precipitation can also change in response to anthropogenic aerosols and GHGs increase. Regional precipitation changes are more complicated to study compared to the global-mean changes. In addition, atmospheric circulation and associated precipitation patterns respond differently to different climate drivers as well (Richardson et al., 2016b; Samset et al., 2017; Tian et al., 2017). Different from global-mean precipitation dominated by the thermodynamics, regional precipitation responses tend to link with dynamical processes (Held and Soden, 2006; Muller and O'Gorman, 2011; Richardson et al., 2018a), particularly at low latitudes (Bond et al., 2013; Dagan et al., 2019).

A warmer climate leads to a poleward expansion of the Hadley cell (Lu et al., 2007; Zhou et al., 2020a), but the circulations will slow down (Held and Soden, 2006; Ma et al., 2018). The lower global-mean precipitation increase rate (around 2 %/°C) compared to the increase rate of water vapour (around 6.7 %/°C) indicates decreased global convective mass fluxes as well as an associated slowed tropical circulation (Ma et al., 2018; Allan et al., 2020). The slowdown can happen in both the zonally

asymmetric (i.e., Walker) and zonal-mean (i.e., Hadley) circulations but is more pronounced in the Walker circulation (Vecchi and Soden, 2007). Global warming also leads to an increase in atmospheric moisture and enhanced horizontal moisture transport, which can amplify the precipitation minu evaporation pattern (Held and Soden, 2006). As a result, precipitation amount can be increased in the moisture convergence zone and decreased in the divergence zone, which is also called the "wet get wetter, dry get drier" mode (Held and Soden, 2006; Allan et al., 2020). However, further studies suggest that this dry-get-drier pattern is a simplified model and does not agree with observed responses over land (Greve et al., 2014; Byrne and O'Gorman, 2015).

The cross-equatorial transport of energy plays an essential role in determining the position of the ITCZ (Bischoff and Schneider, 2016; Byrne et al., 2018) as well as the tropical rainfall associated with it (Boos and Korty, 2016). From an energetic perspective, the ITCZ tends to shift to the warmer hemisphere (Rotstayn and Lohmann, 2002; Schneider et al., 2014; Seo et al., 2014; Undorf et al., 2018; Zhao and Suzuki, 2019). As demonstrated in Section 1.1.1, anthropogenic aerosols have a much higher concentration in the Northern hemisphere than in the Southern hemisphere (Dentener et al., 2006; Mao et al., 2014). An increase in non-absorbing aerosols, e.g. sulphate, can reduce incoming surface solar radiation, which preferentially cools the Northern hemisphere and lead to a northward cross-equatorial energy flux, resulting in a southward shift of ITCZ (Rotstayn and Lohmann, 2002; Allen et al., 2015). Unlike sulphate, an increase in absorbing aerosols, e.g. BC, increases atmospheric radiative heating, leading to a warmer Northern hemisphere and therefore a northward shift of ITCZ (Wang, 2009). Overall, the position of ITCZ can be altered by the spatially heterogeneous pattern of radiative forcing as well as warming patterns caused by aerosols and GHGs (Acosta Navarro et al., 2017; Allan et al., 2010; Zhou et al., 2020a). Climate feedbacks can either amplify (Soden and Chung, 2017) or dampen (Schneider, 2017) the ITCZ shift based on model simulations.

Sahel rainfall variability

One particularly interesting subject for the study of regional precipitation responses to external radiative forcing is the Sahel summertime rainfall, which has experienced large multi-decadal variability during the 20th century with significant socio-economic impacts (Folland et al., 1986; Palmer, 1986; Held et al., 2005; Biasutti, 2013; Scannell et al., 2019; Hirasawa et al., 2020). A number of factors contribute to the Sahel rainfall variability including internal variability (e.g. Held et al., 2005; Giannini and

Kaplan, 2019) and human activities such as the anthropogenic emissions of GHGs and aerosols (e.g. Hoerling et al., 2006; Ackerley et al., 2011; Dong and Sutton, 2015; Hill et al., 2018; Hirasawa et al., 2020). Determining the most important factor contributing to Sahel rainfall variability is complex, as each factor can interact and influence the others (Biasutti, 2019). The importance of each factor can also vary depending on the timescale being considered. Ongoing research aims to better understand and quantify the contributions from each factor in order to improve predictions and develop mitigation strategies (e.g. Hoerling et al., 2006; Dai, 2011; Dong and Sutton, 2015; Hua et al., 2019; Hirasawa et al., 2020).

As described in Section 1.3.2, the response of the Sahel region to external radiative forcing can be also categorised into fast (non-SST mediated) and slow (SST mediated) responses (Liu et al., 2018; Samset et al., 2016; Smith et al., 2018). Sahel rainfall is largely impacted by the large-scale atmospheric circulation patterns, which is related with SST patterns at the same time (e.g. Hoerling et al., 2006; Booth et al., 2012; Hill et al., 2018). The West African monsoon, closely modified by the ITCZ location, brings moisture from the Atlantic Ocean and significantly impacts the rainfall in the Sahelian region (Scannell et al., 2019). It is suggested that anthropogenic aerosols, through a cooling effect on the North Atlantic compared to the South Atlantic, caused the ITCZ to move southward and contributed to the severe drought in the Sahel region during the 1980s (Hoerling et al., 2006; Hwang et al., 2013; Undorf et al., 2018; Biasutti, 2019). A decline in sulphate aerosol burden (as a result of reduced emission of anthropogenic SO_2, a precursor gas of sulphate aerosol) also has led to a northward shift of the ITCZ, which has suggested to contribute to an enhanced Indian monsoon since the 2000s (Hari et al., 2020) and strengthen the West African monsoon (Giannini and Kaplan, 2019). The shift of the ITCZ has also been found to be the critical factor in mediating the observed decadal rainfall seesaw pattern over the southeast Amazon and Sahel from July to September (Hua et al., 2019). Aside from the responses mediated by SST changes, studies also found a direct-atmospheric drying response to aerosols/GHGs perturbations in the Sahel region in atmospheric models with fixed SST fields (Dong et al., 2014; Richardson et al., 2016b; Hirasawa et al., 2020), indicating that anthropogenic aerosols and GHGs can also modulate the Sahel rainfall variability through atmosphere-only (fast) processes. For example, local warming of the North Africa land surface caused by GHGs is responsible for the wetting of the Sahelian region after the 1980s (Dong and Sutton, 2015; Richardson et al., 2016b).

The question of whether the Sahel rainfall variability in the late 20th century was caused by fast or slow responses has been a focus of recent research. Besides the responses to externally driven perturbations, it should also be noted that the internal variability can impact the circulation on decadal scales (e.g. Held et al., 2005; Zhang and Delworth, 2006; L'Heureux et al., 2013; Monerie et al., 2017), which makes it challenging to evaluate and quantify the anthropogenic effects on clouds and precipitation. Attributing contributions to the Sahel rainfall variability are of particular interest (Biasutti, 2019; Dai et al., 2004). However, there is still a lack of consensus on the physical mechanisms behind them (e.g. Biasutti and Giannini, 2006; Bony et al., 2013; Deser et al., 2020; Haywood et al., 2013; He and Soden, 2015; Kasoar et al., 2016; Li et al., 2016; Undorf et al., 2018). Distinguishing the contribution of each driver to Sahel rainfall variability remains uncertain and largely based on the model used in the study (Ackerley et al., 2011; Dong and Sutton, 2015; Jordan et al., 2018; Monerie et al., 2017; Hirasawa et al., 2020).

1.4 Structure of the thesis

Although observational evidence and modelling results show that anthropogenic perturbations have increasingly influenced the hydrological cycle since the last century (Allan et al., 2010; Andreae et al., 2004; Andrews and Forster, 2010; Dai et al., 2004; Douville et al., 2021; Li et al., 2016; Myhre et al., 2017; Pendergrass and Hartmann, 2012; Ramanathan et al., 2001; Trenberth et al., 2014), the sign and magnitude of precipitation responses to anthropogenic perturbations remains considerably uncertain and depends on the types of climate forcing agents, timescale, and spatial scale (Allan et al., 2020; Fläschner et al., 2016; Ming et al., 2010; Rosenfeld et al., 2008; Samset et al., 2016; Stevens and Feingold, 2009).

Existing literature studying the precipitation responses can be categorised into a bottom-up (process-driven) view (e.g. Rosenfeld et al., 2008; Stevens and Feingold, 2009) and a top-down (energetic) view (Muller and O'Gorman, 2011; O'Gorman et al., 2012; Richardson et al., 2018a). This thesis aims to combine the top-down and bottom-up approach to improve the understanding of precipitation responses to anthropogenic perturbations on different spatial and temporal scales and reduces their uncertainties in the current generation of GCMs, with a focus on answering the following three scientific questions:

1. How do absorbing (e.g., BC) and non-absorbing (e.g., sulphate) aerosols differ in the effects on precipitation at different temporal and

spatial scales? Analyses of aerosol effects on precipitation are often complicated by the fact that multiple climate drivers are changing simultaneously. As discussed in previous sections, absorbing and non-absorbing aerosols can have different effects on radiation and precipitation (Douville et al., 2021; Forster et al., 2021). Separating the effects of absorbing and non-absorbing aerosols would advance our understanding of aerosol effects on precipitation. Given the highly regional-dependent nature of aerosol emission and precipitation patterns (Allan et al., 2020; Douville et al., 2021), this thesis also aims to understand the fast and slow precipitation responses to aerosol perturbations on regional scales. Samset et al. (2016), as one of the PDRMIP work, demonstrate the spatial patterns of fast, slow, and total precipitation responses to different climate forcers, including absorbing and non-absorbing aerosols, but with a greater focus on the inter-comparison between different GCMs and different climate forcers. The focus here is to study the underlying mechanisms causing the differences between absorbing and non-absorbing aerosols by distinguishing contributions from each energetic term at various temporal and spatial scales.

In Chapter 2, two sets of simulations with large perturbations in black carbon and sulphate concentration are carried out in ECHAM6-HAM2 to investigate the different effects of absorbing and non-absorbing aerosols on precipitation. A detailed energetic framework is then used to understand the contribution of fast (radiatively or microphysically mediated) and slow (temperature mediated) aerosol effects on precipitation at various spatial scales.

2. How do spatially heterogeneous global warming patterns affect global hydrological sensitivity? Intensification of the hydrological cycle is one of the key consequences of global warming, which has essential impacts on food security, energy supply and economics. However, the percentage increase in global-mean precipitation per degree of global-mean surface temperature increase (η) in the current generation of GCMs still remain considerably uncertain (Douville et al., 2021; Fläschner et al., 2016). Previous studies linked the uncertainties with different treatments of the atmospheric processes responding to the warming, such as different treatments of water vapour shortwave absorption and low cloud schemes. Recent studies suggest that SST warming patterns are important to TOA radiative feedback factors such as lapse rate and clouds (Andrews and Webb, 2018; Ceppi and Gregory, 2017; Dong et al., 2019b; Zhou and Penner, 2016; Zhou et al., 2021). Given that these terms can also affect the atmospheric energy budget (section 1.3.3), it is reasonable to expect that global hydrological cycle intensification is equally dependent on SST warming patterns. However, the relationship between global η (not η_a) and SST warming

patterns has not yet been fully explored, making it an interesting topic to investigate in this chapter.

As a further step from Chapter 2, Chapter 3 focuses on slow responses only and aims at investigating the dependence of global hydrological sensitivity on spatially heterogeneous warming. This chapter analyses an ensemble of simulations forced with 80 SST warming/cooling patches individually placed across the globe in the Community Atmospheric Model 5 (CAM5). The contribution of the pattern effect to hydrological sensitivity uncertainties is further examined in 24 Coupled Model Intercomparison Project (CMIP) models. This chapter also presents reconstructed global-mean precipitation with the pattern effect included, compared with a set of observational data sets to show the importance of the pattern effect when studying hydrological cycle intensification.

3. How do anthropogenic aerosols affect regional rainfall, e.g. Sahel rainfall, and how to disentangle these effects from internal variabilities? Regional precipitation responses to anthropogenic forcing exhibit large uncertainties across GCMs, due to the strong impacts of internal variability (Held et al., 2005; Salzmann et al., 2014), uncertainties in representing aerosol-cloud interactions (Menary et al., 2020), teleconnections with remote aerosol forcing (Hirasawa et al., 2020), signals mixing with GHGs effects (Dong and Sutton, 2015). Sahel rainfall, as one typical example, has experienced significant multidecadal variability over the twentieth century, with large societal implications. Previous work has proposed several drivers to explain the severe drought and the subsequent recovery of Sahel rainfall in the past century, including aerosols, greenhouse gases, and internal variability. Overall, the attribution of Sahel rainfall variability remains ambiguous due to several factors such as the complexity of the factors contributing to it, the limitations of current climate models in accurately representing this region's rainfall variability, and the uncertainty in correctly simulating anthropogenic aerosol climate effects (e.g. ari and aci). This thesis aims to study anthropogenic aerosol effects on Sahel rainfall and investigate their contributions to past Sahel rainfall multidecadal variability.

Inspired by Chapter 3, which demonstrates that global-mean precipitation is sensitive to spatially heterogenous warming, Chapter 4 extends the analysis to regional precipitation and aims to answer the third question. In chapter 4, the anthropogenic aerosol effects on Sahel rainfall are studied by investigating the large ensembles from the Community Earth System Model (CESM-LE) and the Canadian Center for Climate Modeling and Analysis Canadian Earth System Model 2 (CCCma CanESM2-LE). Examining the ensemble mean is expected to eliminate internal variabilities

and help evaluate the effects of anthropogenic aerosols. A detailed process chain is proposed to demonstrate that anthropogenic aerosols have significantly impacted twentieth-century Sahel rainfall multidecadal variability through modifying North Atlantic sea surface temperatures (NASST). This process chain is consistently evidenced by the ensembles of CMIP6 models as well as observational data sets.

Additionally, the results from individual chapters are summarised in Chapter 5. Potential future work is also discussed.

Chapter 2

Aerosol effects on fast and slow precipitation responses

Absorbing and non-absorbing aerosols have distinct effects on both global-mean and regional precipitation. As discussed in Section 1.3.1, the global energy budget strongly constrains the global-mean changes in rainfall in response to aerosol perturbations. Due to the energy transport term, local rainfall changes as responses to aerosol perturbations are more complicated. This chapter uses a detailed energetic framework to understand the contribution of slow (temperature mediated) and fast (radiatively or microphysically mediated) aerosol effects on precipitation at various scales in ECHAM6-HAM2. The energetic framework is used to investigate the different mechanisms of precipitation responses to absorbing and non-absorbing aerosols. It can help us to better understand aerosol-induced precipitation perturbations on different spatio-temporal scales.

This chapter is based on a paper published on Atmospheric Chemistry and Physics with minor changes including reorganising and renumbering the supplementary tables and figures:

Zhang, S., Stier, P., and Watson-Parris, D. (2021). "On the contribution of fast and slow responses to precipitation changes caused by aerosol perturbations". Atmospheric Chemistry and Physics, 21(13), 10179–10197. https://doi.org/10.5194/acp-21-10179-2021.

I designed the study together with the co-authors. I carried out the simulation and analysed the data with input from the co-authors. I wrote and revised the manuscript in response to reviewer comments, with contributions from the co-authors.

2.1 Introduction

Aerosols have been proposed to affect clouds and precipitation to a large extent by interacting with clouds and radiation (Ramanathan et al., 2001). However, aerosol effects on clouds and precipitation remain highly uncertain due to the complex nature of aerosol–cloud–radiation interactions. For example, satellite-estimated and model-simulated aerosol–cloud interactions show large discrepancies in terms of magnitude and even in sign (e.g. Ackerman et al., 2004; Rosenfeld et al., 2019; Wang et al., 2012). Disagreements between different studies can be attributed to methodologies (Gryspeerdt et al., 2014) and model uncertainties (White et al., 2017) and, importantly, are often related to differences in environmental conditions, such as relative humidity, dynamic background, cloud types, and stability (Alizadeh-Choobari, 2018; Khain, 2009; Khain et al., 2008; Lohmann et al., 2007; Zhang et al., 2016). Knowledge about the chain of processes, from aerosol emission to acting as cloud condensation nuclei (CCN) or ice nuclei (IN) and to cloud microphysics, and dynamics, is critical for reducing the uncertainties and understanding the climate system (Ghan et al., 2016), which is referred to as a "bottom-up" approach. However, this is challenging, considering uncertainties can arise from aerosol emissions, activation, cloud microphysics and dynamic regimes (e.g. Gettelman et al., 2013; Ghan et al., 2012; Michibata et al., 2016; Zhang et al., 2016).

An energetic perspective provides an alternative approach to examine aerosol effects on precipitation, which is referred to as a "top-down" approach. For global scales, in equilibrium, latent heat released from rainfall should be energetically balanced by atmospheric radiative cooling together with surface energy fluxes (Allen and Ingram, 2002; Andrews et al., 2010). Climate forcers, such as greenhouse gases (GHGs) and aerosols, which affect the energy budget, can modify the hydrological responses (Kvalevåg et al., 2013; Stephens and Hu, 2010). The energy constraints can be applied to regional rainfall by introducing the energy transport term (H) (Muller and O'Gorman, 2011; Richardson et al., 2016b). The local energy budget at equilibrium can be addressed as the following equation:

$$L\delta P = \delta Q + \delta H, \tag{2.1}$$

where δ denotes the difference between two climate states (e.g., with and without anthropogenic aerosols). L refers to the latent heat of condensation, and P is the precipitation rate, so LP refers to the atmospheric latent heating rate from rainfall. H is the column-integrated divergence of dry static energy, which is expected to be

zero on a global scale. Q is the atmospheric diabatic cooling (except for latent heat released from precipitation), consisting of atmospheric radiative cooling (ARC) and downward surface sensible heat flux (-SH). ARC is the difference of shortwave (SW) and longwave (LW) fluxes between top of the atmosphere (TOA) and the surface. Changes in ARC are largely balanced by latent heat released from global-mean precipitation responses (Allen and Ingram, 2002), while changes in the energy transport term (δH) are essential in determining the spatial pattern of precipitation response (Muller and O'Gorman, 2011). Dagan et al. (2019) further demonstrated that whether precipitation responses are more correlated with changes in Q or H depends on the latitude considered. In the extra-tropics, diabatic cooling/heating perturbations are confined to local scales due to strong Coriolis force (thus weak energy transport), and hence the latent heating must balance diabatic cooling according to the energy budget. However, in the tropics, horizontal gradients of dry static energy are small due to the weak Coriolis force. Therefore, local strong diabatic heating perturbations can lead to thermally direct circulations that drive convergence and divergence of moisture and dry static energy. This low-level convergence of mass and moisture can lead to vertical motion and thus an increase in precipitation. So rainfall does not necessarily have to positively correlate with diabatic cooling (Dagan et al., 2019).

Absorbing and non-absorbing aerosols can have different effects on each energy budget term and thus precipitation. On the global scale, black carbon (BC), a strongly absorbing aerosol, can stabilise the atmosphere and suppress precipitation via strong shortwave absorption for short timescales, but it can also increase precipitation by warming up the surface temperature on longer timescales (e.g. Pendergrass and Hartmann, 2012). The net effect can be uncertain among GCMs (Samset et al., 2016) and is sensitive to the altitude where the BC is added (Ming et al., 2010). Unlike BC, non-absorbing aerosols, for example sulfate (SUL), reduce precipitation predominantly by decreasing SST on long timescales through the dimming effect, whereby SUL scatters incoming solar radiation back to the space (Boucher et al., 2013; Kasoar et al., 2018). Additionally, the surface sensible heat flux is more sensitive to changes in BC than SUL (Myhre et al., 2018; Richardson et al., 2018a). On zonal scales, due to the relatively short life cycle of aerosols, the radiative forcing caused by aerosols is hemispherically asymmetric, which leads to a warmer Northern Hemisphere for the BC case and a colder one for the SUL case. As a result, the cross-equatorial energy fluxes lead to the intertropical convergence zone (ITCZ) shifting towards the warmer hemisphere (Wang, 2009; Bischoff and Schneider, 2016; Zhao and Suzuki, 2019; Keshtgar et al., 2020; Zanis et al., 2020). On regional scales, it is

also worth noting that SUL is usually more suitable as CCN due to its higher hygroscopicity compared to BC. It can therefore alter cloud microphysics and subsequent precipitation formation and regional rainfall by interacting with clouds. However, the susceptibility of precipitation to sulfate aerosols (and the precursors) shows large discrepancies in satellite-estimated precipitation susceptibility to aerosols from several products (Bai et al., 2018; Haynes et al., 2009), and a broad inter-model spread (uncertainty) in GCMs (Ghan et al., 2016; Samset et al., 2016). Some studies also found that the sensitivity of precipitation to sulfate aerosols varies between model-simulated and satellite-estimated results, in terms of magnitude and sometimes in sign (Liu et al., 2020; Wang et al., 2012).

These responses of precipitation have been conventionally suggested to be composed of fast and slow responses (Andrews et al., 2009; Bala et al., 2010). Fast responses, on the timescale from days to months, are independent of changes in sea surface temperature (SST) and mostly dependent on instantaneous changes in atmospheric radiative heating/cooling (O'Gorman et al., 2012; Richardson et al., 2016a). It should be noted that even though SST is unchanged in atmosphere-only models, the land surface temperature is generally still allowed to vary (Stjern et al., 2017). Slow responses, on the timescale of years, are mediated by changes in sea surface temperature (SST) and strongly correlate with top-of-atmosphere (TOA) forcing (Kvalevåg et al., 2013; Lambert and Webb, 2008; Suzuki et al., 2017). Distinguishing contributions from fast and slow responses is essential for understanding the mechanisms that cause the precipitation changes. For example, Bony et al. (2013) examined the responses of tropical rainfall to increasing GHGs. They found that the fast processes weaken the vertical motion and counteract a considerable part of the increasing trend induced by surface warming. Shaw and Voigt (2015) have investigated predicted changes in the summertime Asian monsoon under a warming scenario caused by GHGs, and the fast responses caused by direct radiative effect are generally opposite to the slow impacts caused by the SST warming. The changes in circulation are essential for local climate responses, including clouds, radiation, and precipitation (Johnson et al., 2019), whereas the spatial distribution of aerosols radiative forcing in turn affects atmospheric circulations (Chemke and Dagan, 2018).

Distinguishing contributions from different energetic terms is also helpful for understanding physical processes and model differences (DeAngelis et al., 2015). It has historically been used to distinguish contributions from clouds and aerosols when studying aerosol radiative forcing (Forster et al., 2007; Ghan, 2013). While energetics have been applied before to analyse precipitation responses (e.g. Ming et al.,

2010; Dagan et al., 2019), here we further decompose them into individual terms to provide additional insights. Changes in the energy transport term (δH) can be decomposed into eddy and mean state components, which are further associated with changes in thermodynamics and dynamics (Muller and O'Gorman, 2011; Richardson et al., 2018a). Changes in ARC can be further decomposed into contributions from aerosol (mostly through SW absorption), clouds (mostly through LW radiative cooling), and clear-clean sky (mainly from water vapour, greenhouse gases, and the Planck feedback). While it has long been appreciated that changes in ARC are essential in balancing latent heat release from precipitation responses on global scales, their relationship on zonal-mean or regional scales (and which the ARC component dominates) has not been fully explored.

The Precipitation Driver Response Model Intercomparison Project (PDRMIP) (Myhre et al., 2017) has conducted several experiments to study the response of precipitation to different climate forcers, such as GHGs, aerosols, and solar radiation change (e.g. Samset et al., 2016; Stjern et al., 2018). It has been found that the fast response dominates the global-averaged precipitation responses to BC perturbation, which differs from other drivers of climate change (Samset et al., 2017; Stjern et al., 2017). It has also been shown that BC contributes to the most substantial uncertainties among GCMs in simulating the changes in surface temperature and precipitation, due to different parameterisations of physical, chemical, and dynamical processes involved on the path from BC emission to the final climate impact (e.g. Stjern et al., 2017). However, it is worth noting that most PDRMIP research focuses on global-mean changes and addressing uncertainties among GCMs (e.g. Myhre et al., 2017; Richardson et al., 2018a). For example, Samset et al. (2016) showed the spatial patterns of fast, slow, and total responses of precipitation to different climate forcers including absorbing and non-absorbing aerosols, with a greater focus on the intercomparison between different GCMs and different climate forcers. Here we study the fast and slow response contribution to total response of precipitation with a focus on the comparison between absorbing and non-absorbing aerosols, and in particular on the underlying mechanisms causing the differences by distinguishing contributions from each energetic term at various scales.

In light of previous work illustrating the potential of energy budget constraints for understanding regional precipitation changes, and the fact that absorbing and non-absorbing aerosols impact the response on two distinct timescales, we aim to answer three questions. (1) What are the contributions of fast and slow responses to total precipitation changes on global and regional scales? (2) What is the dominant

energetic term in precipitation responses to absorbing/non-absorbing aerosol perturbations on different spatial and temporal scales? (3) How do we relate changes in local thermodynamics and large-scale circulation to changes in energetic terms and quantify their contribution to precipitation responses?

2.2 Methods

The global aerosol-climate model ECHAM6-HAM2 (Stier et al., 2005; Zhang et al., 2012; Tegen et al., 2019; Neubauer et al., 2019) is used to perform all the experiments. It is based on the general circulation model ECHAM6 (Stevens et al., 2013) and is coupled to the aerosol module HAM2 (Stier et al., 2005; Zhang et al., 2012). A two-moment cloud microphysics schemes is used to prognostically predict the number and mass mixing ratios for both cloud water and ice (Lohmann et al., 2007; Lohmann and Hoose, 2009). The parametrisations for convection, including cumulus convection and deep convection, are based on the scheme by Tiedtke (1989) and Nordeng (1994). The activation of CCN to cloud droplets is adopted from Abdul-Razzak and Ghan (2000), which is based on Köhler theory (Köhler, 1936). It should be noted that freshly emitted BC is assumed to be hydrophobic and does not act as cloud condensation nuclei. However, subsequent condensation of sulfuric acid and mixing with hydrophilic sulfate aerosols will increase its hygroscopicity so that internally mixed BC particles can activate as CCN (Stier et al., 2006). In HAM2.3, BC can act as ice nuclei through heterogeneous freezing, but only in the accumulation and coarse modes (Neubauer et al., 2019). The parameterisation for autoconversion is from Khairoutdinov and Kogan (2000). There are 16 spectral shortwave bands in the solar radiation scheme and 14 spectrum bands in the longwave radiation scheme (Pincus and Stevens, 2013). The general circulation model ECHAM6 provides essential meteorological backgrounds such as temperature, pressure, wind, and humidity and is coupled to HAM2 for the parameterisations of several aerosol processes such as aerosol activation and deposition.

Emissions of anthropogenic BC, organic carbon, and sulfate are from the Atmospheric Chemistry and Climate Model Intercomparison Project (ACCMIP) emission dataset (Lamarque et al., 2010), including emissions from industry, agriculture, aircraft, domestic, ships, and waste. Biomass burning emissions are also from the ACCMIP dataset, including both natural and anthropogenic biomass burning (Lamarque et al., 2010). Dimethyl sulfide (DMS) emission is interactively related to the 10 m

wind speed and concentration in seawater. Biogenic volatile organic carbon and volcanic emissions follow the AeroCom phase II emission dataset (Dentener et al., 2006). All the emissions are prescribed for the year 2000, so there are no interannual variabilities of emissions. Simulations are performed at T63 (1.9° ×1.9°) spectral resolution using 47 vertical levels (L47).

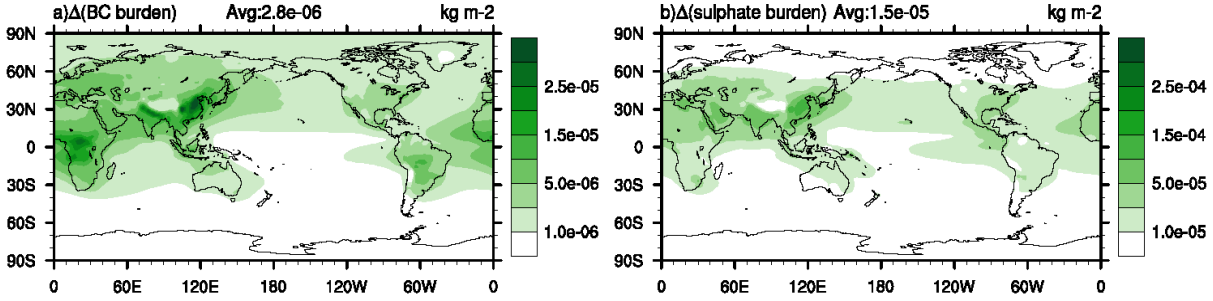

Figure 2.1: Simulated global distribution of (a) BC burden (verticalintegrated aerosol mass) difference between BCx10 case and baseline, (b) sulphate burden difference between SO_2×5 case and baseline.

To study the precipitation response to absorbing and non-absorbing aerosol perturbations, we analyse two scenarios: one with a 10-fold increase in BC emissions (hereafter 10BC) and another with a 5-fold increas e in sulfur dioxide (hereafter 5SUL), relative to baseline emissions in the year 2000 (Tegen et al., 2019). It should also be noted that the increases in BC emissions here include both anthropogenic and natural sources. This is because the biomass burning emission, as a large source of BC, includes both anthropogenic emissions (e.g. agricultural waste burning) and naturally occurring wildfire emissions. The anthropogenic contribution to wildfire emissions is assumed to dominate but subject to significant uncertainties (e.g. Lamarque et al., 2010; van Marle et al., 2017), and it is very uncertain to separate the anthropogenic contribution of wildfires. However, the increases in SO_2 emissions are all anthropogenic because the sources of volcanic sulfur are kept the same. The main purpose of this work is to better understand the mechanisms of aerosol-precipitation interactions, with a focus on, but not limited to, anthropogenic aerosol effects. As only particular aerosol emissions are changed in each perturbation, the differences between baseline and the perturbed case can be interpreted as aerosol effects. Geographical patterns of aerosol burden change are shown in Fig. 2.1. We chose different multipliers for the two aerosol species here to make the aerosol effects statistically large enough and keep their radiative forcing at the same magnitude (Myhre et al., 2017). Another reason is to make our results comparable with PDRMIP work (Samset et al., 2016).

We run the simulations for 100 years with a mixed-layer ocean (MLO), which is 50 m in depth (Dallafior et al., 2016). The ocean heat transport term (also known as the Q flux) is prescribed from the 30-year PDRMIP baseline present day setup (Myhre et al., 2017), which also means the ocean dynamics are unchanged. Therefore, the changes in SST are caused by local responses to net surface heat flux, and the responses in ocean circulations are omitted. To obtain the equilibrium state of precipitation responses to aerosol perturbations, i.e. the total response (ΔP_{total}), we use the last 50 years of the simulations because at that time the model has reached approximate equilibrium (Samset et al., 2016). We acknowledge that it might take more than 100 years for a slab ocean model to fully equilibrate. Therefore we also performed a Gregory-style regression (Gregory and Webb, 2008) to check the equilibrium for the BC and SUL cases (Fig. 2.2).

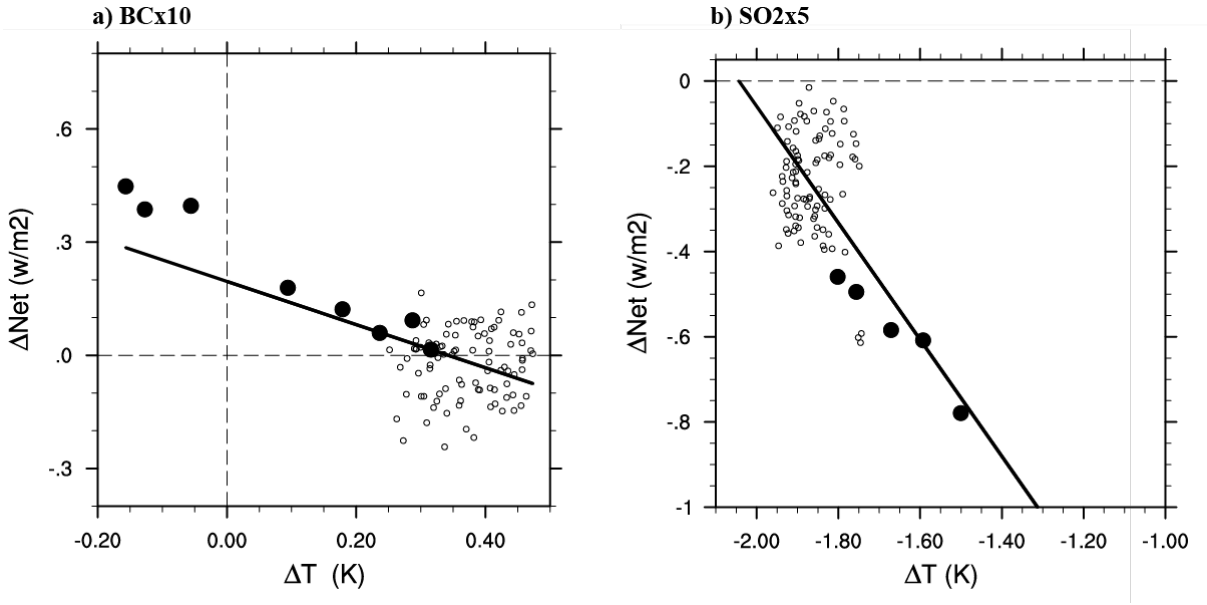

Figure 2.2: A Gregory-style regression between changes in surface temperature and changes in net energy flux at the top of the atmosphere, for (a)10 times black carbon and (b) 5 times sulphur dioxide perturbation experiments, respectively. Each dot represents the annual average of each individual year (100 years in total). The solid dots represent the first 8 years since the aerosol perturbations were added.

For the BC experiment, it is very likely to reach equilibrium after approximately 50 years. For the SUL case, the energy imbalance is significantly reduced and reaches a near equilibrium after a 50-year run as well, but it is suggested that more than 100 years of simulation are needed to fully equilibrate. So the total response of surface temperature to 5-fold SUL should be even lower (more negative). Considering the

purpose of our study is to understand the mechanisms of precipitation responses to aerosols, an exact equilibrium is not critical here and our conclusions still apply to an approximate equilibrium. Another simulation is run for 20 years with fixed sea surface temperatures (fSST) and the last 10 years are used. The precipitation responses for fSST simulations can be interpreted as the fast response (ΔP_{fast}). The slow response is then calculated as the difference between the total response and the fast response (Myhre et al., 2017; Samset et al., 2016):

$$\Delta P_{slow} = \Delta P_{total} - \Delta P_{fast}. \tag{2.2}$$

The length of integration period is sufficient to derive the fast and total responses because the fast response of precipitation occurs on timescales from days to months and a slower response on a timescale of years (Myhre et al., 2017).

Since fast and slow responses are examined from an energetic perspective, we focus on how the atmospheric diabatic cooling (Q) and energy transport terms (H) respond to aerosol perturbations in fSST and MLO simulations. H is calculated offline, as a residual by using the energy budget equation. Following previous studies (e.g. Muller and O'Gorman, 2011; Richardson et al., 2016b), Q is the combination of atmospheric radiative cooling (ARC) and downward surface sensible flux (-SH), as follows:

$$Q = \mathrm{ARC} - \mathrm{SH}. \tag{2.3}$$

ARC is defined as net shortwave (SW) and longwave (LW) radiation loss of the atmospheric column, which can be calculated from the difference between the top of atmosphere (TOA) and surface radiative fluxes (downward positive), defined as

$$\mathrm{ARC} = (\mathrm{LW}_{TOA} + \mathrm{SW}_{TOA}) - (\mathrm{LW}_{SUR} + \mathrm{SW}_{SUR}). \tag{2.4}$$

Ghan (2013) suggested using an additional radiative call in models to distinguish aerosol radiative forcing from aerosols, clouds, and surface albedo. In addition to the radiative call in which cloud absorption and scattering are neglected, the additional radiative call also neglects aerosol scattering and absorption (that is, aerosol optical depth set to zero). This additional radiative call has been widely adopted in current GCMs (including the model ECHAM6-HAM2 used in this study) to better estimate aerosol effects (e.g. Zhang et al., 2016). Following Ghan (2013) and applying the method on atmospheric energy budget, we further decompose ARC into contributions from clouds, aerosols and clear-clean sky (without aerosols and clouds) separately

(Equation 2.5), by using the same additional radiation call to calculate ARC from the clear-clean sky ($ARC_{clear,clean}$):

$$\mathrm{ARC} = \mathrm{ARC}_{aerosol} + \mathrm{ARC}_{cloud} + \mathrm{ARC}_{clear,clean}, \tag{2.5}$$

$$\mathrm{ARC}_{aerosol} = \mathrm{ARC} - \mathrm{ARC}_{clean}, \tag{2.6}$$

$$\mathrm{ARC}_{cloud} = \mathrm{ARC}_{clean} - \mathrm{ARC}_{clear,clean}. \tag{2.7}$$

Since ARC consists of radiative heating/cooling from aerosols (mainly through aerosol direct SW absorption), clouds (primarily through cloud LW absorption/cooling), and clear-clean sky (mainly though LW radiative absorption/cooling from GHGs, water vapour, and Planck feedback), it is helpful to systematically study the effect of absorbing and non-absorbing aerosols on each decomposed energy term and to further connect those to changes in precipitation.

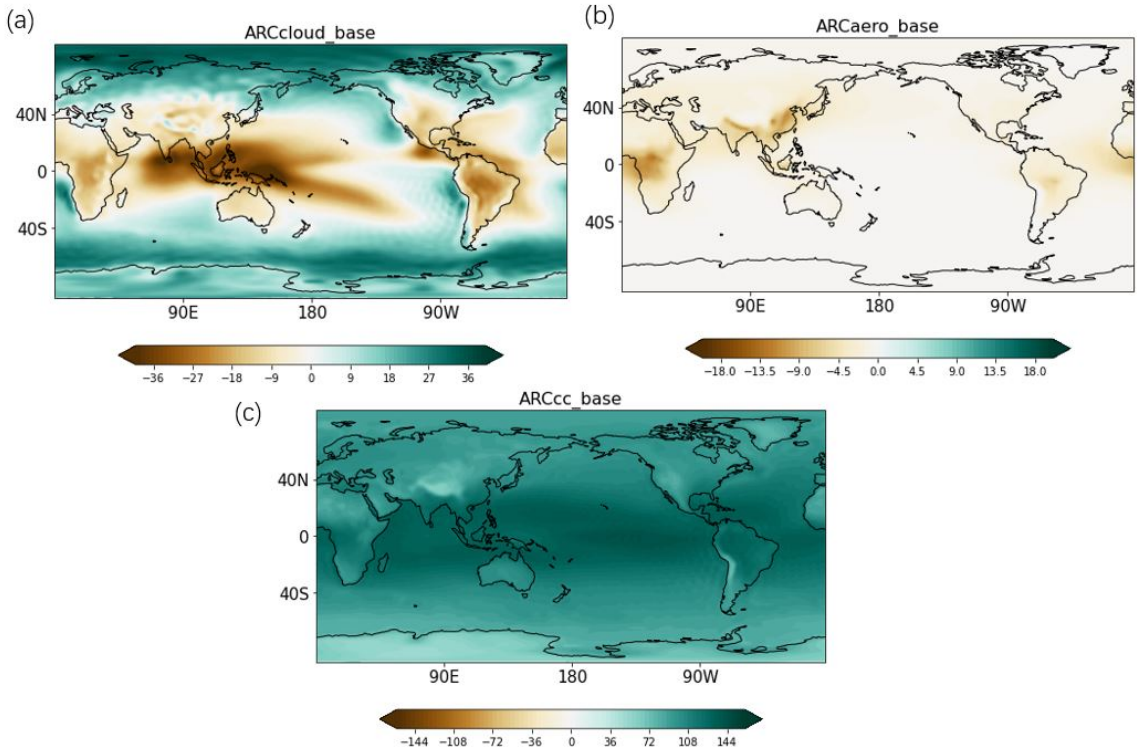

Figure 2.3: ECHAM6-HAM2 simulated global distribution of atmospheric radiative cooling from (a) clouds, (b) aerosols, and (c) clear-clean sky. (Unit: W m^{-2})

It is worth noting that $\Delta ARC_{aerosol}$ only includes direct interactions with radiation here and is much more sensitive to absorbing aerosol burden rather than non-absorbing aerosols. Despite the significant negative radiative forcing at TOA (Boucher

et al., 2013), non-absorbing aerosols do not significantly modify atmospheric radiative absorption, as they act to decrease net SW radiative fluxes at both the surface and TOA in the same way. Non-absorbing aerosols can affect atmospheric radiative absorption via changing absorbing aerosol life cycles (Stier et al., 2006), but the impacts can be very small. It should also be noted here that changes in ARC_{cloud} include aerosol indirect effects (interactions with clouds) on ARC and cloud feedbacks in slow responses, but most of the changes are from LW radiation from clouds (e.g. Lubin and Vogelmann, 2006) rather than SW radiation. And its magnitude depends on the temperature (height) at both cloud top and bottom as well as on the ice concentration at cloud top (see Fig. 2.3a for baseline ARC_{cloud}). As aerosol effects on convective clouds are not explicitly simulated in ECHAM6-HAM2 (or most GCMs) yet, changes of ARC_{cloud} from convective clouds are mostly caused by aerosol-induced changes in dynamics. Baseline ΔARC_{cloud}, $\Delta ARC_{aerosol}$, and $\Delta ARC_{clear,clean}$ can be seen in Fig. 2.3.

2.3 Results

2.3.1 Global mean responses

Table 2.1 shows the global-mean fast, slow, and total responses of the energy budget terms, including atmospheric latent heat release from precipitation ($L\Delta P$) and other atmospheric diabatic cooling terms, in response to increased BC and SUL emission for the fSST and MLO simulations, respectively. Globally averaged precipitation is decreased in both the BC and SUL experiment, and the associated reduced latent heating is primarily balanced by decreased ARC (Table 2.1). However, there are some substantial differences between BC and SUL cases after decomposition into different contributions.

Table 2.1: ECHAM6-HAM2 simulated multi-annual global averaged fast, slow, and total responses of atmospheric energy budget terms (LP - the atmospheric latent heating rate from rainfall, ARC - atmospheric radiative cooling, SH - sensible heat flux) and surface temperature (T) in response to an increase of a factor of 10 in black carbon (BC) emission and a factor of 5 in sulfate (SUL) precursor emission. ARC has been further decomposed into the contribution from aerosols, clouds, and clear-clean sky. All terms are shown in equivalent precipitation units of mm d^{-1}.

W m^{-2}	$L\Delta P$	ΔARC	$\Delta ARC_{\text{aerosol}}$	$\Delta ARC_{\text{cloud}}$	$\Delta ARC_{\text{clear,clean}}$	$-\Delta SH$	ΔT (K)
Fast, 10BC	−0.13	−0.21	−0.29	0.03	0.05	0.08	−0.03
Slow, 10BC	0.01	0.02	−0.01	0.00	0.04	−0.01	0.39
Total, 10BC	−0.11	−0.18	−0.30	0.03	0.09	0.07	0.35
Fast, 5SUL	−0.01	−0.01	0.01	0.00	−0.02	0.00	−0.14
Slow, 5SUL	−0.14	−0.13	0.00	0.02	−0.15	−0.01	−1.73
Total, 5SUL	−0.15	−0.14	0.01	0.01	−0.17	−0.01	−1.87

For the BC case, the decreased precipitation from total responses ($L\Delta P$ around -3.26 W m^{-2}) is mostly contributed by fast responses ($L\Delta P$ around -3.64 W m^{-2}). Slow responses ($L\Delta P$ around 0.38 W m^{-2}) lead to precipitation increases but much smaller in magnitude precipitation compared to the fast responses. Previous studies suggest that fast responses are largely mediated by atmospheric radiative absorption while slow responses scale with surface temperature change (Samset et al., 2016). An increase in BC emissions can increase atmospheric absorption to a large extent, which is a near-instantaneous process. This can be seen from the decomposition of ARC, which shows that the decreased ARC from fast and total responses is mainly due to the increased SW absorption from BC aerosols ($\Delta ARC_{aerosol}$) (Table 2.1). However, the change of global-mean surface temperature in the BC case is small (around 0.4 K). That is because for an increase in BC emissions, reduction of downward SW radiation largely counteracts increased downward LW radiation from the warmer atmosphere. As a result, the change of surface temperature is regionally dependent and globally small (Stjern et al., 2017) (see also Fig. 2.4). Large changes in $\Delta ARC_{aerosol}$ and small changes in global-mean surface temperature lead to a dominating contribution from fast responses to total global-mean rainfall changes for the BC cases.

For the SUL case, the slow response dominates the total response (Table 2.1). Since SUL is a non-absorbing aerosol, which decreases net SW radiative fluxes at both the surface and TOA through scattering solar radiation, atmospheric absorption changes little. Most of the reduced ARC in the total response is from changes in clear-clean sky radiative cooling ($\Delta ARC_{clear,clean}$) from slow responses mediated via surface flux changes. As SUL decreases SW radiation reaching the surface, the global-mean temperature decreases around 2 K on a relatively long timescale due to the

high capacity of oceans (a slow process). Decreased global-mean temperature further leads to reduced $ARC_{clear,clean}$ from decreased atmospheric column temperature (i.e. Planck feedback) (Zelinka et al., 2020) and decreased water vapour content, which is controlled by the Clausius-Clapyron relationship (Suzuki and Takemura, 2019).

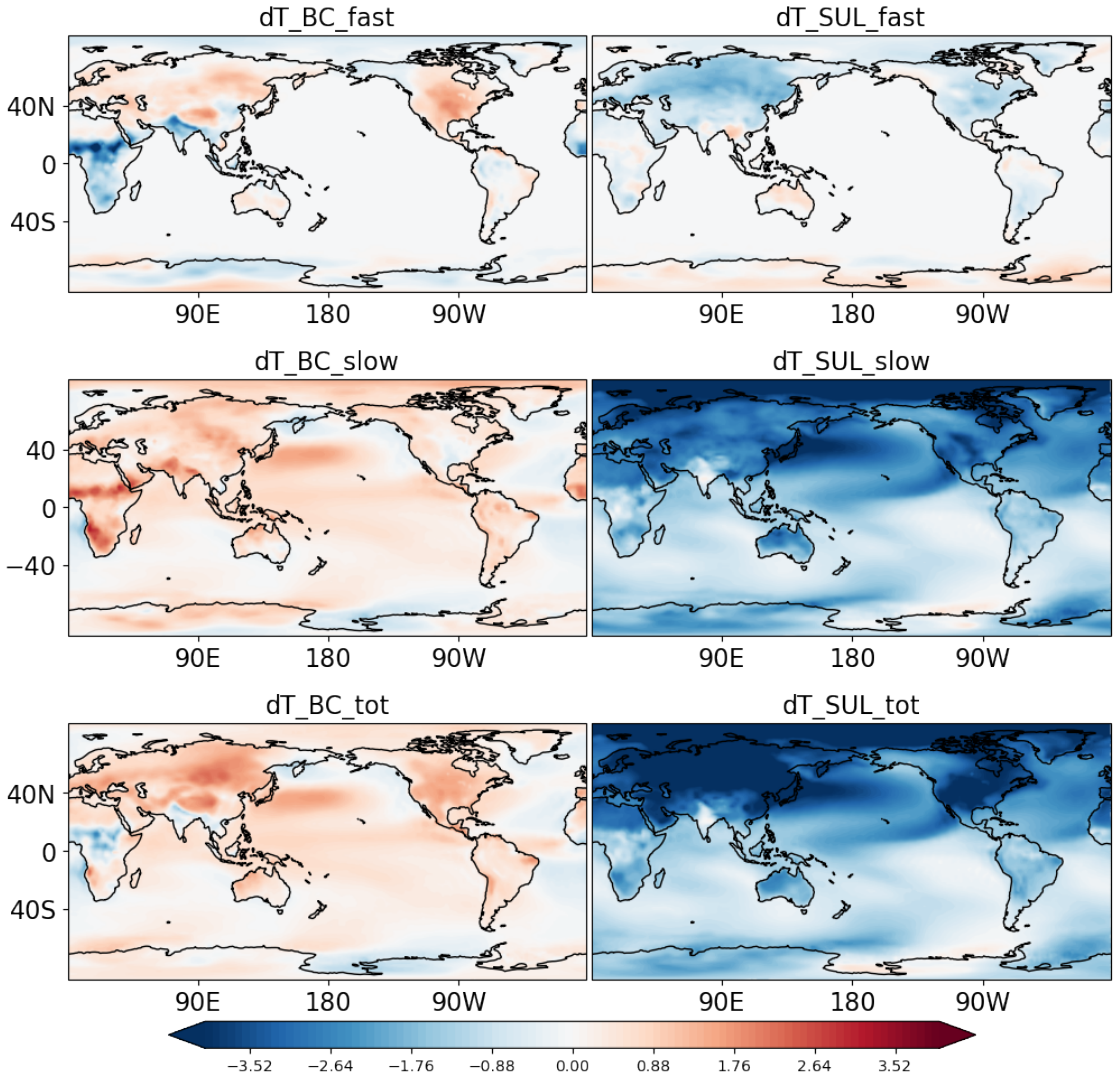

Figure 2.4: ECHAM6-HAM2 simulated geographical patterns of multi-annual mean surface temperature change in response to increasing (left column) 10 times BC emission and (right column) 5 times SUL precursor emission for (first row) total, (second row) fast, and (third row) slow responses. (Unit: K)

The contribution of changes from SH acts to counteract nearly one-third of the decreased ARC in fast and total responses for the BC case, which is much larger than that in the SUL case. This is because the absorbing aerosols heat the atmosphere and decrease the temperature difference between near-surface air and the surface,

resulting in reduced upward SH fluxes. So changes in SH are also dominated by the fast response and mainly act to increase precipitation from an energetic perspective, counteracting the decreasing effect induced by ARC in the BC case (Ming et al., 2010).

2.3.2 Regional responses and their contributions

The geographical patterns of precipitation responses are substantially different between BC and SUL, in both the fast and total responses (Fig. 2.5). The patterns are similar to Samset et al. (2016), in which they showed an ensemble result with a focus on inter-comparison among several models and climate forcers. For the total response, it shows a distinct pattern of an ITCZ shift in response to increased BC and SUL emission. The ITCZ tends to shift northward in the BC case while it shifts southward in the SUL case (Fig. 2.5a and b). Since BC warms (SUL cools) the Northern Hemisphere, there is an enhanced southward (northward) cross-equatorial energy flux in response to the aerosol perturbation, resulting in ITCZ being shifted towards the warmer hemisphere (Bischoff and Schneider, 2016; Wang, 2009). Changes in tropical rainfall are dominated by changes in the Hadley cell in response to the enhanced cross-hemispheric energy fluxes. Fig. 2.5e and f further show that the slow response mainly contributes to the ITCZ shift in both cases. This will be further demonstrated Section 2.3.3 and 2.3.4.

The fast response of precipitation in the BC case (Fig. 2.5c) shows a land-sea contrast pattern in the tropics, in which rainfall increases in central Africa while it decreases in the surrounding tropical ocean. Central Africa is one of the main source regions of BC emission through biomass burning, and tenfold increase of BC emissions makes the burden changes significant (Fig. 2.1). The pattern of the fast precipitation response in the BC case is similar to the pattern of rapid precipitation response to CO_2 shown in (Richardson et al., 2016a). But the mechanism is not exactly the same. In the CO_2 case, even though SST remains unchanged, CO_2 can increase land surface temperature, and the land-sea temperature contrast (warmer land and unchanged ocean) leads to a shift of convection to over land (Richardson et al., 2016a). For an increase in BC emissions, increased downward LW radiation from the warmer atmosphere is largely counteracted by a reduction of downward SW radiation. As a result, surface temperature is decreased in central Africa (Fig. 2.4), which differs from the CO_2 case. But increased BC emission can still warm up the lower troposphere and lead to more ascending motions over central Africa (Fig. 2.6) (Dagan et al., 2019; Roeckner et al., 2006). As for the SUL case, the rapid precipitation response

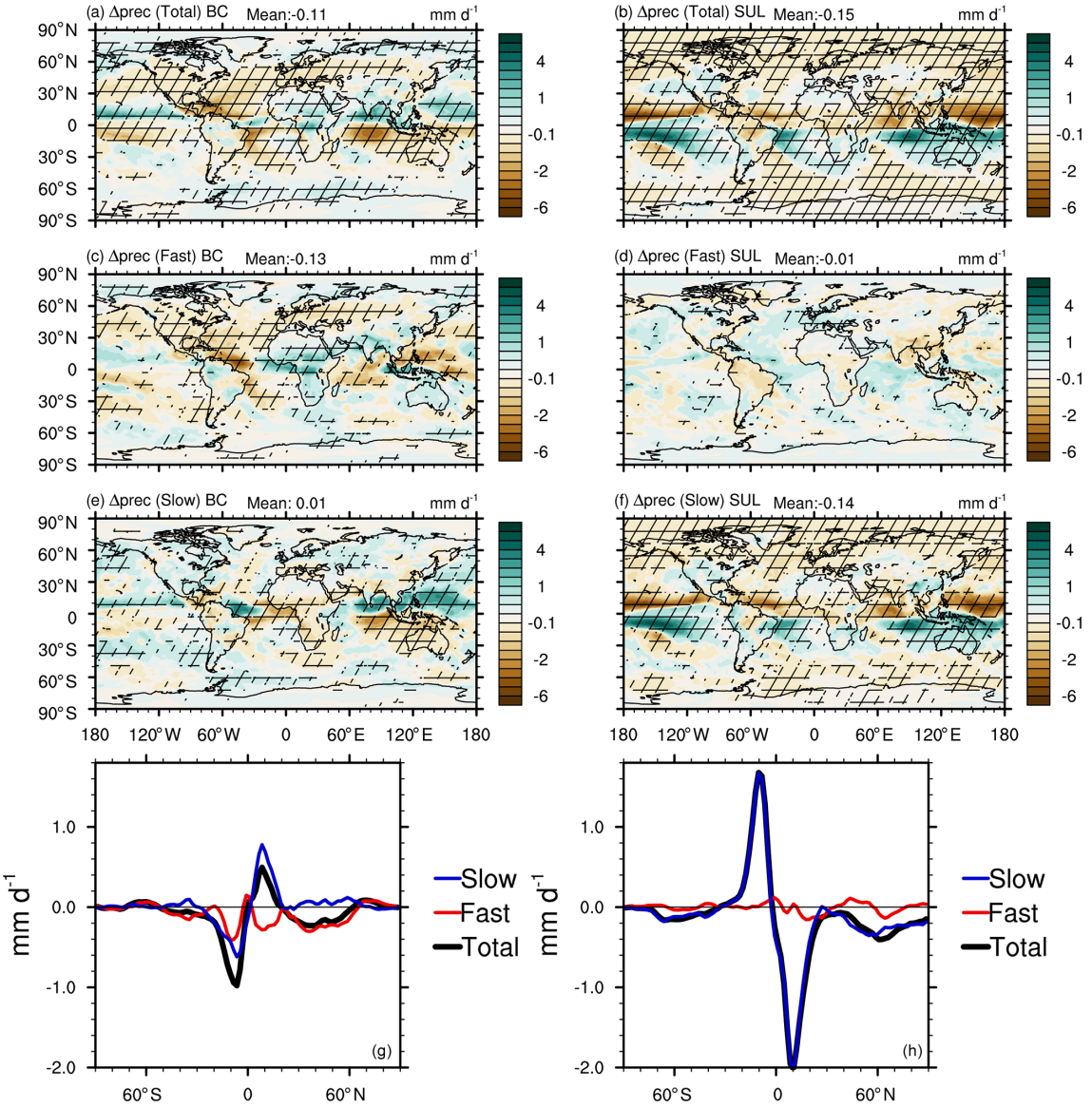

Figure 2.5: ECHAM6-HAM2 simulated geographical patterns of multi-annual mean precipitation change in response to 10-fold increased (a, c, e) BC emissions and (b, d, f) 5-fold increased SUL precursor emissions for (a, b) total, (c, d) fast, and (e, f) slow responses. Hatching indicates where the changes are significant (90% confidence). (g, h) Zonal averages of changes in precipitation in terms of total, fast, and slow responses to 10-fold increased (g) BC emission and (h) 5-fold increased SUL emission.

shows an opposite land-sea contrast pattern in the tropics, because SUL cools the land temperature (Fig. 2.5d) as land surface temperature is not constrained in fSST runs. However, considering SUL does not directly affect the diabatic heating/cooling in the atmosphere, which differs from BC, the changes are small and not statistically significant over most regions. There are still some exceptions. For example, southeast Asia, which has the largest contribution to SUL emission, and SUL impacts on rainfall through cooling of land temperature as well as interactions with monsoon (e.g. Wang et al., 2019). Decreased surface temperature over continents, such as South America, leads to a decrease of precipitation in most land regions as well as an increase in surrounding oceans (i.e. southeast Pacific Ocean) (Fig. 2.5d).

In the zonal mean, precipitation is decreased over Northern Hemispherc mid-latitudes in both BC and SUL cases for total responses, but different processes contribute to the total response. Most of the precipitation changes over high latitudes are contributed by fast responses in the BC case (Fig. 2.5g) and slow responses in the SUL case (Fig. 2.5h). Dagan et al. (2019) showed different responses of rainfall to aerosol perturbation in the tropics and extra-tropics. They demonstrated that precipitation responses are more correlated with the energy transport term (H) in the tropics where heating anomalies can be compensated for by large-scale thermally driven circulations, whereas extra-tropical rainfall responses are constrained by radiative cooling in the extra-tropics due to the stronger Coriolis force (thus weak energy transport). The different contribution from fast and slow processes between the BC and SUL case indicates different responses in the diabatic cooling in the extra-tropics, and this will be addressed later from an energetic perspective.

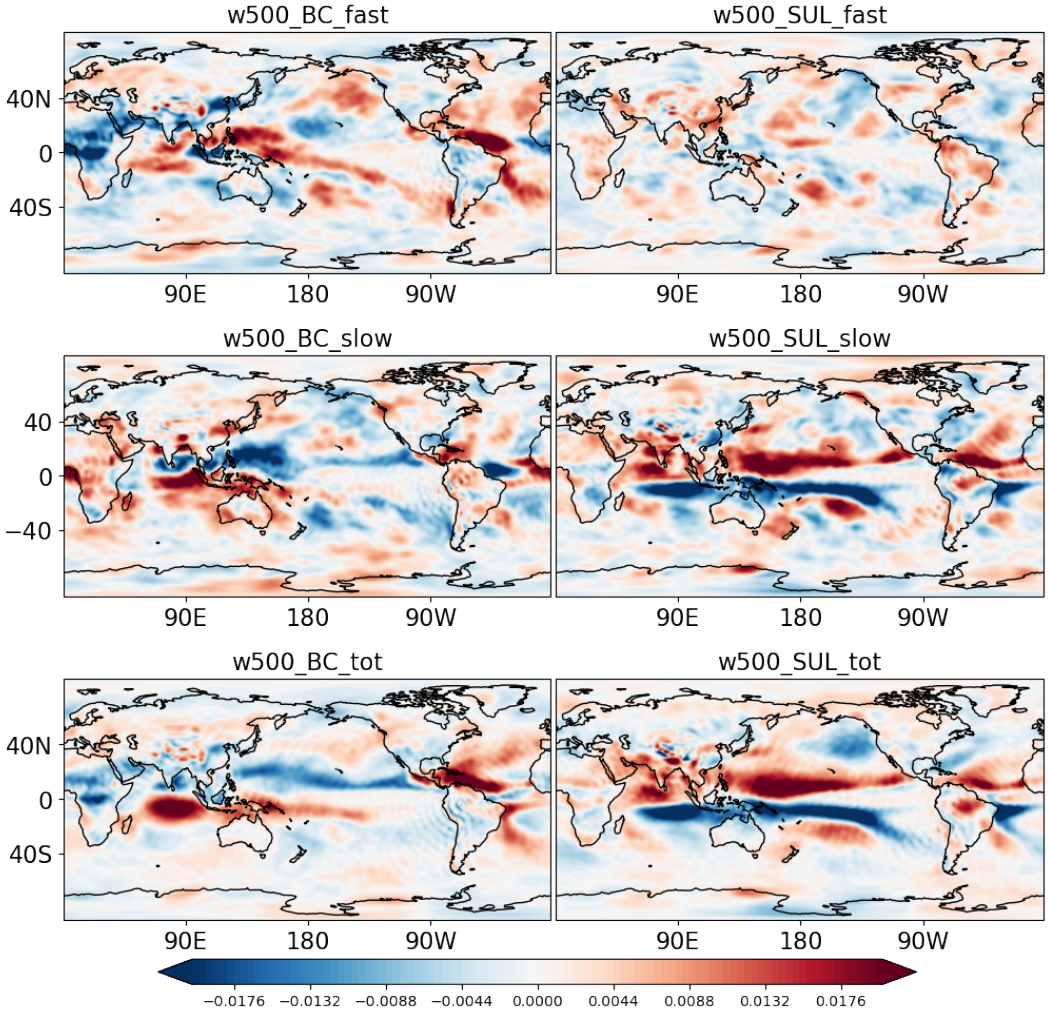

Figure 2.6: Simulated geographical patterns of multi-annual mean vertical pressure velocity change in response to increasing (left column) 10 times BC emission and (right column) 5 times SUL emission for (first row) total, (second row) fast, and (third row) slow responses. Unit: Pa s^{-1}

Fig. 2.7 quantifies how fast and slow responses contribute to total responses of precipitation on regional scales. We used the response ratio which has also been used in Samset et al. (2016), as follows

$$R_{resp} = (|\Delta P_{fast}| - |\Delta P_{slow}|)/(|\Delta P_{fast}| + |\Delta P_{slow}|). \tag{2.8}$$

If R_{resp} is larger than 0 and close to 1, it means most of the total responses are contributed by fast responses. If R_{resp} is less than 0 and close to -1, it means slow responses dominates over fast responses. Samset et al. (2016) showed continentally based results of R_{resp} for different climate forcers and found the variabilities among models. Here Fig. 2.7 focuses only on BC and SUL perturbations and quantitatively

gives us the geographical patterns of contributions from fast and slow responses to total precipitation change. For the BC case, generally the response over Northern Hemispherc mid-latitudes is consistent with the globally averaged result shown in Fig. 2.1, which shows that the precipitation change is dominated by fast responses (Fig. 2.7a). It can be seen from Fig. 2.7a that a significant contribution is from fast response over North America, the northern Atlantic Ocean, Europe, most regions in China, and northeastern Pacifica Ocean. However, as for the changes in tropical rainfall, which is associated with the ITCZ shift seen in the total response, slow responses mainly contribute to the northward shift of ITCZ rather than fast responses in the BC case. One exception is central Africa, where the precipitation changes are still dominated by fast responses, and this will be further examined later. For the SUL case, it has been shown that total responses are dominated by slow responses, both globally and regionally (Fig. 2.7b). Some exceptions are some land regions such as America, China, and the Sahel, where the precipitation change is mostly not significant in total responses.

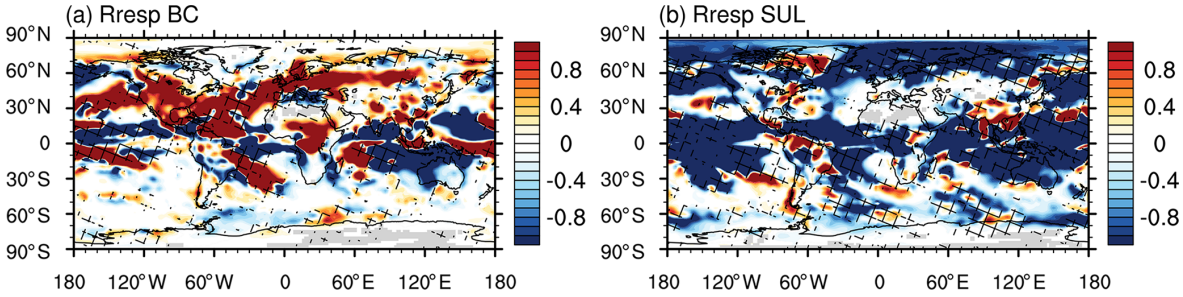

Figure 2.7: Response ratio of fast and slow responses (R_{resp}) (red denotes fast responses dominate the total responses and blue indicates slow responses dominate) for **(a)** BC cases and **(b)** SUL cases. Results have been normalised by total responses of precipitation. Hatching indicates the signs of fast and slow responses are same. If R_{resp} is around 0, contributions from fast and slow responses are similar. If R_{resp} is larger than 0, the total response is dominated by fast responses. If R_{resp} is less than 0, the total response is dominated by slow responses.

2.3.3 Changes in energy budget terms

To explain the different mechanisms between BC and SUL in terms of the contribution from fast and slow responses in more detail, we examine the changes in each energy budget term from Equation 2.1.

For the BC case, in fast responses, most decreases in Q are located over the main BC source regions such as central Africa and northeast China (Fig. 2.8a and 2.1). For zonal-mean results, after decomposing δQ into different terms based on

Eq. 2.3 and 2.5, it shows aerosol SW absorption is the major contributor to changes in Q (Fig. 2.10a). Since BC is a strongly absorbing aerosol, and the effect is near instantaneous, the changes of Q lead to decreased precipitation on global- and zonal-mean scales and happen through fast responses (Table 2.1 and Fig. 2.10a). The zonal-mean plot (Fig. 2.8e) shows that fast responses of δQ caused by aerosol absorption (Fig. 2.10a) lead to reduced rainfall, especially over Northern Hemispherc mid-latitudes (red solid line in Fig. 2.8e).

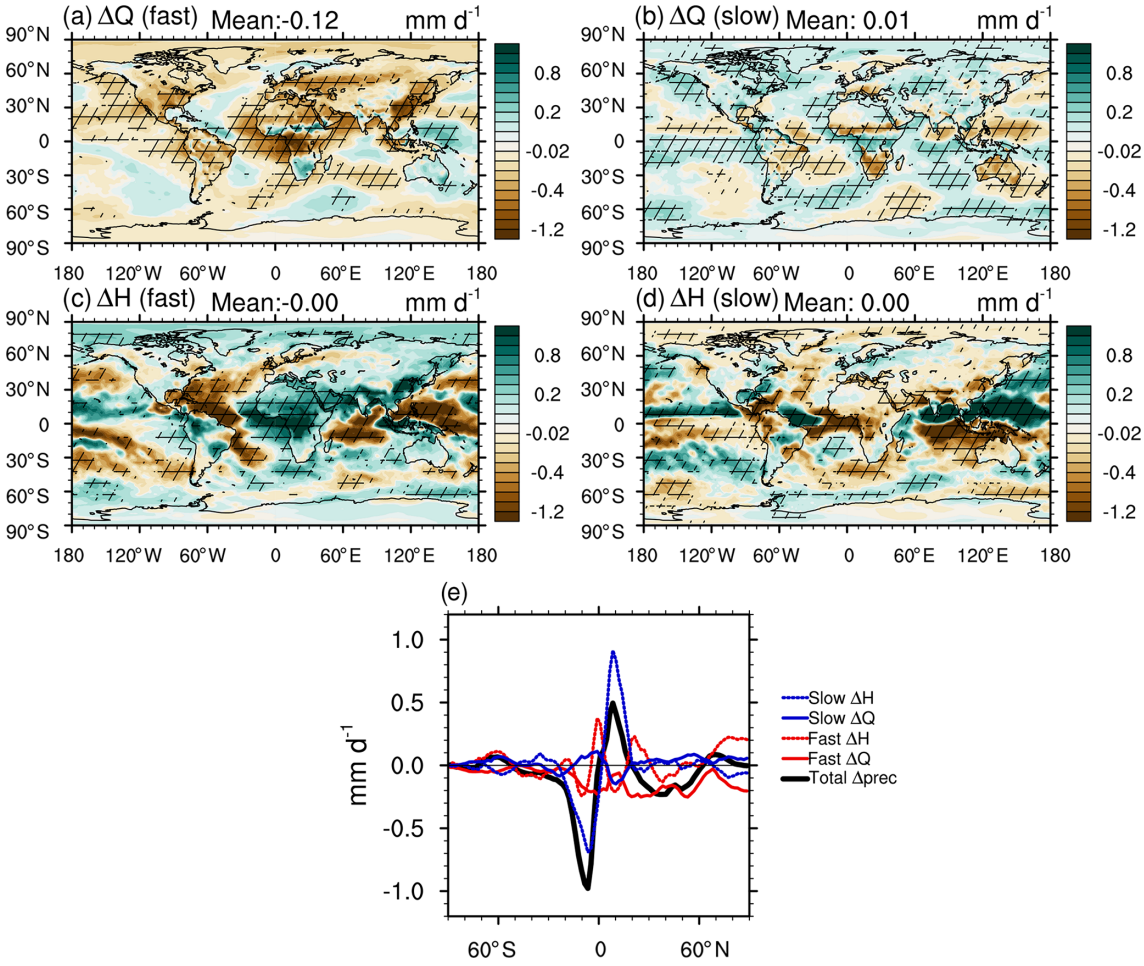

Figure 2.8: ECHAM6-HAM2 simulated geographical patterns of multi-annual mean changes in (a, b) atmospheric diabatic cooling (ΔQ) and (c, d) dry static energy flux divergence (ΔH) for (a, c) fast responses and (b, d) slow responses to 10-fold increased BC emission. Hatching indicates where the changes are significant (90% confidence interval through bootstrapping methods). (e) The zonal mean of total precipitation response and its decompositions, including fast and slow responses of diabatic cooling and dry static energy flux divergence. All of them are shown in equivalent precipitation units of mm d^{-1}.

However, on regional scales, the energy transport term acts to play an impor-

tant role. The geographical pattern of fast precipitation changes (Fig. 2.5c) is more similar to fast response of δH (Fig. 2.8c) (spatial correlation ∼0.9) than δQ (spatial correlation ∼-0.5). The spatial pattern of fast δH (Fig. 2.8c) also shows a land sea contrast in the tropics as in the precipitation change distribution (Fig. 2.5c), and this is most prominent in Central Africa and middle Atlantic Ocean. There is a significant increase of rainfall over Central Africa and decrease over the middle Atlantic Ocean (Fig. 2.5a). This is mostly contributed by fast responses (Fig. 2.5c and Fig. 2.7a). As mentioned, this pattern is similar to the case of CO_2 shown in (Richardson et al., 2016a). Although BC decreased surface temperature in Central Africa through fast responses (Fig. 2.4), BC can still warm up the lower troposphere at central Africa, which results in a thermal driven circulation which favours more convection there. This is evidenced by Fig. 2.8c which shows the dry static energy flux flow from Central Africa to the middle Atlantic Ocean. Dagan et al. (2019) performed an idealised experiment by adding an absorbing plume in the tropics, and found a very similar standing wave pattern of precipitation as a response. Examining δH shows that this is caused by a thermal driven circulation, which favours more convection over central Africa. Positive δH is consistent with more ascending motions at central Africa (Fig. 2.6). BC warms up the lower troposphere at central Africa, which results in more ascending motions (Fig. 2.3), and the dry static energy flux flow from Central Africa to the middle Atlantic Ocean (Fig. 2.8c).

The slow response of δQ leads to a global increase in precipitation (Fig. 2.8b), but the magnitude is an order of magnitude less than the fast response in δQ. This increased precipitation in the slow response is caused by the associated increase in global temperature (Fig. 2.11c) (Table 2.1). From an energetic perspective, it is mainly associated with the clear-clean-sky LW cooling ($ARC_{\text{clear,clean}}$) (Table 2.1 and Fig. 2.10b) as a result of increased atmospheric column temperature (Planck feedback). As precipitation responses in the extra-tropics are more correlated with δQ, larger fast responses of Q explain why rainfall responses in extra-tropics are dominated by the fast response in the BC case (Fig. 2.7a). Fig. 2.8e shows that the ITCZ shift seen in total responses is strongly correlated with slow responses of δH. The warmer Northern Hemisphere caused by an increase in BC leads to a southward cross-equatorial energy flux, which is accompanied by a northward shift of the Hadley cell (Bischoff and Schneider, 2016). Changes in vertical pressure velocity can be found in Fig. 2.11, which also indicates a northward shift of the ascending branch of the Hadley cell. From an energetic view, the changes in vertical pressure velocity drive the dynamic effect on advection of dry static energy, which is a strong component in

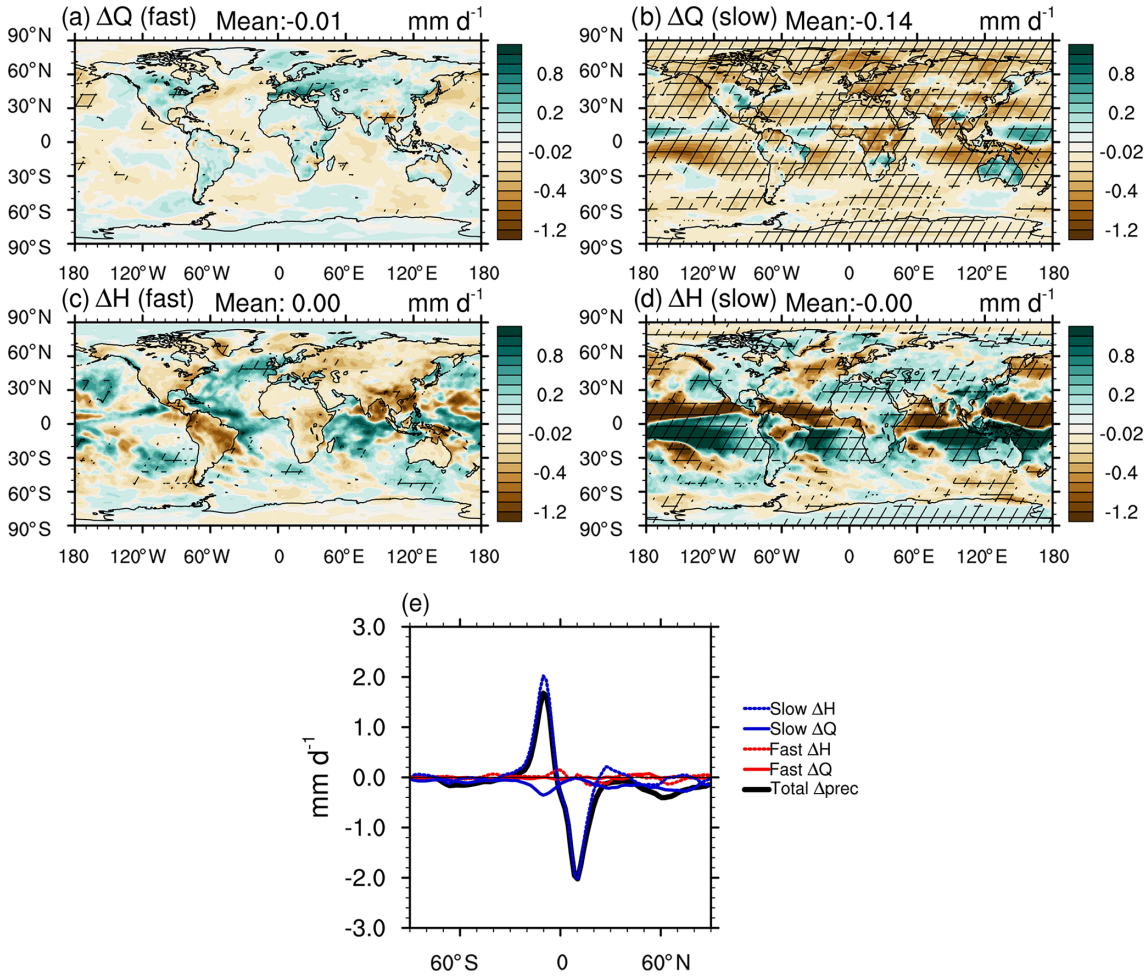

Figure 2.9: ECHAM6-HAM2 simulated geographical patterns of multi-annual mean changes in (a, b) atmospheric diabatic cooling and (c, d) dry static energy flux divergence for (a, c) fast responses and (b, d) slow responses to 5-fold increased SUL emission. Hatching indicates where the changes are significant (90 % confidence interval through bootstrapping methods). (e) The zonal mean of total precipitation response and its decompositions, including fast and slow responses of diabatic cooling and dry static energy flux divergence. All of them are shown in equivalent precipitation units of mm d^{-1}.

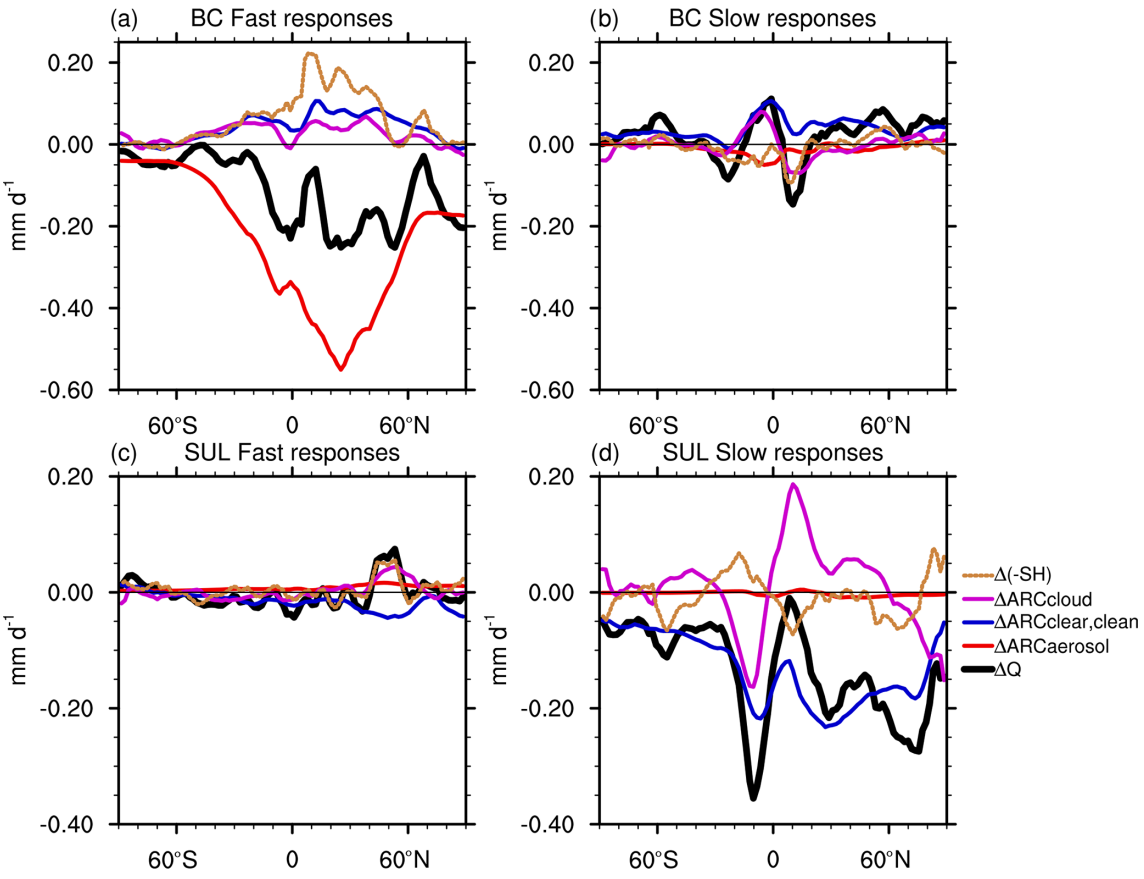

Figure 2.10: ECHAM6-HAM2 simulated multi-annual zonal mean of decomposed changes in atmospheric diabatic cooling (ΔQ), including ARC changes from aerosols ($\Delta ARC_{\text{aerosol}}$), clouds ($\Delta ARC_{\text{cloud}}$), clear-clean sky ($\Delta ARC_{\text{clear,clean}}$), and downward sensible heat flux ($\Delta(-SH)$) for (a) fast responses in the BC case, (b) slow responses in the BC case, (c) fast responses in the SUL case, and (d) slow responses in the SUL case. All items are shown in equivalent precipitation units of mm d^{-1}.

the changes of divergence of dry static energy fluxes (δH) in the tropics (Richardson et al., 2016a).

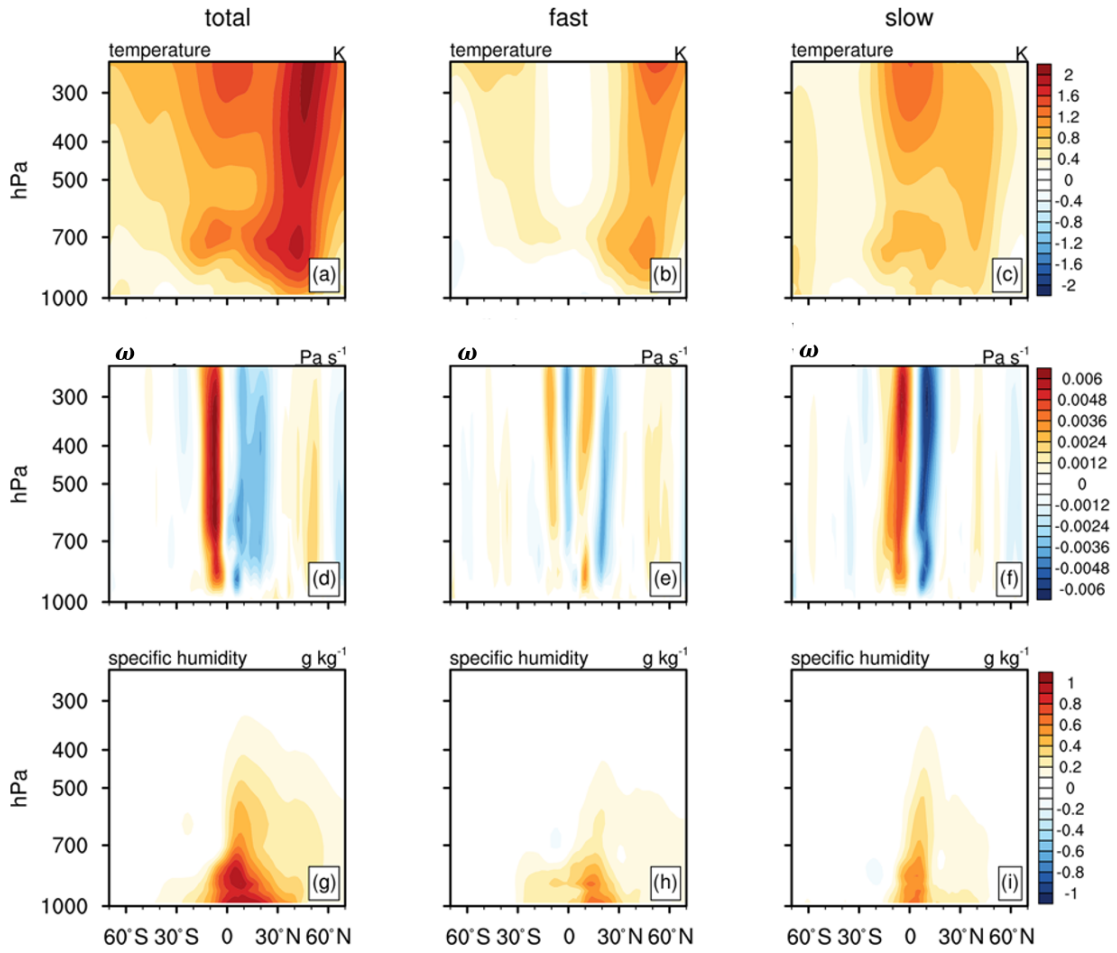

Figure 2.11: ECHAM6-HAM2 simulated multi-annual (a, d, g) total, (b, e, h) fast, and (c, f, i) slow responses of zonally averaged (a-c) temperature, (d-f) vertical pressure velocity (ω), and (g-i) specific humidity in response to 10-fold increased BC emission. Blue colours indicate large-scale ascent, and red colours indicate large-scale descent in (d-f).

For the SUL case, most of the fast responses are not statistically significant (Fig. 2.9a and c), and total responses are dominated by the slow response. For changes in extra-tropics, changes in Q are correlated with changes in precipitation. SUL decreases the temperature of the troposphere through slow responses, which leads to a reduction of specific humidity (Fig. 2.12). From an energetic view, it leads to a decreased clear-clean-sky radiative cooling ($ARC_{\mathrm{clear,clean}}$) (Fig. 2.10d), which contributes to most of the reduced slow responses of δQ. For changes in the tropics, like the BC case, slow responses of δH are consistent with the southward ITCZ shift

in the total response (Fig. 2.9d). In the extra-tropics, for the SUL case, there is also an interesting land-sea contrast in both fast and slow δH, with dry static energy fluxes generally diverging from oceans to lands in fast δH (Fig. 2.9c) and converging in slow δH (Fig. 2.9d). This is because in the fixed SST simulations, land surface temperature is still allowed to decrease in response to increased SUL emission (Fig. 2.4) as a result of reduced downward SW radiation. The land-sea contrast of temperature (colder land) results in more downward large-scale motions and divergence of moisture (see Fig. 2.6 for changes in vertical pressure velocity and column-integrated water vapour) over most land regions, particularly Southeast Asia and South America, in fast responses. Since fast responses have already accounted for part of land temperature reduction, ocean surface temperature decreases more than land surface in slow responses (Fig. 2.4). The colder ocean temperature therefore leads to an opposite land-sea pattern compared to fast responses (Fig. 2.9d).

Changes of Q are more robust in the fast response for the BC case, and the slow response of Q is more robust for the SUL case. Decomposition of diabatic cooling shows its global-mean decrease is dominated by an increase in atmospheric aerosol absorption for fast responses in the BC case (Fig. 2.10a) and decreased radiative cooling from the clear-clean sky for slow responses in the SUL case (Fig. 2.10d). The decreased $ARC_{\text{clear,clean}}$ values are mainly caused by the decreased atmospheric column temperature (Planck feedback) and associated reduced water vapour content (controlled by the Clausius-Clapeyron relationship). Sensible heat flux (upward) is also reduced due to the warmer atmosphere caused by absorption from BC (Fig. 2.10a).

It should also be noted that changes in diabatic cooling counteract the latent heat released from precipitation associated with the ITCZ shift in both cases (Fig. 2.8b and 2.9b). This is mainly caused by ARC_{clouds}, as it contributes a large part of diabatic cooling over tropical regions (Fig. 2.10b and d). This counteraction with the ITCZ shift is caused by the associated change of deep convective clouds, which is consistent with the results shown in Naegele and Randall (2019). They found a negative correlation between tropical rainfall and diabatic cooling and demonstrated this is caused by feedbacks from deep convective clouds. More high clouds lead to a decrease in atmospheric LW radiative cooling but an increase in precipitation, and the negative correlation is robust over tropical regions where deep convective clouds prevail (Naegele and Randall, 2019).

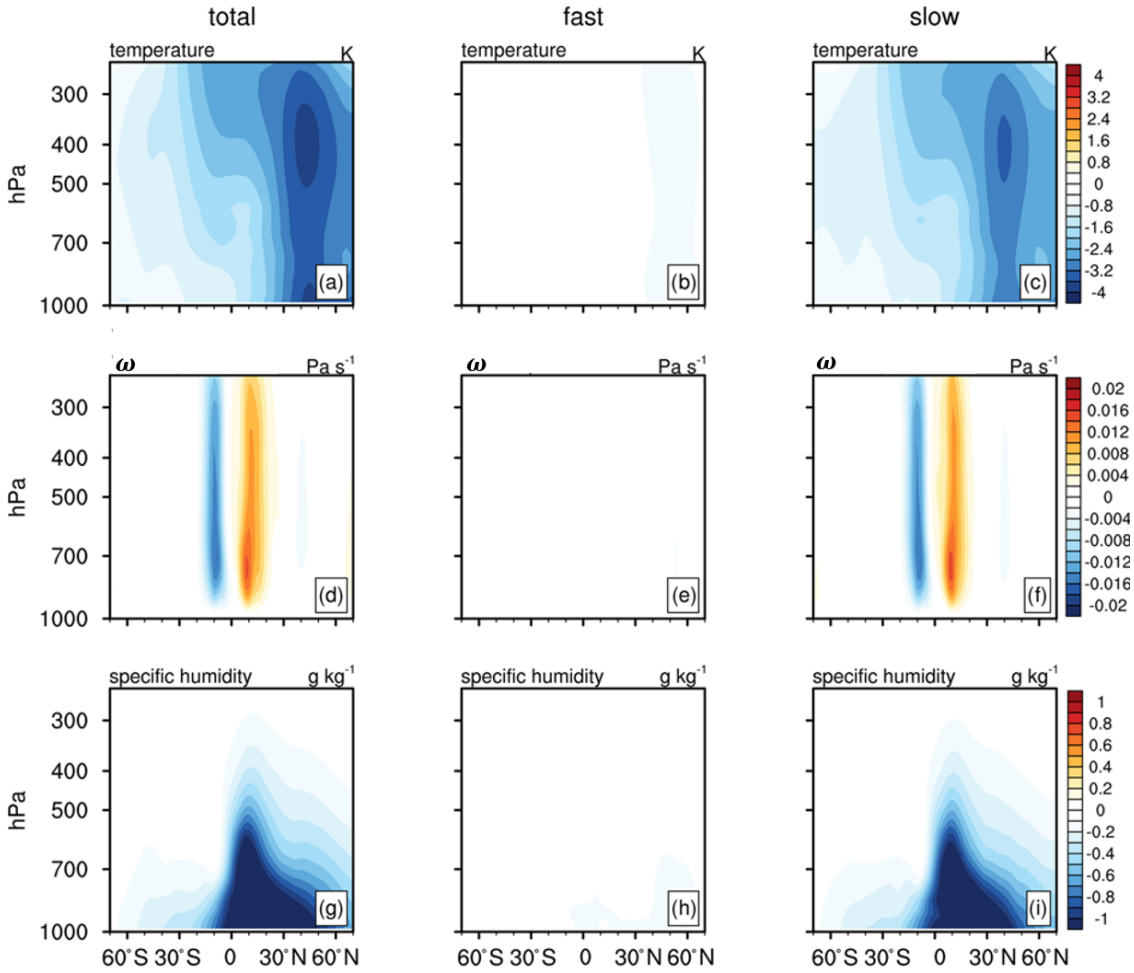

Figure 2.12: ECHAM6-HAM2 simulated multi-annual (a, d, g) total, (b, e, h) fast, and (c, f, i) slow responses of zonally averaged (a-c) temperature, (d-f) vertical pressure velocity (ω), and (g-i) specific humidity in response to 5-fold increased SUL precursor emission. The blue colour indicates large-scale ascent, and the red colour indicates large-scale descent in (d-f).

2.3.4 Responses of large-scale circulation and local thermodynamic conditions

Fig. 2.8e and 2.9e show that changes in tropical rainfall are strongly associated with slow responses of the energy transport term, independent of aerosol types (absorbing or non-absorbing), whereas changes in mid-latitude precipitation are dependent on aerosol types, which are dominated by fast responses of aerosol SW absorption in the BC case and slow responses of clear-clean-sky radiative cooling in the SUL case. To help understand the mechanisms of the tropospheric response in different regions, we study the response of the large-scale circulation and thermodynamic conditions, by examining the changes in vertical pressure velocity (ω), temperature T, and specific humidity q (Fig. 2.11 and 2.12). The vertical pressure velocity (ω) at 500 hPa is a useful method to distinguish different cloud dynamic regimes and a metric to quantify the strength of large-scale circulation (Bony and Dufresne, 2005; Zhang et al., 2016). Here we only show zonal-mean analysis as a compliment to the energetic perspective in Fig. 2.10.

As shown in Fig. 2.11, BC warms up the atmosphere through SW absorption, and the warming is confined mainly in the Northern Hemisphere (NH) where the BC emissions prevail. This leads to southward cross-equatorial energy fluxes and a northward shift of the Hadley cell (Wang, 2009; Bischoff and Schneider, 2016; Zhao and Suzuki, 2019). The changes in ω demonstrate the northward shift of the ascending branch of the Hadley cell, which show an increased upward motion in NH tropics and decreased ascending motion in SH tropics (Fig. 2.11d). Therefore, the tropical rainfall associated with ITCZ changes in response to the changes of large circulation. Fig. 2.11f further demonstrates that slow responses contribute to most of the changes in tropical large-scale circulations in Fig. 2.11d. It is consistent with Fig. 2.8 that changes in tropical latent heat released from precipitation are mostly contributed by δH_{slow}, because the dynamic component associated with changes in vertical velocity dominates the energy transport term over the tropics (Richardson et al., 2016a). Outside the tropics, changes in ω are not as significant as in the tropics (Fig. 2.11d), and zonal-mean rainfall is more related to local changes in thermodynamic conditions. Absorbing aerosols directly heat the mid-troposphere through fast processes (Fig. 2.11b). Heating the mid-troposphere will stabilise the column and suppress precipitation. This is consistent with the energetic perspective shown in Fig. 2.8 and 2.10a that fast responses of radiative cooling caused by BC SW absorption (reduced ARC_{aerosol}) account for the decreased latent heat in the extra-tropics. An interesting aspect here is that while BC induces the ITCZ shift, the fast response

(Fig. 2.11e) seems to counteract the stronger slow response shown in Fig. 2.11f. This is because of the strong non-zonal effect from central Africa (see geographical pattern of vertical pressure velocity changes in Fig. 2.6), where BC warms up the lower troposphere, resulting in more ascending motions in fast responses. It is also consistent with Fig. 2.5g that fast responses of rainfall in the southern tropical branch act to enhance ITCZ while only the northern branch acts to decrease ITCZ.

For the SUL case, the tropical rainfall response is opposite to that in the BC case, but the mechanism is similar. Increasing sulfate aerosols induces a dimming effect and causes a negative radiative forcing at the surface, which is a fast process. Subsequently, global surface temperatures are decreased, a slow process controlled by ocean heat capacity, and this cooling is more significant in the NH (Fig. 2.12a and c). As a result, the northward cross-equatorial energy fluxes lead to a southward shift of the Hadley cell (Fig. 2.12d). The slow responses of the large-scale circulation (caused by SST difference between hemispheres) contribute most of the shift of the Hadley cell (Fig. 2.12e). In the extra-tropics, a decrease in precipitation is also found in response to changes in thermodynamics. However, unlike black carbon, SUL decreases surface temperature through slow processes and leads to a cooling of the whole column in the extra-tropics (Fig. 2.12a and c). As a result, the specific humidity shows a large reduction (Fig. 2.12i), which is associated with a reduction of rainfall in the extra-tropics. This is consistent with the energetic perspective shown in Fig. 2.9 and 2.10d that reduced clear-clean-sky radiative cooling ($ARC_{\mathrm{clear,clean}}$) accounts for the decreased latent heat in extra-tropics.

It is worth mentioning that Fig. 2.11 and 2.12, as a bottom-up method, qualitatively show how the changes in large-scale circulation and local thermodynamics affect rainfall in terms of total, fast, and slow responses, whereas the energy budget view (Fig. 2.8, 2.9, and 2.10), as a top-down method, more easily quantifies these contributions through energetic terms (e.g. the energy transport term, ARC_{aerosol}, and $ARC_{\mathrm{clear,clean}}$). Combining these two methods makes the link between precipitation and aerosols explicit.

2.4 Conclusions

We have examined the response of precipitation to absorbing and non-absorbing aerosol perturbations by separately increasing BC emission and SUL emission in ECHAM6-HAM2 by 10 times and 5 times their baseline emission, following the PDRMIP protocol (Myhre et al., 2017; Samset et al., 2016). The precipitation response

is separated into fast (mediated by near-instantaneous changes in atmospheric radiative cooling) and slow responses (mediated by changes in SST) on both global and regional scales. An energetic perspective has been adopted to study precipitation changes. Global-averaged energetics have previously been used to study precipitation responses (e.g. Ming et al., 2010, some PDRMIP work); here, we further decompose atmospheric heating rates into individual terms separately for fast and slow responses. Changes in atmospheric latent heat release from precipitation are balanced by changes in atmospheric radiative cooling (ARC), surface sensible heat flux, and local energy transport. We introduce a method, based on Ghan (2013), to further decompose ARC into contributions from aerosols (through aerosol direct SW absorption), clouds (through cloud LW absorption/cooling), and clear-clean sky (without aerosols or clouds; mainly though LW radiative absorption/cooling from GHGs, water vapour, i.e. Planck feedback).

While it has long been appreciated that changes in ARC are essential in balancing latent heat released from precipitation on global scales, their relationship on zonal-mean or regional scales has not been fully explored. For global means, although SUL and BC have a different sign of radiative forcing at TOA (Boucher et al., 2013), we found that precipitation is decreased for both cases, which is energetically balanced by reduced atmospheric diabatic cooling δQ (Table 2.1). This response occurs at different timescales, dominated by fast responses for BC and by slow responses for SUL. For BC, on the global scale, the most significant effect is that absorbing aerosols directly heat the mid-troposphere, stabilise the column, and suppress precipitation. Therefore, most of the changes are due to aerosol absorption (ARC_{aerosol}) from fast responses. Meanwhile BC warms up the lower troposphere and decreases the temperature differences between the surface and near-surface temperature, which results in a decreased upward sensible heat. Investigating the energy balance, we found this decreased upward surface heat flux from the fSST experiment acts to cancel almost one-third of the decreasing effect caused by increased aerosol SW absorption. For SUL, although non-absorbing aerosol does not directly affect ARC through aerosol absorption, the net negative radiative forcing at TOA in fSST experiments and associated surface forcing leads to a decrease in global surface temperature through slow responses. As a result, it cools the whole atmospheric column, accompanied by reduced specific humidity, which leads to reduced precipitation. This can also be seen from the decreased radiative cooling from the clear-clean-sky ($ARC_{\text{clear,clean}}$) in slow responses.

Zonally averaged patterns of precipitation changes for the BC and SUL cases are different (Fig. 2.5). Tropical rainfall is primarily associated with the ITCZ, which shifts northward for BC increases and southward for SUL increases. Extra-tropical rainfall is reduced in both cases. For BC, slow responses account for most of the changes in tropical rainfall, while fast responses dominate changes in other regions (Fig. 2.7a). BC warms the Northern Hemisphere through slow responses, which leads to a southward energy flux (Bischoff and Schneider, 2016; Rotstayn and Lohmann, 2002). From an energetic perspective, in the tropics where intense convection and large-scale thermally driven circulations prevail, slow responses of the energy transport term dominate the changes in tropical rainfall (Fig. 2.8e), which is associated with the northward shift of Hadley cells (Fig. 2.11). Outside the tropics, BC warms up the mid-troposphere, stabilises the atmosphere (Fig. 2.11), and suppresses precipitation, which is a fast response. Energetically, different from the tropics, BC-induced increased diabatic heating is locally confined due to a stronger Coriolis force. This geographic confinement of the diabatic heating associated with increased aerosol shortwave absorption has to be balanced by reduced latent heat from precipitation (a fast response) (Fig. 2.10a). For the SUL case, the slow response dominates in nearly all regions (Fig. 2.7b), which is not surprising given that sulfate aerosol does not directly affect the column diabatic cooling. In the extra-tropics, SUL decreases surface temperatures, primarily through slow processes; cools the whole column; and reduces specific humidity (Fig. 2.12). From an energetic perspective, this can also be seen from the decreased radiative cooling from the clear-clean sky (without clouds and aerosols) (Fig. 2.10d) due to the reduced water vapour content and decreased atmospheric column temperature (Planck feedback).

There exist some interesting regions where the responses are distinct from globally or zonally averaged results. Rainfall is significantly increased over central Africa, in the BC case, together with reduced precipitation over the middle Atlantic Ocean, and this pattern is most prominent in fast responses. This pattern shows clear similarities with the standing wave pattern response of precipitation to an idealised plume of absorbing aerosols in the tropics (Dagan et al., 2019). Examining δH shows that this is caused by a thermally driven circulation, which favours more convection over central Africa. BC warms up the lower troposphere in central Africa, which results in more ascending motions (Fig. 2.6). The low latitude (thus weak Coriolis force) allows for the dry static energy to be efficiently diverged from central Africa to the middle Atlantic Ocean (Fig. 2.8c). In the SUL case, while most regions are dominated by slow responses, in some regions, such as most parts of China and South America,

rainfall changes are still dominated by fast responses (Fig. 2.7b), where the surface temperature is significantly decreased (Fig. 2.4). This is due to the dimming effect from SUL and associated surface flux changes, and because changes of land surface temperature are not constrained in fSST experiments. Reduced surface fluxes and temperatures therefore lead to a decrease in precipitation over most land regions as well as an increase in surrounding oceans (e.g. southeast Pacific Ocean).

Changes in zonally averaged vertical pressure velocity, temperature profile, and specific humidity (Figs. 2.11 and 2.12) show consistency with zonally averaged energetics. Changes in vertical pressure velocity indicate a northward shift of the ascending branch of the Hadley cell in the BC case and SUL case. It is consistent with the changes in the divergence of dry static energy fluxes, which is dominated by the changes in vertical velocity (the dynamic component) in the tropics (Richardson et al., 2016a). In the extra-tropics, stabilisation induced by BC through fast response is consistent with increased atmospheric radiative heating from aerosol SW absorption. Reduced specific humidity as well as decreased atmospheric column temperature in the SUL case is consistent with decreased radiative cooling from the clear-clean sky. The changes in large-scale circulations and local thermodynamics qualitatively explain the responses of precipitation, whereas the energetic perspective provides a method to quantify and make their contributions explicit.

In summary, we examined the relationship between aerosol-induced changes in atmospheric energetics and precipitation changes across different scales. Generally, changes in ARC and latent heat from precipitation are largely balanced globally and in the extra-tropics (Dagan et al., 2019) However, these two terms are less balanced in the tropics due to efficient local energy transport. We introduced a new decomposition method, derived from (Ghan, 2013), to examine aerosol effects on precipitation. For absorbing aerosols, decreased global-mean and extra-tropical precipitation is associated with increased atmospheric aerosol SW absorption from fast responses, while for non-absorbing aerosols, reduced rainfall is more correlated with decreased clear-clean-sky atmospheric radiative cooling from slow responses. This top-down method, together with the traditional bottom-up method, can make the link between precipitation and aerosols explicit and quantify contributions to global and regional rainfall changes.

We acknowledge that high resolutions are desirable for the analysis of regional precipitation changes. However, climate models in configurations similar to those used here (with resolustion around 2°) have been widely used (e.g. most CMIP and PDRMIP exercises rely on this) and been shown to have skills in examining regional

rainfalls as well as their responses (e.g. Liu et al., 2018; Myhre et al., 2017; Samset et al., 2016). It might also be worth noting that increasing resolution while retaining parameterised convection, as done in many regional climate modelling studies, raises other concerns as many assumptions underlying these parameterisations are no longer valid (Prein et al., 2015). In the context of the focus of this work, with focus on constraints from the energy budget and the underlying physical constraints in general, GCMs are in fact a very robust tool (and ECHAM6-HAM is, unlike other GCMs or many cloud resolving models, fully energy conserving). We therefore believe our approach to be useful, in line with previous studies on this very topic (e.g. Jordan et al., 2018; Myhre et al., 2017; Roeckner et al., 2006; Samset et al., 2016; Shawki et al., 2018). We also note that internal variability on regional scales is significant, in particular in coupled simulations. However, since we are examining the average of last fifty years results instead of the transient evolution, the impacts from internal variability should be small in this case. Therefore, this does not take away from our analysis of physical constraints on precipitation changes.

Idealised simulations of large increases in climate forcing agent emissions and concentrations provide further insights into the model variability in simulating rainfall and their responses to different climate forcers, as shown by some PDRMIP research (e.g. Richardson et al., 2018b; Stjern et al., 2018). For example, it has been demonstrated that the response from BC perturbations contribute to a large part of the substantial uncertainties among GCMs in simulating the changes in surface temperature and therefore precipitation (Stjern et al., 2017). Distinguishing contributions from individual energetic terms is helpful to assess uncertainties from aerosol absorption, or feedbacks from clouds, water vapour, and surface sensible heat flux. This will improve our understanding of GCMs and the climate system, which will be the focus of our follow-up work.

There exist some caveats when considering real-world implications of our results. The aerosol perturbation follows the PDRMIP protocol designed to reveal the fundamental mechanisms and to make the aerosol effect strong enough to be distinguishable from natural variability. However, these perturbations are too large to be representative for real-world situations, in particular considering anthropogenic SO_2 (the precursor of SUL) emissions that are starting to decrease in Southeast Asia (Zheng et al., 2018). As for Northern Hemispherc mid-latitudes, where the population is concentrated, results here show that increased BC or SUL will lead to decreased precipitation, but this happens at different timescales. Increased BC may lead to a near-instantaneous decreased precipitation over China or America, while

increased SUL will reduce precipitation via the slow response, modulated by SSTs, at a much longer timescale. Transient changes are a combination of both fast and slow responses, which is dependent on temperature patterns (Chapter 3) and aerosol emission scenarios (Chapter 4) and will be explored in further parts of the thesis. In the real world, it should be mentioned that the anthropogenic emissions create a mixture of absorbing and non-absorbing aerosols, so the changes in rainfall strongly depend on the timescale and the real-world emission scenario. It should also be noted that the total responses of precipitation in this work are derived from mixed-layer ocean experiments and therefore differ from real-world changes involving changes in the ocean circulation. There are several studies that have addressed the importance of using ocean-coupled models to accurately simulates regional and global precipitation responses (e.g. Wang et al., 2017; Zhao and Suzuki, 2019).

Chapter 3

Hydrological sensitivity uncertainties traced to sea surface warming patterns

Chapter 2 shows that precipitation changes are dominated by slow responses in the non-absorbing aerosol perturbation case, consistent with previous studies suggesting that the response of precipitation is dominated by slow responses rather than fast responses for most climate forcers such as GHGs and solar radiation (Samset et al., 2016). In the real world, intensification of the hydrological cycle, as a slow response, is one of the key consequences of global warming, which has essential impacts on energy security, food supply and economics. Compared to Chapter 2, which investigates both fast and slow responses, this chapter focuses on slow responses and the factors contributing to their uncertainties.

As explained in Section 1.3.3, hydrological sensitivity (η) refers to increase rate in global-mean precipitation in response to global-mean surface temperature increase, and is a metric commonly used to measure the intensification of the hydrological cycle under global warming scenarios (Allan et al., 2014; Fläschner et al., 2016; Kvalevåg et al., 2013). It differs from the apparent hydrological sensitivity (η_a), which takes into account both the fast and slow precipitation responses (Andrews and Forster, 2010; Bala et al., 2010; Fläschner et al., 2016; Samset et al., 2016). Studies examining CMIP3 models have found that aerosols, particularly black carbon, exert a significant impact on the spread of η_a (Previdi, 2010; Pendergrass and Hartmann, 2012). Further work (e.g. DeAngelis et al., 2015; Fläschner et al., 2016) investigated the spread of η rather than η_a and found that the spread is significantly reduced in CMIP5 models, because η excludes the fast precipitation responses. Nevertheless, the spread of η among models is still large. For example, an inter-model spread up to a factor of 3.3

has been found in the CMIP5 models (Andrews et al., 2009; DeAngelis et al., 2015). Moreover, this inter-model spread changes little from CMIP5 to CMIP6 (Pendergrass, 2020), compared to the changes in equilibrium climate sensitivity (Zelinka et al., 2020).

Continuous efforts have been put to investigate and narrow the inter-model spread of η. Previous studies linked the uncertainties with different treatments of the atmospheric processes responding to the warming, such as different treatments of water vapour shortwave absorption and low cloud schemes. Recent studies have suggested an important role of SST patterns in determining the magnitude of TOA radiative feedback factors such as lapse rate and clouds (Andrews et al., 2015; Ceppi and Gregory, 2017; Zhou et al., 2017). Given that these terms can also affect the atmospheric energy budget (section 1.3.3), it is reasonable to expect that hydrological cycle intensification is equally dependent on SST warming patterns.

Indeed, the impact of spatially heterogeneous warming patterns, known as the pattern effect, has been found to be important in several topics, such as large-scale circulation (Ma et al., 2013, 2018; Zhou et al., 2020a), cloud fields (Zhou et al., 2017; Dong et al., 2019b), or climate feedback (Andrews et al., 2015; Ceppi and Gregory, 2017). In particular, studies by Xie et al. (2010) and Ma et al. (2013) have shown the SST warming anomaly effects on regional rainfall and dynamics at the tropics and referred to the pattern effect on regional rainfall. However, different from the regional water cycle system, the SST warming pattern effect on η has not been fully examined yet, to the best of our knowledge, in existing literature. In fact, one strong motivation of this chapter is that the recent Working Group I IPCC report (AR6) noted the SST pattern effect on climate feedback parameter in Chapter 7 (Forster et al., 2021), while Chapter 8, which focuses on the water cycle response, has recognised the inter-model uncertainty in η but did not discuss the potential role of the SST pattern effect contributing to it (Douville et al., 2021). Therefore, this chapter aims to investigate the dependence of η on SST warming patterns. Additionally, the energetic framework proposed in Chapter 2 provides a quantitative tool to understand the mechanisms driving the relationship between η and SST warming patterns.

This chapter is based on a manuscript submitted to a peer-reviewed journal with changes including reorganising and renumbering the supplementary tables and figures:

Zhang, S., Stier, P., Dagan G., Zhou C., and Wang, M. (2023). "Hydrological sensitivity uncertainties traced to sea surface warming pattern", Nature Climate Change,

in print.

I designed the study together with the co-authors. Chen Zhou (Nanjing University, China) provided the data sets of CAM5 SST patch simulations. I carried out the analysis. I interpreted the results with input from the co-authors. I wrote the manuscript with contributions from all co-authors.

3.1 Introduction

It is an essential but challenging goal to improve the projection of precipitation change under global warming, even for the global-mean changes (DeAngelis et al., 2015; Myhre et al., 2017; Trenberth, 2011). The Clausius-Clapeyron (CC) relationship provides a strong constraint on increasing water vapour content per unit temperature warming (at around 7% K^{-1}). However, this does not apply to the global-mean precipitation change, which is constrained by the atmospheric energy budget (Allen and Ingram, 2002; Muller and O'Gorman, 2011). The latent heat released from precipitation has to be balanced by the atmospheric radiative cooling and the surface sensible heat flux in equilibrium. Increasing greenhouse emissions will initially reduce global-mean rainfall (Allen and Ingram, 2002; Bala et al., 2010), corresponding to the decreased atmospheric radiative cooling when the surface temperature remains unchanged (i.e., a rapid adjustment). For longer timescales, after the surface subsequently gets warmer, the atmospheric radiative cooling is enhanced as well, allowing for an intensification of the hydrological cycle (Held and Soden, 2006; Yang et al., 2003).

Accurately estimating hydrological intensification is critical for understanding future climate impacts. The change in temperature-mediated global-mean precipitation (P) is suggested to be proportional to surface temperature (T) increase (O'Gorman et al., 2012; Samset et al., 2016), and the ratio is referred to as hydrological sensitivity (η), defined as:

$$\eta = \partial P / \partial T \quad (\text{in } \% \text{ K}^{-1}), \tag{3.1}$$

which is a widely used metric for evaluating hydrological intensification under global warming. Compared to the apparent hydrological sensitivity, which also takes into account the rapid adjustments, the spread of η has been largely reduced and has been estimated to be around 2% K^{-1} (Allen and Ingram, 2002; DeAngelis et al., 2015; O'Gorman et al., 2012), predominately determined by the increased rate of radiative cooling from a deepening troposphere (Jeevanjee and Romps, 2018). However, there remains a large inter-model spread in current GCMs (DeAngelis et al., 2015), even when keeping the methodology consistent (Fläschner et al., 2016; Samset et al., 2016).

Any temperature-mediated changes that affect the atmospheric energy budget can eventually impact η. These can come from the responses of water vapour (DeAngelis et al., 2015), lapse rate (O'Gorman et al., 2012; Andrews and Webb, 2018), as well as clouds (Watanabe et al., 2018; Mauritsen and Stevens, 2015), to surface temperature changes. Previous studies focused on the global-mean temperature changes when

studying η without considering the surface warming patterns. However, the pattern effect from sea surface temperature (SST) inhomogeneous warming has recently been shown to be important for clouds feedbacks (Ceppi and Gregory, 2017; Dong et al., 2019b; Zhou and Penner, 2016), as well as radiative feedback parameters more generally (Andrews et al., 2015; Xie et al., 2016). Given that these terms can also affect the atmospheric energy budget (Muller and O'Gorman, 2011; Zhang et al., 2021), it is reasonable to expect that hydrological cycle intensification is equally dependent on SST warming patterns. Considering that the SST pattern was and will be changing due to the internal variability of the climate system (Watanabe et al., 2014; Kosaka and Xie, 2013) and that spatially inhomogeneous warming is to be expected under the global warming scenario (Andrews et al., 2015; Zhou et al., 2021; Vecchi and Soden, 2007), it is therefore of interest to investigate the dependence of η on SST warming patterns.

3.2 Methods

3.2.1 SST warming patch experiments description

The SST warming patch experiments are based on the Community Atmospheric Model 5.3 (CAM5.3) (Neale et al., 2010) in the Community Earth System Model 1.2.1, with a resolution of 1.9 degrees latitude × 2.5 degrees longitude and 30 vertical levels. A baseline run is conducted with monthly SST, sea ice and external forcings fixed at the level of year 2000. Next, 80 simulations are conducted with a warming patch individually applied on the prescribed SST in the baseline run. Each SST anomaly patch p (p=1, ..., 80) takes the form of a cosine hump (Barsugli and Sardeshmukh, 2002; Zhou et al., 2017):

$$\Delta SST_p\left(lat, lon\right) = A\cos^2\left(\frac{\pi}{2}\frac{lat - lat_p}{lat_w}\right)\cos^2\left(\frac{\pi}{2}\frac{lon - lon_p}{lon_w}\right), \tag{3.2}$$

with a maximum of 4K (A = 4K) warming at the patch centre (lat_p, lon_p) and a radius of 10 degree latitude ($lat_w = 10°$) and 40 degree longitude ($lon_w = 40°$), where $|lat - lat_p| \leq lat_w$ and $|lon - lon_p| \leq lon_w$. Another set of 80 simulations are conducted similarly to the warming patch experiments but replacing the warming patches with cooling patches of the same magnitude (A=-4K). All simulations are run for 40 years and the average of last 30 years are used to avoid spin-up effects in the first months or years.

It should be noted that the land surface temperature is still allowed to adjust in the model, despite fixing SSTs. Thus, there are some land surface temperature responses to the SST anomaly patch, which could lead to a spread of changes in global-mean surface temperature among the experiments. To avoid division by small responses of global-mean surface temperature, which could lead to unrealistically large η, we only use cases which showed significantly different ($p<0.05$) global-mean surface temperature between the experimental and baseline run during the 30 years of simulations used. There are 78 out of 80 experiments in which global-mean temperature are significantly different with baseline experiment.

3.2.2 CMIP models

24 CMIP5 models are used in this study to investigate the inter-model spread of η. The model information is documented in Table 3.1. Sea ice, ocean, land, and atmosphere are fully coupled for the pre-industrial control (PiControl) and abrupt quadrupled CO_2 (abrupt4xCO_2) experiments. We use monthly output from one ensemble member (r1i1p1) in the CMIP5 models. In addition to the fully coupled simulations, we also use the atmosphere-only experiments from the Atmospheric Models Intercomparison Project (AMIP) (Taylor et al., 2012; Gates et al., 1999). Sea surface temperature is prescribed to present day values in the standard AMIP experiment. The SST is uniformly increased by 4K in AMIP4K experiment compared to the standard AMIP experiment. The increased warming is patterned in AMIPFuture experiment, while keeping the global-mean SST increased still to 4K.

Our analysis of historical precipitation is based on output from eleven CMIP6 models, including the fully copuled CMIP6 historical simualtions and the AMIP-hist simulations (Table 3.2). Both sets of simulations use the same external forcing fields. However, sea ice, ocean, land and atmosphere are coupled in CMIP6 historical simulations, while sea ice and ocean are prescribed from observations in AMIP-hist simulations (from 1980 to 2014) (Eyring et al., 2016).

3.2.3 Calculation of the hydrological sensitivity

Hydrological sensitivity (η) quantifies the sensitivity of global-mean precipitation to an increase in global-mean surface temperature (Allen and Ingram, 2002; Andrews et al., 2009; Bala et al., 2008; Fläschner et al., 2016; Held and Soden, 2006; Pendergrass and Hartmann, 2012). For SST patch experiments in this work, since the only changes in our patch experiments are from SST (see experiment description section), fast

Table 3.1: CMIP5 models and the experiments used in this study. Y indicates that the experiment from this model has been used in this study.

Institution	Model name	abrupt-4xCO2	AMIP-4K	AMIP-Future	Reference
Commonwealth Scientific and Industrial Research Organization and Bureau of Meteorology, Australia	ACCESS1-0	Y			Bi et al. (2013)
	ACCESS1-3	Y			Bi et al. (2013)
Beijing Climate Center, China	BCC-CSM1-1	Y	Y	Y	Wu et al. (2014)
	BCC-CSM1-1-m	Y			Wu et al. (2014)
Canadian Centre for Climate Modelling and Analysis, Canada	CanESM2	Y			Arora et al. (2011)
National Center for Atmospheric Research (NCAR), USA	CCSM4	Y	Y	Y	Meehl et al. (2012)
Centre National de Recherches Meteorologiques, France	CNRM-CM5	Y	Y	Y	Voldoire et al. (2013)
Geophysical Fluid Dynamics Laboratory, United States	GFDL-CM3	Y			Donner et al. (2011)
	GFDL-ESM2G	Y			Dunne et al. (2012)
	GFDL-ESM2M	Y			Dunne et al. (2012)
NASA Goddard Institute for Space Studies, United States	GISS-E2-H	Y			Schmidt et al. (2014)
	GISS-E2-R	Y			Schmidt et al. (2014)
Met Office Hadley Centre, UK	HadGEM2-ES	Y			Collins et al. (2011)
Institute for Numerical Mathematics, Russia	INM-CM4	Y			Volodin et al. (2010)
Institut Pierre-Simon Laplace, France	IPSL-CM5A-LR	Y	Y	Y	Dufresne et al. (2013)
	IPSL-CM5A-MR	Y			Dufresne et al. (2013)
	IPSL-CM5B-LR	Y	Y	Y	Hourdin et al. (2013)
Japan Agency for Marine-Earth Science and Technology, Atmosphere and Ocean Research Institute, Japan	MIROC5	Y	Y	Y	Watanabe et al. (2010)
	MIROC-ESM	Y			Watanabe et al. (2011)
Max Planck Institute for Meteorology, Germany	MPI-ESM-LR	Y	Y	Y	Stevens et al. (2013)
	MPI-ESM-MR	Y	Y	Y	Giorgetta et al. (2013)
	MPI-ESM-P	Y			Giorgetta et al. (2013)
Meteorological Research Institute, Japan	MRI-CGCM3	Y	Y	Y	Yukimoto et al. (2012)
Norwegian Climate Centre, Norway	NorESM1-M	Y			Bentsen et al. (2013)

Table 3.2: CMIP6 models and the experiments used in this study. Y indicates that the experiment from this model has been used in this study.

Institution	Model name	historical	AMIP-hist	Reference
Beijing Climate Center, China	BCC-CSM2-MR	Y	Y	Wu et al. (2019)
	BCC-ESM1	Y	Y	Wu et al. (2019)
Canadian Centre for Climate Modelling and Analysis, Canada	CanESM5	Y	Y	Swart et al. (2019)
National Center for Atmospheric Research (NCAR), USA	CESM2	Y	Y	Gettelman et al. (2019)
Centre National de Recherches Meteorologiques, France	CNRM-CM6-1	Y	Y	Voldoire et al. (2019)
	CNRM-ESM2-1	Y	Y	Séférian et al. (2019)
Institut Pierre-Simon Laplace, France	IPSL-CM6A-LR	Y	Y	Boucher et al. (2020)
Japan Agency for Marine-Earth Science and Technology, Atmosphere and Ocean Research Institute, Japan	MIROC6	Y	Y	Tatebe et al. (2019)
Meteorological Research Institute, Japan	MRI-ESM2-0	Y	Y	Yukimoto et al. (2019)
Norwegian Climate Centre, Norway	NorESM2-lM	Y	Y	Seland et al. (2020)

adjustments are therefore not considered and the changes in precipitation are only SST-mediated responses (i.e., slow responses). We therefore directly derive η (based on Equation 3.1) for SST patch experiments as follows:

$$\eta = \frac{\Delta P}{P_0 \Delta T_s}, \tag{3.3}$$

where ΔT_s is the global-mean surface temperature change, P_0 denotes the baseline precipitation rate and ΔP refers to the changes in global-mean precipitation in SST patch experiments, so that the numerator indicates the relative change in precipitation.

Another way to derive η is to calculate the slope of a Gregory-style regression (Gregory and Webb, 2008) between global-mean precipitation and surface temperature changes (DeAngelis et al., 2015; Andrews et al., 2009; Kvalevåg et al., 2013). It is also helpful to separate the adjustment and temperature-mediated responses to climate forcers such as greenhouse gases and anthropogenic aerosols (Fläschner et al., 2016). We use the Gregory-style approach to derive η from fully-coupled CMIP5 models (Taylor et al., 2012). Following the method from DeAngelis et al. (2015), we use 150 years (except for IPSL-CM5A-MR which has only 140 years data available) annual averages of precipitation and near-surface air temperature from piControl and abrupt4xCO_2 experiments. For each year in the abrupt4xCO_2 run, the response of precipitation and temperature is calculated as the difference relative to the same year in the 21-year smoothed piControl run, which allows to reduce the possible impacts from climate model drift. The hydrological sensitivity is then calculated as the

slope between global-mean precipitation and near-surface temperature, whilst the y-intercept denotes the rapid adjustment. The good regressions show the reliability of η derived from this method (Fig. 3.1).

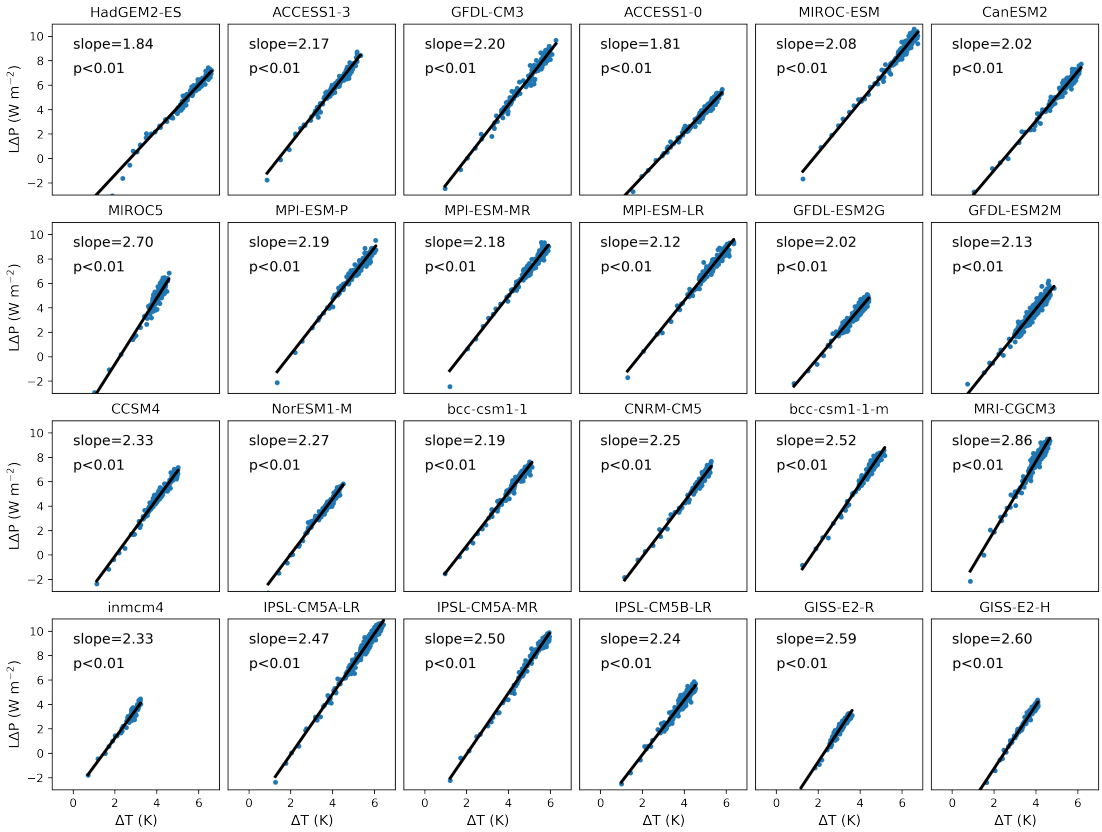

Figure 3.1: Scatter plot of global-mean near-surface temperature responses (x-axis) and model estimated annual precipitation responses (y-axis) for abrupt4xCO2 experiments from 24 CMIP5 models. Each dot indicates the annual average for each model year (150 years in total). Also shown is the regression slope and p value calculated based on the statistical F-test.

3.2.4 Energetic decompositions

The latent heat released from global-mean preciptiation is balanced by atmospheric radiative cooling and downward surface sensible flux (-SH), which is widely used as an energetic constraint to study global precipitation responses (Muller and O'Gorman, 2011; Zhang et al., 2021).

$$L_c \Delta P = \Delta \mathrm{ARC} - \Delta \mathrm{SH}, \tag{3.4}$$

where L_c denotes the latent heat of condensation and ARC refers the atmospheric radiative cooling, which is the difference of longwave (LW) and shortwave (SW) fluxes

between top of the atmosphere (TOA) and the surface (SUR):

$$\mathrm{ARC} = (\mathrm{LW}_{TOA} + \mathrm{SW}_{TOA}) - (\mathrm{LW}_{SUR} + \mathrm{SW}_{SUR}), \tag{3.5}$$

where all the radiative fluxes are defined as positive downward.

We can therefore decompose η into contributions from ARC:

$$\eta_{ARC} = \frac{\Delta \mathrm{ARC}}{L_c P_0 \Delta T_s}, \tag{3.6}$$

and contributions from sensible heat flux by replacing ARC with SH:

$$\eta_{SH} = \frac{\Delta(-\mathrm{SH})}{L_c P_0 \Delta T_s}. \tag{3.7}$$

Using a radiative call to calculate the radiative fluxes at TOA and surface, we are able to further derive the contributions from clouds (ARC_{cloud}) and clear sky ($\mathrm{ARC}_{clear-sky}$):

$$\mathrm{ARC} = \mathrm{ARC}_{cloud} + \mathrm{ARC}_{clear-sky}. \tag{3.8}$$

This decomposition enables us to distinguish energetic constraints arising from clouds or clear sky, by replacing ARC with ARC_{cloud} or $\mathrm{ARC}_{clear-sky}$.

3.2.5 The Green's function approach

We make use of the Green's function approach to examine the local contributions to global precipitation changes. The change of a global-mean variable can be interpreted as the sum of a linear contribution from each grid box i and an error term, in a discrete form of Green's function following Zhou et al. (2017):

$$\Delta y = \sum_i \frac{\partial y}{\partial SST_i} \Delta SST_i + \varepsilon, \tag{3.9}$$

where y denotes any global-mean variables of interest, SST_i refers to the SST in a grid box i, and ε denotes error term which contains all the nonlinear components (Barsugli and Sardeshmukh, 2002; Dong et al., 2019b). The grid-wise sensitivity of y to SST_i (i.e., $\frac{\partial y}{\partial SST_i}$) is the weighted sum of the patch-wise sensitivity of y to SST_p of the patches which covers the grid i:

$$\frac{\partial y}{\partial SST_i} = \frac{\sum_p \Delta SST_p \frac{y_w - y_c}{SST_{p,w} - SST_{p,c}} \frac{S_i}{S_p}}{\sum_p \Delta SST_p}, \tag{3.10}$$

where the subscript w in $SST_{p,w}$ denotes a warming SST patch, the subscript c in $SST_{p,c}$ denotes the conjugating cooling patch, S_i and S_p refer to the area of the specific grid box i and patch p respectively.

3.2.6 Observational and reanalysis datasets

HadCRUT observed gridded sea surface temperature data (Morice et al., 2021) from Met office Hadley Centre is available from January 1850 to present day, on a resolution of 5 degrees, and can be found at `https://www.metoffice.gov.uk/hadobs/hadcrut5/data/current/download.html`. NOAA monthly reconstructed SST data (Huang et al., 2017) is available from 1854 with resolution at 2 degrees. The data sets are available at `https://psl.noaa.gov/data/gridded/data.noaa.ersst.v5.html`. ERA5 (Hersbach et al., 2020) (`https://www.ecmwf.int/en/forecasts/dataset/ecmwf-reanalysis-v5`) is the fifth generation ECMWF atmospheric reanalysis data set and covers from 1950 to present, with resolution at approximately 30km. The global precipitation climatology project (GPCP) observational dataset (Adler et al., 2003), derived from rain gauge stations, ground sounding, and satellites observations, is available from 1979. The monthly precipitation data set is at resolution of 2.5 degree.

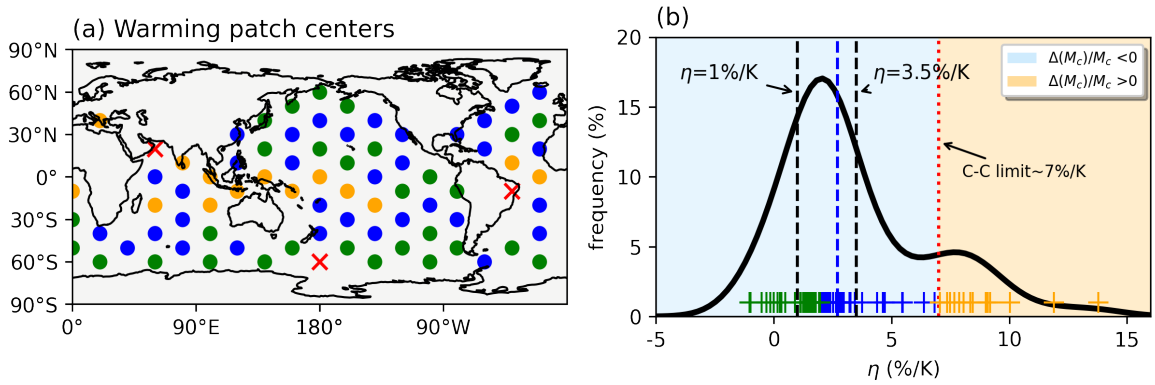

Figure 3.2: (a) The geographical location of warming patches centre. Each red dot denotes the centre of a warming patch which is a cosine hump with 20° latitude and 80° longitude width. Orange dots indicate the patch experiments which show larger η than the 7 % K^{-1}, whereas green refers to η <2 % K^{-1} and blue refers to the middle. Additionally, red crosses indicate the experiments with no statistically significant changes in near-surface global-mean temperature. (b) The estimated probability density function (PDF) of hydrological sensitivities (η) derived from patch experiments. Each cross indicates the values of η estimated from the corresponding patch experiment shown in a. Vertical dashed black lines denote the approximate upper and lower bound of η estimated from current GCMs. The vertical dashed red line denotes the water vapour increase rate suggested by Clausius–Clapeyron (CC) relation. The blue area indicates a decrease of convective mass flux ($\Delta M_c/M_c < 0$) and a slowed-down circulation, whereas the orange area denotes experiments with an increase of convective mass flux ($\Delta M_c/M_c > 0$) and a speed-up circulation.

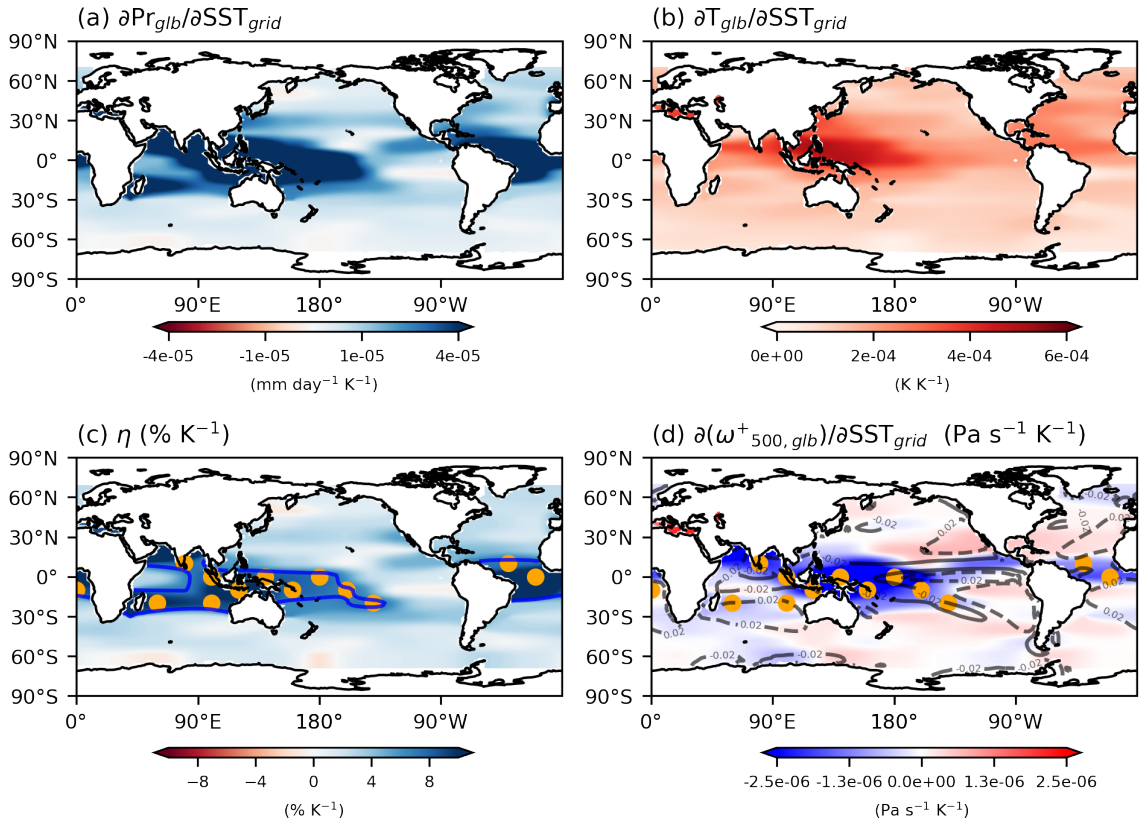

Figure 3.3: Dependence of global-mean (a) precipitation, (b) near-surface temperature, (c) η, and (d) upward vertical pressure velocity at 500 hPa (ω^{+}_{500}) with amplitude larger than 0.05 hPa s^{-1} to SST changes in each grid box. The blue contour line in e indicates the rate of 7 % K^{-1}. Orange dots in c and d indicate the patch experiments which show η larger than 7 % K^{-1}. Blue colours in d indicate enhanced upward motion, and red colours indicate otherwise. Contour lines in d refer to the baseline vertical pressure velocity at 500 hPa, with solid for upward motions and dash for downward motions.

3.3 Dependence of hydrological sensitivity on regional warming

To examine the SST warming pattern effect on η, we start with analysing the values of η estimated from an ensemble of simulations with Community Atmospheric Model 5 (CAM5) (Neale et al., 2010; Zhou et al., 2017) forced with 80 SST warming/cooling patches individually placed across the globe (Fig. 3.2a). Since the only changes in the patch experiments are from SST, this approach allows us to rule out the rapid adjustments and explore the dependence of the temperature-mediated responses of precipitation on inhomogeneous warming patterns.

Previously η was normally treated as a time-independent parameter in each model, reflecting its distinct parameterisations (DeAngelis et al., 2015; Samset et al., 2016; Thorpe and Andrews, 2014). However, Fig. 3.2b shows the estimated probability density function (PDF) of η derived from patch experiments and indicates otherwise. There is a remarkable spread of η (Fig. 3.2b) due to the various location of the warming patch superposed on the climatological SST pattern in CAM5. The peak (2.2% K^{-1}) of the estimated probability density function of η interestingly falls within the approximate range of η (1% K^{-1} to 3% K^{-1}) estimated by tens of GCMs (DeAngelis et al., 2015; Fläschner et al., 2016; Pendergrass, 2020). Fig. 3.2b demonstrates that by changing only the warming pattern, one model can reproduce an even wider spread of η than estimated by tens of GCMs, thus suggesting a high sensitivity of η to warming patterns.

Further investigation into different patch experiments implies that the magnitude of η is generally latitude-dependent (Fig. 3.4), and its variability can be traced back to the dependence of global-mean precipitation and temperature on the localised SST warming (3.5 and 3.6). Instead of showing the precipitation and temperature changes individually from 80 experiments, we use the Green's function approach (Section 3.2.5) to demonstrate the geographical dependence of global-mean precipitation (Fig. 3.3a) and temperature (Fig. 3.3b) to local SST warming. Both global-mean precipitation and temperature responses are more sensitive to warming in the tropical west-Pacific and Atlantic oceans than other regions, where the localised increase in SST can remotely warm the tropical free troposphere due to the intense convection and strong circulation (Dong et al., 2019b; Zhou et al., 2017), which will be examined in detail in the following part. Dividing the global precipitation response (Fig. 3.3a) by the surface temperature anomaly (Fig. 3.3b) gives the dependence of η on localised SST changes (Fig. 3.3c). It is suggested that the model tends to predict a much larger

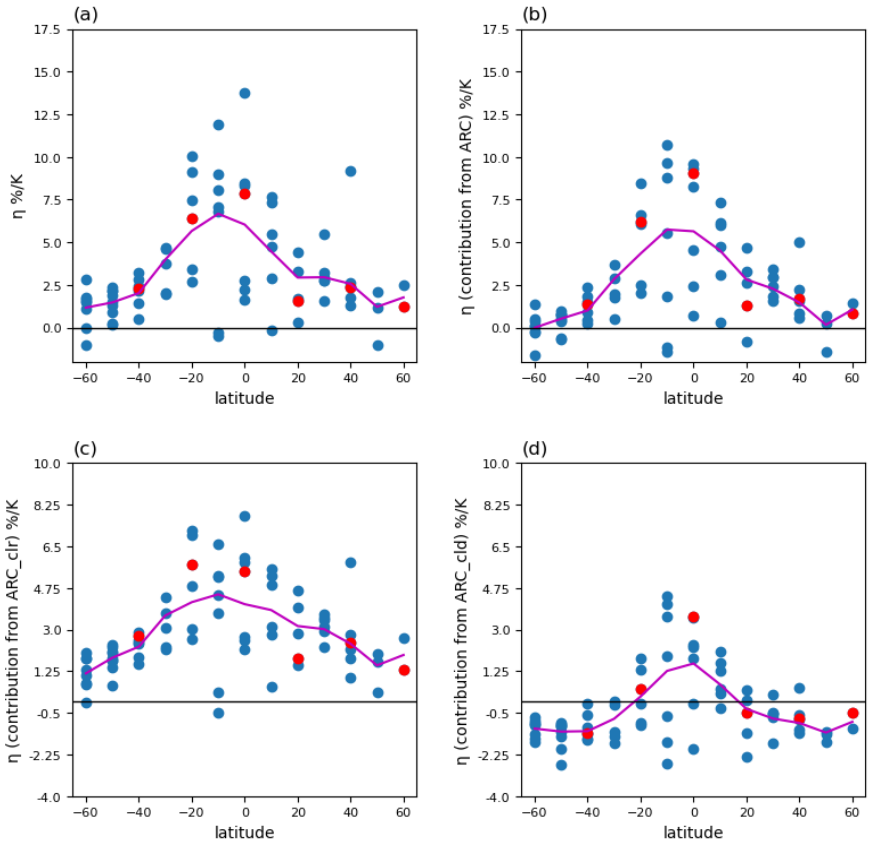

Figure 3.4: The distribution of estimated (a) hydrological sensitivity (η), (b) η contribution from atmospheric radiative cooling (ARC), (c) η contribution from clear-sky ARC, (d) η contribution from cloudy-sky ARC as a function of latitudes where the warming patches are placed in CAM5 model. 80 simulations are conducted with a warming patch individually applied on the prescribed sea surface temperature climatology in the baseline run. Each dot represents individual patch experiment. Red dots denote the experiments where the warming patch is placed along longitude 180 degree. The solid purple line indicates the averages as a function of latitude.

global-mean precipitation increase rate, i.e., larger η, in response to warming in regions of significant large-scale ascent (Fig. 3.7), such as the Indo-west-Pacific tropical Ocean and tropical Atlantic (Fig. 3.3c). More interestingly, some experiments with the SST warming localised on those strong tropical ascent regions have shown η larger than 7 % K^{-1} (Fig. 3.2b and 3.3c), i.e. a super Clausius-Clapeyron rate. These high values are robust and cannot be simply explained by the small global-mean temperature changes (Fig. 3.3b).

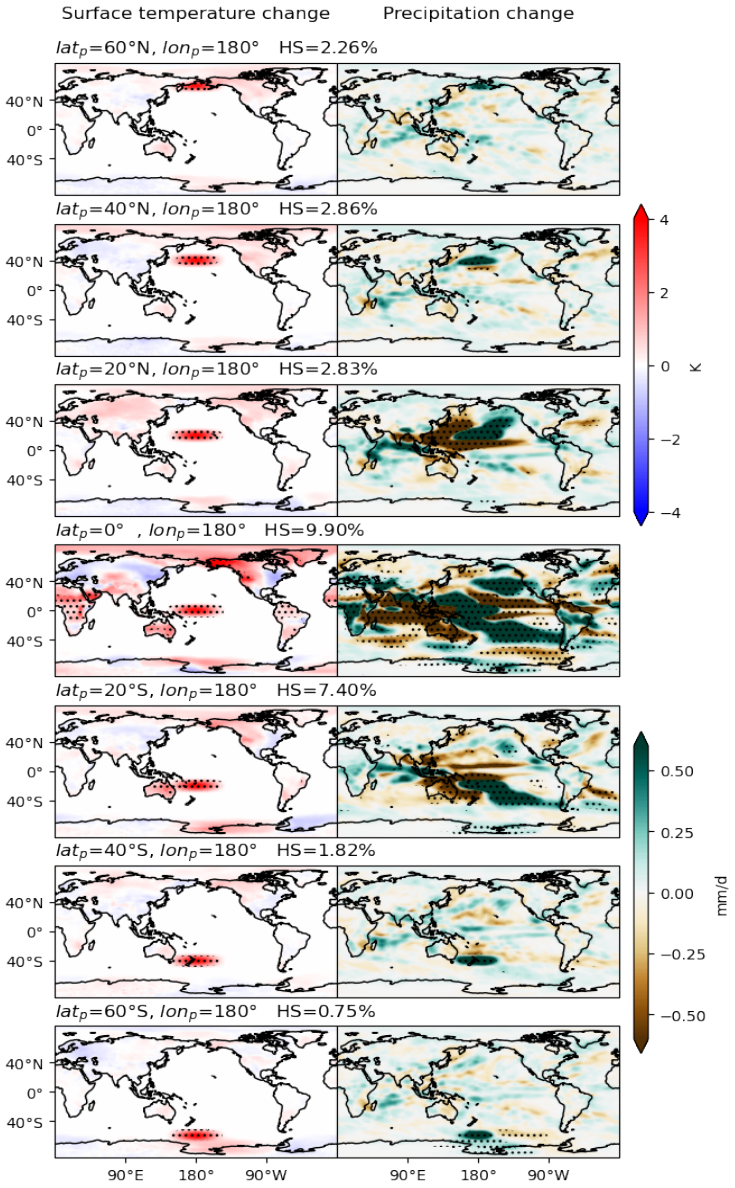

Figure 3.5: The geographical distribution of surface temperature (left column) and precipitation (right column) changes in the representative warming patch experiments in which the centre location varies along the longitude 180 degree. Also shown is the patch center location of each experiment and corresponding estimated hydrological sensitivity.

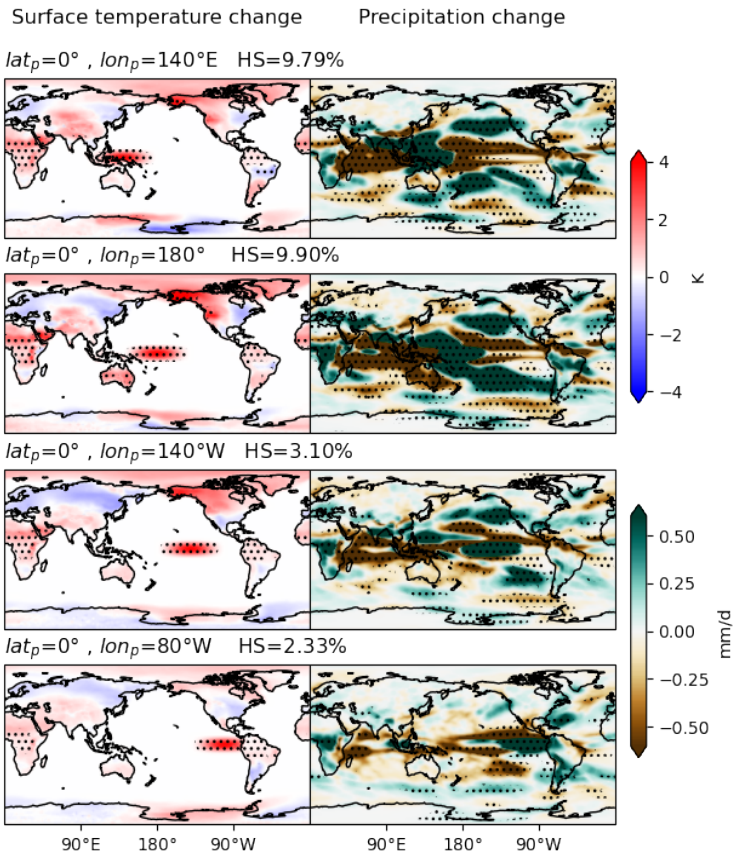

Figure 3.6: The geographical distribution of surface temperature (left column) and precipitation (right column) changes in the representative warming patch experiments in which the centre location varies along the equator. Also shown is the patch center location of each experiment and corresponding estimated hydrological sensitivity.

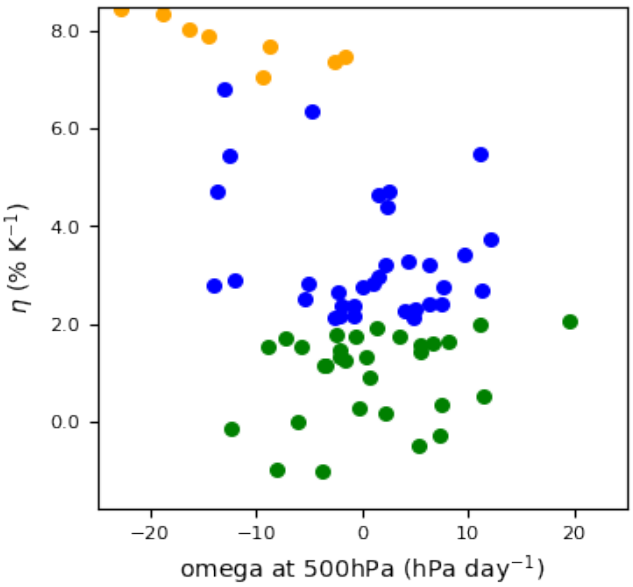

Figure 3.7: Scatter plot of hydrological sensitivity (η) parameters estimated from the CAM5 SST warming patch experiments and the corresponding vertical pressure velocity at 500 hPa at the patch centre. Orange dots indicate the patch experiments which show larger η than the 7 % K^{-1}, whereas green refers to η <2 % K^{-1} and blue refers to the middle.

Why is the magnitude of hydrological intensification more sensitive (sometimes even at super-Clausius–Clapeyron rate) to warming in strong tropical ascent regions? This could be explained through the response of atmospheric circulation to inhomogeneous warming. The water cycle can be approximated as a process carrying water vapour from the boundary layer to the free troposphere through ascending motion and associated condensation, with precipitation of a significant fraction of the water (Held and Soden, 2006). In the global mean, this process can be written as $P = M_c q$, where P is the global-mean precipitation, M_c is the convective mass flux, and q is the boundary layer mixing ratio. The relative changes in precipitation can be written as $\delta P/P = \delta M_c/M_c + \delta q/q$. Therefore, the response of global-mean precipitation can be understood theoretically from changes in its thermodynamical (i.e. $\delta q/q$; due to changes in atmospheric moisture content) and dynamical (i.e. $\delta M_c/M_c$; due to changes in circulations) components. It is well understood that changes in q closely follows the CC scaling at around 7 % K^{-1} (Allan et al., 2020; Trenberth et al., 2003), and this is also true in these patch experiments (Fig. 3.8) with slight deviations due to the responses over lands (O'Gorman and Muller, 2010). Therefore, $\delta M_c/M_c = \delta P/P - 0.07\delta T$ can diagnose the response of convective mass flux and circulation (Held and Soden, 2006; Vecchi and Soden, 2007; Ming et al., 2010).

Under a global warming scenario, the global-mean precipitation increase rate (at around 2 % K^{-1}) is smaller than the water vapour increase rate (at around 7 % K^{-1}) (Allen and Ingram, 2002). As a result, the circulation is slowed at around 5% K^{-1} (Held and Soden, 2006; Vecchi and Soden, 2007). However, in response to spatially inhomogeneous SST pattern changes, both the zonally asymmetric (i.e., Walker) (Bjerknes, 1969; Keshavamurty, 1982; Ma and Zhou, 2016; Stephens et al., 2018) and zonal-mean (i.e., Hadley) (Brayshaw et al., 2008; Zhou et al., 2020a) circulations can be either slowed down or accelerated depending on the SST pattern changes. If global circulation has been accelerated and convective mass flux is increased ($\Delta M_c/M_c > 0$), then the global-mean precipitation increase rate can exceed the CC rate (i.e. $\delta P/P > \delta T$). The SST patch experiments provide an ideal example to examine the circulation response to significantly inhomogeneous warming (Zhou et al., 2020a). Although convective mass flux field is not available in CAM5 output, changes in large-scale vertical pressure velocity at 500 hPa ($\Delta\omega^{+}_{500}$) have shown to be a good metric of global circulation changes and correlated well with changes in convective mass flux (Vecchi and Soden, 2007). Fig. 3.3d shows that there are stronger upward motions in response to warming localised at strong ascending regions, indicating an acceleration of the circulation. The locations of warming patches in experiments with super-Clausius–Clapeyron η (orange dots in Fig. 3.3d) also correlated well with the strong baseline ascending regions. On the other hand, warming patches in experiments with η lower than the average value under global warming scenario ($\eta < 2\%$ K^{-1}; green dots Fig. 3.3d) are mostly located in regions of strong descent (i.e. the descending branch of the Walker and Hadley circulation), indicating an even more slowed-down circulation. The similar pattern, particularly over the tropical Pacific ocean, between Fig. 3.3c and d suggests the underlying link between η and circulation changes. It is worth noting that there is an inconsistency between η responses and $\Delta\omega^{+}_{500}$ over the Indian Ocean. This may be because $\Delta\omega^{+}_{500}$ still can not fully capture the convective mass flux responses. It has been demonstrated that although changes in convective mass flux often have the same sign as $\Delta\omega^{+}_{500}$, the magnitudes of changes are not linearly proportional (Vecchi and Soden, 2007).

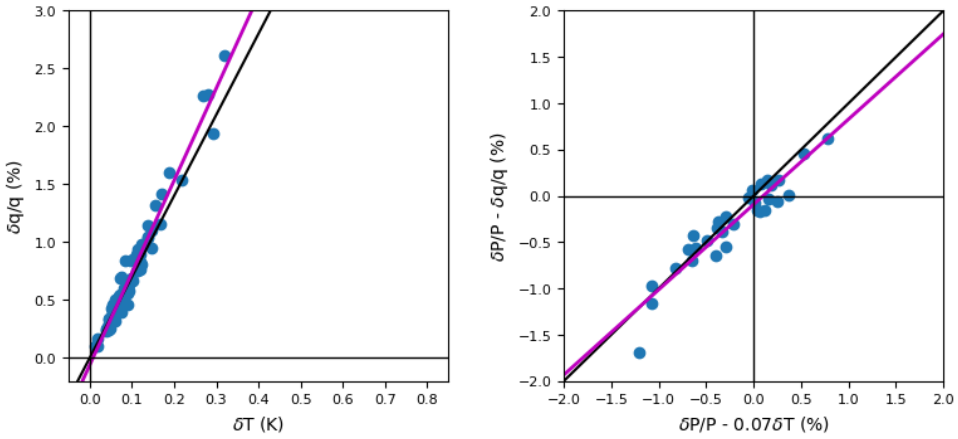

Figure 3.8: Scatter plot of the changes in global-mean surface temperature and relative changes in boundary layer mixing ratio from 80 SST warming patch experiments in the CAM5 model. The purple line indicates the linear fit. The solid black line refers to the Clausius-Clapeyron rate at 7% K^{-1}.

Fig. 3.9 demonstrates the schematic illustration of circulation response to inhomogeneous SST warming using the Walker circulation as an example. The equatorial SST gradient is one of the fundamental drivers of the Walker circulation (Bjerknes, 1969) (Fig. 3.9a). The strong ascents at the warm pool serve as a water vapour 'pump' to transport water vapour to the free troposphere. When the warming is pronounced in the warm pool, it enhances the prevailing large-scale ascent, increases the SST gradient, and strengthens the circulation (Fig. 3.9b). As a result, the global-mean convective mass flux is increased ($\Delta M_c/M_c > 0$), which can lead to a super CC η ($\delta P/P > 0.07\delta T$). In contrast, when the warming is pronounced at the cold pool, it offsets part of the background descent motions, decreases SST gradient, and slows down the circulation (Fig. 3.9c). The convective mass flux is therefore decreased ($\Delta M_c/M_c < 0$), leading to a smaller η than the CC rate ($\delta P/P < 0.07\delta T$). Note however that the Hadley circulation is also sensitive to inhomogeneous warming patterns with different mechanisms, but the conclusions remain the same (Zhou et al., 2020a). The tropical west-Pacific Ocean is the ascending centre of both Walker and Hadley circulations, making it a critical role in driving global circulation and transporting water vapour to the free troposphere. It is also worth noting that the perturbation is not limited to SST, strong absorbing aerosols have been shown to have the ability to alter the circulation and then the effective radiative effect as well (Williams et al., 2022).

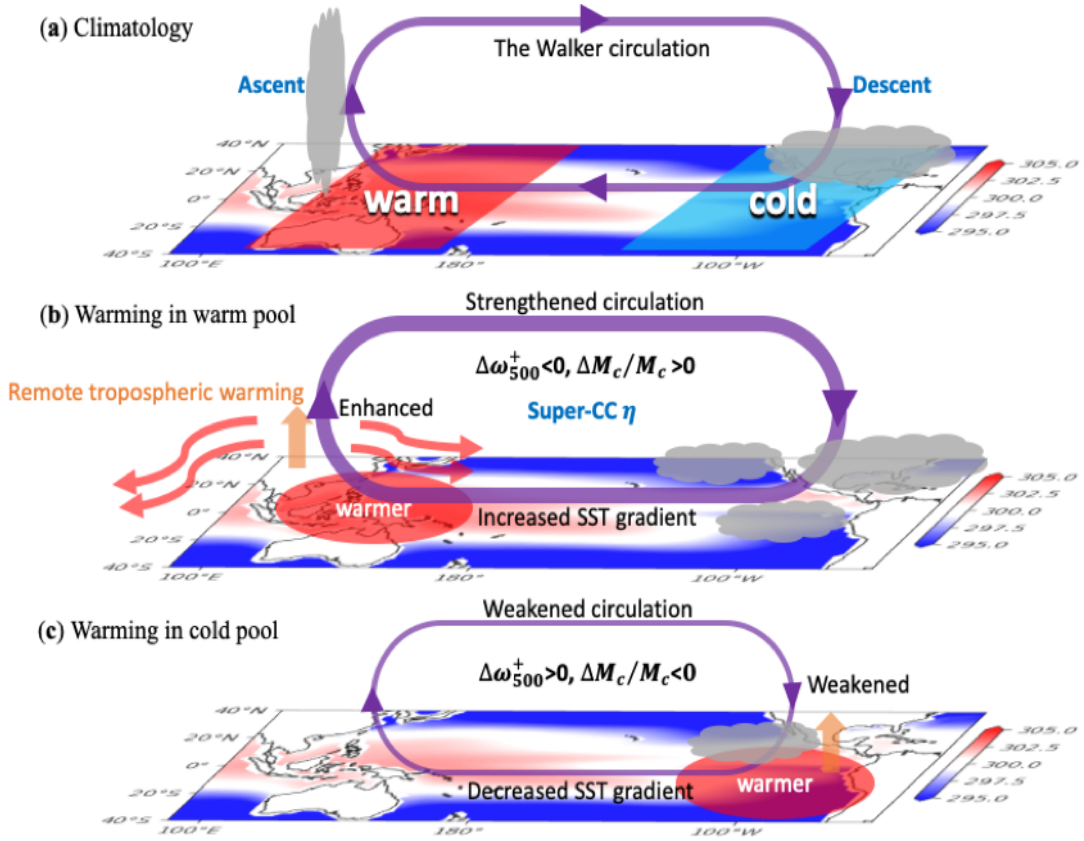

Figure 3.9: Schematic illustration of the tropical Walker circulation response to heterogenous SST warming. (a) The Walker circulation is predominately driven by the equatorial SST gradient (Bjerknes, 1969), which can be simplified as a warm pool located near the western equatorial Pacific and a cold pool located near the eastern equatorial Pacific. The warm pool is accompanied by strong large-scale ascents, whilst the cold pool is accompanied by prevailing descents. (b) Warming patch superposed on the warm pool induces an anomalous ascent and increased equatorial SST gradient, leading to a strengthening of the circulation. This can be quantified as stronger global-mean ascents at 500 hPa ($\Delta\omega^{+}_{500} < 0$), and an increase of convective mass flux ($\Delta M_c/M_c > 0$). Besides, the warming in the strong ascending region can be communicated to the remote free troposphere and increase inversion strength, leading to an increased low-cloud cover. (c) The anomalous ascent induced by the warming patch superposed on the cold pool reduces the prevailing descent, which opposes the Walker circulation. Together with the decreased equatorial SST gradient, it weakens the circulation, leading to weakened global-mean ascents at 500 hPa ($\Delta\omega^{+}_{500} > 0$), and a decrease of convective mass flux ($\Delta M_c/M_c < 0$). The background figure in (a-c) is the SST climatology in the CAM5 model.

The dependence of global-mean precipitation on SST warming patterns is also consistent with the energy budget framework (Section 3.2.4), which involves a balance between global-mean latent heat released from precipitation, atmospheric radiative

cooling (ARC) and surface sensible heat flux (Muller and O'Gorman, 2011; Dagan and Stier, 2020). The sensible heat flux responses are small and contribute little to global-mean preciptiation change (Fig. 3.10). The responses from ARC account for most of the η spread (Fig. 3.10) and resemble the global precipitation response distribution (Fig. 3.11). Given both clear sky and cloudy sky contribute to the ARC changes (Voigt et al., 2021; Zhang et al., 2021) (Section 3.2.4), we further decompose ARC responses into contributions from the clear and cloudy sky to understand the mechanisms, respectively (Fig. 3.12a and b).

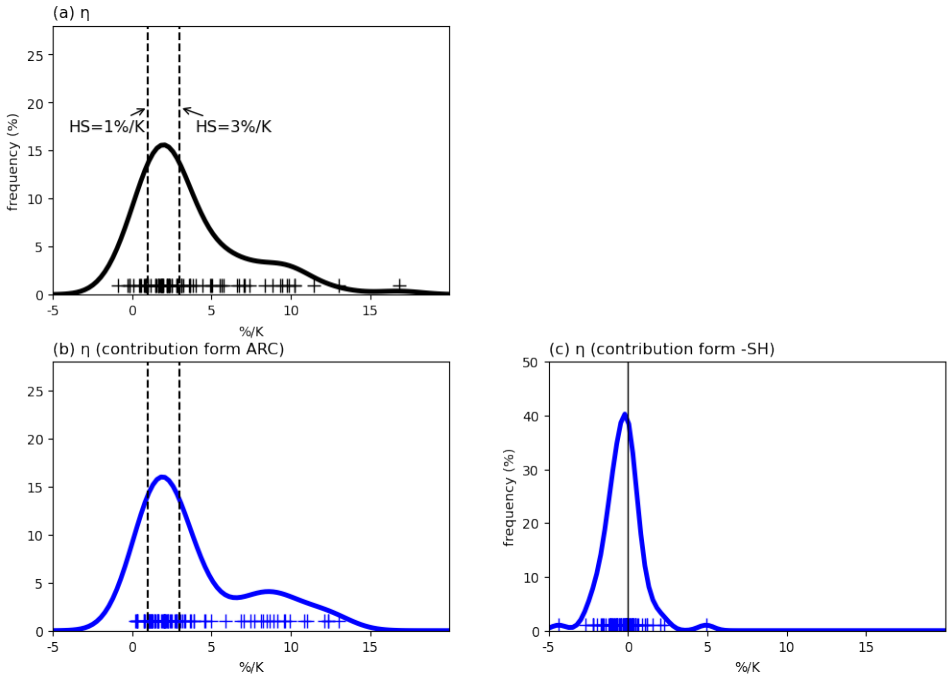

Figure 3.10: Estimated probability distribution of (a) η, (b) η caused by atmospheric radiative cooling, (c) η caused by sensible heat flux derived from patch experiments, which show significantly different (p value<0.05) global-mean surface temperature to baseline experiment. Each cross indicates the value of η estimated from the corresponding patch experiment.

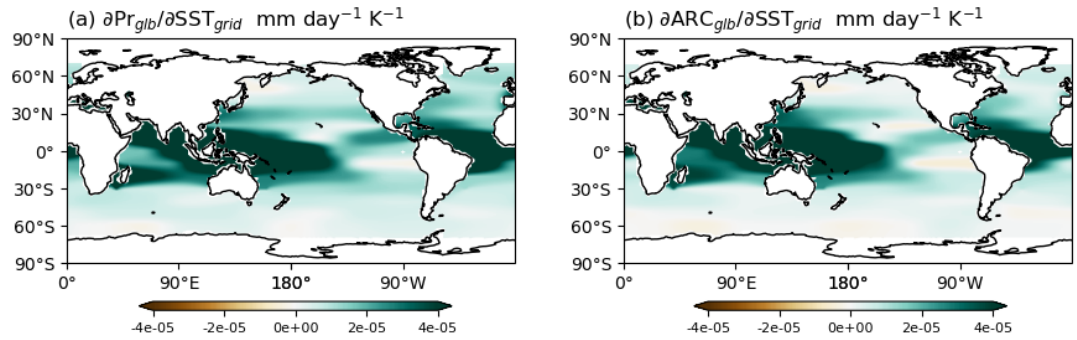

Figure 3.11: Dependence of annually global-mean (a) precipitation, (b) atmospheric radiative cooling (ARC) to SST warming in each grid box in the CAM5 SST patch experiments.All energetics are shown in equivalent precipitation units of mm day^{-1}.

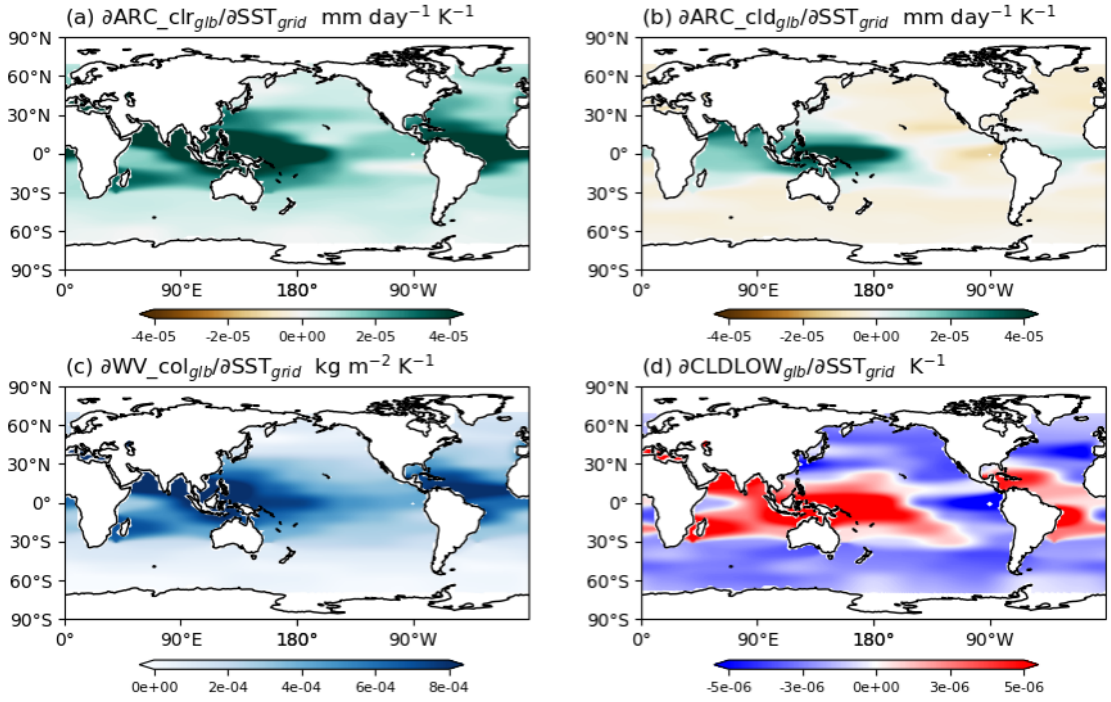

Figure 3.12: Geographical attribution of global responses to local SST changes. Dependence of global-mean (a) atmospheric radiative cooling from clear sky, (b) atmospheric radiative cooling from cloudy sky, (c) column-integrated water vapour, (d) low cloud fraction to SST changes ineach grid box. All energetics are shown in equivalent precipitation units of mm day^{-1}.

For clear sky, the dependences of global-mean near-surface temperature (Fig. 3.3b) and column-integrated water vapour (Fig. 3.12c) on local SST changes explain why the changes of clear-sky ARC are most sensitive in the ascending regions. Warming in tropical ascent regions can be propagated to the upper troposphere and

communicated to remote regions due to the intense convection and stronger circulation (Fig. 3.9b). This leads to increased temperature in remote regions of the globe and is associated with increased column-integrated water vapour, consistent with previous work (Dong et al., 2019b). These changes are associated with an increase in global clear-sky atmospheric radiative cooling (Fig. 3.12a) due to the Planck effect, which supports enhanced precipitation. On the other hand, warming in the extratropics and tropical descent regions (e.g. the Eastern tropical Pacific) is confined at local scales because of the less efficient horizontal transport. Therefore, the changes in atmospheric temperature and water vapour are localised and much smaller than those from warming in the ascent regions (but still positive).

Although atmospheric radiative cooling from cloudy-sky regions is small in global mean, it is highly spatially heterogeneous (Voigt et al., 2021) and sensitive to regional SST changes (Fig. 3.12b). Low clouds tend to increase ARC (i.e. cool the atmosphere), whilst high clouds tend to decrease ARC (i.e. warm the atmosphere) via the longwave radiation, reflecting their cloud altitude (Zhang et al., 2021; Voigt et al., 2021; Naegele and Randall, 2019). From the Green's function of cloud fraction response, we find most of the changes are from low clouds (Fig. 3.12d) rather than high clouds (Fig. 3.13). For extratropical or tropical descent regions, the warming is localised. An increase in surface temperature leads to a decrease in local tropospheric stability or estimated inversion strength (EIS) (Bretherton and Blossey, 2014), and therefore a reduction of local low cloud amounts and ARC (Wood and Bretherton, 2006). On the other hand, for tropical ascent regions, local low clouds decrease in response to regional warming as well. However, in contrast to descent regions, warming in the tropics can be communicated to remote regions and warm up the upper troposphere in remote regions due to moist adiabatic processes (Fig. 3.9b), which results in increased tropospheric stability and non-local low clouds amount. Generally, there will be a positive response of global-mean ARC from remote clouds when the SST perturbation is applied in the tropical ascending regions, and a negative response from local clouds when the SST perturbation is applied in the tropical descending regions and subtropics (Zhou et al., 2017).

Both ARC from the cloudy and clear sky in tropical ascent regions show a strong positive sensitivity to local warming (Fig. 3.9c and d), highlighting again the essential role of the Indo-Pacific warm pool area in determining the η magnitude, in addition to the dynamical perspective. To summarise, both the qualitative large-scale response perspective and the quantitative energy budget perspective suggest that warming in the tropic ascent region leads to an 'invigorated' response of circulation and ARC,

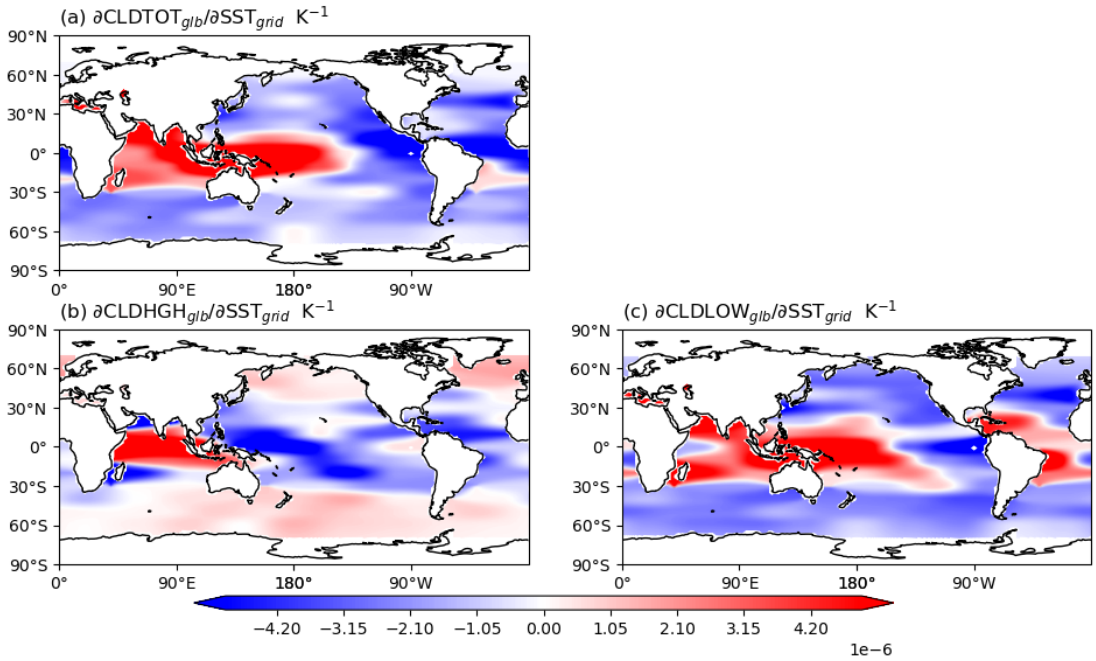

Figure 3.13: Dependence of annually global-mean (a) total cloud fraction, (b) high cloud fraction, and (c) low cloud fraction to SST warming in each grid box in the CAM5 SST patch experiments.

whereas warming in the descent region lead to a 'dampened' response, which results in a bimodal distribution of η in Fig. 3.2b as well.

3.4 Estimates of the pattern effect among different GCMs

The dependence of η on SST warming pattern demonstrated above suggests that the differences in warming patterns can also contribute to the inter-model spread, as the SST warming pattern is evolving differently in fully-coupled models even for identical forcing (Eyring et al., 2016; Andrews et al., 2012).

Here we quantify the pattern effect contribution to the spread of η among GCMs. The spread of η among GCMs can arise from: (1) different global-mean precipitation responses to a given warming pattern; and (2) different SST warming patterns per degree global-mean warming (under the same external forcing). The calculation of η based on equation 3.1 can then be expanded as follows:

$$\eta = \frac{\partial P(glb)}{\partial SST(pattern)} * \frac{\partial SST(pattern)}{\partial T(glb)}. \tag{3.11}$$

In this framework, the first term on the right-hand side accounts for the atmospheric model differences in estimating precipitation responses to a certain warming pattern, hereafter denoted the atmospheric model term. The second term on the right-hand side accounts for the variability of different SST warming patterns, hereafter denoted the pattern effect term.

We take advantage of Green's function from CAM5 SST patch experiments to derive the spread of both terms across 24 fully coupled CMIP5 models for the abrupt4xCO_2 experiments. We use the Green's function derived from CAM5 SST patch experiments to reproduce the global-mean precipitation changes for other models by inputting the spatial SST warming pattern only. For example, for model k, which is a GCM with a patterned SST warming, the reconstructed precipitation change is

$$\Delta P_{k,greens} = \sum_i \left(\frac{\partial P}{\partial SST_i}\right)_{CAM5} \Delta SST_i, \tag{3.12}$$

where $\left(\frac{\partial P}{\partial SST_i}\right)_{CAM5}$ is the Green's function derived from CAM5 for each grid box (equation 3.10). It is worth noting that we do not expect this CAM5 Green's function reconstructed precipitation to perfectly reproduce another model's estimated precipitation, due to model differences, other physical processes that impact on precipitation yet not associated with SST changes, as well as non-linear contributions (equation 3.9). However, the reconstructed precipitation changes are found to predict the model estimated precipitation responses in the 24 CMIP5 models reasonably well, with robust correlations (Fig. 3.14), although the relationships do not follow the 1:1 ratio and vary from model to model (Fig. 3.15), as following

$$\Delta P_k = \frac{\partial P_k}{\partial P_{greens}} * \Delta P_{k,greens} = \alpha_k * \Delta P_{k,greens}, \tag{3.13}$$

$$\eta_k = \alpha_k * \frac{\partial P_{k,greens}}{\partial T} = \alpha_k * \left(\sum_i \left(\frac{\partial P}{\partial SST_i}\right)_{CAM5} * \frac{\partial SST_i}{\partial T\,(glb)}\right). \tag{3.14}$$

The differences in regression slope (α) manifest atmospheric model differences. On the other side, the differences in Green's function approach reconstructed precipitation changes account for the different warming pattern effect, as the patterned SST warming is the only input. Therefore, we can use the regression slope between the model-estimated and reconstructed precipitation changes as a factor representing model differences (α), which accounts for models differences other than the warming pattern, and the spread of Green's function reconstructed precipitation in the 24 CMIP5 models to account for the pattern effect.

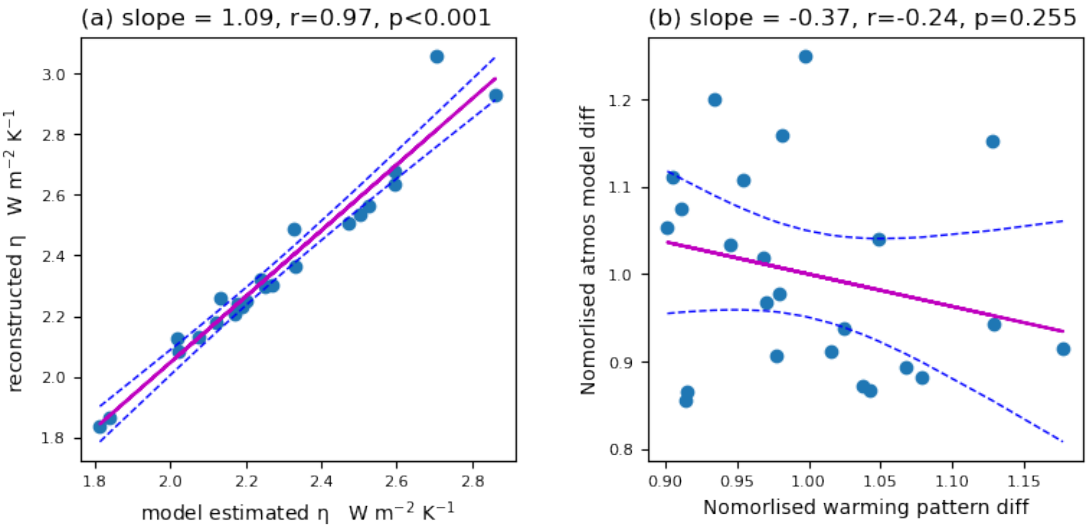

Figure 3.14: (a) Scatter plot of reconstructed η (y-axis) and Gregory-style derived η. (b) Scatter plot of the pattern effect term (x-axis) and atmosphere model difference term (y-axis) derived from 24 CMIP5 models.Also shown are the slope of regression, the correlation coefficient (r), and p-value.

This framework reasonably reproduces the model-estimated η from the CMIP5 models (Fig. 3.14a). The weak relationship between the atmospheric model term and pattern effect term (Fig. 3.14b) indicates that both independently contribute to the estimated η.

While previous work focused on analysing the atmospheric model term when studying the spread of η (DeAngelis et al., 2015; Samset et al., 2016; Watanabe et al., 2018), here we show that the contribution from different SST warming patterns is as important (Fig. 3.16). The variation of the warming pattern effect is as large as the atmospheric model difference and the spread of η (Fig. 3.16a). It is worth noting that in the framework of equation 3.11, reconstructed η is the product of the atmospheric model term and pattern effect term, which means the spread is non-linearly contributed by the averages and deviations of the two terms at the same time. This is different from the concept of radiative forcing, for which the uncertainties can first order be linearly added (Bellouin et al., 2020).

Fig. 3.16b further shows the spread of η from 24 CMIP5 models in reconstructed η space based on equation 3.11 (blue colours), which is determined by both pattern effect and atmospheric model difference (x and y axis, respectively). The decomposition helps to distinguish contributions to large difference in η among models from differences in atmospheric models or warming patterns. The large difference in η from GISS-E2-H and ACCESS1-0, which have similar warming patterns, is caused by

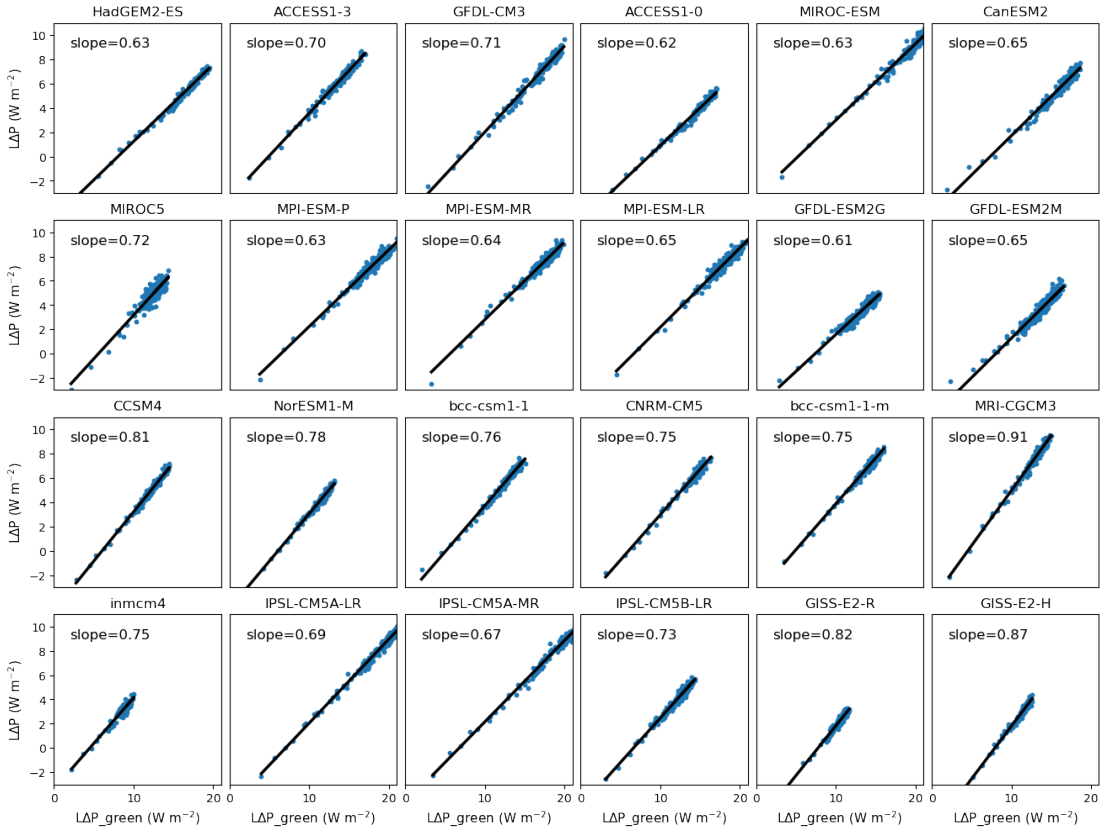

Figure 3.15: Scatter plot of Green's function derived annual precipitation responses (x-axis) and model estimated annual precipitation responses (y-axis) for abrupt4xCO2 experiments from 24 CMIP5 models. Each dot indicates the annual average for each model year (150 years in total). Also shown is the regression slope and p value calculated based on the statistical F-test.

different atmospheric model parameterisation, consistent with previous work (DeAngelis et al., 2015) suggesting these two models having different shortwave absorption efficiencies. On the other hand, the model with the largest pattern effect (IPSL-CM5A-MR) has much more warming concentrated in the tropics compared to the lowest one (ACCESS1-0) (Fig. 3.17), leading to a large η from IPSL-CM5A-MR, which is consistent with our proposed mechanisms and further supports our conclusions. Furthermore, this decomposition also reveals different mechanisms between models with close η values. For example, Fig 3.16b suggests that the similar magnitude of η from GISS-E2-H and MIROC-ESM are due to the different contributions from the atmospheric model term and pattern effect term (Fig 3.16b), with larger atmospheric model contribution and smaller warming pattern contribution for GISS-E2-H and the opposite for MIROC-ESM. The compensation between the different mechanisms results in close η values between these two models.

Aside from using fully ocean-atmosphere coupled experiments, some studies also perturb the prescribed SST of non-coupled atmosphere-only experiments to study the response of the hydrological cycle (Fläschner et al., 2016; Thorpe and Andrews, 2014; He et al., 2014). We compare the η parameters estimated from abrupt4xCO_2 (fully coupled), AMIP4K (prescribed SST with uniformly 4K increase compared to present-day SST), and AMIPFuture (prescribed SST with global mean 4K but patterned SST increase) experiments. η parameters estimated from AMIPFuture are systematically larger than those from AMIP4K, which are then larger than those from the fully coupled abrupt4xCO_2 experiments (Fig. 3.18). Fläschner et al. (2016) also noticed this and assumed that if the larger η in the AMIP4K experiment compared to abrupt4xCO2 was due to the pattern effect in abrupt4xCO2, then the value of η in the AMIPFuture experiments (which also involve patterned warming) would be smaller compared to AMIP4K as well. However, since η from AMIPFuture experiments are larger than AMIP4K, they argued that the pattern effect is not the reason for the difference in η and suggested that it could be caused by the non-linear responses to CO_2 concentration. However, based on our analysis, the pattern effect is not necessarily monotonic and it can contribute either to a larger or a smaller η. A comparison of the warming patterns from each experiment shows that SST warming in AMIPFuture is more pronounced at low latitudes than AMIP4K, while warming in AMIP4K is more pronounced at low latitudes than abrupt4xCO_2 (Fig. 3.19). Quantitatively, the different values of pattern effect (vertical lines in Fig. 3.16b) can also explain the differences in η from different experiments. Conclusions remain the same

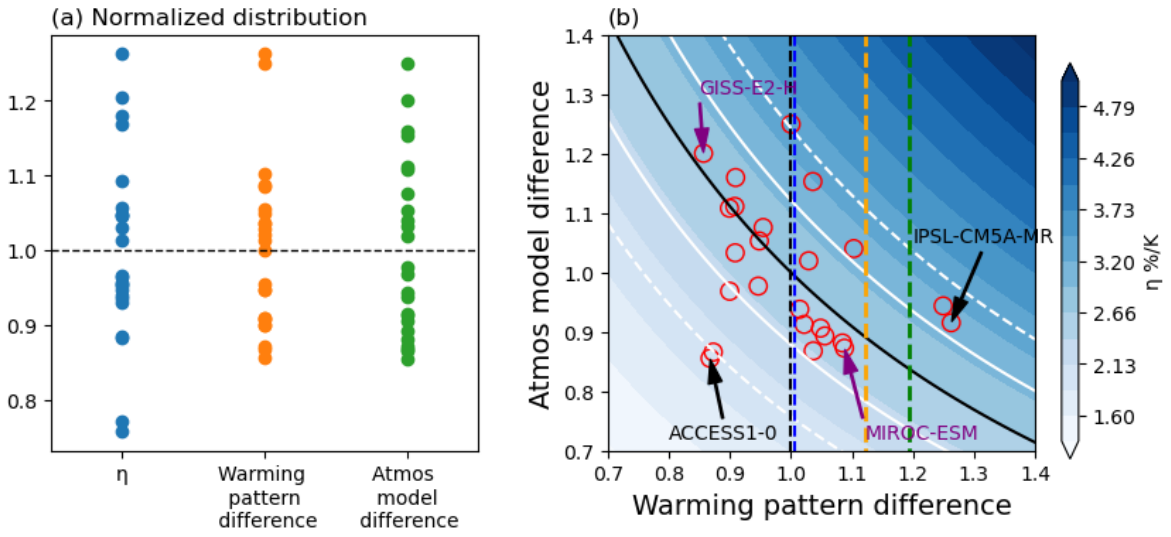

Figure 3.16: Attribution of hydrological sensitivity uncertainties from CMIP5 models. (a) Values of η, warming pattern term (which accounts for the variability of different SST warming patterns), and atmospheric model difference term (which indicates the different atmospheric model responses to a certain warming pattern) from equation 3.11 for 24 CMIP5 models for abrupt4xCO2 experiment, normalised by the multi-model mean. (b) Contribution of the normalised pattern effect and atmospheric model differences to the hydrological sensitivity space. Blue colours denote the η space estimated based on equation 3.11. Red circles denote the 24 CMIP5 models. The solid black line, white solid lines, and white dashed lines refer to the ensemble mean, one inter-model standard deviation, and two inter-model standard deviations of the η parameters estimated from the 24 CMIP5 models abrupt4xCO2 experiment, respectively. The vertical black dashed line, blue dashed line, orange dashed line, and green dashed line indicate the ensemble mean of pattern effect estimated from the abrupt4xCO_2, AMIP4K, and AMIPFuture experiment, respectively. The vertical blue dashed line is same as the black dashed line, but for the ensemble mean of the 9 CMIP models which are also used in the AMIP experiments in this study.

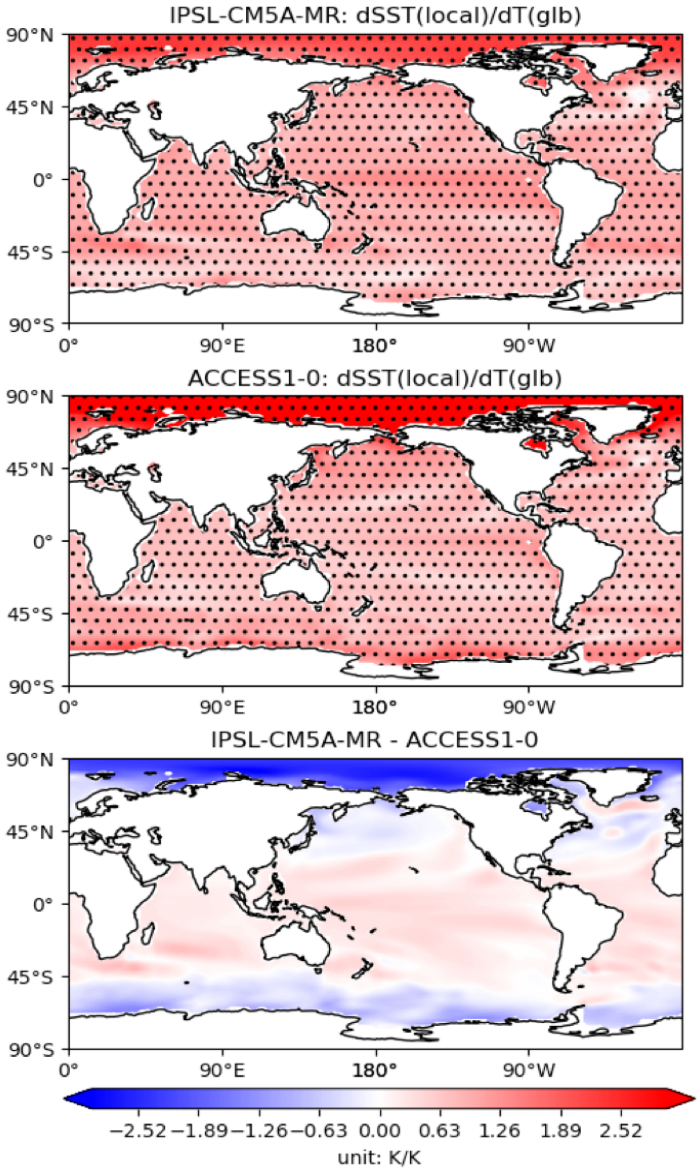

Figure 3.17: Grid-wise regression between local sea surface temperature changes and global SST changes for models (a)IPSL-CM5A-MR and (b) ACCESS1-0. The dots denote the regression is robust (at 99% significance). (c) The difference between the two models.

after replacing the pattern effect term from CMIP all-members (24 models) ensemble mean (black vertical line) with the AMIP-members (9 models) ensemble mean (blue dashed line in Fig. 3.16b. This suggests that future work needs to consider the differences in SST warming patterns when using different SST setups to study hydrological intensification. It is noteworthy that the spread of η in AMIP models does not significantly decrease compared to the fully-coupled CMIP5 models (Fig. 3.18). This is because the two contributing terms (atmospheric model difference and pattern effect difference) are multiplied rather than added.Without the pattern effect contribution (as the models have the same warming pattern), the spread of η in AMIP models is dominated by the atmospheric model differences, which is consistent with the fact that the spread of model difference term is nearly as large as the spread of η in CMIP5 coupled experiments in Fig. 3.16a.

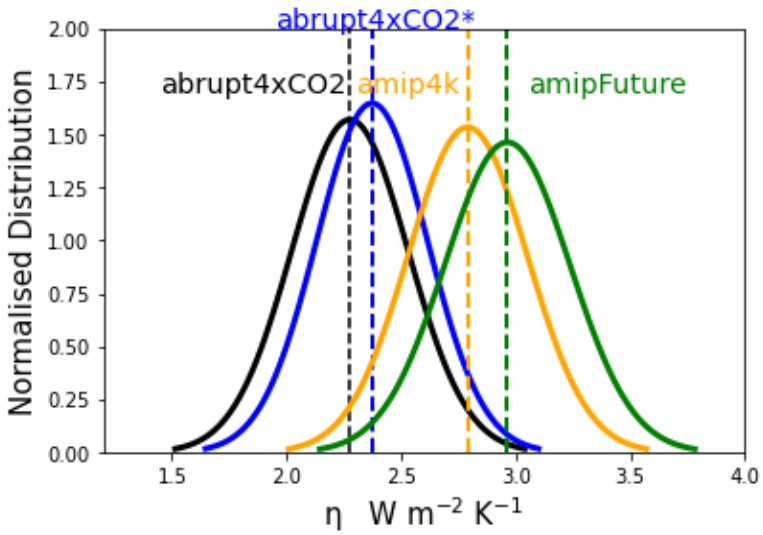

Figure 3.18: The estimated distribution of hydrological sensitivity estimated from 24 CMIP5 abrupt4xCO2 models (black line), 9 CMIP5 abrupt4xCO2 models which are also used in AMIP experiments (blue line), AMIP4k (orange line), and AMIPFuture experiments (green line).

3.5 Observational evidence of pattern effect on the hydrological cycle

Properly accounting for the warming pattern is important not only for better predicting future hydrological intensification, but also for understanding the historical changes in the hydrological cycle. The change in global-mean precipitation is energetically modulated by the sum of a fast component (ΔAA; the changes in atmospheric

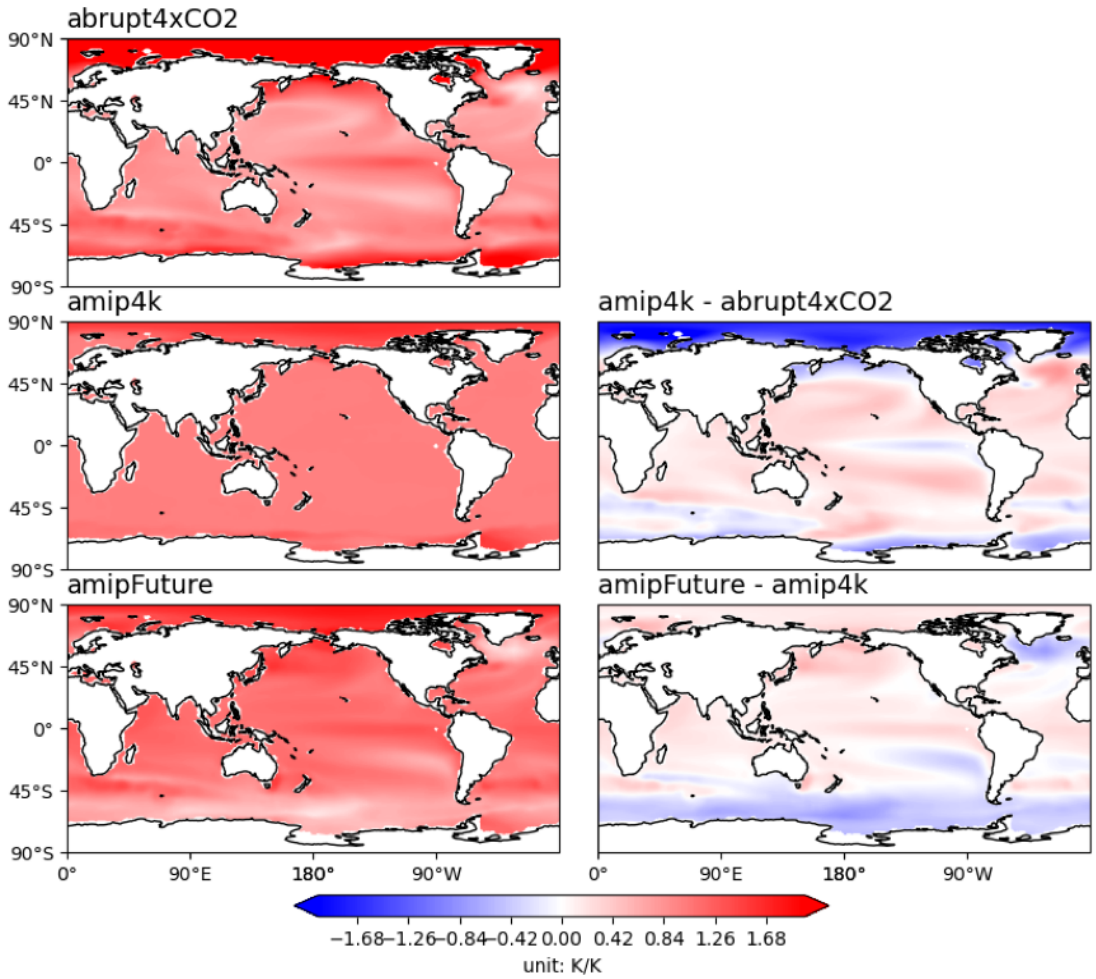

Figure 3.19: The ensemble-mean warming pattern from 24 models for abrupt4xCO2, AMIP4K, and AMIPFuture experiments, respectively (first column). Also shown are the differences between them (second column).

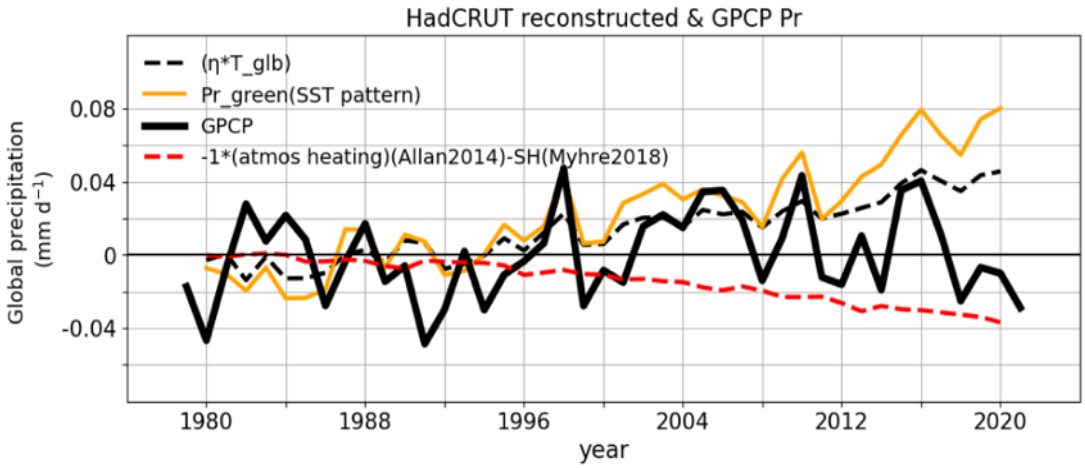

Figure 3.20: Time series of GPCP global-mean precipitation (solid black line), reconstructed slow component of precipitation change without pattern effect (dashed black line), reconstructed slow component of precipitation change with pattern effect based on HadCRUT SST data (orange line), and fast component of precipitation change based on atmospheric heating data from Allan et al. (2014).

absorption directly induced by aerosols and GHGs through atmospheric-only processes; independent of surface temperature changes and proportional to TOA forcing) (O'Gorman et al., 2012; Ming et al., 2010; Allan et al., 2014) and a slow component ($\eta\Delta T$; through variation of atmospheric shortwave and longwave radiation induced by changes in surface temperature through various feedback mechanisms; scaled with global-mean temperature changes) (Allen and Ingram, 2002; O'Gorman et al., 2012; Samset et al., 2016; Thorpe and Andrews, 2014; Allan et al., 2014), assuming little contribution from the surface sensible heat (O'Gorman et al., 2012), as equation 3.15,

$$\Delta P = \eta \Delta T * P_0 - \Delta \mathrm{AA}/L, \tag{3.15}$$

where L denote the latent heat of condensation so all terms are in unit of mm d^{-1}. Conventionally the slow component is derived from the value of η multiplied by global-mean temperature changes (Thorpe and Andrews, 2014; Allan et al., 2014). Here we set η to 2.3 % K^{-1}, which is the ensemble mean from 24 CMIP5 models. However, this framework does not consider the pattern effect, which modulates the precipitation changes through the slow component and has been shown to be important in the early part of this work (Sec 3.3). Therefore, we put forward a new framework to account for the pattern effect,

$$\Delta P = \sum_i \left(\frac{\partial P}{\partial SST_i} \right) \Delta SST_i - \Delta \mathrm{AA}/L, \tag{3.16}$$

where $\left(\frac{\partial P}{\partial SST_i}\right)$ is the Green's function derived from CAM5 for each grid box and SST_i refers to the SST in a grid box i. The fast component is kept the same for both approaches, using the values reported from Allan et al. (2014), so the differences are only caused by the pattern effect. Fig. 3.20 demonstrates each component used to reconstruct precipitation using HadCRUT observed SST data sets.

The reconstructed precipitation based on HadCRUT observed SST including the pattern effect well reproduces the observed precipitation, not only in magnitude but also in interannual variation, whilst a reconstruction without the pattern effect does not (Fig. 3.21a). This is also evident through the improved correlation coefficient between observed and reconstructed precipitation. The correlation relationship is better after 1995, when the GPCP dataset is suggested to be more reliable (Liu et al., 2012). Attribution from fast and slow components indicates that the interannual variability can be traced to the slow component accounting for the pattern effect (Fig. 3.20). Our conclusions remain robust when replacing the HadCRUT observed SST datasets with NOAA observed SST (Fig. 3.21b) and ERA5 SST reanalysis (Fig. 3.21c). One interesting result is that the reconstructed precipitation based on the ERA5 patterned SST dataset is even better than ERA5 precipitation dataset (Fig. 3.21c), even though this approach is relatively simple. Moreover, during strong El Niño events, the observed and reconstructed (with the pattern effect) global-mean precipitation show larger magnitude of changes than the reconstructed one without the pattern effect (Fig. 3.21). This is consistent with previous studies suggesting that El Niño significantly enhances the zonal-mean (Hadley) circulation (Lu et al., 2008; Rollings and Merlis, 2021) and convective mass flux as a result of tropical-mean warming and increased meridional SST gradient, although the Walker circulation is weakened at the same time (Ma et al., 2018).

The implication of pattern effects on CMIP models can be seen by comparing CMIP6 and AMIP6 historical simulations (Fig. 3.21d). Both sets of simulations use the same external forcing fields, the difference being that the SST is free to evolve in CMIP6 historical simulations while it is prescribed from observations in AMIP6 simulations. AMIP6 simulated precipitation much better captures observed inter-annual variability than CMIP6 historical simulations (Fig. 3.21d), despite the fact that global-mean SST in CMIP6 historical simulations reasonably resembles the observed SST (Fig. 3.22). This demonstrates that the observed SST patterns are not reproduced in CMIP6 historical simulations, affecting their ability to simulate the global-mean precipitation variability, which highlights the importance of accurately simulating not only the global-mean but also the patterns of SST in order to better

simulate global-mean precipitation. There is almost no trend in observed and AMIP6 simulated global-mean precipitation, while there is an increasing trend in CMIP6 simulations. This is associated with the observed suppressed global warming during 1998-2013 (Fig. 3.22) due to a La-Nina-like Pacific cooling (Kosaka and Xie, 2013), which further led to a weakened water vapour (Allan et al., 2022) and precipitation response. However, this La-Nina-like Pacific cooling pattern is not captured in CMIP6 historical simulations (Kosaka and Xie, 2013; Allan et al., 2022) which therefore results in a stronger precipitation trend.

3.6 Discussions

Knowledge about the dependence of hydrological intensification on spatially inhomogeneous warming is lacking as previous work focused on global-mean temperature changes. We show that the intensification of the hydrological cycle under climate change depends on the surface warming patterns, highlighting a non-linearity of the climate systems. This means that the magnitude of η could be time-dependent, climate forcer dependent, model-dependent, and experiment-dependent (prescribed SST or fully coupled setup) via the pattern effect, rather than being constant for each model (DeAngelis et al., 2015; Thorpe and Andrews, 2014). Accounting for the pattern effect will help to reduce uncertainties in our estimates of the intensification of the hydrological cycle in responses to global warming (Samset et al., 2016; Frieler et al., 2011; Dai, 2006). For future studies, it is desirable to separate the uncertainties caused by different warming patterns from the differences arising from atmospheric model parameterisations.

We show that the variation of η is mediated by atmospheric radiative cooling and global circulation response to heterogeneous warming. If the warming is confined to regions with strong ascent, it will accelerate the circulation, enhance the transport of water vapour from the boundary layer to the free troposphere, increase the global-mean atmospheric radiative cooling from both clear sky and clouds, and lead to a potential super-Clausius-Clapeyron η. It is, however, worth noting that the distribution of might be dependent on the experiment design (such as patch size and magnitude of temperature increase) and the model used. Furthermore, this idealised patch-like warming is not likely to be sustained in the real world or a coupled model due to interactive responses between the wind, evaporation, ocean dynamics, and thermocline (Xie et al., 2010). Under real-world global warming scenarios, most

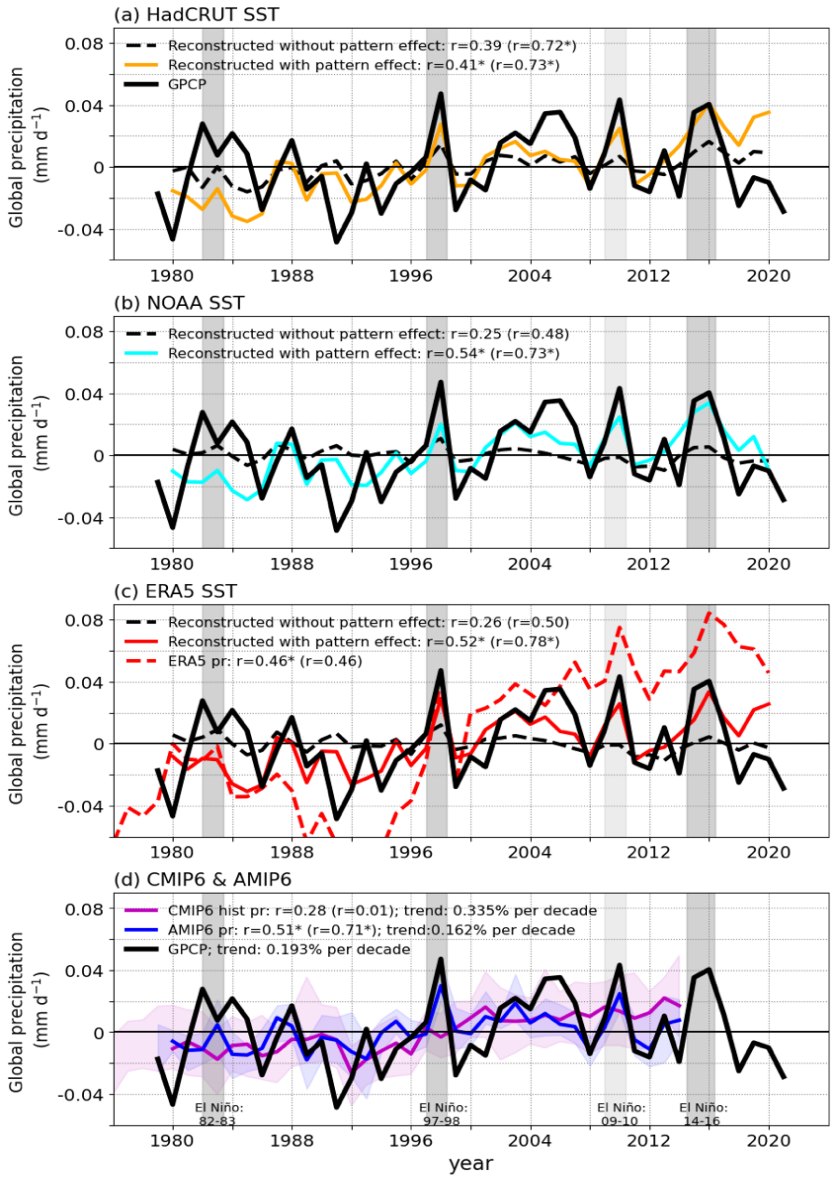

Figure 3.21: (a) Timeseries of observed precipitation anomaly from GPCP (solid black line), reconstructed annual precipitation anomaly without pattern effect (based on equation 3.15; black dashed line), and reconstructed with pattern effect (based on equation 3.16; orange line) based on HadCRUT observed SST datasets. (b) Same as a but for reconstructed precipitation based on NOAA observed SST datasets. (c) Same as a but for reconstructed precipitation based on SST from ERA reanalysis. The solid red line denotes the global-mean precipitation anomaly from ERA reanalysis. (d) Simulated global-mean precipitation from CMIP6 (purple line) and AMIP6 (blue line) ensemble mean with shading representing the inter-model range. Dark grey shading indicates very extreme El Niño events (year 1982-1983, 1997-1998, and 2014-2016) and light grey indicates strong El Niño events (year 2009-2010). r denotes the correlation coefficient between reconstructed or simulated precipitation and GPCP observed precipitation datasets, and the asterisk mark $*$ indicates the correlation is statistically significant (at 95% confidence level). r in brackets refers to the correlation coefficient after year 1995 when the GPCP dataset is suggested to be more reliable (Liu et al., 2012).

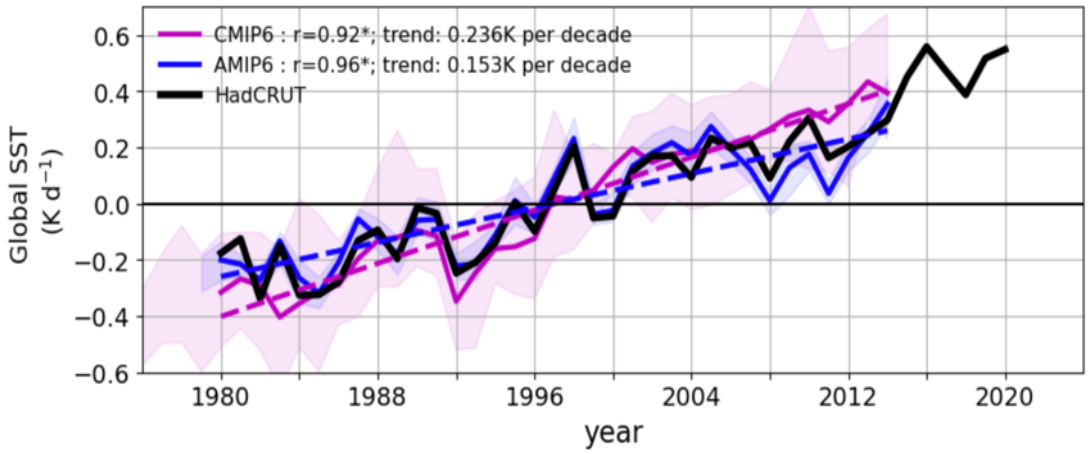

Figure 3.22: Simulated global-mean near-surface temperature from CMIP6 (purple line) and AMIP6 (blue line) ensemble mean with shading representing the inter-modal range. r denotes the correlation coefficient between reconstructed or simulated near-surface temperature and HadCRUT datasets, and the asterisk mark indicates the correlation is statistically significant (at 95% confidence level).

warming is happening at higher latitudes and the tropical SST remains nearly unchanged (Vecchi and Soden, 2007). Besides, the SST pattern change can also lead to circulation shifts instead of altering their magnitude, which can be model-dependent (Ma and Zhou, 2016).

However, this high dependence of η on tropical Indo-west-Pacific SST does have important implications for inter-annual variability, such as variations related with ENSO (Fig. 3.21). Previous work estimates the temperature-mediated precipitation responses as the product of η and global-mean temperature responses, which we found to neglect the important role of spatial temperature patterns. We show that accounting for the pattern effect significantly improves the reconstructed global-mean precipitation variations compared with observations. The temperature-mediated component of precipitation change can be caused by the variation of SST pattern, sometimes even without changes in global-mean temperature. This suggests that future studies need to account for the spatial inhomogeneities in SST changes rather than only considering global-mean temperature changes.

Despite the fact that we derive the Green's function from only one model (CAM5), and that nonlinear contributions have been ignored for simplification, the application of our framework to reconstruct precipitation from transient sea surface temperature patterns reasonably reproduce both model-estimated and observed precipitation. Nevertheless, future work is needed to compare the Green's function for global precipitation from different global climate models to understand its model dependency.

The pattern effects on η also have implications for regional and extreme rainfall variabilities, which are particularly of interest to social development and policy relevant. Changes in η can be used to diagnose the changes in general circulation as well as water vapour lifetime, which are directly relevant to regional rainfall and extreme events (Sillmann et al., 2019). η over land is generally lower than the global mean due to the limitation of availability of water vapour over land (Gimeno et al., 2012), thus strongly relies on the moisture transport and can be influenced by SST warming patterns (Ma et al., 2018; Bony et al., 2013). Additionally, the evolving patterns of warming can drive different land-sea contrast responses (Ma et al., 2018; He and Soden, 2015) which can strongly influence regional and extreme rainfall events (Taylor et al., 2017). Therefore, we hope our work could motivate further efforts on studying the changes in extreme rainfall events driven by the pattern effects as well.

Chapter 4

Anthropogenic aerosols modulated 20th-century Sahel rainfall variability via their impacts on North Atlantic sea surface temperature

As demonstrated in Chapter 3, global hydrological sensitivity can be affected by sea surface warming patterns, which has not been given adequate consideration in previous studies. Different from global-mean precipitation, the SST pattern effect on regional rainfall has been well recognised by a large number of previous works. For example, early literature suggested that the zonal/equatorial SST gradient is one of the fundamental drivers of the Hadley cell (Held and Hou, 1980) and Walker cell (Bjerknes, 1969), which implies that the SST pattern can influence the large-scale circulation properties. More specifically, existing literature has well established that regional water cycle systems strongly rely on spatially heterogeneous warming patterns (e.g. Barsugli and Sardeshmukh, 2002; Xie et al., 2010; Ma et al., 2018)).

The African monsoon system is particularly sensitive to the global distribution of ocean temperatures (Palmer, 1986; Hoerling et al., 2006; Watanabe and Tatebe, 2019). The majority of rainfall in the Sahelian region occurs between June and September, and the amount of rainfall has experienced significant multidecadal variability over the twentieth century, which has been linked to some severe impacts such as economic losses and high mortality rates during drought periods in the 1970s and 1980s. Many studies over the past few decades have put efforts on understanding the mechanisms which drove the significant variation in Sahel rainfall. As discussed, Sahel rainfall is sensitive to SST warming patterns through modifications of the dynamics and water

vapour transport. It is important for climate models to correctly simulate the SST spatial patterns to capture the Sahel rainfall variability. Studies using atmospheric global climate models, which use prescribed sea surface temperatures and sea ice data from observations, have shown that some models can reasonably reproduce multidecadal Sahel rainfall variability and magnitude (Lu and Seinfeld, 2005; Held et al., 2005; Hoerling et al., 2006), although the result is model-dependent (Scaife et al., 2009). Moreover, it has been suggested that variations in SST in remote oceans, such as the Atlantic, Indian, and Pacific Ocean, are important in determining the variability of Sahel rainfall (Palmer, 1986; Folland et al., 1986; Giannini et al., 2003; Zhang and Delworth, 2006; Villamayor and Mohino, 2015). In addition to the variability caused by changes in sea surface temperature patterns, local land-atmosphere interactions induced by external forcings, such as anthropogenic aerosols and greenhouse gases, are also found to contribute to the variability of Sahel rainfall (Held et al., 2005; Dong and Sutton, 2015; Hirasawa et al., 2020).

Several drivers, including aerosols, greenhouse gases, and internal variability can contribute to the Sahel rainfall variability via mechanisms involved with SST or not. However, attribution remains ambiguous. In particular, the mechanism connecting anthropogenic aerosol forcing to Sahel rainfall via North Atlantic SST anomalies has been discussed across literature studying the aerosol attribution and the Atlantic Multidecadal Variability (Rotstayn and Lohmann, 2002; Ackerley et al., 2011; Booth et al., 2012; Undorf et al., 2018; Hua et al., 2019). Chapter 1 demonstrates that aerosols can reduce surface solar radiative flux directly (aerosol-radiative interactions) and indirectly (aerosol-cloud interactions) and the estimated radiative forcing due to aerosol-cloud interactions (ERFaci) is greater than that of aerosol-radiative interactions (ERFari) on a global scale (Figure 1.1). However, the magnitude of the estimation remains uncertain and is model-dependent. Furthermore, it is unclear whether this global-scale relationship between ari and aci (i.e. which one is larger) applies to regional scales, such as the Sahel region. Therefore, it is of interest to investigate the relative importance of aerosol-radiative interactions and aerosol-cloud interactions in determining Sahel rainfall variability. This differentiation is important for models to reduce the uncertainties and better predict future Sahel rainfall.

Therefore, this chapter further examines the Sahel rainfall responses to anthropogenic aerosol perturbations as an example showing how aerosols affect regional precipitation. This work combines ensembles of state-of-the-art global climate models with observational datasets to demonstrate that anthropogenic aerosols have significantly impacted twentieth-century Sahel rainfall multidecadal variability through

modifying North Atlantic (7.5°W-75°W, 10°N-60 °N) sea surface temperatures. This study aims to understand the relative importance of aerosol-radiative interactions and aerosol-cloud interactions in the chain of processes leading to Sahel rainfall variability. It can help us to better understand the impacts of anthropogenic aerosols on climate and improve future projections of Sahel rainfall.

This chapter is based on a manuscript published on Geophysical Research Letters with slight formatting adaptions:

Zhang, S., Stier, P., Dagan, G. and Wang, M. (2022). "Anthropogenic Aerosols Modulated 20th-Century Sahel Rainfall Variability Via Their Impacts on North Atlantic Sea Surface Temperature", Geophysical Research Letters, 49(1), `https://doi.org/10.1029/2021GL095629`.

I designed the study together with the co-authors. I carried out the analysis and interpreted the results with input from the co-authors. I wrote the manuscript and underwent the peer-review process with contributions from the co-authors.

4.1 Introduction

The Sahel region experienced a large multi-decadal rainfall variability during the 20th century, with a severe drought from the 1950s to 1980s and subsequent recovery up to the present day (Held et al., 2005; Wood, 2015). This significant multidecadal regional variability caused substantial impacts on the local ecosystem and population and triggered large scientific interest. Previous studies have proposed several drivers of the drying and wetting trends over different periods and drew various conclusions. Proposed mechanisms include the subtropical drying due to the ongoing global warming (Dai, 2011; Held et al., 2005), wetting resulting from the direct warming of North Africa caused by greenhouse gases (GHGs) (Dong and Sutton, 2015; Richardson et al., 2016b) or absorbing aerosols (Samset et al., 2016; Zhang et al., 2021), teleconnections with varying regional sea surface temperature (SST) (Jordan et al., 2018; Palmer, 1986) caused by GHGs and aerosols (Hill et al., 2018; Hirasawa et al., 2020) and internal variability (Held et al., 2005; Martin et al., 2014; Monerie et al., 2017; Qin et al., 2020). However, the conclusions generally remained model dependent (Biasutti, 2013; Giannini and Kaplan, 2019), with significant uncertainties on distinguishing contributions from different drivers to the Sahel rainfall variability (Ackerley et al., 2011; Dong and Sutton, 2015; Held et al., 2005; Hirasawa et al., 2020; Jordan et al., 2018; Monerie et al., 2017).

The mechanisms can be further separated into SST mediated and non-SST mediated effects (Biasutti et al., 2008; Dong and Sutton, 2015; Hirasawa et al., 2020; Undorf et al., 2018), depending on whether the processes are involved with changes in oceanic properties. External forcers, such as GHGs and aerosols, can lead to a change in local surface temperature, which then lead to an increase or decrease of precipitation, although the relative contribution of each external forcer to real-world Sahel rainfall remains uncertain (Dong and Sutton, 2015; Hirasawa et al., 2020). As for the SST-mediated effects, earlier studies suggest that North Atlantic sea surface temperature (NASST) explicitly affects the Hadley cell strength and the ITCZ position (Cvijanovic and Chiang, 2013; Zhang and Delworth, 2006). When the Northern Hemisphere gets warmer compared to the southern hemisphere, the ITCZ shifts northward, which can in turn dynamically modify the west African monsoon and Sahel rainfall (Biasutti, 2019; Dixon et al., 2018; Hua et al., 2019; Watanabe and Tatebe, 2019). The Atlantic Multidecadal Variability (AMV), a multidecadal oscillation in NASST (Folland et al., 1986) which has large impacts on regional climate system (e.g. Zhang and Delworth, 2006; Hua et al., 2019) and even global-mean temperature

(e.g. Dai et al., 2015), has been observed to switch between a negative and positive phase on a decadal timescale during the past century (Booth et al., 2012; Zhang and Delworth, 2006). Aerosols have been proposed to substantially impact this NASST variability, although the mechanisms (via aerosol-induced changes in radiative fluxes or ocean circulations) have remained uncertain (Booth et al., 2012; Dagan et al., 2020; Menary et al., 2020). Therefore, it could be expected that aerosols could also influence Sahel rainfall multidecadal variability via their effect on NASST variability. Here, we focus on the SST-mediated changes in Sahel precipitation and examine the role of anthropogenic aerosols. We systematically explore the process chain, from regional anthropogenic emissions of aerosols and their precursors, to changes in North Atlantic surface net radiative fluxes, via NASST variability to a shift of ITCZ, and eventually Sahel rainfall variability, in ensembles of state-of-the-art global climate models (GCMs) as well as in observations.

4.2 Methods

4.2.1 Large Ensemble simulations

This study uses the Community Earth System Model 1 large ensemble simulations (CESM1-LE) (Kay et al., 2015), with coupled atmosphere, ocean, land, and sea-ice components. CAM5 is used as the atmospheric component, with a resolution of approximately 1° latitude/longitude and 30 vertical levels. The all-forcing experiment includes 40 ensemble members, forced with historical external forcing from 1920 to 2005. For XAER (XGHG) experiments, the 20 ensemble members are forced with the same historical forcing but with industrial aerosol emission (GHG emission) fixed at the 1920 level (Deser et al., 2020). Both aerosol direct and indirect effects are included in these simulations. Details of CESM1-LE can be also found in Kay et al. (2015). We also use the large ensembles from the Canadian Centre for Climate Modeling and Analysis Canadian Earth System Model 2 (CCCma CanESM2-LE) (Kushner et al., 2018). We use the all-forcing experiment which has 50 members with a resolution of approximately 2° latitude/longitude, starting from 1950 to 2020 (noting that the starting year is different from CESM1-LE).

Each ensemble member is run using the same external radiative forcing scenario, but with different initial states. This means that the spread among the ensemble members is only caused by the internal variability, which also means the externally forced response can be estimated from the ensemble mean. The large ensemble simulations

in CESM1-LE are initialised based on a historical simulation in 1920. This historical simulation itself was initialized based on a pre-industrial condition beginning in 1850. All ensemble member simulations in CESM1-LE have the same initial ocean conditions branched from the first simulation at year 1920 but having small (about the level of "round-off" error in the CAM5 model), randomly generated changes to their initial atmospheric temperature fields (Kay et al., 2015; Deser et al., 2020). The CanESM2-LE, different from CESM1-LE, firstly run 10 original simulations which are initialized by randomly sampling the pre-industrial ocean-atmosphere states at 1850 from a control simulation. The large ensemble members are further initialized by perturbed (5 members in each group) atmospheric conditions based on the 10 original simulations at year 1950 (Kushner et al., 2018).

It has been shown that the observed Sahel rainfall temporal variation as well as its linear trend fall within the ensemble range in the CESM-LE simulations (Yeager et al., 2018; Hirasawa et al., 2020). However, the CESM1-LE ensemble mean has been shown to have difficulty in accurately simulating the observed magnitude of variation in sub-Saharan Africa rainfall during the summer season (McKinnon and Deser, 2018). This deficiency is not unique to the CESM1-LE and CanESM2-LE simulations and is also found in CMIP5 models (Biasutti, 2013; Undorf et al., 2018).

Both CESM1 and CanESM2 take into account aerosol-cloud interactions in their aerosol schemes but with different representations. Specifically, CESM1 adopts the Modal Aerosol Model version 3 (Liu et al., 2012) and takes into account the aerosol effects on both cloud albedo and lifetime, while CanESM2 uses a bulk aerosol model (von Salzen et al., 2013) and only considers the aerosol effect on cloud albedo. Additionally, CESM1-CAM5 and CanESM2 have been found to simulate similar patterns of Sahel precipitation response to projected greenhouse gas forcing (Monerie et al., 2017), although this may not necessarily apply to the response to anthropogenic aerosol perturbations.

Following previous studies (Dai et al., 2015; Hua et al., 2019), the internal variability (IV) of individual members can be calculated as

$$\mathrm{IV}_i = \mathrm{ALL}_i - \mathrm{ALL}_{em}, \tag{4.1}$$

where the subscript i denotes each member and the subscript em denotes the ensemble mean of a specific experiment. ALL indicates the all-forcing experiment. Similarly, we can also obtain a spread of members with anthropogenic aerosols only and greenhouse gases only, with the data sets from XAER and XGHG experiments, following

(Hirasawa et al., 2020),

$$\mathrm{AER}_i = (\mathrm{XAER}_i - \mathrm{XAER}_{em}) + (\mathrm{ALL}_{em} - \mathrm{XAER}_{em}), \tag{4.2}$$

$$\mathrm{GHG}_i = (\mathrm{XGHG}_i - \mathrm{XGHG}_{em}) + (\mathrm{ALL}_{em} - \mathrm{XGHG}_{em}). \tag{4.3}$$

Nevertheless, it is worth noting that the relatively limited ensemble size of the simulations used in this study may result in a variance estimation that is biased low. Therefore, caution is advised when interpreting the variance as the 'true' spread.

4.2.2 CMIP6

We also use data sets from the Coupled Model Intercomparision Project Phase 6 (CMIP6). Nine models are included in this work (Tabel 4.1). All participating models are coupled with sea-ice, ocean, land as well as atmosphere. Specifically, we use simulations from the Detection and Attribution Model Intercomparion Project (DAMIP) (Gillett et al., 2016) (`http://damip.lbl.gov/experiments`). For historical experiments, models simulate the historical period from 1850 to 2020 with all historical forcing. The DAIMP experiment design is based on a linearity assumption that the simulated climate responses to perturbations from different external climate forcers were approximately additive (Gillett et al., 2016; Deser et al., 2020). To separate out the effect from a single forcing agent, we further use hist-aer, hist-ghg, and hist-nat experiments. Individually, hist-aer experiments are subject to only historical anthropogenic aerosol forcing, hist-ghg experiments subject to only historical greenhouse gases forcing, and hist-nat subject to only historical natural forcing. We note that the starting year is different from the simulations from CESM1-LE (year 1920). The emission data set of anthropogenic sulphur dioxide (Hoesly et al., 2018) is from the input4MIPS (input data sets for Model Intercomparison Projects).

Table 4.1: The information of participating CMIP6 models used in this study

Model name	Institution	Resolution	Reference
BCC-CSM2-MR	Beijing Climate Center, China	320x160	Wu et al. (2019)
CanESM5	Canadian Centre fro Climate Modelling and Analysis (CCCma), Canada	128x64	Swart et al. (2019)
IPSL-CM6A-LR	L'Institut Pierre-Simon Laplace (IPSL), France	144x143	Boucher et al. (2020)
MIROC6	Model for Interdisciplinary Research on Climate (MIROC), Japan	256x128	Tatebe et al. (2019)
MRI-ESM2-0	Meteorological Research Institute (MRI), Japan	320x160	Yukimoto et al. (2019)
GISS-E2-1-G	NASA Goddard Institute for Space Studies (GISS), United States	144x90	Elsaesser et al. (2017)
CESM2	National Center for Atmospheric Research (NCAR), United States	288x192	Gettelman et al. (2019)
NorESM2-LM	Norwegian Climate Centre (NCC), Norway	144x96	Seland et al. (2020)
GFDL-ESM4	Geophysical Fluid Dynamics Laboratory (GFDL), United States	288x180	Zhao et al. (2018)

4.2.3 Observational Data Sets

Two observational data sets of SST are used in this study, the Hadley Centre HadISST (Rayner, 2003) and the NOAA reconstructed SST (Huang et al., 2017) data sets. The HadISST data set is available from 1870 with 1° resolution. The NOAA SST is available from 1854 with resolution at 2°. We also use the CRU station-based precipitation observational data set from the Climate Research Unit (CRU), University of East Anglia, which covers almost all 20th-century precipitation measurements over land, at around 2.5° resolution (Harris et al., 2020).

4.3 Results

We first examine the ensemble-mean NASST (10-yr low-pass filtered) in simulations using transient historical forcings (all-forcing) in CESM1-LE. NASST slightly increase during the 20th century (around 0.1K per century) (Fig. 4.1a), mainly driven by GHG-induced global warming (Fig. 4.2) and partly masked by cooling effects from

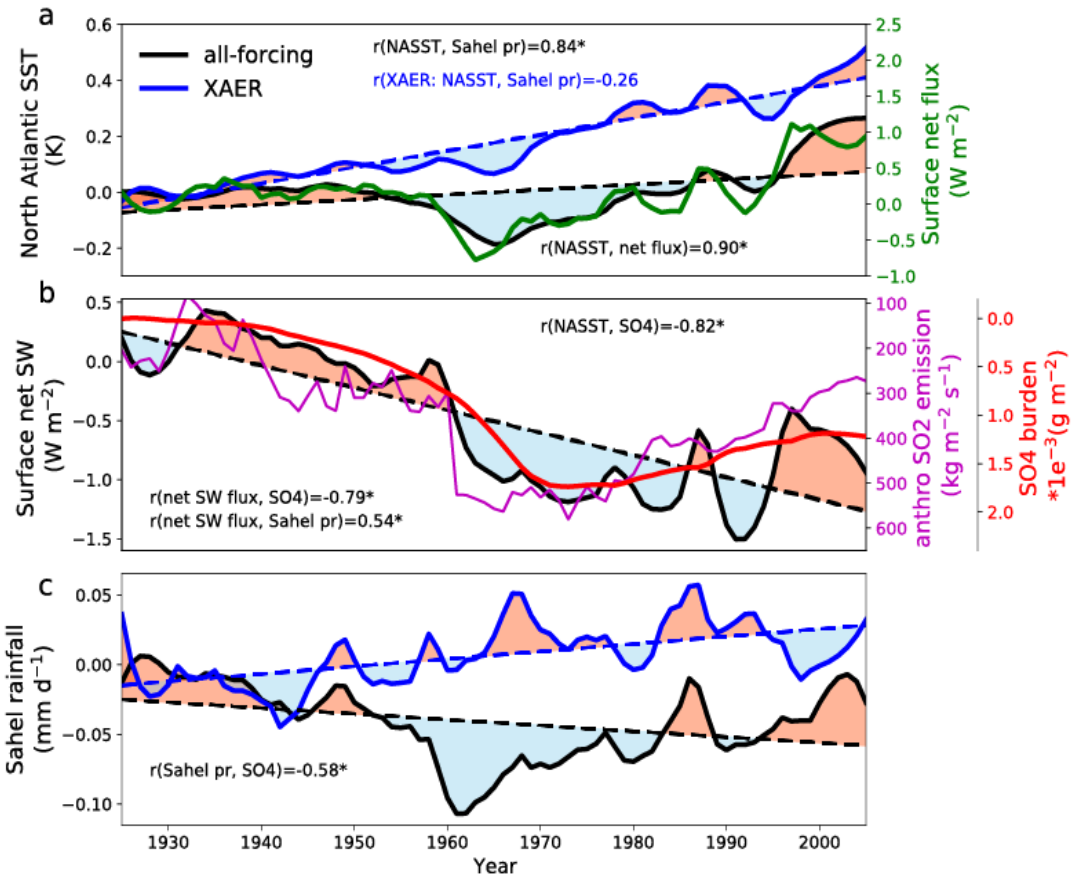

Figure 4.1: (a) CESM1-LE simulated North Atlantic (7.5°W-75°W, 10°N-60°N, see magenta box in Fig. 4.7d) SST for all-forcing simulations (black line) and XAER simulations (blue line). Also shown is the North Atlantic net surface energy flux (defined as downward positive, green line). (b) CESM1-LE all-forcing experiments simulated net surface solar radiative flux (black line), and the sulphate aerosol burden (red line, notice the reversed y-axis) over the North Atlantic Ocean. The purple line indicates the 20th-century anthropogenic sulphur dioxide emissions from the North Atlantic Ocean as well as East North America and West Europe (95°W-20°E, 10°N-60°N, see Fig. 4.5 for the regional information). (c) CESM1-LE simulated ensemble-mean Sahel (20°W-40°E, 10°N-20°N; see black box in Fig. 4.7a) rainfall for all-forcing (black line), and XAER (blue line) experiments. All data sets are shown as the anomalies (10 years low-pass filtered) relative to the 1920-1925 average. The mark $*$ after the correlation coefficient indicates the correlation is significant (p value<0.01). Dashed lines indicate the linear trend and red/blue patches indicate the positive/negative phase of detrended data sets.

aerosols (Fig. 4.1a). We detrended the time series to isolate AMV and examine the multi-decadal variability on top of the time evolution. The detrended ensemble-mean NASST shows a pattern of multidecadal variability, with a generally positive phase lasting from 1925 to 1955 and a subsequent negative phase during 1955 and 1985, followed by another positive phase to 2005 (Fig. 4.1a). This pattern exists in observed detrended NASST as well (Fig. 4.3a) with larger magnitude: NASSTs from two datasets indicate that the AMV has gone through a positive-negative-positive phase pattern with almost the same timing as suggested by CESM1-LE results. Although NASST can also be significantly impacted by internal oceanic variability (Knight et al., 2006), this consistency between observations and the CESM1-LE ensemble-mean (which is expected to eliminate internal variability) results suggests that detrended 20th-century NASST multidecadal variability emerges due to external forcings. This pattern is consistent with previous work based on a different model (Booth et al., 2012). Furthermore, this pattern does not emerge in ensemble-mean results averaged over simulations with anthropogenic aerosol emissions fixed at year 1920 levels (XAER) (Fig. 4.1a), which suggests that anthropogenic aerosols are the main driver of the variability in CESM1-LE.

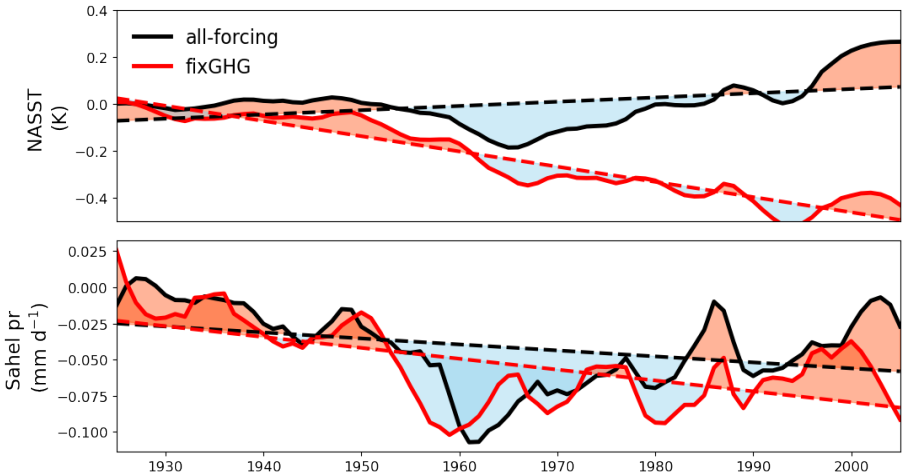

Figure 4.2: CESM-LE simulated (a) North Atlantic (7.5°W-75°W, 10°N-60°N) SST and (b) Sahel rainfall for All-forcing simulations (black line) and fixGHG simulations (red line). All datasets are shown as the anomalies (10 years low-pass filtered) relative to the 1920-1925 average. Dashed lines indicate the linear trend and red/blue patches indicate the positive/negative phase of detrended datasets. Thin lines indicate each ensemble members.

The strong correlation between NASST and the net surface energy flux (the sum of surface net longwave flux, shortwave flux, sensible and latent heat flux) over the North

Atlantic Ocean (correlation coefficient r=0.90, p<0.01) suggests that the variability of NASST is modulated by the local surface energy budget. Emissions of anthropogenic sulphate aerosols and their precursors from Europe and North America (see Fig. 4.5 for regional emission) have increased until the 1970s and decreased afterwards (purple line in Fig. 4.1b) (Smith et al., 2011). Sulphate aerosols reduce downwelling solar radiation and subsequently sea surface temperatures by directly scattering sunlight back to space or indirectly, via interactions with clouds (Bellouin et al., 2020; Boucher et al., 2013; Wild, 2009). These aerosol radiative effects explain the strong relationship between the sulphate burden and the surface net solar radiative fluxes over the North Atlantic Ocean (r=-0.79, p<0.01; Fig. 4.1b), which in turn impacts NASST multidecadal variability (correlation coefficient between NASST and sulphate burden r=-0.82, p<0.01). Previous studies (Dagan et al., 2020; Menary et al., 2020) also noted that aerosol-induced changes in oceanic circulations may contribute to NASST variability as well, which we will explore in Fig. 4.7.

CESM1-LE ensemble-mean 20th-century detrended Sahel rainfall exhibits a multidecadal variability (Fig. 4.1c), consistently in phase with the detrended NASST (r=0.84, p<0.01) as well as the North-Atlantic surface solar radiation (r=0.54, p<0.01; Fig. 1b). This consistency suggests a relationship between North Atlantic aerosol burden and Sahel rainfall (r=-0.58, p<0.01; Fig. 4.1c). A similar pattern is also found in observed detrended twentieth-century Sahel rainfall (Fig. 4.3b), except for a discrepancy from 1950 to 1970, but this could be obscured by internal variability, which is another essential driver of Sahel rainfall variability (Held et al., 2005; Monerie et al., 2017), or due to the fact that early rainfall observation data (before 1950) are sparser and less reliable (Dai et al., 2004). Again, this multidecadal phase-to-phase change of Sahel rainfall is not present in XAER simulations, with a much weaker correlation between the Sahel rainfall and NASST (r=-0.26, p>0.01). It suggests that the simulated and observed Sahel rainfall multidecadal variability is primarily caused by aerosols. Similar relationships are also found in CanESM2-LE (Fig. 4.6), both in terms of the sign (i.e. phase change) and correlation (correlation coefficient between North Atlantic aerosol burden and Sahel rainfall r=-0.63, p<0.01).

Although the positive long-term trend of NASST differs from the negative long-term trend of Sahel rainfall, there exists a positive-negative-positive pattern of multidecadal variability in both detrended NASST and Sahel rainfall, as suggested by CESM1-LE all-forcing ensemble-mean results (Fig. 4.1). This pattern is also evidenced by CanESM2-LE (r=0.91), observational data sets (r=0.77 and 0.51 respectively) and CMIP6 (the Coupled Model Intercomparison Project Phase 6) ensemble-

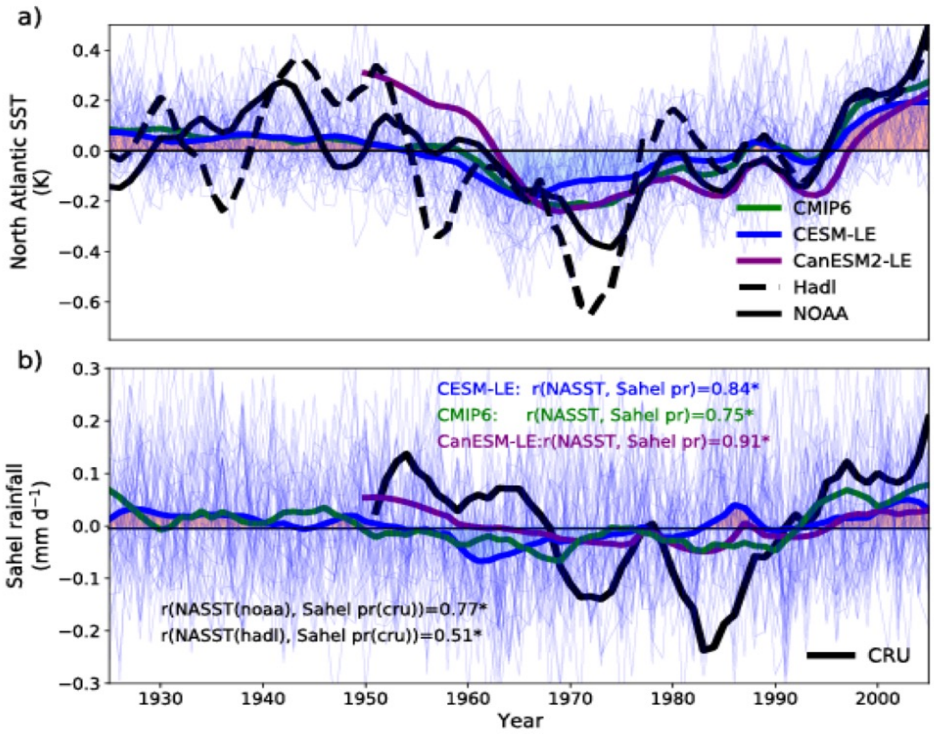

Figure 4.3: (a) Time series of detrended North Atlantic sea surface temperature (10 years low-pass filtered), derived from CESM1-LE (blue line), CanESM2-LE (purple line) and CMIP6 (green line) ensemble-mean as well as observed SST data from Hadley Centre HadISST (black dash line) and the NOAA reconstructed SST (black line). Thin blue lines are the individual members from CESM1-LE. (b) Same as (a) but for detrended Sahel rainfall anomalies. Also shown are observed Sahel rainfall from Climate Research Unit (CRU, black line). All datasets in (a) and (b) are shown as anomalies relative to the 1920-1925 average. The mark "$*$" after the correlation coefficient indicates the correlation is significant (p value$<$0.01). The red/blue shading indicates the positive/negative phase of detrended NASST or Sahel rainfall.

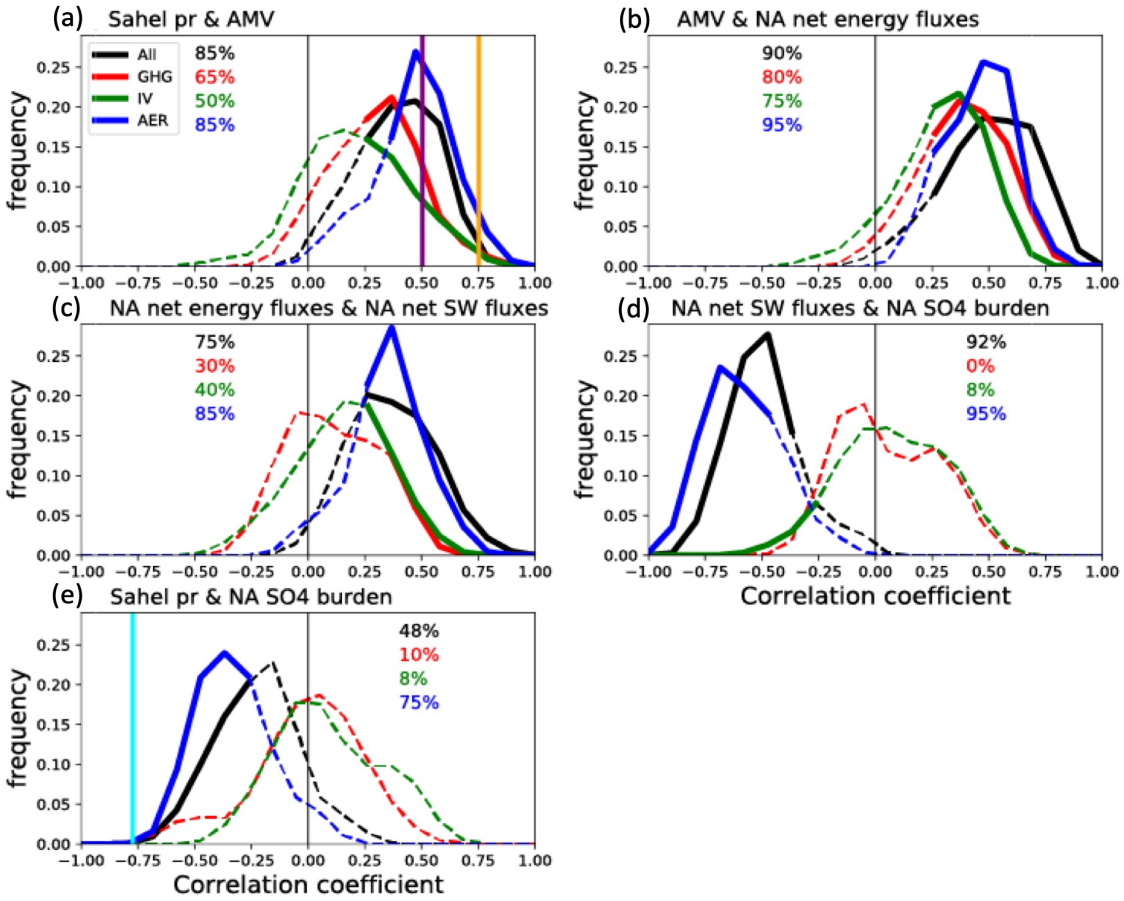

Figure 4.4: (a) The estimated probability density distribution of the correlation coefficients between the CESM1-LE simulated 1925-2005 (10 years low-pass filtered) detrended annual Sahel rainfall and NASST from individual ensemble members with all-forcing (black line), greenhouse only (red line), anthropogenic aerosols only (blue line) and internal variability (green line). Solid lines indicate where the correlations are significant (p value<0.05), while dash lines indicate otherwise. Numbers in percent indicate the fraction of members showing significant correlations. The vertical purple (orange) line in (a) indicates the correlation coefficient between CRU Sahel rainfall and Hadley SST (NOAA SST) from year 1950 to 2005. (b) Same as (a) but for correlations between AMV and North Atlantic surface net energetic fluxes. (c) Same as (a) but for correlations between North Atlantic surface net energetic fluxes and net shortwave fluxes. (d) Same as (a) but for correlations between North Atlantic surface net shortwave fluxes and SO4 burden. (e) Same as (a) but for correlations between Sahel rainfall and North Atlantic SO4 burden. The light blue line in (e) indicates the correlation coefficient between CRU Sahel rainfall and CESM1-LE simulated SO4 burden over the North Atlantic Ocean from year 1950 to 2005.

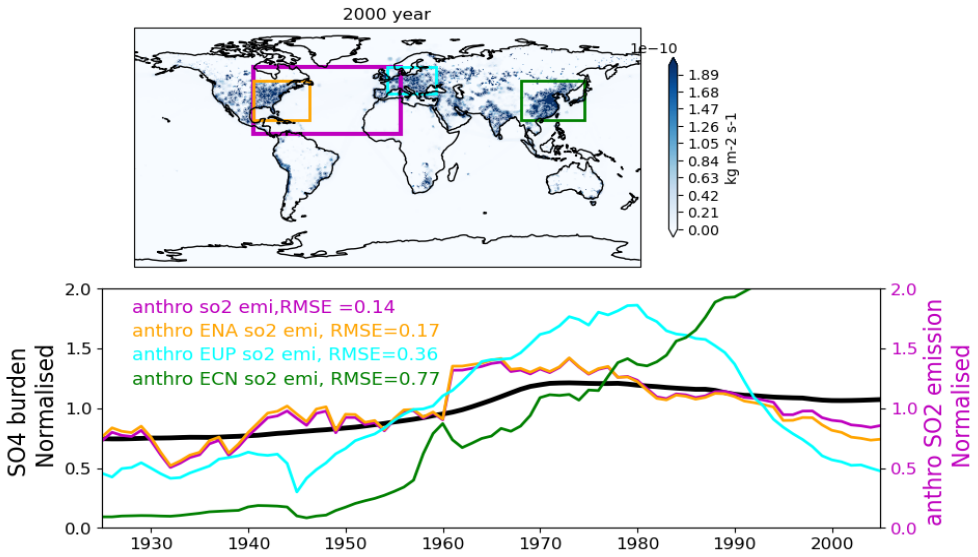

Figure 4.5: (upper panel) Normalised (divided by averages) anthropogenic sulphur dioxide emissions provided by input4MIPS at year 2000. (lower panel) Normalised (divided by averages) CESM-LE all-forcing experiment simulated sulphate aerosol burden over the North Atlantic Ocean (black line) and 20th-century anthropogenic sulphur dioxide emissions from the region chosen in Fig. 4.1b (purple line), North-East America (orange line), Europe (cyan line), and East China (green line), respectively. The numbers indicate the root-mean-square deviation (RMSE) between regional anthropogenic SO2 emissions and SO4 burden over the North Atlantic Ocean.

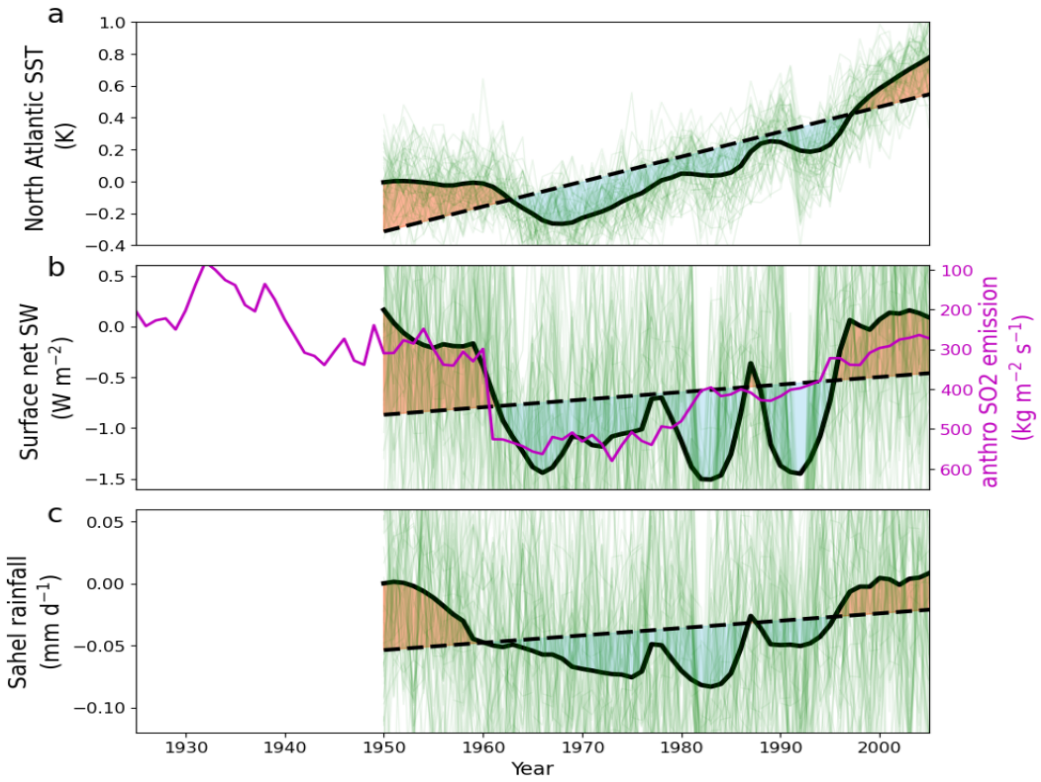

Figure 4.6: Similar to Fig. 4.1 but with CanESM2-LE data, which starts from year 1950. (a) CanESM2-LE simulated North Atlantic (7.5°W-75°W, 10°N-60°N) SST for all-forcing simulations (black line). (b) CanESM2-LE all-forcing experiments simulated net surface solar radiative flux (black line). The purple line indicates the 20thcentury anthropogenic sulphur dioxide emissions from the North Atlantic Ocean as well as East North America and West Europe (notice the y-axis has been reversed). (c) CanESM2-LE simulated ensemble mean Sahel rainfall for all-forcing experiments. All datasets are shown as anomalies (10 years low-pass filtered) relative to the 1950-1955 average. Dashed lines indicate the linear trend, and red/blue patches indicate the positive/negative phase of detrended datasets. Thin green lines are the individual members from CanESM2-LE.

mean results (r=0.75; Fig. 4.3). It is worth noting that although the observational NASST and Sahel rainfall fall into the range estimated by CESM1-LE members, the ensemble-mean results largely underestimate the magnitude, which has also been recognized by previous studies (Hoerling et al., 2006; Hirasawa et al., 2020; Hua et al., 2019; Undorf et al., 2018). Nevertheless, the consistent relationship between Sahel rainfall and NASST found in models and observations provides independent support of our conclusions.

Fig. 4.4 gives a more quantitative understanding of the process chain, and the role of its different drivers (see Section 4.2.1). Most (85% of them) CESM1-LE all-forcing ensemble members present a significant positive correlation ($p<0.05$) between the Sahel rainfall and AMV, as found in observations (orange and purple lines in Fig. 4.4a) and previous studies (Martin et al., 2014; Zhang and Delworth, 2006). AMV is then found to be significantly correlated with the net surface energy flux over the North Atlantic Ocean in the all-forcing experiments (Fig. 4.4b). The positive correlations arises due to the strong role of NASST in setting the location of the ITCZ (Hua et al., 2019), and this is found for all drivers. Among three drivers, AER, however, shows the most cases with significant correlation, which suggested that aerosols contribute most to the inter-decadal variation in AMV and therefore the Sahel rainfall. Furthermore, the variations of net surface energy flux is driven by the net surface shortwave flux variations over the North Atlantic Ocean (Fig. 4.4c), which is further driven by the sulphate burden (Fig. 4.4d). This is only happening for members including the effect of aerosols. Finally, almost half of all-forcing ensemble members show significant negative correlations between SO4 burden over the North Atlantic Ocean and the Sahel rainfall. More than half of the members (75%) with only anthropogenic aerosols also indicate such a significant negative correlation, while other drivers (GHG and IV) do not (Fig. 4.4e). It is interesting to note that the observed CRU Sahel rainfall indicates an even stronger (more negative) correlation (light blue line in Fig. 4.4e – at the edge of the CESM1-LE distribution). This result suggests the important role of anthropogenic aerosols in the process chain.

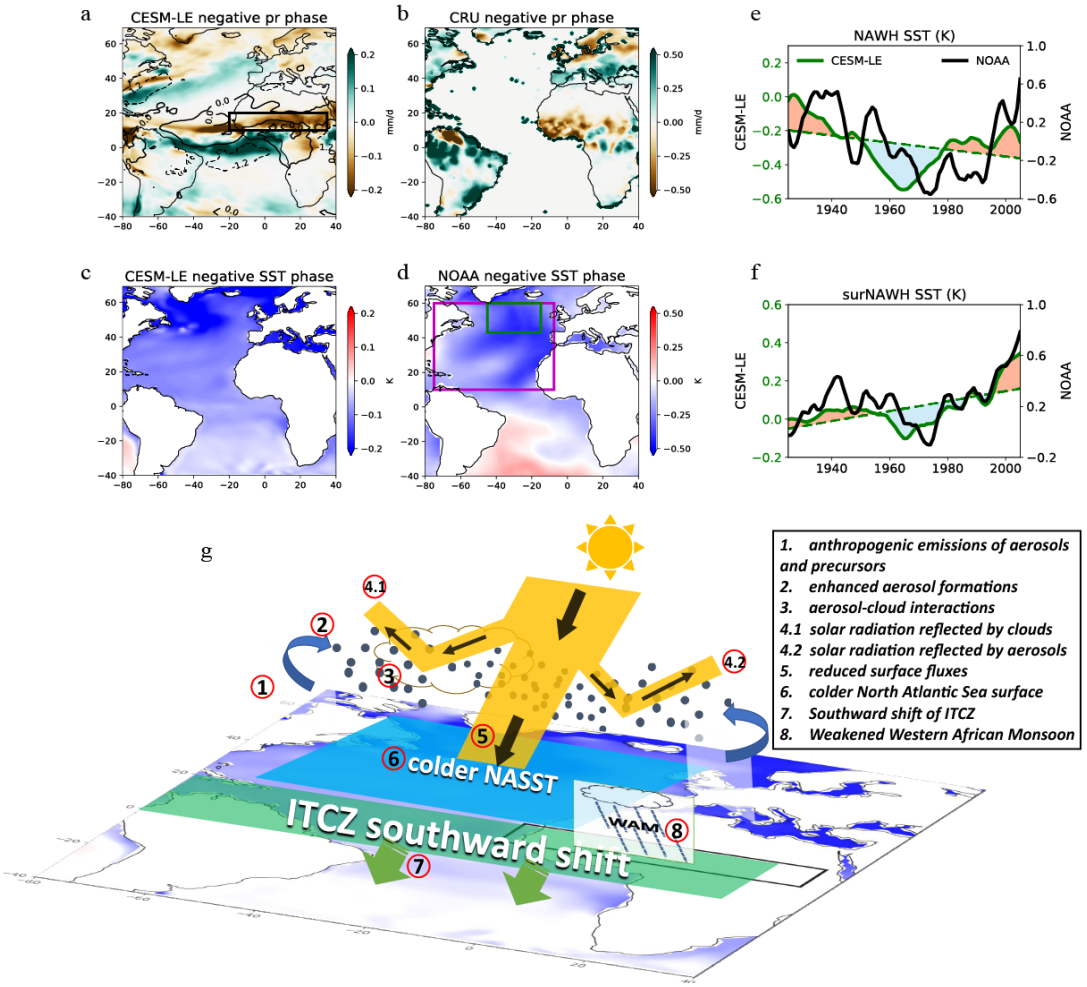

Figure 4.7: Spatial pattern of grid-point detrended rainfall averaged over the negative phase (year 1970 to 1980) period, derived from the (a) CESM1-LE All-forcing experiment and the (b) CRU dataset. The black box in subplot a indicates the Sahel region. Spatial patterns of grid-point detrended SST averaging over the negative phase period, derived from the (c) CESM1-LE all-forcing experiment and (d) NOAA SST dataset. Also shown in subplot a is the detrended outgoing longwave radiation (OLR; contour lines) over the same period. The magenta box and the green box in subplot d indicate the North Atlantic region and the North Atlantic warming hole region (NAWH, 15°-45°W, 43°-60°N), respectively. (e) Twentieth-century timeseries of SST over the NAWH derived from the CESM1-LE All forcing experiment (green line) and the NOAA SST dataset (black line; notice the different scale). (f) Twentieth-century timeseries of SST over the rest of North Atlantic region surrounding NAWHSST (surNAWH) derived from the CESM1-LE All forcing experiment (green line) and the NOAA SST dataset (black line). Dashed lines indicate the linear trend, and red/blue patches indicate the positive/negative phase of detrended SST. (g) A schematic plot based on subplot c to illustrate the process chain of anthropogenic aerosols effects on Sahel rainfall variability.

We next investigate the mechanisms involved in the process chain from aerosols to Sahel precipitation, showing that this teleconnection acts via the interaction of the ITCZ and the West African monsoon. We sample the CESM1-LE simulated detrended Sahel rainfall (Fig. 4.7a) and SST (Fig. 4.7c) at a negative phase (year 1970 to 1980) for both NASST and Sahel rainfall, respectively. It shows that when there is a negative phase of AMV simulated in CESM1-LE (Fig. 4.7c), the shift of the thermal equator associated with a colder Northern Hemisphere leads to a southward shift of ITCZ (Ridley et al., 2015; Wang, 2009) as well as an accompanied shift of tropical rain belt (Fig. 4.7a), weakening the strength of the West African monsoon, resulting in a negative phase of detrended Sahel rainfall (Fig. 4.7a), and vice versa for the positive phase of AMV (year 1995 to 2005, see Fig. 4.8). This teleconnection is also found in observational datasets (Fig. 4.7b and d).

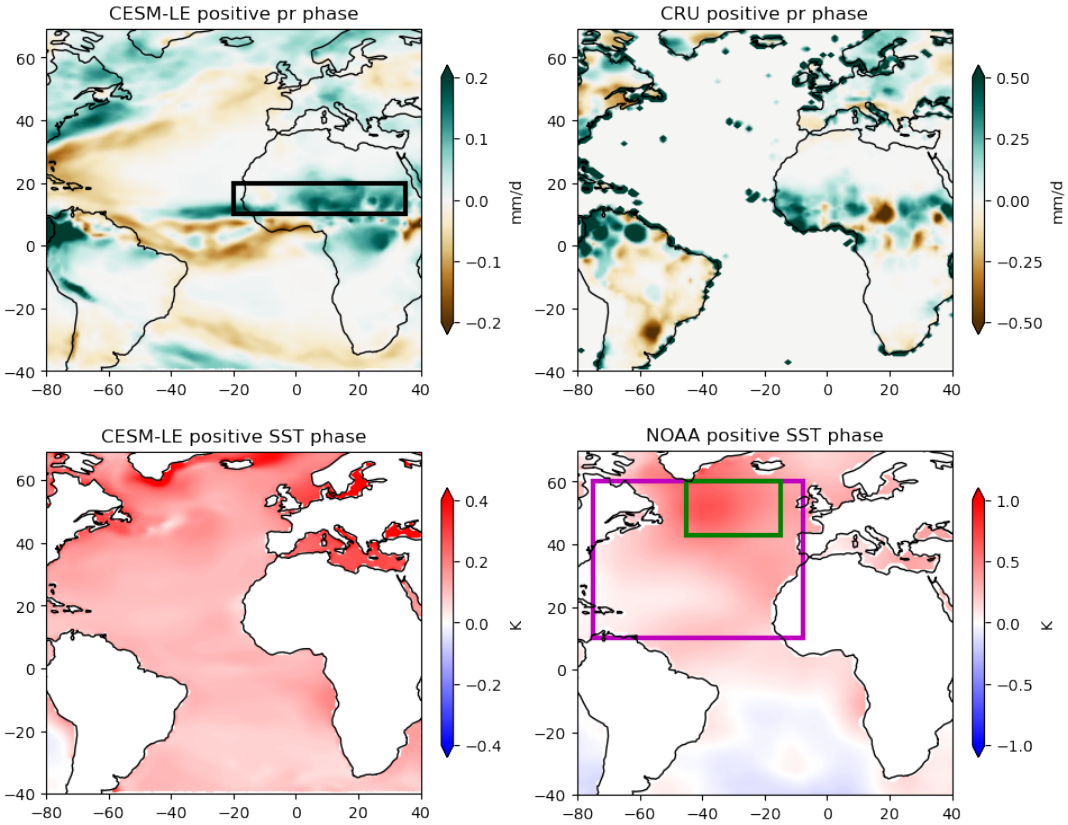

Figure 4.8: Same as Fig. 4.7 but for the positive phase (year 1995 to 2005) of detrend NASST, and the pattern of precipitation at the same period.

Previous studies have already acknowledged the aerosol effects on NASST, but the attribution (from aerosol-induced changes in radiation or ocean dynamics) remained unclear (Booth et al., 2012; Dagan et al., 2020; Menary et al., 2020). We note that

the net North Atlantic surface energy fluxes and NASST well correlate (Fig. 4.1a). This close relationship suggests that the detrended NASST variability is associated with aerosol-induced changes in surface radiation. Several studies demonstrated that aerosol induced changes in ocean circulation (e.g. AMOC) modulates NASST, especially in the North Atlantic warming hole (NAWH) region, where the SST changes are more sensitive to ocean circulation than radiative fluxes changes (Dagan et al., 2020; Menary et al., 2020). Therefore, we split the North Atlantic Ocean region into two sub-regions, NAWH and its surrounding area (see the green and magenta boxes in Fig. 4.7d). Fig. 4.7e shows that NAWH exhibits a cooling trend, opposite to the warming trend shown in the rest of the North Atlantic Ocean (Fig. 4.7f). The opposite trends of NASST between NAWH and the rest of the North Atlantic Ocean could be caused by changes in ocean dynamics or the impacts of the Atlantic Meridional Overturning Circulation on the global-mean temperature trend, which could be examined by future studies. However, the detrended SST variability is similar between NAWH and the rest of the North Atlantic Ocean. Therefore, we suggest that while SST is sensitive to changes in ocean dynamics in the NAWH region, this is manifested in determining the trend, and the detrended variability is still modulated by changes in surface radiative fluxes. This is consistent with observational datasets (Fig. 4.7e and f), although there is a discrepancy in magnitude and a lag between observed and CESM1-LE NAWH SST.

Our results link the process chain from changing sulphate emissions from Europe and North America, to changes in North Atlantic surface net radiative fluxes, via NASST variability to a shift of ITCZ and changes in West African monsoon, and finally Sahel rainfall variability, as illustrated in Fig. 4.7g.

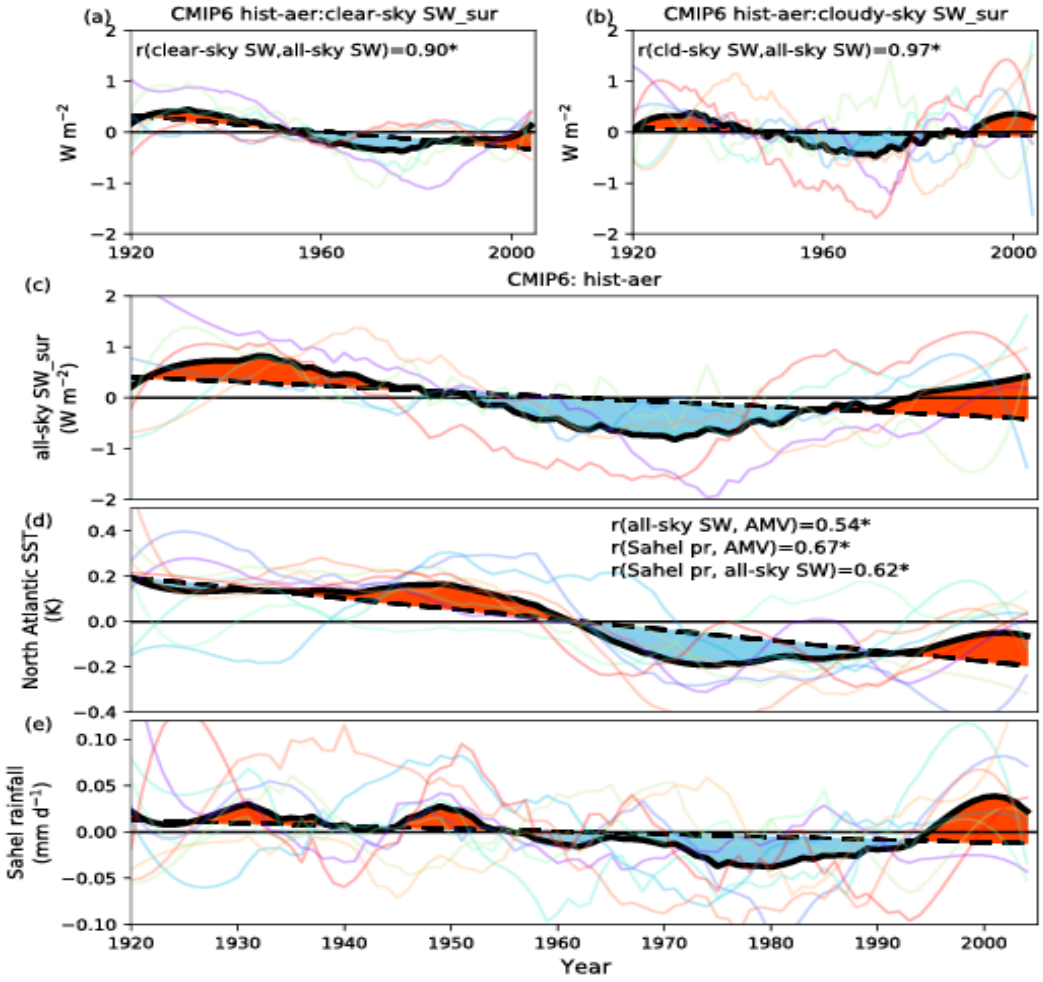

Figure 4.9: (a-c), Coupled Model Intercomparision Project Phase 6 (CMIP6) hist-aer experiments derived (a) clear-sky shortwave surface radiative flux, (b) cloudy-sky (difference between all-sky and clear-sky) shortwave surface radiative flux and (c) all-sky shortwave surface radiative flux, over the North Atlantic Ocean surface. All radiative fluxes are defined as downward positive. Each colored line indicates a CMIP6 participating model. (d) NASST for hist-aer experiments. (e) Sahel rainfall anomalies for historical simulations with only anthropogenic aerosol forcing (hist-aer). All anomalies are relative to the 1920-1925 average. The mark "$*$" after the correlation coefficient indicates the correlation is significant (p value$<$0.01). Dashed lines indicate the linear trend and red/blue patches indicate the positive/negative phase.

To strengthen the robustness of our conclusions in the light of model uncertainties, we further analyse CMIP6 historical simulations. We note that while an ensemble mean from eight CMIP6 models cannot entirely eliminate the natural variability, it can significantly reduce its impact. While the individual models suggest various

patterns of 20th-century AMV and Sahel rainfall, the correlation between AMV and Sahel rainfall is high (Fig. 4.10). Fig. 4.3 has already illustrated an agreement of the CMIP6 historical ensemble-mean with the multidecadal detrended variability of 20th-century NASST and Sahel rainfall found in CEMS-LE and observations. Furthermore, historical simulations with only anthropogenic aerosol emissions (hist-aer) also show significant positive correlations among surface radiative fluxes, NASST and Sahel rainfall variability (Fig. 4.9a-e). In contrast, simulations with only GHG emissions (hist-ghg) do not reproduce this pattern (Fig. 4.11), indicating that anthropogenic aerosol changes cause this multidecadal variability.

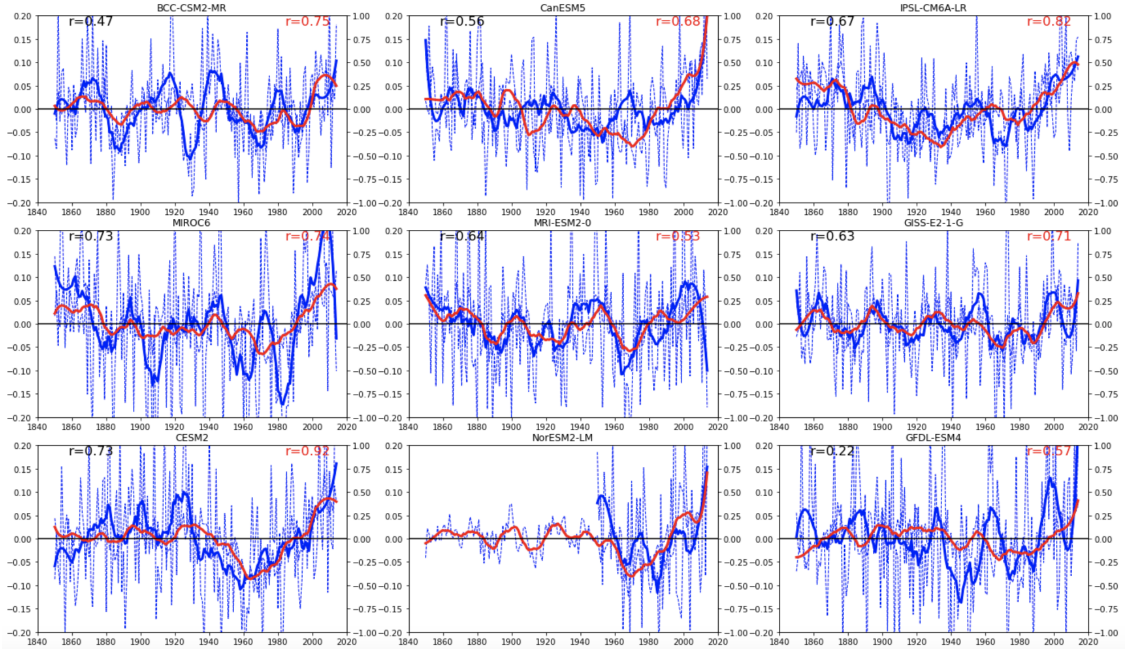

Figure 4.10: The relationship between North Atlantic sea surface temperature (anomaly, red line, right yaxis, unit K) and Sahel rainfall (anomaly, blue line, left y-axis, unit mm/d) in each CMIP6 model. Black numbers on each panel indicate the correlation coefficients between North Atlantic sea surface temperature and Sahel rainfall since 1850, while red numbers indicate the correlation coefficients since 1920.

Considering that aerosols can reduce surface solar radiation through direct effects and through their interaction with clouds (Boucher et al., 2013), it would be of interest to know which processes (aerosol-cloud interactions or aerosol-radiation interactions) contribute more to the variability of NASST and ultimately Sahel rainfall. We note that there might also be cloud feedbacks due to the change of NASST in coupled experiments. CESM1-LE ensemble-mean results imply that the multidecadal aerosol effect on NASST is dominated by aerosol-cloud interactions (around two thirds) rather than aerosol-radiation interactions (around one third) (supplementary Fig. 4.12).

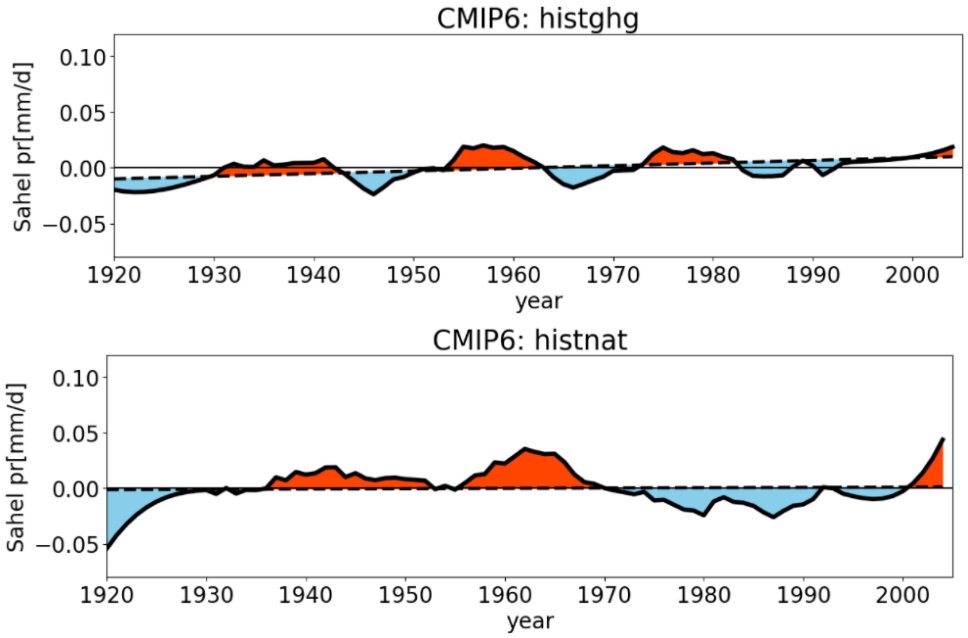

Figure 4.11: CMIP6 ensemble-mean Sahel rainfall for (a) hist-ghg and (b) hist-nat experiments.

Considering aerosol effects exhibit significant uncertainties among GCMs (Ghan et al., 2016; Zhang et al., 2016; Bellouin et al., 2020), and that CESM-CAM5 has a large sensitivity of cloud liquid water path to aerosols (Wang et al., 2012), we also analyse this split across CMIP6 hist-aer simulations. Clear-sky and cloudy-sky surface fluxes shown in Fig. 4.9a and b imply that both aerosol direct and indirect effects contribute to this positive-negative-positive pattern of detrended net surface shortwave radiative flux (Fig. 4.9c), with similar magnitude. However, we find that the uncertainties (as indicated by model diversity) arise primarily from aerosol-cloud interactions (Fig. 4.9b), and these uncertainties may also propagate to simulated NASST variability (Fig. 4.9d) and subsequently Sahel rainfall variability (Fig. 4.9e).

4.4 Conclusions and Discussions

Previous studies (Biasutti and Giannini, 2006; Dong and Sutton, 2015; Held et al., 2005; Herman et al., 2020; Hirasawa et al., 2020; Palmer, 1986) proposed several drivers to understand the severe drought and the subsequent recovery of Sahel rainfall during the past century. However, the attribution remained ambiguous and model-dependent. We assess the temporal evolution of the 20th-century North Atlantic SST and Sahel rainfall and decompose them into a linear trend and detrended variabil-

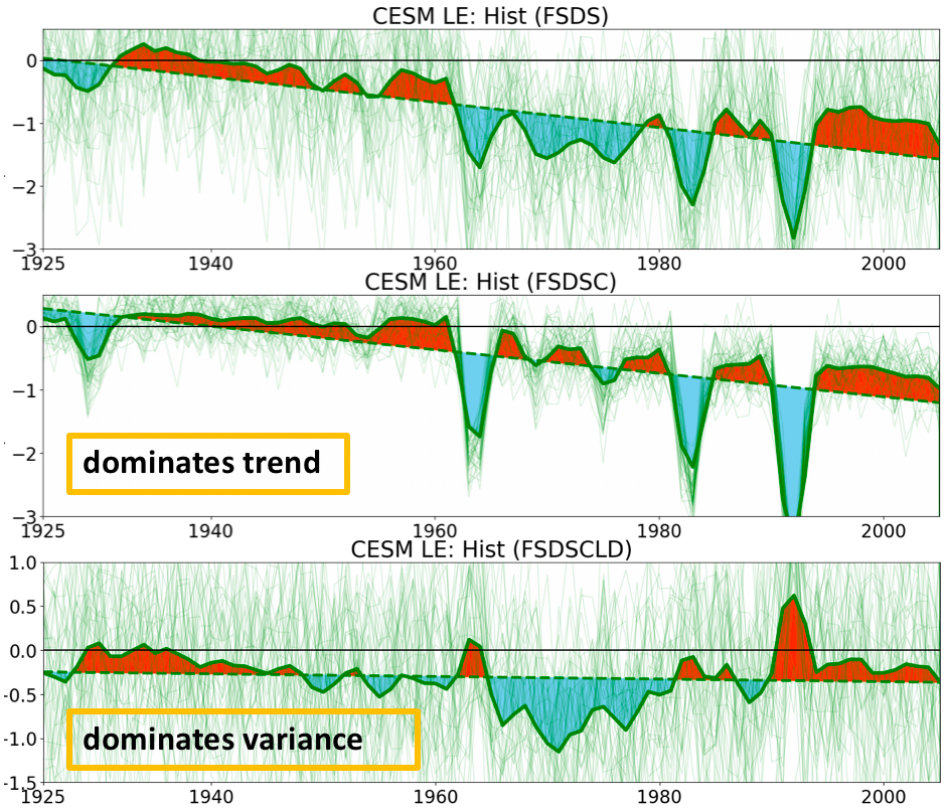

Figure 4.12: (a) All-sky downward shortwave radiative flux, (b) clear-sky downward shortwave radiative flux and (c) cloudy-sky downward shortwave radiative flux over the North Atlantic Ocean surface. All radiative fluxes are defined as downward positive. Thin lines indicate each ensemble members.

ity. Although the linear trend will be affected by a mix of external forcings and internal variability and the aerosol effect does not stand out alone, we show that anthropogenic aerosol effects modulate the detrended multidecadal variability. Our results robustly demonstrate a chain of processes from aerosol (precursor) emissions, their direct and indirect effects on shortwave radiative fluxes, via North Atlantic SST variability, to changes in the ITCZ position due to the inter-hemispheric temperature difference, subsequently modulating the West African monsoon and, finally, Sahel rainfall (Fig. 4.7g). This conclusion is consistently supported by independent data from the CESM1-LE, CanESM2-LE simulations, CMIP6 models, and observational datasets.

This work suggests that anthropogenic aerosols have contributed to the 20th century multidecadal variability of Sahel rainfall. The significant correlations between anthropogenic aerosol emission, North Atlantic shortwave surface radiation anomalies, North Atlantic SST, and Sahel precipitation imply a potential chain process as previously discussed. While this correlation method has also been used in previous studies (e.g. Zhang and Delworth, 2006; Martin et al., 2014; Hua et al., 2019) and the correlations presented in the analysis are clear, caution is recommended when interpreting the causal relationship involved in the chain processes for several reasons: (1) Previous studies suggested that both Pacific and Indian ocean variability (e.g. Palmer, 1986; Mohino et al., 2011; Villamayor and Mohino, 2015) and fast responses (mechanisms not mediated by changes in SST) (e.g. Dong and Sutton, 2015; Hirasawa et al., 2020) can also also influence the Sahel rainfall, so they may co-vary due to the same forcing. (2) Additionally, both CESM1-LE and CanESM2-LE ensemble mean underestimate the observed magnitude of the multidecadal Sahel rainfall variability (Figure 4.3), although they do capture the timing of these changes. For these reasons, we would like to explicitly note that other mechanisms, e.g. internal variability, will contribute to the Sahel rainfall multidecadal variability, to avoid any ambiguity.

Our work suggested that the forced variability of North Atlantic SST is contributed by aerosol-induced changes in surface radiative fluxes rather than changes in ocean circulations. It is also worth noting that aerosol-cloud interactions contribute most to the inter-model uncertainties in simulating North Atlantic SST variability and potentially Sahel rainfall (Fig. 4.9). Our results highlight the critical role of anthropogenic aerosols on 20th-century Sahel rainfall multidecadal variability through their impacts on North Atlantic SST. Therefore, it is essential to correctly simulate regional aerosol radiative effects (especially aerosol-cloud interactions) for future projections of Sahel rainfall.

Chapter 5

Conclusion

Precipitation plays an essential role in the Earth's water cycle, providing water for soil moisture, rivers, and groundwater recharge and altering the sea surface salinity which can modify the density and circulation of the ocean. Precipitation is also responsible for transporting energy and redistributing water in the climate system. There is scientific consensus and observational evidence indicating that anthropogenic perturbations have increasingly influenced precipitation at various spatial and temporal scales since the last century (Douville et al., 2021). Understanding the anthropogenic effects on precipitation has important implications for energy supply, food security, and economic prosperity. Yet, anthropogenic effects on precipitation are still one of the most significant sources of uncertainty in quantifying and projecting future climate change.

This thesis aims to improve the understanding of precipitation responses to anthropogenic perturbations through a focus on fast and slow responses and reducing their uncertainties in the current generation of General Circulation Models (GCMs). A combination of energetic (top-down) and process-driven (bottom-up) methodologies is used to investigate the precipitation responses at global and regional scales in an ensemble of GCMs. This concluding chapter summarises the findings of the previous chapters and their implications. Potential avenues for further research are also discussed here.

Precipitation responses to aerosol perturbations fundamentally depend on aerosol types due to their distinct effects on energetics. Absorbing aerosols, such as black carbon, can suppress precipitation in the short-term due to its absorption of shortwave radiation, but can also increase precipitation in the long-term by warming the surface temperature. Non-absorbing aerosols, such as sulphate, primarily reduce precipitation by decreasing surface temperature through the "dimming effect", in which

incoming solar radiation is scattered back to space. Chapter 2 investigates the response of precipitation to large perturbations in absorbing and non-absorbing aerosol perturbations separately. Uncertainties related to aerosol-cloud-precipitation interactions are challenging to quantify and constrain due to the lack of a comprehensive understanding of the chain of processes including aerosol emissions, the activation of cloud condensation nuclei and ice nuclei, and responses of atmospheric dynamics. An energetic framework has been introduced to decompose atmospheric radiative cooling (ARC) into contributions from aerosols (through aerosol direct shortwave absorption), clouds (through cloud longwave absorption/cooling), and clear-clean sky (without aerosols or clouds; mainly through radiative heating/cooling from GHGs and water vapour). Previous work demonstrated that precipitation responses could be divided into a fast (mediated by near-instantaneous changes in atmospheric adiabatic heating/cooling) and a slow component (mediated by changes in surface temperature). Therefore, we further decompose individual terms in the energy budget into fast and slow responses.

By increasing black carbon (BC) and sulphate (SUL) emissions respectively in a GCM, ECHAM6-HAM2, we find there are different precipitation responses on global and regional scales. Although SUL and BC have different signs of radiative forcing, a decrease in global-mean precipitation is found in both cases. For the BC experiment, decreased global-mean precipitation is mainly a fast response, energetically associated with enhanced atmospheric shortwave absorption from aerosols. We also note that the decreased upward surface sensible heat flux is non-negligible and counteracts part of the reduced precipitation. For the SUL experiment, reduced rainfall is a slow response related to the decreased clear-clean sky atmospheric radiative cooling. The negative radiative forcing from SUL leads to a decrease in global surface temperature, cools the whole atmospheric column, reduces water vapour content, and eventually reduces precipitation.

Chapter 2 also finds that the relationship between aerosol-induced changes in ARC and precipitation response is latitude-dependent. Generally, extra-tropical changes in ARC and latent heat from precipitation are primarily balanced, similar to that on a global scale. However, they are less balanced in the tropics due to the weak Coriolis force and efficient local energy transport. Changes in the energy transport term are essential in determining changes in tropical rainfall. BC warms (and SUL cools) the northern hemisphere mainly through a slow response, which leads to a southward (northward) energy flux. The intertropical convergence zone (ITCZ), accompanied by tropical rainfall, is found to shift northward (southward) in the BC

(SUL) experiment in response to the cross-equatorial energy flux. This is energetically consistent with the changes in the divergence of dry static energy fluxes and the changes in vertical pressure velocity in the tropics. Chapter 2 shows that changes in large-scale circulations and local thermodynamics explain the precipitation responses qualitatively, whilst the energetic view provides a quantitative approach that makes their contributions explicit.

Previous studies suggest that most of the uncertainty in precipitation responses to external radiative forcing can be attributed to fast responses, and that the inter-model spread of hydrological sensitivity (η) among models is reduced when the contributions of fast responses are removed (Fläschner et al., 2016; Samset et al., 2017). This is also shown in Chapter 2: although the global-mean precipitation changes between SUL and BC experiments are distinct, the magnitude of η, namely slow responses normalized by the surface temperature change, are relatively consistent. However, these results are only based on one GCM. Considering that there is still a considerable inter-model spread of η in current GCMs (DeAngelis et al., 2015; Fläschner et al., 2016; Watanabe et al., 2018), we focus on slow responses and analyse the factors contributing to the inter-model spread of η in Chapter 3.

To investigate the dependence of η on spatially heterogeneous warming, we analyse an ensemble of simulations forced with 80 SST warming/cooling patches individually placed across the globe in the Community Atmospheric Model 5 (CAM5) in Chapter 3. We find that by changing only the warming pattern, one model can reproduce a wide spread of η, thus suggesting a high sensitivity of η to SST warming patterns.

The change of global-mean precipitation and temperature can be interpreted as the sum of a linear contribution from each grid box and an error term in a discrete form of Green's function. In Chapter 3, we use a Green's function approach to demonstrate the geographical dependence of η on local SST warming, rather than investigating individually from 80 experiments. It is found that both global-mean precipitation and temperature responses are more sensitive to warming in the tropical west-Pacific and Atlantic oceans than in other regions, where the localised increase in SST can remotely warm the tropical free troposphere due to the intense convection and strong circulations.

More interestingly, warming in strong tropical ascending regions could produce η larger than would expect from the Clausius-Clapeyron relationship (7 % K^{-1}). Using the energetic decomposition approach developed in Chapter 2, we find that both the clear-sky and cloudy-sky atmospheric radiative cooling are sensitive to heterogeneous sea surface temperature warming. The sensitivity is especially large when the

warming is located in strong ascending regions. From a bottom-up perspective, the super-Clausius-Clapeyron η could be explained through the response of circulation to heterogeneous warming. The strong ascent at the warm pool serves as a water vapour 'pump' to transport water vapour to the free troposphere. When the warming is pronounced in the warm pool, it enhances the prevailing large-scale ascent, increases the SST gradient, and strengthens the circulation. As a result, the global-mean convective mass flux is increased, and more water vapour is brought to the free troposphere, which can lead to a super-Clausius-Clapeyron η.

Further investigation into the abrupt4xCO2 experiments in CMIP models shows that the warming pattern effect is as important as the atmospheric model differences in determining the inter-model spread of η, which has been overlooked before. The model with the largest pattern effect (IPSL-CM5A-MR) has more warming concentrated in the tropics compared to the lowest one (GISS-E2-H), and therefore tends to predict a higher η as well. The dependence of η on warming patterns suggests that η could be potentially state-dependent, model-dependent, and experiment-dependent (i.e. prescribed SST or fully coupled), instead of being treated as an unchanged parameter (DeAngelis et al., 2015; Thorpe and Andrews, 2014).

Chapter 3 also demonstrates that properly accounting for the warming pattern effect is important in reconstructing historical transient precipitation changes. This highlights the need for further research and development in simulating ocean dynamics and the interactions between the ocean and atmosphere, in order to improve our understanding of historical precipitation changes. The warming pattern effect modulates the precipitation changes mainly through the slow component. Previously the slow component was derived from the value of η multiplied by global mean temperature changes, which did not consider the pattern effect. Chapter 3 shows that after accounting for the pattern effect, the reconstructed global-mean precipitation agrees much better with observations in terms of both magnitude and variability compared to the conventionally reconstructed one (without pattern effect). The result is still robust with different observational and reanalysis datasets, highlighting the importance of pattern effects when studying hydrological intensification.

Not only global-mean precipitation but also regional precipitation is sensitive to spatially heterogeneous warming patterns. Sahel rainfall is one particular example. In Chapter 4, the 20th-century North Atlantic SST and Sahel rainfall are decomposed into a linear trend and detrended variabilities. The anthropogenic aerosol effects on Sahel rainfall are studied by investigating the large ensembles from Community

Earth System Model large ensemble simulations (CESM-LE) and the Canadian Center for Climate Modeling and Analysis Canadian Earth System Model 2 (CCCma CanESM2-LE). Examining the ensemble mean is expected to eliminate internal variabilities. Additional experiments with anthropogenic aerosol emissions fixed further help to assess the effects of anthropogenic aerosols. Our analysis demonstrates that anthropogenic aerosols have modulated 20th-century Sahel rainfall multidecadal variability through their impacts on North Atlantic SST. We propose a process chain, from changing anthropogenic sulphate emissions in North America to changes in North Atlantic surface net radiative fluxes, via North Atlantic sea surface temperature variability to a shift of ITCZ and changes in West African monsoon, and finally, Sahel rainfall variability. This process chain is consistently evidenced by ensembles of state-of-the-art global climate models (the CESM and CanESM large ensemble simulations and CMIP6 models) as well as observational data sets.

Further examinations suggest that this process chain is modulated by aerosol-induced changes in radiative surface fluxes rather than changes in ocean circulations. The aerosol-radiation interactions and aerosol-cloud interactions are both critical processes in this chain. Moreover, we show that the discrepancy of aerosol-cloud interactions significantly contributes to the inter-model uncertainties of NASST and potentially the Sahel rainfall variability in CMIP models. Although internal variabilities also contribute, Chapter 4 suggests that anthropogenic aerosols contributed to the multidecadal variability of 20th century Sahel rainfall and highlights the importance of accurate representation of regional aerosol-cloud-radiation interactions for the simulation of Sahel rainfall. However, it is worth noting that large-ensemble mean underestimate the observed magnitude of the multidecadal Sahel rainfall variability, although they do capture the timing of these changes. Therefore, it is challenging to distinguish the proportion of influence between external forcing and internal variability contributing to the changes in Sahel rainfall.

The analyses in this thesis lead to a number of further work directions. The energetic decomposition approach proposed in Chapter 2 allows for distinguishing contributions from clouds, aerosol, and clear-clean sky separately when analysing precipitation changes, similar to decomposing aerosol radiative forcing to contributions from clouds and aerosols (Ghan, 2013). This helps to understand physical processes as well as the source of inter-model uncertainties. The methodology presented in Chapter 2 is based on one GCM but can be applied to other GCMs as well. For example, previous studies have demonstrated that precipitation response to BC increase has the largest inter-model uncertainties among GCMs (Samset et al., 2016; Stjern

et al., 2017) compared to other climate forcing agents. By using this decomposition approach and distinguishing contributions from aerosols, clouds, and clear-clean sky, respectively, it would be helpful to diagnose the inter-model uncertainties from direct aerosol shortwave absorption, adjustments, or feedbacks from clouds and water vapour. This can also further help to identify the direction to reduce the uncertainties.

Chapter 3 demonstrates the importance of the SST pattern effect on global-mean precipitation responses. It is suggested that accounting for the pattern effect can help to reduce uncertainties in our estimates of the intensification of the hydrological cycle in response to global warming. For future studies, it is desirable to separate the uncertainties caused by different warming patterns from the differences arising from atmospheric model parameterisations. This is a direction to reduce the uncertainties in projecting future water cycle change.

Previous work estimated the temperature-mediated precipitation responses as the product of η parameter and global-mean temperature changes (Allan et al., 2014; Thorpe and Andrews, 2014). We found this conventional approach fails to capture the observed inter-annual variation of global-mean precipitation timeseries, as it does not account for the pattern effect. The temperature-mediated component of precipitation change can be caused by variations of the SST pattern, sometimes even without changes in global-mean temperature. Therefore, for future work to reconstruct global-mean precipitation changes from a sum of fast and slow responses, it is suggested to account for the spatial heterogeneities in SST changes, especially the SST variations in tropical ascent regions. This is particularly essential for work focusing on the transient inter-annual variation of global-mean precipitation.

The Green's function used in Chapter 3 is derived from the SST patch experiments in the CAM5 model. Although it is based on only one model, Green's function reconstructed precipitation reasonably reproduces both model-estimated and observed precipitation. However, it is of interest to compare Green's function for global precipitation from different global climate models to understand its model dependency by performing the same SST patch experiments in different GCMs. This can help to examine and understand the model dependency of the results presented in Chapter 3.

As shown in Chapter 4, Sahel rainfall is sensitive to regional SST changes. By using the SST patch experiments in Chapter 3 but focusing on the impacts on regional precipitation, future work can derive the dependence of Sahel rainfall on the spatial pattern of SST change with a Green's function. This approach can systematically

quantify the linear contributions of regional SST changes to Sahel rainfall. Moreover, this approach can apply to other regional rainfall sensitive to the regional SST changes, such as the South Asia monsoon. The focus can also shift from precipitation to surface temperature or cloud properties that are tele-connected with remote SST patterns.

This thesis aims to gain a deeper understanding of how precipitation patterns are affected by external climate change factors, such as anthropogenic aerosols and greenhouse gases. An energetic framework is used in this thesis to evaluate the impact of perturbed aerosol emissions and SST warming patterns on global and regional precipitation. In particular, this framework has been used to study both rapid and slow precipitation responses, and further decompose the changes into contributions from clouds, aerosols, and clear-clean sky. Moreover, this methodology can be easily applied to other climate models and provides a useful tool for identifying the causes of differences in precipitation responses to climate agent changes. Overall, this thesis brings together a top-down and bottom-up approach to enhance our understanding of how precipitation responds to externally driven changes across different spatial and temporal scales, and to decrease the uncertainties in precipitation projections in current generation of global climate models.

Bibliography

Abdul-Razzak, H. and Ghan, S. J. (2000). A parameterization of aerosol activation: 2. Multiple aerosol types. *Journal of Geophysical Research: Atmospheres*, 105(D5):6837–6844.

Ackerley, D., Booth, B. B., Knight, S. H., Highwood, E. J., Frame, D. J., Allen, M. R., and Rowell, D. P. (2011). Sensitivity of Twentieth-Century Sahel rainfall to sulfate aerosol and CO2 forcing. *Journal of Climate*, 24(19):4999–5014.

Ackerman, A. S., Kirkpatrick, M. P., Stevens, D. E., and Toon, O. B. (2004). The impact of humidity above stratiform clouds on indirect aerosol climate forcing. *Nature*, 432(7020):1014–1017.

Acosta Navarro, J. C., Ekman, A. M., Pausata, F. S., Lewinschal, A., Varma, V., Seland, Ø., Gauss, M., Iversen, T., Kirkevåg, A., Riipinen, I., and Hansson, H. C. (2017). Future response of temperature and precipitation to reduced aerosol emissions as compared with increased greenhouse gas concentrations. *Journal of Climate*, 30(3):939–954.

Adam, O., Schneider, T., and Brient, F. (2018). Regional and seasonal variations of the double-ITCZ bias in CMIP5 models. *Climate Dynamics*, 51(1-2):101–117.

Adler, R. F., Gu, G., Sapiano, M., Wang, J.-J., and Huffman, G. J. (2017). Global Precipitation: Means, Variations and Trends During the Satellite Era (1979–2014). *Surveys in Geophysics*, 38(4):679–699.

Adler, R. F., Huffman, G. J., Chang, A., Ferraro, R., Xie, P.-P., Janowiak, J., Rudolf, B., Schneider, U., Curtis, S., Bolvin, D., Gruber, A., Susskind, J., Arkin, P., and Nelkin, E. (2003). The Version-2 Global Precipitation Climatology Project (GPCP) Monthly Precipitation Analysis (1979–Present). *Journal of Hydrometeorology*, 4(6):1147–1167.

Albrecht, B. A. (1989). Aerosols, Cloud Microphysics, and Fractional Cloudiness. *Science*, 245(4923):1227–1230.

Alizadeh-Choobari, O. (2018). Impact of aerosol number concentration on precipitation under different precipitation rates. *Meteorological Applications*, 25(4):596–605.

Allan, R. P., Barlow, M., Byrne, M. P., Cherchi, A., Douville, H., Fowler, H. J., Gan, T. Y., Pendergrass, A. G., Rosenfeld, D., Swann, A. L. S., Wilcox, L. J., and Zolina, O. (2020). Advances in understanding large-scale responses of the water cycle to climate change. *Annals of the New York Academy of Sciences*, 1472(1):49–75.

Allan, R. P., Liu, C., Zahn, M., Lavers, D. A., Koukouvagias, E., and Bodas-Salcedo, A. (2014). Physically Consistent Responses of the Global Atmospheric Hydrological Cycle in Models and Observations. *Surveys in Geophysics*, 35(3):533–552.

Allan, R. P., Soden, B. J., John, V. O., Ingram, W., and Good, P. (2010). Current changes in tropical precipitation. *Environmental Research Letters*, 5(2):025205.

Allan, R. P., Willett, K. M., John, V. O., and Trent, T. (2022). Global Changes in Water Vapor 1979–2020. *Journal of Geophysical Research: Atmospheres*, 127(12):1–23.

Allen, M. R. and Ingram, W. J. (2002). Constraints on future changes in climate and the hydrologic cycle. *Nature*, 419(6903):228–232.

Allen, R. J., Amiri-Farahani, A., Lamarque, J.-F., Smith, C., Shindell, D., Hassan, T., and Chung, C. E. (2019). Observationally constrained aerosol–cloud semi-direct effects. *npj Climate and Atmospheric Science*, 2(1):16.

Allen, R. J., Evan, A. T., and Booth, B. B. (2015). Interhemispheric aerosol radiative forcing and tropical precipitation shifts during the late Twentieth Century. *Journal of Climate*, 28(20):8219–8246.

Anderson, T. L., Charlson, R. J., Winker, D. M., Ogren, J. A., and Holmén, K. (2003). Mesoscale Variations of Tropospheric Aerosols. *Journal of the Atmospheric Sciences*, 60(1):119–136.

Andreae, M. O., Rosenfeld, D., Artaxo, P., Costa, A. A., Frank, G. P., Longo, K. M., and Silva-Dias, M. A. F. (2004). Smoking Rain Clouds over the Amazon. *Science*, 303(5662):1337–1342.

Andrews, T. (2014). Using an AGCM to Diagnose Historical Effective Radiative Forcing and Mechanisms of Recent Decadal Climate Change. *Journal of Climate*, 27(3):1193–1209.

Andrews, T. and Forster, P. M. (2010). The transient response of global-mean precipitation to increasing carbon dioxide levels. *Environmental Research Letters*, 5(2):025212.

Andrews, T., Forster, P. M., Boucher, O., Bellouin, N., and Jones, A. (2010). Precipitation, radiative forcing and global temperature change. *Geophysical Research Letters*, 37(14).

Andrews, T., Forster, P. M., and Gregory, J. M. (2009). A surface energy perspective on climate change. *Journal of Climate*, 22(10):2557–2570.

Andrews, T., Gregory, J. M., and Webb, M. J. (2015). The dependence of radiative forcing and feedback on evolving patterns of surface temperature change in climate models. *Journal of Climate*, 28(4):1630–1648.

Andrews, T., Gregory, J. M., Webb, M. J., and Taylor, K. E. (2012). Forcing, feedbacks and climate sensitivity in CMIP5 coupled atmosphere-ocean climate models. *Geophysical Research Letters*, 39(9):1–7.

Andrews, T. and Webb, M. J. (2018). The dependence of global cloud and lapse rate feedbacks on the spatial structure of tropical pacific warming. *Journal of Climate*, 31(2):641–654.

Archer, D., Eby, M., Brovkin, V., Ridgwell, A., Cao, L., Mikolajewicz, U., Caldeira, K., Matsumoto, K., Munhoven, G., Montenegro, A., and Tokos, K. (2009). Atmospheric Lifetime of Fossil Fuel Carbon Dioxide. *Annual Review of Earth and Planetary Sciences*, 37(1):117–134.

Armour, K. C., Marshall, J., Scott, J. R., Donohoe, A., and Newsom, E. R. (2016). Southern Ocean warming delayed by circumpolar upwelling and equatorward transport. *Nature Geoscience*, 9(7):549–554.

Arora, V. K., Scinocca, J. F., Boer, G. J., Christian, J. R., Denman, K. L., Flato, G. M., Kharin, V. V., Lee, W. G., and Merryfield, W. J. (2011). Carbon emission limits required to satisfy future representative concentration pathways of greenhouse gases. *Geophysical Research Letters*, 38(5).

Bai, H., Gong, C., Wang, M., Zhang, Z., and L'Ecuyer, T. (2018). Estimating precipitation susceptibility in warm marine clouds using multi-sensor aerosol and cloud products from A-Train satellites. *Atmospheric Chemistry and Physics*, 18(3):1763–1783.

Baker, H. S., Millar, R. J., Karoly, D. J., Beyerle, U., Guillod, B. P., Mitchell, D., Shiogama, H., Sparrow, S., Woollings, T., and Allen, M. R. (2018). Higher CO2 concentrations increase extreme event risk in a 1.5 °C world. *Nature Climate Change*, 8(7):604–608.

Bala, G., Caldeira, K., and Nemani, R. (2010). Fast versus slow response in climate change: Implications for the global hydrological cycle. *Climate Dynamics*, 35(2):423–434.

Bala, G., Duffy, P. B., and Taylor, K. E. (2008). Impact of geoengineering schemes on the global hydrological cycle. *Proceedings of the National Academy of Sciences*, 105(22):7664–7669.

Barsugli, J. J. and Sardeshmukh, P. D. (2002). Global Atmospheric Sensitivity to Tropical SST Anomalies throughout the Indo-Pacific Basin. *Journal of Climate*, 15(23):3427–3442.

Bauer, P., Amayenc, P., Kummerow, C. D., and Smith, E. A. (2001). Over-Ocean Rainfall Retrieval from Multisensor Data of the Tropical Rainfall Measuring Mission. Part II: Algorithm Implementation. *Journal of Atmospheric and Oceanic Technology*, 18(11):1838–1855.

Bellouin, N., Quaas, J., Gryspeerdt, E., Kinne, S., Stier, P., Watson-Parris, D., Boucher, O., Carslaw, K. S., Christensen, M., Daniau, A., Dufresne, J., Feingold, G., Fiedler, S., Forster, P., Gettelman, A., Haywood, J. M., Lohmann, U., Malavelle, F., Mauritsen, T., McCoy, D. T., Myhre, G., Mülmenstädt, J., Neubauer, D., Possner, A., Rugenstein, M., Sato, Y., Schulz, M., Schwartz, S. E., Sourdeval, O., Storelvmo, T., Toll, V., Winker, D., and Stevens, B. (2020). Bounding Global Aerosol Radiative Forcing of Climate Change. *Reviews of Geophysics*, 58(1):1–45.

Bentsen, M., Bethke, I., Debernard, J. B., Iversen, T., Kirkevåg, A., Seland, Ø., Drange, H., Roelandt, C., Seierstad, I. A., Hoose, C., and Kristjánsson, J. E. (2013). The Norwegian Earth System Model, NorESM1-M – Part 1: Description

and basic evaluation of the physical climate. *Geoscientific Model Development*, 6(3):687–720.

Bi, D., Dix, M., Marsland, S., O'Farrell, S., Rashid, H., Uotila, P., Hirst, A., Kowalczyk, E., Golebiewski, M., Sullivan, A., Yan, H., Hannah, N., Franklin, C., Sun, Z., Vohralik, P., Watterson, I., Zhou, X., Fiedler, R., Collier, M., Ma, Y., Noonan, J., Stevens, L., Uhe, P., Zhu, H., Griffies, S., Hill, R., Harris, C., and Puri, K. (2013). The ACCESS coupled model: description, control climate and evaluation. *Australian Meteorological and Oceanographic Journal*, 63(1):41–64.

Biasutti, M. (2013). Forced Sahel rainfall trends in the CMIP5 archive. *Journal of Geophysical Research Atmospheres*, 118(4):1613–1623.

Biasutti, M. (2019). Rainfall trends in the African Sahel: Characteristics, processes, and causes. *Wiley Interdisciplinary Reviews: Climate Change*, 10(4):1–22.

Biasutti, M. and Giannini, A. (2006). Robust Sahel drying in response to late 20th century forcings. *Geophysical Research Letters*, 33(11):2006GL026067.

Biasutti, M., Held, I. M., Sobel, A. H., and Giannini, A. (2008). SST forcings and Sahel rainfall variability in simulations of the twentieth and twenty-first centuries. *Journal of Climate*, 21(14):3471–3486.

Bischoff, T. and Schneider, T. (2016). The equatorial energy balance, ITCZ position, and double-ITCZ bifurcations. *Journal of Climate*, 29(8):2997–3013.

Bjerknes, J. (1969). Atmospheric teleconnections from equatorial pacific 1. *Monthly Weather Review*, 97(3):163–172.

Bond, T. C., Doherty, S. J., Fahey, D. W., Forster, P. M., Berntsen, T., DeAngelo, B. J., Flanner, M. G., Ghan, S., Kärcher, B., Koch, D., Kinne, S., Kondo, Y., Quinn, P. K., Sarofim, M. C., Schultz, M. G., Schulz, M., Venkataraman, C., Zhang, H., Zhang, S., Bellouin, N., Guttikunda, S. K., Hopke, P. K., Jacobson, M. Z., Kaiser, J. W., Klimont, Z., Lohmann, U., Schwarz, J. P., Shindell, D., Storelvmo, T., Warren, S. G., and Zender, C. S. (2013). Bounding the role of black carbon in the climate system: A scientific assessment. *Journal of Geophysical Research: Atmospheres*, 118(11):5380–5552.

Bony, S., Bellon, G., Klocke, D., Sherwood, S., Fermepin, S., and Denvil, S. (2013). Robust direct effect of carbon dioxide on tropical circulation and regional precipitation. *Nature Geoscience*, 6(6):447–451.

Bony, S., Colman, R., Kattsov, V. M., Allan, R. P., Bretherton, C. S., Dufresne, J.-L., Hall, A., Hallegatte, S., Holland, M. M., Ingram, W., Randall, D. A., Soden, B. J., Tselioudis, G., and Webb, M. J. (2006). How Well Do We Understand and Evaluate Climate Change Feedback Processes? *Journal of Climate*, 19(15):3445–3482.

Bony, S. and Dufresne, J. L. (2005). Marine boundary layer clouds at the heart of tropical cloud feedback uncertainties in climate models. *Geophysical Research Letters*, 32(20):1–4.

Boos, W. R. and Korty, R. L. (2016). Regional energy budget control of the intertropical convergence zone and application to mid-Holocene rainfall. *Nature Geoscience*, 9(12):892–897.

Booth, B. B., Dunstone, N. J., Halloran, P. R., Andrews, T., and Bellouin, N. (2012). Aerosols implicated as a prime driver of twentieth-century North Atlantic climate variability. *Nature*, 484(7393):228–232.

Boucher, O., Randall, D., Artaxo, P., Bretherton, C., Feingold, G., Forster, P., Kerminen, V.-M., Kondo, Y., Liao, H., Lohmann, U., Rasch, P., Satheesh, S. K., Sherwood, S., Stevens, B., and Zhang, X. Y. (2013). Clouds and Aerosols. In Intergovernmental Panel on Climate Change, editor, *Climate Change 2013 - The Physical Science Basis*, pages 571–658. Cambridge University Press, Cambridge.

Boucher, O., Servonnat, J., Albright, A. L., Aumont, O., Balkanski, Y., Bastrikov, V., Bekki, S., Bonnet, R., Bony, S., Bopp, L., Braconnot, P., Brockmann, P., Cadule, P., Caubel, A., Cheruy, F., Codron, F., Cozic, A., Cugnet, D., D'Andrea, F., Davini, P., de Lavergne, C., Denvil, S., Deshayes, J., Devilliers, M., Ducharne, A., Dufresne, J. L., Dupont, E., Éthé, C., Fairhead, L., Falletti, L., Flavoni, S., Foujols, M. A., Gardoll, S., Gastineau, G., Ghattas, J., Grandpeix, J. Y., Guenet, B., Guez, Lionel, E., Guilyardi, E., Guimberteau, M., Hauglustaine, D., Hourdin, F., Idelkadi, A., Joussaume, S., Kageyama, M., Khodri, M., Krinner, G., Lebas, N., Levavasseur, G., Lévy, C., Li, L., Lott, F., Lurton, T., Luyssaert, S., Madec, G., Madeleine, J. B., Maignan, F., Marchand, M., Marti, O., Mellul, L., Meurdesoif, Y., Mignot, J., Musat, I., Ottlé, C., Peylin, P., Planton, Y., Polcher, J., Rio, C., Rochetin, N., Rousset, C., Sepulchre, P., Sima, A., Swingedouw, D., Thiéblemont, R., Traore, A. K., Vancoppenolle, M., Vial, J., Vialard, J., Viovy, N., and Vuichard, N. (2020). Presentation and Evaluation of the IPSL-CM6A-LR Climate Model. *Journal of Advances in Modeling Earth Systems*, 12(7).

Brayshaw, D. J., Hoskins, B., and Blackburn, M. (2008). The Storm-Track Response to Idealized SST Perturbations in an Aquaplanet GCM. *Journal of the Atmospheric Sciences*, 65(9):2842–2860.

Bretherton, C. S. and Blossey, P. N. (2014). Low cloud reduction in a greenhouse-warmed climate: Results from Lagrangian LES of a subtropical marine cloudiness transition. *Journal of Advances in Modeling Earth Systems*, 6(1):91–114.

Byrne, M. P. and O'Gorman, P. A. (2015). The response of precipitation minus evapotranspiration to climate warming: Why the "Wet-get-wetter, dry-get-drier" scaling does not hold over land. *Journal of Climate*, 28(20).

Byrne, M. P., Pendergrass, A. G., Rapp, A. D., and Wodzicki, K. R. (2018). Response of the Intertropical Convergence Zone to Climate Change: Location, Width, and Strength. *Current Climate Change Reports*, 4(4):355–370.

Cai, M. (2005). Dynamical amplification of polar warming. *Geophysical Research Letters*, 32(22).

Cai, S., Hsu, P.-C., and Liu, F. (2021). Changes in polar amplification in response to increasing warming in CMIP6. *Atmospheric and Oceanic Science Letters*, 14(3):100043.

Caldeira, K. and Myhrvold, N. P. (2013). Projections of the pace of warming following an abrupt increase in atmospheric carbon dioxide concentration. *Environmental Research Letters*, 8(3).

Cao, L., Bala, G., and Caldeira, K. (2011). Why is there a short-term increase in global precipitation in response to diminished CO2 forcing? *Geophysical Research Letters*, 38(6).

Ceppi, P. and Gregory, J. M. (2017). Relationship of tropospheric stability to climate sensitivity and Earth's observed radiation budget. *Proceedings of the National Academy of Sciences*, 114(50):13126–13131.

Charlson, R. J., Schwartz, S. E., Hales, J. M., Cess, R. D., Coakley, J. A., Hansen, J. E., and Hofmann, D. J. (1992). Climate forcing by anthropogenic aerosols. *Science*, 255(5043).

Chemke, R. and Dagan, G. (2018). The effects of the spatial distribution of direct anthropogenic aerosols radiative forcing on atmospheric circulation. *Journal of Climate*, 31(17):7129–7145.

Christensen, M. W. and Stephens, G. L. (2011). Microphysical and macrophysical responses of marine stratocumulus polluted by underlying ships: Evidence of cloud deepening. *Journal of Geophysical Research Atmospheres*, 116(3).

Collins, W. J., Bellouin, N., Doutriaux-Boucher, M., Gedney, N., Halloran, P., Hinton, T., Hughes, J., Jones, C. D., Joshi, M., Liddicoat, S., Martin, G., O'Connor, F., Rae, J., Senior, C., Sitch, S., Totterdell, I., Wiltshire, A., and Woodward, S. (2011). Development and evaluation of an Earth-System model - HadGEM2. *Geoscientific Model Development*, 4(4).

Cvijanovic, I. and Chiang, J. C. H. (2013). Global energy budget changes to high latitude North Atlantic cooling and the tropical ITCZ response. *Climate Dynamics*, 40(5-6):1435–1452.

Dagan, G. and Stier, P. (2020). Constraint on precipitation response to climate change by combination of atmospheric energy and water budgets. *npj Climate and Atmospheric Science*, 3(1):34.

Dagan, G., Stier, P., and Watson-Parris, D. (2019). Contrasting Response of Precipitation to Aerosol Perturbation in the Tropics and Extratropics Explained by Energy Budget Considerations. *Geophysical Research Letters*, 46(13):7828–7837.

Dagan, G., Stier, P., and Watson-Parris, D. (2020). Aerosol Forcing Masks and Delays the Formation of the North Atlantic Warming Hole by Three Decades. *Geophysical Research Letters*, 47(22):1–10.

Dai, A. (2006). Precipitation characteristics in eighteen coupled climate models. *Journal of Climate*, 19(18):4605–4630.

Dai, A. (2011). Drought under global warming: A review. *Wiley Interdisciplinary Reviews: Climate Change*, 2(1):45–65.

Dai, A. (2013). Increasing drought under global warming in observations and models. *Nature Climate Change*, 3(1):52–58.

Dai, A., Fyfe, J. C., Xie, S.-p., and Dai, X. (2015). Decadal modulation of global surface temperature by internal climate variability. *Nature Climate Change*, 5(6):555–559.

Dai, A., Lamb, P. J., Trenberth, K. E., Hulme, M., Jones, P. D., and Xie, P. (2004). The recent Sahel drought is real. *International Journal of Climatology*, 24(11):1323–1331.

Dallafior, T. N., Folini, D., Knutti, R., and Wild, M. (2016). Mixed-layer ocean responses to anthropogenic aerosol dimming from 1870 to 2000. *Journal of Geophysical Research: Atmospheres*, 121(1):49–66.

DeAngelis, A. M., Qu, X., Zelinka, M. D., and Hall, A. (2015). An observational radiative constraint on hydrologic cycle intensification. *Nature*, 528(7581):249–253.

Dentener, F., Kinne, S., Bond, T., Boucher, O., Cofala, J., Generoso, S., Ginoux, P., Gong, S., Hoelzemann, J. J., Ito, A., Marelli, L., Penner, J. E., Putaud, J.-P., Textor, C., Schulz, M., van der Werf, G. R., and Wilson, J. (2006). Emissions of primary aerosol and precursor gases in the years 2000 and 1750 prescribed data-sets for AeroCom. *Atmospheric Chemistry and Physics*, 6(12):4321–4344.

Deser, C., Phillips, A. S., Simpson, I. R., Rosenbloom, N., Coleman, D., Lehner, F., Pendergrass, A. G., DiNezio, P., and Stevenson, S. (2020). Isolating the Evolving Contributions of Anthropogenic Aerosols and Greenhouse Gases: A New CESM1 Large Ensemble Community Resource. *Journal of Climate*, 33(18):7835–7858.

Dixon, R. D., Vimont, D. J., and Daloz, A. S. (2018). The relationship between tropical precipitation biases and the Saharan heat low bias in CMIP5 models. *Climate Dynamics*, 50(9-10):3729–3744.

Dong, B. and Sutton, R. (2015). Dominant role of greenhouse-gas forcing in the recovery of Sahel rainfall. *Nature Climate Change*, 5(8):757–760.

Dong, B., Sutton, R. T., Highwood, E., and Wilcox, L. (2014). The impacts of European and Asian anthropogenic sulfur dioxide emissions on Sahel rainfall. *Journal of Climate*, 27(18):7000–7017.

Dong, W., Lin, Y., Wright, J. S., Xie, Y., Yin, X., and Guo, J. (2019a). Precipitable water and CAPE dependence of rainfall intensities in China. *Climate Dynamics*, 52(5-6):3357–3368.

Dong, Y., Proistosescu, C., Armour, K. C., and Battisti, D. S. (2019b). Attributing Historical and Future Evolution of Radiative Feedbacks to Regional Warming Patterns using a Green's Function Approach: The Preeminence of the Western Pacific. *Journal of Climate*, 32(17):5471–5491.

Donner, L. J., Wyman, B. L., Hemler, R. S., Horowitz, L. W., Ming, Y., Zhao, M., Golaz, J. C., Ginoux, P., Lin, S. J., Schwarzkopf, M. D., Austin, J., Alaka, G., Cooke, W. F., Delworth, T. L., Freidenreich, S. M., Gordon, C. T., Griffies, S. M., Held, I. M., Hurlin, W. J., Klein, S. A., Knutson, T. R., Langenhorst, A. R., Lee, H. C., Lin, Y., Magi, B. I., Malyshev, S. L., Milly, P. C., Naik, V., Nath, M. J., Pincus, R., Ploshay, J. J., Ramaswamy, V., Seman, C. J., Shevliakova, E., Sirutis, J. J., Stern, W. F., Stouffer, R. J., Wilson, R. J., Winton, M., Wittenberg, A. T., and Zeng, F. (2011). The dynamical core, physical parameterizations, and basic simulation characteristics of the atmospheric component AM3 of the GFDL global coupled model CM3. *Journal of Climate*, 24(13).

Douville, H., Raghavan, K., and Renwick, J. (2021). Water Cycle Changes. In Masson-Delmotte, V., Zhai, P., Pirani, A., Connors, S. L., Péan, C., Berger, S., Caud, N., Chen, Y., Goldfarb, L., Gomis, M. I., Huang, M., Leitzell, K., Lonnoy, E., Matthews, J. B. R., Maycock, T. K., Waterfield, T., Yelekçi, O., Yu, R., and Zhou, B., editors, *Climate Change 2021: The Physical Science Basis. Contribution of Working Group I to the Sixth Assessment Report of the IPCC*, pages 1055–1210. Cambridge University Press, Cambridge, United Kingdom and New York, NY, USA.

Dufresne, J. L., Foujols, M. A., Denvil, S., Caubel, A., Marti, O., Aumont, O., Balkanski, Y., Bekki, S., Bellenger, H., Benshila, R., Bony, S., Bopp, L., Braconnot, P., Brockmann, P., Cadule, P., Cheruy, F., Codron, F., Cozic, A., Cugnet, D., de Noblet, N., Duvel, J. P., Ethé, C., Fairhead, L., Fichefet, T., Flavoni, S., Friedlingstein, P., Grandpeix, J. Y., Guez, L., Guilyardi, E., Hauglustaine, D., Hourdin, F., Idelkadi, A., Ghattas, J., Joussaume, S., Kageyama, M., Krinner, G., Labetoulle, S., Lahellec, A., Lefebvre, M. P., Lefevre, F., Levy, C., Li, Z. X., Lloyd, J., Lott, F., Madec, G., Mancip, M., Marchand, M., Masson, S., Meurdesoif, Y., Mignot, J., Musat, I., Parouty, S., Polcher, J., Rio, C., Schulz, M., Swingedouw, D., Szopa, S., Talandier, C., Terray, P., Viovy, N., and Vuichard, N. (2013). Climate change projections using the IPSL-CM5 Earth System Model: From CMIP3 to CMIP5. *Climate Dynamics*, 40(9-10).

Dunne, J. P., John, J. G., Adcroft, A. J., Griffies, S. M., Hallberg, R. W., Shevliakova, E., Stouffer, R. J., Cooke, W., Dunne, K. A., Harrison, M. J., Krasting, J. P., Malyshev, S. L., Milly, P. C., Phillipps, P. J., Sentman, L. T., Samuels, B. L., Spelman, M. J., Winton, M., Wittenberg, A. T., and Zadeh, N. (2012). GFDL's ESM2 global coupled climate-carbon earth system models. Part I: Physical formulation and baseline simulation characteristics. *Journal of Climate*, 25(19).

Ellis, T. D., L'Ecuyer, T., Haynes, J. M., and Stephens, G. L. (2009). How often does it rain over the global oceans? the perspective from CloudSat. *Geophysical Research Letters*, 36(3).

Elsaesser, G. S., Del Genio, A. D., Jiang, J. H., and van Lier-Walqui, M. (2017). An improved convective ice parameterization for the NASA GISS global climate model and impacts on cloud ice simulation. *Journal of Climate*, 30(1).

Eyring, V., Bony, S., Meehl, G. A., Senior, C. A., Stevens, B., Stouffer, R. J., and Taylor, K. E. (2016). Overview of the Coupled Model Intercomparison Project Phase 6 (CMIP6) experimental design and organization. *Geoscientific Model Development*, 9(5):1937–1958.

Fischer, E. M. and Knutti, R. (2016). Observed heavy precipitation increase confirms theory and early models. *Nature Climate Change*, 6(11):986–991.

Fläschner, D., Mauritsen, T., and Stevens, B. (2016). Understanding the Intermodel Spread in Global-Mean Hydrological Sensitivity. *Journal of Climate*, 29(2):801–817.

Folland, C. K., Palmer, T. N., and Parker, D. E. (1986). Sahel rainfall and worldwide sea temperatures, 1901–85. *Nature*, 320(6063):602–607.

Forster, P., Ramaswamy, V., Artaxo, P., Berntsen, T., Betts, R., Fahey, D. W., Haywood, J., Lean, J., Lowe, D. C., Myhre, G., Nganga, J., Prinn, R., Raga, G., Schulz, M., and Dorland, R. V. (2007). Changes in Atmospheric Constituents and in Radiative Forcing. In Solomon, S., Qin, D., Manning, M., Chen, Z., Marquis, M., Averyt, K., Tignor, M., and Miller, H., editors, *Climate Change 2007: The Physical Science Basis. Contribution of Working Group I to the Fourth Assessment Report of the Intergovernmental Panel on Climate Change*. Cambridge University Press, Cambridge, United Kingdom and New York, NY, USA.

Forster, P. M., Storelvmo, T., Armour, K., Collins, W., Dufresne, J. L., Frame, D., Lunt, D. J., Mauritsen, T., Palmer, M. D., Watanabe, M., Wild, M., and Zhang, H. (2021). The Earth's Energy Budget, Climate Feedbacks, and Climate Sensitivity. In Masson-Delmotte, V., Zhai, P., Pirani, A., Connors, S. L., Péan, C., Berger, S., Caud, N., Chen, Y., Goldfarb, L., Gomis, M. I., Huang, M., Leitzell, K., Lonnoy, E., Matthews, J. B. R., Maycock, T. K., Waterfield, T., Yelekçi, O., Yu, R., and Zhou, B., editors, *Climate Change 2021: The Physical Science Basis. Contribution of Working Group I to the Sixth Assessment Report of the Intergovernmental Panel on Climate Change*, pages 923–1054. Cambridge University Press, Cambridge, United Kingdom and New York, NY, USA.

Frieler, K., Meinshausen, M., Schneider Von Deimling, T., Andrews, T., and Forster, P. (2011). Changes in global-mean precipitation in response to warming, greenhouse gas forcing and black carbon. *Geophysical Research Letters*, 38(4):1–5.

Gates, W. L., Boyle, J. S., Covey, C., Dease, C. G., Doutriaux, C. M., Drach, R. S., Fiorino, M., Gleckler, P. J., Hnilo, J. J., Marlais, S. M., Phillips, T. J., Potter, G. L., Santer, B. D., Sperber, K. R., Taylor, K. E., and Williams, D. N. (1999). An Overview of the Results of the Atmospheric Model Intercomparison Project (AMIP I). *Bulletin of the American Meteorological Society*, 80(1):29–55.

Gettelman, A., Hannay, C., Bacmeister, J. T., Neale, R. B., Pendergrass, A. G., Danabasoglu, G., Lamarque, J. F., Fasullo, J. T., Bailey, D. A., Lawrence, D. M., and Mills, M. J. (2019). High Climate Sensitivity in the Community Earth System Model Version 2 (CESM2). *Geophysical Research Letters*, 46(14).

Gettelman, A. and Morrison, H. (2015). Advanced two-moment bulk microphysics for global models. Part I: Off-line tests and comparison with other schemes. *Journal of Climate*, 28(3):1268–1287.

Gettelman, A., Morrison, H., Terai, C. R., and Wood, R. (2013). Microphysical process rates and global aerosol-cloud interactions. *Atmospheric Chemistry and Physics*, 13(19):9855–9867.

Ghan, S., Wang, M., Zhang, S., Ferrachat, S., Gettelman, A., Griesfeller, J., Kipling, Z., Lohmann, U., Morrison, H., Neubauer, D., Partridge, D. G., Stier, P., Takemura, T., Wang, H., and Zhang, K. (2016). Challenges in constraining anthropogenic aerosol effects on cloud radiative forcing using present-day spatiotemporal variability. *Proceedings of the National Academy of Sciences*, 113(21):5804–5811.

Ghan, S. J. (2013). Technical Note: Estimating aerosol effects on cloud radiative forcing. *Atmospheric Chemistry and Physics*, 13(19):9971–9974.

Ghan, S. J., Abdul-Razzak, H., Nenes, A., Ming, Y., Liu, X., Ovchinnikov, M., Shipway, B. J., Meskhidze, N., Xu, J., and Shi, X. (2011). Droplet nucleation: Physically-based parameterizations and comparative evaluation. *Journal of Advances in Modeling Earth Systems*, 3(4):1–33.

Ghan, S. J., Liu, X., Easter, R. C., Zaveri, R., Rasch, P. J., Yoon, J. H., and Eaton, B. (2012). Toward a minimal representation of aerosols in climate models: Comparative decomposition of aerosol direct, semidirect, and indirect radiative forcing. *Journal of Climate*, 25(19):6461–6476.

Giannini, A. and Kaplan, A. (2019). The role of aerosols and greenhouse gases in Sahel drought and recovery. *Climatic Change*, 152(3-4):449–466.

Giannini, A., Saravanan, R., and Chang, P. (2003). Oceanic Forcing of Sahel Rainfall on Interannual to Interdecadal Time Scales. *Science*, 302(5647).

Gillett, N. P., Shiogama, H., Funke, B., Hegerl, G., Knutti, R., Matthes, K., Santer, B. D., Stone, D., and Tebaldi, C. (2016). The Detection and Attribution Model Intercomparison Project (DAMIP v1.0) contribution to CMIP6. *Geoscientific Model Development*, 9(10):3685–3697.

Gimeno, L., Stohl, A., Trigo, R. M., Dominguez, F., Yoshimura, K., Yu, L., Drumond, A., Durán-Quesada, A. M., and Nieto, R. (2012). Oceanic and terrestrial sources of continental precipitation. *Reviews of Geophysics*, 50:RG4003.

Giorgetta, M. A., Jungclaus, J., Reick, C. H., Legutke, S., Bader, J., Böttinger, M., Brovkin, V., Crueger, T., Esch, M., Fieg, K., Glushak, K., Gayler, V., Haak, H., Hollweg, H.-D., Ilyina, T., Kinne, S., Kornblueh, L., Matei, D., Mauritsen, T., Mikolajewicz, U., Mueller, W., Notz, D., Pithan, F., Raddatz, T., Rast, S., Redler, R., Roeckner, E., Schmidt, H., Schnur, R., Segschneider, J., Six, K. D., Stockhause, M., Timmreck, C., Wegner, J., Widmann, H., Wieners, K.-H., Claussen, M., Marotzke, J., and Stevens, B. (2013). Climate and carbon cycle changes from 1850 to 2100 in MPI-ESM simulations for the Coupled Model Intercomparison Project phase 5. *Journal of Advances in Modeling Earth Systems*, 5(3).

Grabowski, W. W. (2001). Coupling cloud processes with the large-scale dynamics using the clouds-resolving convection parameterization (CRCP). *Journal of the Atmospheric Sciences*, 58(9).

Gregory, J. and Webb, M. (2008). Tropospheric Adjustment Induces a Cloud Component in CO2 Forcing. *Journal of Climate*, 21(1):58–71.

Greve, P., Orlowsky, B., Mueller, B., Sheffield, J., Reichstein, M., and Seneviratne, S. I. (2014). Global assessment of trends in wetting and drying over land. *Nature Geoscience*, 7(10).

Groisman, P. Y. and Legates, D. R. (1994). The Accuracy of United States Precipitation Data. *Bulletin of the American Meteorological Society*, 75(2):215–227.

Gryspeerdt, E., Quaas, J., Ferrachat, S., Gettelman, A., Ghan, S., Lohmann, U., Morrison, H., Neubauer, D., Partridge, D. G., Stier, P., Takemura, T., Wang, H., Wang, M., and Zhang, K. (2017). Constraining the instantaneous aerosol influence on cloud albedo. *Proceedings of the National Academy of Sciences*, 114(19):4899–4904.

Gryspeerdt, E., Stier, P., and Partridge, D. G. (2014). Links between satellite-retrieved aerosol and precipitation. *Atmospheric Chemistry and Physics*, 14(18):9677–9694.

Guo, H., Golaz, J. C., Donner, L. J., Wyman, B., Zhao, M., and Ginoux, P. (2015). CLUBB as a unified cloud parameterization: Opportunities and challenges. *Geophysical Research Letters*, 42(11):4540–4547.

Hall, A., Cox, P., Huntingford, C., and Klein, S. (2019). Progressing emergent constraints on future climate change. *Nature Climate Change*, 9(4):269–278.

Hari, V., Villarini, G., Karmakar, S., Wilcox, L. J., and Collins, M. (2020). Northward Propagation of the Intertropical Convergence Zone and Strengthening of Indian Summer Monsoon Rainfall. *Geophysical Research Letters*, 47(23).

Harris, I., Osborn, T. J., Jones, P., and Lister, D. (2020). Version 4 of the CRU TS monthly high-resolution gridded multivariate climate dataset. *Scientific Data*, 7(1):109.

Haynes, J. M., L'Ecuyer, T. S., Stephens, G. L., Miller, S. D., Mitrescu, C., Wood, N. B., and Tanelli, S. (2009). Rainfall retrieval over the ocean with spaceborne W-band radar. *Journal of Geophysical Research Atmospheres*, 114(8):1–18.

Haywood, J. and Boucher, O. (2000). Estimates of the direct and indirect radiative forcing due to tropospheric aerosols: A review. *Reviews of Geophysics*, 38(4):513–543.

Haywood, J. M., Jones, A., Bellouin, N., and Stephenson, D. (2013). Asymmetric forcing from stratospheric aerosols impacts Sahelian rainfall. *Nature Climate Change*, 3(7):660–665.

He, J. and Soden, B. J. (2015). Anthropogenic weakening of the tropical circulation: The relative roles of direct CO2 forcing and sea surface temperature change. *Journal of Climate*, 28(22).

He, J., Soden, B. J., and Kirtman, B. (2014). The robustness of the atmospheric circulation and precipitation response to future anthropogenic surface warming. *Geophysical Research Letters*, 41(7):2614–2622.

Held, I. M., Delworth, T. L., Lu, J., Findell, K. L., and Knutson, T. R. (2005). Simulation of Sahel drought in the 20th and 21st centuries. *Proceedings of the National Academy of Sciences*, 102(50):17891–17896.

Held, I. M. and Hou, A. Y. (1980). Nonlinear Axially Symmetric Circulations in a Nearly Inviscid Atmosphere. *Journal of the Atmospheric Sciences*, 37(3):515–533.

Held, I. M. and Soden, B. J. (2006). Robust Responses of the Hydrological Cycle to Global Warming. *Journal of Climate*, 19(21):5686–5699.

Held, I. M., Winton, M., Takahashi, K., Delworth, T., Zeng, F., and Vallis, G. K. (2010). Probing the Fast and Slow Components of Global Warming by Returning Abruptly to Preindustrial Forcing. *Journal of Climate*, 23(9):2418–2427.

Herman, R. J., Giannini, A., Biasutti, M., and Kushnir, Y. (2020). The effects of anthropogenic and volcanic aerosols and greenhouse gases on twentieth century Sahel precipitation. *Scientific Reports*, 10(1):1–11.

Hersbach, H., Bell, B., Berrisford, P., Hirahara, S., Horányi, A., Muñoz-Sabater, J., Nicolas, J., Peubey, C., Radu, R., Schepers, D., et al. (2020). The ERA5 global

reanalysis. *Quarterly Journal of the Royal Meteorological Society*, 146(730):1999–2049.

Hill, S. A., Ming, Y., Held, I. M., and Zhao, M. (2017). A Moist Static Energy Budget–Based Analysis of the Sahel Rainfall Response to Uniform Oceanic Warming. *Journal of Climate*, 30(15):5637–5660.

Hill, S. A., Ming, Y., and Zhao, M. (2018). Robust responses of the Sahelian hydrological cycle to global warming. *Journal of Climate*, 31(24):9793–9814.

Hirasawa, H., Kushner, P. J., Sigmond, M., Fyfe, J., and Deser, C. (2020). Anthropogenic Aerosols Dominate Forced Multidecadal Sahel Precipitation Change through Distinct Atmospheric and Oceanic Drivers. *Journal of Climate*, 33(23):10187–10204.

Hoerling, M., Hurrell, J., Eischeid, J., and Phillips, A. (2006). Detection and Attribution of Twentieth-Century Northern and Southern African Rainfall Change. *Journal of Climate*, 19(16):3989–4008.

Hoesly, R. M., Smith, S. J., Feng, L., Klimont, Z., Janssens-Maenhout, G., Pitkanen, T., Seibert, J. J., Vu, L., Andres, R. J., Bolt, R. M., Bond, T. C., Dawidowski, L., Kholod, N., Kurokawa, J. I., Li, M., Liu, L., Lu, Z., Moura, M. C., O'Rourke, P. R., and Zhang, Q. (2018). Historical (1750-2014) anthropogenic emissions of reactive gases and aerosols from the Community Emissions Data System (CEDS). *Geoscientific Model Development*, 11(1):369–408.

Hou, A. Y., Kakar, R. K., Neeck, S., Azarbarzin, A. A., Kummerow, C. D., Kojima, M., Oki, R., Nakamura, K., and Iguchi, T. (2014). The Global Precipitation Measurement Mission. *Bulletin of the American Meteorological Society*, 95(5):701–722.

Hourdin, F., Grandpeix, J. Y., Rio, C., Bony, S., Jam, A., Cheruy, F., Rochetin, N., Fairhead, L., Idelkadi, A., Musat, I., Dufresne, J. L., Lahellec, A., Lefebvre, M. P., and Roehrig, R. (2013). LMDZ5B: The atmospheric component of the IPSL climate model with revisited parameterizations for clouds and convection. *Climate Dynamics*, 40(9-10).

Houze Jr, R. A. (2014). *Cloud dynamics*. Academic press.

Hua, W., Dai, A., Zhou, L., Qin, M., and Chen, H. (2019). An Externally Forced Decadal Rainfall Seesaw Pattern Over the Sahel and Southeast Amazon. *Geophysical Research Letters*, 46(2):923–932.

Huang, B., Thorne, P. W., Banzon, V. F., Boyer, T., Chepurin, G., Lawrimore, J. H., Menne, M. J., Smith, T. M., Vose, R. S., and Zhang, H.-M. (2017). Extended Reconstructed Sea Surface Temperature, Version 5 (ERSSTv5): Upgrades, Validations, and Intercomparisons. *Journal of Climate*, 30(20):8179–8205.

Huffman, G. J., Adler, R. F., Bolvin, D. T., Gu, G., Nelkin, E. J., Bowman, K. P., Hong, Y., Stocker, E. F., and Wolff, D. B. (2007). The TRMM Multisatellite Precipitation Analysis (TMPA): Quasi-global, multiyear, combined-sensor precipitation estimates at fine scales. *Journal of Hydrometeorology*, 8(1).

Huffman, G. J., Adler, R. F., Rudolf, B., Schneider, U., and Keehn, P. R. (1995). Global precipitation estimates based on a technique for combining satellite-based estimates, rain gauge analysis, and NWP model precipitation information. *Journal of Climate*, 8(5).

Hwang, Y. T., Frierson, D. M., and Kang, S. M. (2013). Anthropogenic sulfate aerosol and the southward shift of tropical precipitation in the late 20th century. *Geophysical Research Letters*, 40(11):2845–2850.

Iguchi, T. and Meneghini, R. (1994). Intercomparison of single-frequency methods for retrieving a vertical rain profile from airborne or spaceborne radar data. *Journal of Atmospheric & Oceanic Technology*, 11(6).

Jeevanjee, N. and Romps, D. M. (2018). Mean precipitation change from a deepening troposphere. *Proceedings of the National Academy of Sciences*, 115(45):11465–11470.

Jiang, J. H., Su, H., Huang, L., Wang, Y., Massie, S., Zhao, B., Omar, A., and Wang, Z. (2018). Contrasting effects on deep convective clouds by different types of aerosols. *Nature Communications*, 9(1):3874.

Johnson, B. T., Haywood, J. M., and Hawcroft, M. K. (2019). Are Changes in Atmospheric Circulation Important for Black Carbon Aerosol Impacts on Clouds, Precipitation, and Radiation? *Journal of Geophysical Research: Atmospheres*, 124(14):7930–7950.

Jordan, A. K., Gnanadesikan, A., and Zaitchik, B. (2018). Simulated Dust Aerosol Impacts on Western Sahelian Rainfall: Importance of Ocean Coupling. *Journal of Climate*, 31(22):9107–9124.

Joshi, M. M., Gregory, J. M., Webb, M. J., Sexton, D. M. H., and Johns, T. C. (2008). Mechanisms for the land/sea warming contrast exhibited by simulations of climate change. *Climate Dynamics*, 30(5):455–465.

Kashiwase, H., Ohshima, K. I., Nihashi, S., and Eicken, H. (2017). Evidence for ice-ocean albedo feedback in the Arctic Ocean shifting to a seasonal ice zone. *Scientific Reports*, 7(1):8170.

Kasoar, M., Shawki, D., and Voulgarakis, A. (2018). Similar spatial patterns of global climate response to aerosols from different regions. *npj Climate and Atmospheric Science*, 1(1):12.

Kasoar, M., Voulgarakis, A., Lamarque, J. F., Shindell, D. T., Bellouin, N., Faluvegi, G., and Tsigaridis, K. (2016). Regional and global temperature response to anthropogenic SO2 emissions from China in three climate models. *Atmospheric Chemistry and Physics*, 16(15):9785–9804.

Kay, J. E., Deser, C., Phillips, A., Mai, A., Hannay, C., Strand, G., Arblaster, J. M., Bates, S. C., Danabasoglu, G., Edwards, J., Holland, M., Kushner, P., Lamarque, J.-F., Lawrence, D., Lindsay, K., Middleton, A., Munoz, E., Neale, R., Oleson, K., Polvani, L., and Vertenstein, M. (2015). The Community Earth System Model (CESM) Large Ensemble Project: A Community Resource for Studying Climate Change in the Presence of Internal Climate Variability. *Bulletin of the American Meteorological Society*, 96(8):1333–1349.

Keshavamurty, R. N. (1982). Response of the Atmosphere to Sea Surface Temperature Anomalies over the Equatorial Pacific and the Teleconnections of the Southern Oscillation. *Journal of the Atmospheric Sciences*, 39(6):1241–1259.

Keshtgar, B., Alizadeh-Choobari, O., and Irannejad, P. (2020). Seasonal and interannual variations of the intertropical convergence zone over the Indian Ocean based on an energetic perspective. *Climate Dynamics*, 54(7-8):3627–3639.

Khain, A. P. (2009). Notes on state-of-the-art investigations of aerosol effects on precipitation: a critical review. *Environmental Research Letters*, 4(1):015004.

Khain, A. P., Beheng, K. D., Heymsfield, A., Korolev, A., Krichak, S. O., Levin, Z., Pinsky, M., Phillips, V., Prabhakaran, T., Teller, A., van den Heever, S. C., and Yano, J.-I. (2015). Representation of microphysical processes in cloud-resolving

models: Spectral (bin) microphysics versus bulk parameterization. *Reviews of Geophysics*, 53(2):247–322.

Khain, A. P., BenMoshe, N., and Pokrovsky, A. (2008). Factors Determining the Impact of Aerosols on Surface Precipitation from Clouds: An Attempt at Classification. *Journal of the Atmospheric Sciences*, 65(6):1721–1748.

Khairoutdinov, M. and Kogan, Y. (2000). A New Cloud Physics Parameterization in a Large-Eddy Simulation Model of Marine Stratocumulus. *Monthly Weather Review*, 128(1):229–243.

Kidd, C. (2001). Satellite rainfall climatology: A review. *International Journal of Climatology*, 21(9).

Kidd, C., Becker, A., Huffman, G. J., Muller, C. L., Joe, P., Skofronick-Jackson, G., and Kirschbaum, D. B. (2017). So, how much of the Earth's surface is covered by rain gauges? *Bulletin of the American Meteorological Society*, 98(1).

Knight, J. R., Folland, C. K., and Scaife, A. A. (2006). Climate impacts of the Atlantic multidecadal oscillation. *Geophysical Research Letters*, 33(17):2–5.

Koch, D. and Del Genio, A. D. (2010). Black carbon semi-direct effects on cloud cover: review and synthesis. *Atmospheric Chemistry and Physics*, 10(16):7685–7696.

Köhler, H. (1936). The nucleus in and the growth of hygroscopic droplets. *Trans. Faraday Soc.*, 32:1152–1161.

Koren, I., Altaratz, O., Remer, L. A., Feingold, G., Martins, J. V., and Heiblum, R. H. (2012). Aerosol-induced intensification of rain from the tropics to the mid-latitudes. *Nature Geoscience*, 5(2).

Koren, I., Remer, L. A., Kaufman, Y. J., Rudich, Y., and Martins, J. V. (2007). On the twilight zone between clouds and aerosols. *Geophysical Research Letters*, 34(8).

Koren, I., Vanderlei Martins, J., Remer, L. A., and Afargan, H. (2008). Smoke invigoration versus inhibition of clouds over the amazon. *Science*, 321(5891).

Kosaka, Y. and Xie, S. P. (2013). Recent global-warming hiatus tied to equatorial Pacific surface cooling. *Nature*, 501(7467):403–407.

Kummerow, C., Hong, Y., Olson, W. S., Yang, S., Adler, R. F., McCollum, J., Ferraro, R., Petty, G., Shin, D. B., and Wilheit, T. T. (2001). The evolution of the Goddard profiling algorithm (GPROF) for rainfall estimation from passive microwave sensors. *Journal of Applied Meteorology*, 40(11).

Kushner, P. J., Mudryk, L. R., Merryfield, W., Ambadan, J. T., Berg, A., Bichet, A., Brown, R., Derksen, C., Déry, S. J., Dirkson, A., Flato, G., Fletcher, C. G., Fyfe, J. C., Gillett, N., Haas, C., Howell, S., Laliberté, F., McCusker, K., Sigmond, M., Sospedra-Alfonso, R., Tandon, N. F., Thackeray, C., Tremblay, B., and Zwiers, F. W. (2018). Canadian snow and sea ice: assessment of snow, sea ice, and related climate processes in Canada's Earth system model and climate-prediction system. *The Cryosphere*, 12(4):1137–1156.

Kvalevåg, M. M., Samset, B. H., and Myhre, G. (2013). Hydrological sensitivity to greenhouse gases and aerosols in a global climate model. *Geophysical Research Letters*, 40(7):1432–1438.

Lamarque, J.-F., Bond, T. C., Eyring, V., Granier, C., Heil, A., Klimont, Z., Lee, D., Liousse, C., Mieville, A., Owen, B., Schultz, M. G., Shindell, D., Smith, S. J., Stehfest, E., Van Aardenne, J., Cooper, O. R., Kainuma, M., Mahowald, N., McConnell, J. R., Naik, V., Riahi, K., and van Vuuren, D. P. (2010). Historical (1850–2000) gridded anthropogenic and biomass burning emissions of reactive gases and aerosols: methodology and application. *Atmospheric Chemistry and Physics*, 10(15):7017–7039.

Lambert, F. H. and Webb, M. J. (2008). Dependency of global mean precipitation on surface temperature. *Geophysical Research Letters*, 35(16):1–5.

Langhans, W., Schmidli, J., and Schär, C. (2012). Bulk convergence of cloud-resolving simulations of moist convection over complex terrain. *Journal of the Atmospheric Sciences*, 69(7).

Larson, V. E. and Golaz, J. C. (2005). Using probability density functions to derive consistent closure relationships among higher-order moments. *Monthly Weather Review*, 133(4).

L'Heureux, M. L., Lee, S., and Lyon, B. (2013). Recent multidecadal strengthening of the Walker circulation across the tropical Pacific. *Nature Climate Change*, 3(6).

Li, Z., Lau, W. K., Ramanathan, V., Wu, G., Ding, Y., Manoj, M. G., Liu, J., Qian, Y., Li, J., Zhou, T., Fan, J., Rosenfeld, D., Ming, Y., Wang, Y., Huang, J., Wang, B., Xu, X., Lee, S. S., Cribb, M., Zhang, F., Yang, X., Zhao, C., Takemura, T., Wang, K., Xia, X., Yin, Y., Zhang, H., Guo, J., Zhai, P. M., Sugimoto, N., Babu, S. S., and Brasseur, G. P. (2016). Aerosol and monsoon climate interactions over Asia. *Reviews of Geophysics*, 54(4):866–929.

Liu, C., Allan, R. P., and Huffman, G. J. (2012). Co-variation of temperature and precipitation in CMIP5 models and satellite observations. *Geophysical Research Letters*, 39(13).

Liu, F., Zhao, T., Wang, B., Liu, J., and Luo, W. (2018). Different Global Precipitation Responses to Solar, Volcanic, and Greenhouse Gas Forcings. *Journal of Geophysical Research: Atmospheres*, 123(8):4060–4072.

Liu, H., Guo, J., Koren, I., Altaratz, O., Dagan, G., Wang, Y., Jiang, J. H., Zhai, P., and Yung, Y. L. (2019). Non-Monotonic Aerosol Effect on Precipitation in Convective Clouds over Tropical Oceans. *Scientific Reports*, 9(1).

Liu, Z., Wang, M., Rosenfeld, D., Zhu, Y., Bai, H., Cao, Y., and Liang, Y. (2020). Evaluation of Cloud and Precipitation Response to Aerosols in WRF-Chem With Satellite Observations. *Journal of Geophysical Research: Atmospheres*, 125(18):1–25.

Lohmann, U., Friebel, F., Kanji, Z. A., Mahrt, F., Mensah, A. A., and Neubauer, D. (2020). Future warming exacerbated by aged-soot effect on cloud formation. *Nature Geoscience*, 13(10):674–680.

Lohmann, U. and Hoose, C. (2009). Sensitivity studies of different aerosol indirect effects in mixed-phase clouds. *Atmospheric Chemistry and Physics*, 9(22):8917–8934.

Lohmann, U., Lüönd, F., and Mahrt, F. (2016). *An Introduction to Clouds*. Cambridge University Press.

Lohmann, U., Stier, P., Hoose, C., Ferrachat, S., Kloster, S., Roeckner, E., and Zhang, J. (2007). Cloud microphysics and aerosol indirect effects in the global climate model ECHAM5-HAM. *Atmospheric Chemistry and Physics*, 7(13):3425–3446.

Lu, J., Chen, G., and Frierson, D. M. (2008). Response of the zonal mean atmospheric circulation to El Niño versus global warming. *Journal of Climate*, 21(22).

Lu, J., Vecchi, G. A., and Reichler, T. (2007). Expansion of the Hadley cell under global warming. *Geophysical Research Letters*, 34(6).

Lu, M.-L. and Seinfeld, J. H. (2005). Study of the Aerosol Indirect Effect by Large-Eddy Simulation of Marine Stratocumulus. *Journal of the Atmospheric Sciences*, 62(11):3909–3932.

Lubin, D. and Vogelmann, A. M. (2006). A climatologically significant aerosol longwave indirect effect in the Arctic. *Nature*, 439(7075):453–456.

Ma, J., Chadwick, R., Seo, K.-H., Dong, C., Huang, G., Foltz, G. R., and Jiang, J. H. (2018). Responses of the Tropical Atmospheric Circulation to Climate Change and Connection to the Hydrological Cycle. *Annual Review of Earth and Planetary Sciences*, 46(1):549–580.

Ma, P. L., Rasch, P. J., Wang, H., Zhang, K., Easter, R. C., Tilmes, S., Fast, J. D., Liu, X., Yoon, J. H., and Lamarque, J. F. (2013). The role of circulation features on black carbon transport into the Arctic in the Community Atmosphere Model version 5 (CAM5). *Journal of Geophysical Research Atmospheres*, 118(10):4657–4669.

Ma, S. and Zhou, T. (2016). Robust Strengthening and Westward Shift of the Tropical Pacific Walker Circulation during 1979–2012: A Comparison of 7 Sets of Reanalysis Data and 26 CMIP5 Models. *Journal of Climate*, 29(9):3097–3118.

Ma, X., Von Salzen, K., and Li, J. (2008). Modelling sea salt aerosol and its direct and indirect effects on climate. *Atmospheric Chemistry and Physics*, 8(5).

Mahowald, N., Albani, S., Kok, J. F., Engelstaeder, S., Scanza, R., Ward, D. S., and Flanner, M. G. (2014). The size distribution of desert dust aerosols and its impact on the Earth system. *Aeolian Research*, 15:53–71.

Malavelle, F. F., Haywood, J. M., Jones, A., Gettelman, A., Clarisse, L., Bauduin, S., Allan, R. P., Karset, I. H. H., Kristjánsson, J. E., Oreopoulos, L., Cho, N., Lee, D., Bellouin, N., Boucher, O., Grosvenor, D. P., Carslaw, K. S., Dhomse, S., Mann, G. W., Schmidt, A., Coe, H., Hartley, M. E., Dalvi, M., Hill, A. A., Johnson, B. T., Johnson, C. E., Knight, J. R., O'Connor, F. M., Partridge, D. G., Stier,

P., Myhre, G., Platnick, S., Stephens, G. L., Takahashi, H., and Thordarson, T. (2017). Strong constraints on aerosol–cloud interactions from volcanic eruptions. *Nature*, 546(7659):485–491.

Manabe, S. (2019). Role of greenhouse gas in climate change. *Tellus A: Dynamic Meteorology and Oceanography*, 71(1):1620078.

Manabe, S., Bryan, K., and Spelman, M. J. (1990). Transient Response of a Global Ocean-Atmosphere Model to a Doubling of Atmospheric Carbon Dioxide. *Journal of Physical Oceanography*, 20(5):722–749.

Manabe, S. and Wetherald, R. T. (1975). EFFECTS OF DOUBLING THE CO2 CONCENTRATION ON THE CLIMATE OF A GENERAL CIRCULATION MODEL. *Journal of the Atmospheric Sciences*, 32(1).

Mao, K. B., Ma, Y., Xia, L., Chen, W. Y., Shen, X. Y., He, T. J., and Xu, T. R. (2014). Global aerosol change in the last decade: An analysis based on MODIS data. *Atmospheric Environment*, 94.

Marinescu, P. J., Van Den Heever, S. C., Heikenfeld, M., Barrett, A. I., Barthlott, C., Hoose, C., Fan, J., Fridlind, A. M., Matsui, T., Miltenberger, A. K., Stier, P., Vie, B., White, B. A., and Zhang, Y. (2021). Impacts of varying concentrations of cloud condensation nuclei on deep convective cloud updrafts a multimodel assessment. *Journal of the Atmospheric Sciences*, 78(4).

Martin, E. R., Thorncroft, C., and Booth, B. B. (2014). The multidecadal atlantic SST-sahel rainfall teleconnection in CMIP5 simulations. *Journal of Climate*, 27(2):784–806.

Mauritsen, T. and Stevens, B. (2015). Missing iris effect as a possible cause of muted hydrological change and high climate sensitivity in models. *Nature Geoscience*, 8(5):346–351.

McKinnon, K. A. and Deser, C. (2018). Internal Variability and Regional Climate Trends in an Observational Large Ensemble. *Journal of Climate*, 31(17):6783–6802.

Meehl, G. A., Washington, W. M., Arblaster, J. M., Hu, A., Teng, H., Tebaldi, C., Sanderson, B. N., Lamarque, J. F., Conley, A., Strand, W. G., and White, J. B. (2012). Climate system response to external forcings and climate change projections in CCSM4. *Journal of Climate*, 25(11).

Mekonnen, M. M. and Hoekstra, A. Y. (2016). Four billion people facing severe water scarcity. *Science Advances*, 2(2).

Menary, M. B., Robson, J., Allan, R. P., Booth, B. B., Cassou, C., Gastineau, G., Gregory, J., Hodson, D., Jones, C., Mignot, J., Ringer, M., Sutton, R., Wilcox, L., and Zhang, R. (2020). Aerosol-Forced AMOC Changes in CMIP6 Historical Simulations. *Geophysical Research Letters*, 47(14).

Menne, M. J., Durre, I., Vose, R. S., Gleason, B. E., and Houston, T. G. (2012). An overview of the global historical climatology network-daily database. *Journal of Atmospheric and Oceanic Technology*, 29(7).

Michibata, T., Suzuki, K., Sato, Y., and Takemura, T. (2016). The source of discrepancies in aerosol–cloud–precipitation interactions between GCM and A-Train retrievals. *Atmospheric Chemistry and Physics*, 16(23):15413–15424.

Ming, Y., Ramaswamy, V., and Persad, G. (2010). Two opposing effects of absorbing aerosols on global-mean precipitation. *Geophysical Research Letters*, 37(13):1–4.

Mitchell, J. F., Wilson, C. A., and Cunnington, W. M. (1987). On Co2 climate sensitivity and model dependence of results. *Quarterly Journal of the Royal Meteorological Society*, 113(475).

Mohino, E., Janicot, S., and Bader, J. (2011). Sahel rainfall and decadal to multi-decadal sea surface temperature variability. *Climate Dynamics*, 37(3-4):419–440.

Monerie, P. A., Sanchez-Gomez, E., Pohl, B., Robson, J., and Dong, B. (2017). Impact of internal variability on projections of Sahel precipitation change. *Environmental Research Letters*, 12(11).

Monerie, P. A., Wainwright, C. M., Sidibe, M., and Akinsanola, A. A. (2020). Model uncertainties in climate change impacts on Sahel precipitation in ensembles of CMIP5 and CMIP6 simulations. *Climate Dynamics*, 55(5-6):1385–1401.

Morice, C. P., Kennedy, J. J., Rayner, N. A., and Jones, P. D. (2012). Quantifying uncertainties in global and regional temperature change using an ensemble of observational estimates: The HadCRUT4 data set. *Journal of Geophysical Research Atmospheres*, 117(8).

Morice, C. P., Kennedy, J. J., Rayner, N. A., Winn, J. P., Hogan, E., Killick, R. E., Dunn, R. J. H., Osborn, T. J., Jones, P. D., and Simpson, I. R. (2021). An Updated Assessment of Near-Surface Temperature Change From 1850: The HadCRUT5 Data Set. *Journal of Geophysical Research: Atmospheres*, 126(3):1–28.

Morrison, H., van Lier-Walqui, M., Fridlind, A. M., Grabowski, W. W., Harrington, J. Y., Hoose, C., Korolev, A., Kumjian, M. R., Milbrandt, J. A., Pawlowska, H., Posselt, D. J., Prat, O. P., Reimel, K. J., Shima, S. I., van Diedenhoven, B., and Xue, L. (2020). Confronting the Challenge of Modeling Cloud and Precipitation Microphysics. *Journal of Advances in Modeling Earth Systems*, 12(8).

Muller, C. J. and O'Gorman, P. A. (2011). An energetic perspective on the regional response of precipitation to climate change. *Nature Climate Change*, 1(5):266–271.

Myhre, G., Forster, P. M., Samsmset, B. H., Odnebrog, Sillmann, J., Aalbergsjø, S. G., Andrews, T., Boucher, O., Faluvegi, G., Fläschner, D., Iversen, T., Kasoar, M., Kharin, V., Kirkevag, A., Lamarque, J. F., Olivié, D., Richardson, T. B., Shindell, D., Shine, K. P., Stjern, C. W., Takemura, T., Voulgarakis, A., and Zwiers, F. (2017). PDRMIP: A precipitation driver and response model intercomparison project-protocol and preliminary results. *Bulletin of the American Meteorological Society*, 98(6):1185–1198.

Myhre, G., Samset, B. H., Hodnebrog, Ø., Andrews, T., Boucher, O., Faluvegi, G., Fläschner, D., Forster, P. M., Kasoar, M., Kharin, V., Kirkevåg, A., Lamarque, J.-F., Olivié, D., Richardson, T. B., Shawki, D., Shindell, D., Shine, K. P., Stjern, C. W., Takemura, T., and Voulgarakis, A. (2018). Sensible heat has significantly affected the global hydrological cycle over the historical period. *Nature Communications*, 9(1):1922.

Myhre, G., Samset, B. H., Schulz, M., Balkanski, Y., Bauer, S., Berntsen, T. K., Bian, H., Bellouin, N., Chin, M., Diehl, T., Easter, R. C., Feichter, J., Ghan, S. J., Hauglustaine, D., Iversen, T., Kinne, S., Kirkevåg, A., Lamarque, J.-F., Lin, G., Liu, X., Lund, M. T., Luo, G., Ma, X., van Noije, T., Penner, J. E., Ruiz, A., Rasch, P. J., Seland, Ø., Skeie, R. B., Stier, P., Takemura, T., Tsigaridis, K., Wang, P., Wang, Z., Xu, L., Yu, H., Yu, F., Yoon, J.-H., Zhang, K., Zhang, H., and Zhou, C. (2013). Radiative forcing of the direct aerosol effect from AeroCom Phase II simulations. *Atmospheric Chemistry and Physics*, 13(4):1853–1877.

Myhre, G., Shindell, D., Bréon, F.-M., Collins, W., Fuglestvedt, J., Huang, J., Koch, D., Lamarque, J.-F., Lee, D., Mendoza, B., Nakajima, T., Robock, A., Stephens, G., Takemura, T., and Zhang, H. (2014). Anthropogenic and Natural Radiative Forcing. In *Climate Change 2013 – The Physical Science Basis*, pages 659–740. Cambridge University Press.

Na, Y., Fu, Q., and Kodama, C. (2020). Precipitation Probability and Its Future Changes From a Global Cloud-Resolving Model and CMIP6 Simulations. *Journal of Geophysical Research: Atmospheres*, 125(5).

Naegele, A. C. and Randall, D. A. (2019). Geographical and Seasonal Variability of Cloud-Radiative Feedbacks on Precipitation. *Journal of Geophysical Research: Atmospheres*, 124(2):684–699.

Neale, R. B., Chen, C.-C., Gettelman, A., Lauritzen, P. H., Park, S., Williamson, D. L., Conley, A. J., Garcia, R., Kinnison, D., Lamarque, J.-F., et al. (2010). Description of the ncar community atmosphere model (cam 5.0). *NCAR Tech. Note NCAR/TN-486+ STR*, 1(1):1–12.

Neelin, J. D. and Held, I. M. (1987). Modeling Tropical Convergence Based on the Moist Static Energy Budget. *Monthly Weather Review*, 115(1):3–12.

Neelin, J. D., Sahany, S., Stechmann, S. N., and Bernstein, D. N. (2017). Global warming precipitation accumulation increases above the current-climate cutoff scale. *Proceedings of the National Academy of Sciences of the United States of America*, 114(6).

Neubauer, D., Ferrachat, S., Siegenthaler-Le Drian, C., Stier, P., Partridge, D. G., Tegen, I., Bey, I., Stanelle, T., Kokkola, H., and Lohmann, U. (2019). The global aerosol–climate model ECHAM6.3–HAM2.3 – Part 2: Cloud evaluation, aerosol radiative forcing, and climate sensitivity. *Geoscientific Model Development*, 12(8):3609–3639.

Nordeng, T. E. (1994). Extended versions of the convective parametrization scheme at ecmwf and their impact on the mean and transient activity of the model in the tropics. *Research Department Technical Memorandum*, 206:1–41.

O'Brien, T. A., Collins, W. D., Kashinath, K., Rübel, O., Byna, S., Gu, J., Krishnan, H., and Ullrich, P. A. (2016). Resolution dependence of precipitation statistical

fidelity in hindcast simulations. *Journal of Advances in Modeling Earth Systems*, 8(2):976–990.

O'Gorman, P. A. (2015). Precipitation Extremes Under Climate Change. *Current Climate Change Reports*, 1(2):49–59.

O'Gorman, P. A., Allan, R. P., Byrne, M. P., and Previdi, M. (2012). Energetic Constraints on Precipitation Under Climate Change. *Surveys in Geophysics*, 33(3-4):585–608.

O'Gorman, P. A. and Muller, C. J. (2010). How closely do changes in surface and column water vapor follow Clausius–Clapeyron scaling in climate change simulations? *Environmental Research Letters*, 5(2):025207.

Palmer, T. N. (1986). Influence of the Atlantic, Pacific and Indian Oceans on sahel rainfall. *Nature*, 322(6076):251–253.

Pendergrass, A. G. (2020). The Global-Mean Precipitation Response to CO 2 -Induced Warming in CMIP6 Models. *Geophysical Research Letters*, 47(17):1–10.

Pendergrass, A. G. and Hartmann, D. L. (2012). Global-mean precipitation and black carbon in AR4 simulations. *Geophysical Research Letters*, 39(1):1–6.

Pendergrass, A. G., Reed, K. A., and Medeiros, B. (2016). The link between extreme precipitation and convective organization in a warming climate: Global radiative-convective equilibrium simulations. *Geophysical Research Letters*, 43(21).

Penner, J. E., Xu, L., and Wang, M. (2011). Satellite methods underestimate indirect climate forcing by aerosols. *Proceedings of the National Academy of Sciences of the United States of America*, 108(33):13404–13408.

Pfahl, S., O'Gorman, P. A., and Fischer, E. M. (2017). Understanding the regional pattern of projected future changes in extreme precipitation. *Nature Climate Change*, 7(6).

Pincus, R. and Stevens, B. (2013). Paths to accuracy for radiation parameterizations in atmospheric models. *Journal of Advances in Modeling Earth Systems*, 5(2):225–233.

Prein, A. F., Langhans, W., Fosser, G., Ferrone, A., Ban, N., Goergen, K., Keller, M., Tölle, M., Gutjahr, O., Feser, F., Brisson, E., Kollet, S., Schmidli, J., Lipzig, N. P. M., and Leung, R. (2015). A review on regional convection-permitting climate modeling: Demonstrations, prospects, and challenges. *Reviews of Geophysics*, 53(2):323–361.

Previdi, M. (2010). Radiative feedbacks on global precipitation. *Environmental Research Letters*, 5(2):025211.

Qin, M., Dai, A., and Hua, W. (2020). Quantifying Contributions of Internal Variability and External Forcing to Atlantic Multidecadal Variability Since 1870. *Geophysical Research Letters*, 47(22):1–11.

Quaas, J., Stevens, B., Stier, P., and Lohmann, U. (2010). Interpreting the cloud cover-Aerosol optical depth relationship found in satellite data using a general circulation model. *Atmospheric Chemistry and Physics*, 10(13).

Ramanathan, V., Crutzen, P. J., Kiehl, J. T., and Rosenfeld, D. (2001). Aerosols, Climate, and the Hydrological Cycle. *Science*, 294(5549):2119–2124.

Rayner, N. A. (2003). Global analyses of sea surface temperature, sea ice, and night marine air temperature since the late nineteenth century. *Journal of Geophysical Research*, 108(D14):4407.

Richardson, M., Cowtan, K., Hawkins, E., and Stolpe, M. B. (2016a). Reconciled climate response estimates from climate models and the energy budget of Earth. *Nature Climate Change*, 6(10):931–935.

Richardson, T. B., Forster, P. M., Andrews, T., Boucher, O., Faluvegi, G., Fläschner, D., Hodnebrog, Ø., Kasoar, M., Kirkevåg, A., Lamarque, J.-F., Myhre, G., Olivié, D., Samset, B. H., Shawki, D., Shindell, D., Takemura, T., and Voulgarakis, A. (2018a). Drivers of Precipitation Change: An Energetic Understanding. *Journal of Climate*, 31(23):9641–9657.

Richardson, T. B., Forster, P. M., Andrews, T., Boucher, O., Faluvegi, G., Fläschner, D., Kasoar, M., Kirkevåg, A., Lamarque, J. F., Myhre, G., Olivié, D., Samset, B. H., Shawki, D., Shindell, D., Takemura, T., and Voulgarakis, A. (2018b). Carbon Dioxide Physiological Forcing Dominates Projected Eastern Amazonian Drying. *Geophysical Research Letters*, 45(6):2815–2825.

Richardson, T. B., Forster, P. M., Andrews, T., and Parker, D. J. (2016b). Understanding the rapid precipitation response to CO2and aerosol forcing on a regional scale. *Journal of Climate*, 29(2):583–594.

Ridley, H. E., Asmerom, Y., Baldini, J. U., Breitenbach, S. F., Aquino, V. V., Prufer, K. M., Culleton, B. J., Polyak, V., Lechleitner, F. A., Kennett, D. J., Zhang, M., Marwan, N., Macpherson, C. G., Baldini, L. M., Xiao, T., Peterkin, J. L., Awe, J., and Haug, G. H. (2015). Aerosol forcing of the position of the intertropical convergence zone since ad 1550. *Nature Geoscience*, 8(3):195–200.

Robock, A. (2000). Volcanic eruptions and climate. *Reviews of Geophysics*, 38(2).

Roeckner, E., Stier, P., Feichter, J., Kloster, S., Esch, M., and Fischer-Bruns, I. (2006). Impact of carbonaceous aerosol emissions on regional climate change. *Climate Dynamics*, 27(6):553–571.

Rollings, M. and Merlis, T. M. (2021). The Observed Relationship between Pacific SST Variability and Hadley Cell Extent Trends in Reanalyses. *Journal of Climate*, 34(7):2511–2527.

Rosenfeld, D. (2000). Suppression of rain and snow by urban and industrial air pollution. *Science*, 287(5459).

Rosenfeld, D., Lahav, R., Khain, A., and Pinsky, M. (2002). The role of sea spray in cleansing air pollution over ocean via cloud processes. *Science*, 297(5587).

Rosenfeld, D., Lohmann, U., Raga, G. B., O'Dowd, C. D., Kulmala, M., Fuzzi, S., Reissell, A., and Andreae, M. O. (2008). Flood or Drought: How Do Aerosols Affect Precipitation? *Science*, 321(5894):1309–1313.

Rosenfeld, D., Zhu, Y., Wang, M., Zheng, Y., Goren, T., and Yu, S. (2019). Aerosol-driven droplet concentrations dominate coverage and water of oceanic low-level clouds. *Science*, 363(6427):eaav0566.

Rotstayn, L. D. and Lohmann, U. (2002). Tropical Rainfall Trends and the Indirect Aerosol Effect. *Journal of Climate*, 15(15):2103–2116.

Salzmann, M., Weser, H., and Cherian, R. (2014). Robust response of Asian summer monsoon to anthropogenic aerosols in CMIP5 models. *Journal of Geophysical Research: Atmospheres*, 119(19):11,321–11,337.

Samset, B. H., Myhre, G., Forster, P. M., Hodnebrog, Andrews, T., Faluvegi, G., Fläschner, D., Kasoar, M., Kharin, V., Kirkevåg, A., Lamarque, J. F., Olivié, D., Richardson, T., Shindell, D., Shine, K. P., Takemura, T., and Voulgarakis, A. (2016). Fast and slow precipitation responses to individual climate forcers: A PDRMIP multimodel study. *Geophysical Research Letters*, 43(6):2782–2791.

Samset, B. H., Myhre, G., Forster, P. M., Hodnebrog, Ø., Andrews, T., Boucher, O., Faluvegi, G., Fläschner, D., Kasoar, M., Kharin, V., Kirkevåg, A., Lamarque, J.-F., Olivié, D., Richardson, T. B., Shindell, D., Takemura, T., and Voulgarakis, A. (2017). Weak hydrological sensitivity to temperature change over land, independent of climate forcing. *npj Climate and Atmospheric Science*, 1(1):3.

Satoh, M., Stevens, B., Judt, F., Khairoutdinov, M., Lin, S.-J., Putman, W. M., and Düben, P. (2019). Global Cloud-Resolving Models. *Current Climate Change Reports*, 5(3):172–184.

Scaife, A. A., Kucharski, F., Folland, C. K., Kinter, J., Brönnimann, S., Fereday, D., Fischer, A. M., Grainger, S., Jin, E. K., Kang, I. S., Knight, J. R., Kusunoki, S., Lau, N. C., Nath, M. J., Nakaegawa, T., Pegion, P., Schubert, S., Sporyshev, P., Syktus, J., Yoon, J. H., Zeng, N., and Zhou, T. (2009). The CLIVAR C20C project: selected twentieth century climate events. *Climate Dynamics*, 33(5):603–614.

Scannell, C., Booth, B. B., Dunstone, N. J., Rowell, D. P., Bernie, D. J., Kasoar, M., Voulgarakis, A., Wilcox, L. J., Acosta Navarro, J. C., Seland, Ø., and Paynter, D. J. (2019). The influence of remote aerosol forcing from industrialized economies on the future evolution of East and West African rainfall. *Journal of Climate*, 32(23):8335–8354.

Schmidt, G. A., Kelley, M., Nazarenko, L., Ruedy, R., Russell, G. L., Aleinov, I., Bauer, M., Bauer, S. E., Bhat, M. K., Bleck, R., Canuto, V., Chen, Y. H., Cheng, Y., Clune, T. L., Del Genio, A., De Fainchtein, R., Faluvegi, G., Hansen, J. E., Healy, R. J., Kiang, N. Y., Koch, D., Lacis, A. A., Legrande, A. N., Lerner, J., Lo, K. K., Matthews, E. E., Menon, S., Miller, R. L., Oinas, V., Oloso, A. O., Perlwitz, J. P., Puma, M. J., Putman, W. M., Rind, D., Romanou, A., Sato, M., Shindell, D. T., Sun, S., Syed, R. A., Tausnev, N., Tsigaridis, K., Unger, N., Voulgarakis, A., Yao, M. S., and Zhang, J. (2014). Configuration and assessment of the GISS ModelE2 contributions to the CMIP5 archive. *Journal of Advances in Modeling Earth Systems*, 6(1).

Schneider, T. (2017). Feedback of Atmosphere-Ocean Coupling on Shifts of the Intertropical Convergence Zone. *Geophysical Research Letters*, 44(22):11,644–11,653.

Schneider, T., Bischoff, T., and Haug, G. H. (2014). Migrations and dynamics of the intertropical convergence zone. *Nature*, 513(7516):45–53.

Schnell, R. C. and Vali, G. (1976). Biogenic Ice Nuclei: Part I. Terrestrial and Marine Sources. *Journal of the Atmospheric Sciences*, 33(8):1554–1564.

Schwartz, S. E. (2007). Heat capacity, time constant, and sensitivity of Earth's climate system. *Journal of Geophysical Research Atmospheres*, 112(24).

Séférian, R., Nabat, P., Michou, M., Saint-Martin, D., Voldoire, A., Colin, J., Decharme, B., Delire, C., Berthet, S., Chevallier, M., Sénési, S., Franchisteguy, L., Vial, J., Mallet, M., Joetzjer, E., Geoffroy, O., Guérémy, J. F., Moine, M. P., Msadek, R., Ribes, A., Rocher, M., Roehrig, R., Salas-y Mélia, D., Sanchez, E., Terray, L., Valcke, S., Waldman, R., Aumont, O., Bopp, L., Deshayes, J., Éthé, C., and Madec, G. (2019). Evaluation of CNRM Earth System Model, CNRM-ESM2-1: Role of Earth System Processes in Present-Day and Future Climate. *Journal of Advances in Modeling Earth Systems*, 11(12).

Seinfeld, J. H. and Pandis, S. N. (1998). *Atmospheric Chemistry and Physics: From Air Pollution to Global Change*. John Wiley and Sons, New Jersey.

Seland, Ø., Bentsen, M., Olivié, D., Toniazzo, T., Gjermundsen, A., Graff, L. S., Debernard, J. B., Gupta, A. K., He, Y. C., Kirkeväg, A., Schwinger, J., Tjiputra, J., Schanke Aas, K., Bethke, I., Fan, Y., Griesfeller, J., Grini, A., Guo, C., Ilicak, M., Karset, I. H. H., Landgren, O., Liakka, J., Moseid, K. O., Nummelin, A., Spensberger, C., Tang, H., Zhang, Z., Heinze, C., Iversen, T., and Schulz, M. (2020). Overview of the Norwegian Earth System Model (NorESM2) and key climate response of CMIP6 DECK, historical, and scenario simulations. *Geoscientific Model Development*, 13(12).

Seo, J., Kang, S. M., and Frierson, D. M. (2014). Sensitivity of intertropical convergence zone movement to the latitudinal position of thermal forcing. *Journal of Climate*, 27(8).

Shaw, T. A. and Voigt, A. (2015). Tug of war on summertime circulation between radiative forcing and sea surface warming. *Nature Geoscience*, 8(7):560–566.

Shawki, D., Voulgarakis, A., Chakraborty, A., Kasoar, M., and Srinivasan, J. (2018). The South Asian Monsoon Response to Remote Aerosols: Global and Regional Mechanisms. *Journal of Geophysical Research: Atmospheres*, 123(20):11,585–11,601.

Sherwood, S. C., Bony, S., Boucher, O., Bretherton, C., Forster, P. M., Gregory, J. M., and Stevens, B. (2015). Adjustments in the forcing-feedback framework for understanding climate change. *Bulletin of the American Meteorological Society*, 96(2):217–228.

Sillmann, J., Stjern, C. W., Myhre, G., Samset, B. H., Hodnebrog, Ø., Andrews, T., Boucher, O., Faluvegi, G., Forster, P., Kasoar, M. R., Kharin, V. V., Kirkevåg, A., Lamarque, J.-F., Olivié, D. J. L., Richardson, T. B., Shindell, D., Takemura, T., Voulgarakis, A., and Zwiers, F. W. (2019). Extreme wet and dry conditions affected differently by greenhouse gases and aerosols. *npj Climate and Atmospheric Science*, 2(1):1–7.

Skofronick-Jackson, G., Petersen, W. A., Berg, W., Kidd, C., Stocker, E. F., Kirschbaum, D. B., Kakar, R., Braun, S. A., Huffman, G. J., Iguchi, T., Kirstetter, P. E., Kummerow, C., Meneghini, R., Oki, R., Olson, W. S., Takayabu, Y. N., Furukawa, K., and Wilheit, T. (2017). The global precipitation measurement (GPM) mission for science and Society. *Bulletin of the American Meteorological Society*, 98(8).

Smith, C. J., Kramer, R. J., Myhre, G., Forster, P. M., Soden, B. J., Andrews, T., Boucher, O., Faluvegi, G., Fläschner, D., Hodnebrog, Kasoar, M., Kharin, V., Kirkevåg, A., Lamarque, J. F., Mülmenstädt, J., Olivié, D., Richardson, T., Samset, B. H., Shindell, D., Stier, P., Takemura, T., Voulgarakis, A., and Watson-Parris, D. (2018). Understanding Rapid Adjustments to Diverse Forcing Agents. *Geophysical Research Letters*, 45(21):12,023–12,031.

Smith, S. J., van Aardenne, J., Klimont, Z., Andres, R. J., Volke, A., and Delgado Arias, S. (2011). Anthropogenic sulfur dioxide emissions: 1850–2005. *Atmospheric Chemistry and Physics*, 11(3):1101–1116.

Soden, B. and Chung, E. S. (2017). The large-scale dynamical response of clouds to aerosol forcing. *Journal of Climate*, 30(21).

Soden, B. J., Held, I. M., Colman, R. C., Shell, K. M., Kiehl, J. T., and Shields, C. A. (2008). Quantifying climate feedbacks using radiative kernels. *Journal of Climate*, 21(14):3504–3520.

Sophie, S., Naik, V., Adhikary, B., Artaxo, P., Berntsen, T., Collins, W., Fuzzi, S., Gallardo, L., Kiendler-Scharr, A., Klimont, Z., Liao, H., Unger, N., and Zanis, P. (2021). Short-lived Climate Forcers. In Masson-Delmotte, V., Zhai, P., Pirani, A., Connors, S. L., Péan, C., Berger, S., Caud, N., Chen, Y., Goldfarb, L., Gomis, M. I., Huang, M., Leitzell, K., Lonnoy, E., Matthews, J. B. R., Maycock, T. K., Waterfield, T., Yelekçi, O., Yu, R., and Zhou, B., editors, *Climate Change 2021: The Physical Science Basis. Contribution of Working Group I to the Sixth Assessment Report of the Intergovernmental Panel on Climate Change*, chapter 6, pages 817–922. Cambridge University Press.

Stephens, G. and Ellis, T. (2008). Controls of Global-Mean Precipitation Increases in Global Warming. *Journal of Climate*, 21:6141–6155.

Stephens, G. L., Hakuba, M. Z., Webb, M. J., Lebsock, M., Yue, Q., Kahn, B. H., Hristova-Veleva, S., Rapp, A. D., Stubenrauch, C. J., Elsaesser, G. S., and Slingo, J. (2018). Regional Intensification of the Tropical Hydrological Cycle During ENSO. *Geophysical Research Letters*, 45(9):4361–4370.

Stephens, G. L. and Hu, Y. (2010). Are climate-related changes to the character of global-mean precipitation predictable? *Environmental Research Letters*, 5(2).

Stephens, G. L., L'Ecuyer, T., Forbes, R., Gettlemen, A., Golaz, J. C., Bodas-Salcedo, A., Suzuki, K., Gabriel, P., and Haynes, J. (2010). Dreary state of precipitation in global models. *Journal of Geophysical Research Atmospheres*, 115(24):1–13.

Stephens, G. L., Vane, D. G., Tanelli, S., Im, E., Durden, S., Rokey, M., Reinke, D., Partain, P., Mace, G. G., Austin, R., L'Ecuyer, T., Haynes, J., Lebsock, M., Suzuki, K., Waliser, D., Wu, D., Kay, J., Gettelman, A., Wang, Z., and Marchand, R. (2009). CloudSat mission: Performance and early science after the first year of operation. *Journal of Geophysical Research Atmospheres*, 114(8).

Stevens, B. and Feingold, G. (2009). Untangling aerosol effects on clouds and precipitation in a buffered system. *Nature*, 461(7264):607–613.

Stevens, B., Giorgetta, M., Esch, M., Mauritsen, T., Crueger, T., Rast, S., Salzmann, M., Schmidt, H., Bader, J., Block, K., Brokopf, R., Fast, I., Kinne, S., Kornblueh, L., Lohmann, U., Pincus, R., Reichler, T., and Roeckner, E. (2013). Atmospheric component of the MPI-M Earth System Model: ECHAM6. *Journal of Advances in Modeling Earth Systems*, 5(2):146–172.

Stevens, B., Satoh, M., Auger, L., Biercamp, J., Bretherton, C. S., Chen, X., Düben, P., Judt, F., Khairoutdinov, M., Klocke, D., Kodama, C., Kornblueh, L., Lin, S.-J., Neumann, P., Putman, W. M., Röber, N., Shibuya, R., Vanniere, B., Vidale, P. L., Wedi, N., and Zhou, L. (2019). DYAMOND: the DYnamics of the Atmospheric general circulation Modeled On Non-hydrostatic Domains. *Progress in Earth and Planetary Science*, 6(1):61.

Stier, P., Feichter, J., Kinne, S., Kloster, S., Vignati, E., Wilson, J., Ganzeveld, L., Tegen, I., Werner, M., Balkanski, Y., Schulz, M., Boucher, O., Minikin, A., and Petzold, A. (2005). The aerosol-climate model ECHAM5-HAM. *Atmospheric Chemistry and Physics*, 5(4):1125–1156.

Stier, P., Seinfeld, J. H., Kinne, S., Feichter, J., and Boucher, O. (2006). Impact of nonabsorbing anthropogenic aerosols on clear-sky atmospheric absorption. *Journal of Geophysical Research Atmospheres*, 111(18):1–11.

Stjern, C. W., Richardson, T., Myhre, G., Faluvegi, G., Olivié, D., Stier, P., Samset, B. H., Fläschner, D., Takemura, T., Lamarque, J.-F., Smith, C. J., Forster, P., Kirkevåg, A., Boucher, O., Soden, B. J., Voulgarakis, A., Shindell, D., Kasoar, M., Hodnebrog, Ø., Kramer, R. J., Andrews, T., and Watson-Parris, D. (2018). Quantifying the Importance of Rapid Adjustments for Global Precipitation Changes. *Geophysical Research Letters*, 45(20):11,399–11,405.

Stjern, C. W., Samset, B. H., Myhre, G., Forster, P. M., Hodnebrog, Ø., Andrews, T., Boucher, O., Faluvegi, G., Iversen, T., Kasoar, M., Kharin, V., Kirkevåg, A., Lamarque, J.-F., Olivié, D., Richardson, T., Shawki, D., Shindell, D., Smith, C. J., Takemura, T., and Voulgarakis, A. (2017). Rapid Adjustments Cause Weak Surface Temperature Response to Increased Black Carbon Concentrations. *Journal of Geophysical Research: Atmospheres*, 122(21):11,462–11,481.

Sun, Q., Miao, C., Duan, Q., Ashouri, H., Sorooshian, S., and Hsu, K. (2018). A Review of Global Precipitation Data Sets: Data Sources, Estimation, and Intercomparisons. *Reviews of Geophysics*, 56(1):79–107.

Suzuki, K., Stephens, G. L., and Golaz, J.-C. (2017). Significance of aerosol radiative effect in energy balance control on global precipitation change. *Atmospheric Science Letters*, 18(10):389–395.

Suzuki, K. and Takemura, T. (2019). Perturbations to Global Energy Budget Due to Absorbing and Scattering Aerosols. *Journal of Geophysical Research: Atmospheres*, 124(4):2194–2209.

Swart, N. C., Cole, J. N., Kharin, V. V., Lazare, M., Scinocca, J. F., Gillett, N. P., Anstey, J., Arora, V., Christian, J. R., Hanna, S., Jiao, Y., Lee, W. G., Majaess, F., Saenko, O. A., Seiler, C., Seinen, C., Shao, A., Sigmond, M., Solheim, L., Von Salzen, K., Yang, D., and Winter, B. (2019). The Canadian Earth System Model version 5 (CanESM5.0.3). *Geoscientific Model Development*, 12(11).

Tao, W.-K., Chen, J.-P., Li, Z., Wang, C., and Zhang, C. (2012). Impact of aerosols on convective clouds and precipitation. *Reviews of Geophysics*, 50(2):2011RG000369.

Tatebe, H., Ogura, T., Nitta, T., Komuro, Y., Ogochi, K., Takemura, T., Sudo, K., Sekiguchi, M., Abe, M., Saito, F., Chikira, M., Watanabe, S., Mori, M., Hirota, N., Kawatani, Y., Mochizuki, T., Yoshimura, K., Takata, K., O'Ishi, R., Yamazaki, D., Suzuki, T., Kurogi, M., Kataoka, T., Watanabe, M., and Kimoto, M. (2019). Description and basic evaluation of simulated mean state, internal variability, and climate sensitivity in MIROC6. *Geoscientific Model Development*, 12(7).

Taylor, C. M., Belusic, D., Guichard, F., Parker, D. J., Vischel, T., Bock, O., Harris, P. P., Janicot, S., Klein, C., and Panthou, G. (2017). Frequency of extreme sahelian storms tripled since 1982 in satellite observations. *Nature*, 544.

Taylor, J. W., Allan, J. D., Allen, G., Coe, H., Williams, P. I., Flynn, M. J., Le Breton, M., Muller, J. B., Percival, C. J., Oram, D., Forster, G., Lee, J. D., Rickard, A. R., Parrington, M., and Palmer, P. I. (2014). Size-dependent wet removal of black carbon in Canadian biomass burning plumes. *Atmospheric Chemistry and Physics*, 14(24).

Taylor, K. E., Stouffer, R. J., and Meehl, G. A. (2012). An Overview of CMIP5 and the Experiment Design. *Bulletin of the American Meteorological Society*, 93(4):485–498.

Tegen, I., Neubauer, D., Ferrachat, S., Drian, C. S. L., Bey, I., Schutgens, N., Stier, P., Watson-Parris, D., Stanelle, T., Schmidt, H., Rast, S., Kokkola, H., Schultz, M., Schroeder, S., Daskalakis, N., Barthel, S., Heinold, B., and Lohmann, U. (2019). The global aerosol-climate model echam6.3-ham2.3 -Part 1: Aerosol evaluation. *Geoscientific Model Development*, 12(4):1643–1677.

Textor, C., Schulz, M., Guibert, S., Kinne, S., Balkanski, Y., Bauer, S., Berntsen, T., Berglen, T., Boucher, O., Chin, M., Dentener, F., Diehl, T., Easter, R., Feichter, H., Fillmore, D., Ghan, S., Ginoux, P., Gong, S., Grini, A., Hendricks, J., Horowitz, L., Huang, P., Isaksen, I., Iversen, I., Kloster, S., Koch, D., Kirkevåg, A., Kristjansson, J. E., Krol, M., Lauer, A., Lamarque, J. F., Liu, X., Montanaro, V., Myhre, G., Penner, J., Pitari, G., Reddy, S., Seland, Ø., Stier, P., Takemura, T., and Tie, X. (2006). Analysis and quantification of the diversities of aerosol life cycles within AeroCom. *Atmospheric Chemistry and Physics*, 6(7):1777–1813.

Thorpe, L. and Andrews, T. (2014). The physical drivers of historical and 21st century global precipitation changes. *Environmental Research Letters*, 9(6):064024.

Tian, B. and Dong, X. (2020). The Double-ITCZ Bias in CMIP3, CMIP5, and CMIP6 Models Based on Annual Mean Precipitation. *Geophysical Research Letters*, 47(8).

Tian, D., Dong, W., Gong, D., Guo, Y., and Yang, S. (2017). Fast responses of climate system to carbon dioxide, aerosols and sulfate aerosols without the mediation of SST in the CMIP5. *International Journal of Climatology*, 37(3).

Tiedtke, M. (1989). A Comprehensive Mass Flux Scheme for Cumulus Parameterization in Large-Scale Models. *Monthly Weather Review*, 117(8):1779–1800.

Toll, V., Christensen, M., Quaas, J., and Bellouin, N. (2019). Weak average liquid-cloud-water response to anthropogenic aerosols. *Nature*, 572(7767).

Trenberth, K. (2011). Changes in precipitation with climate change. *Climate Research*, 47(1):123–138.

Trenberth, K. E., Dai, A., Rasmussen, R. M., and Parsons, D. B. (2003). The changing character of precipitation. *Bulletin of the American Meteorological Society*, 84(9):1205–1217+1161.

Trenberth, K. E., Dai, A., Van Der Schrier, G., Jones, P. D., Barichivich, J., Briffa, K. R., and Sheffield, J. (2014). Global warming and changes in drought. *Nature Climate Change*, 4(1):17–22.

Twomey, S. (1977). The Influence of Pollution on the Shortwave Albedo of Clouds. *Journal of the Atmospheric Sciences*, 34(7).

Undorf, S., Polson, D., Bollasina, M. A., Ming, Y., Schurer, A., and Hegerl, G. C. (2018). Detectable Impact of Local and Remote Anthropogenic Aerosols on the 20th Century Changes of West African and South Asian Monsoon Precipitation. *Journal of Geophysical Research: Atmospheres*, 123(10):4871–4889.

van Marle, M. J. E., Kloster, S., Magi, B. I., Marlon, J. R., Daniau, A.-L., Field, R. D., Arneth, A., Forrest, M., Hantson, S., Kehrwald, N. M., Knorr, W., Lasslop, G., Li, F., Mangeon, S., Yue, C., Kaiser, J. W., and van der Werf, G. R. (2017). Historic global biomass burning emissions for CMIP6 (BB4CMIP) based on merging satellite observations with proxies and fire models (1750–2015). *Geoscientific Model Development*, 10(9):3329–3357.

Vecchi, G. A. and Soden, B. J. (2007). Global Warming and the Weakening of the Tropical Circulation. *Journal of Climate*, 20(17):4316–4340.

Villamayor, J. and Mohino, E. (2015). Robust Sahel drought due to the Interdecadal Pacific Oscillation in CMIP5 simulations. *Geophysical Research Letters*, 42(4):1214–1222.

Voigt, A., Albern, N., Ceppi, P., Grise, K., Li, Y., and Medeiros, B. (2021). Clouds, radiation, and atmospheric circulation in the present-day climate and under climate change. *WIREs Climate Change*, 12(2):1–22.

Voldoire, A., Saint-Martin, D., Sénési, S., Decharme, B., Alias, A., Chevallier, M., Colin, J., Guérémy, J. F., Michou, M., Moine, M. P., Nabat, P., Roehrig, R., Salas y Mélia, D., Séférian, R., Valcke, S., Beau, I., Belamari, S., Berthet, S., Cassou, C., Cattiaux, J., Deshayes, J., Douville, H., Ethé, C., Franchistéguy, L., Geoffroy, O., Lévy, C., Madec, G., Meurdesoif, Y., Msadek, R., Ribes, A., Sanchez-Gomez, E., Terray, L., and Waldman, R. (2019). Evaluation of CMIP6 DECK Experiments With CNRM-CM6-1. *Journal of Advances in Modeling Earth Systems*, 11(7).

Voldoire, A., Sanchez-Gomez, E., Salas y Mélia, D., Decharme, B., Cassou, C., Sénési, S., Valcke, S., Beau, I., Alias, A., Chevallier, M., Déqué, M., Deshayes, J., Douville, H., Fernandez, E., Madec, G., Maisonnave, E., Moine, M. P., Planton, S., Saint-Martin, D., Szopa, S., Tyteca, S., Alkama, R., Belamari, S., Braun, A., Coquart, L., and Chauvin, F. (2013). The CNRM-CM5.1 global climate model: Description and basic evaluation. *Climate Dynamics*, 40(9-10).

Volodin, E. M., Dianskii, N. A., and Gusev, A. V. (2010). Simulating present-day climate with the INMCM4.0 coupled model of the atmospheric and oceanic general circulations. *Izvestiya - Atmospheric and Ocean Physics*, 46(4).

von Salzen, K., Scinocca, J. F., McFarlane, N. A., Li, J., Cole, J. N. S., Plummer, D., Verseghy, D., Reader, M. C., Ma, X., Lazare, M., and Solheim, L. (2013). The Canadian Fourth Generation Atmospheric Global Climate Model (CanAM4). Part I: Representation of Physical Processes. *Atmosphere-Ocean*, 51(1):104–125.

Wang, C. (2009). The sensitivity of tropical convective precipitation to the direct radiative forcings of black carbon aerosols emitted from major regions. *Annales Geophysicae*, 27(10):3705–3711.

Wang, C. (2013). Impact of anthropogenic absorbing aerosols on clouds and precipitation: A review of recent progresses. *Atmospheric Research*, 122:237–249.

Wang, H., Xie, S. P., Kosaka, Y., Liu, Q., and Du, Y. (2019). Dynamics of Asian summer monsoon response to anthropogenic aerosol forcing. *Journal of Climate*, 32(3):843–858.

Wang, M., Ghan, S., Liu, X., L'Ecuyer, T. S., Zhang, K., Morrison, H., Ovchinnikov, M., Easter, R., Marchand, R., Chand, D., Qian, Y., and Penner, J. E. (2012). Constraining cloud lifetime effects of aerosols using A-Train satellite observations. *Geophysical Research Letters*, 39(15):3–9.

Wang, M., Larson, V. E., Ghan, S., Ovchinnikov, M., Schanen, D. P., Xiao, H., Liu, X., Rasch, P., and Guo, Z. (2015). A multiscale modeling framework model (super-parameterized CAM5) with a higher-order turbulence closure: Model description and low-cloud simulations. *Journal of Advances in Modeling Earth Systems*, 7(2).

Wang, T. and Li, T. (2020). Diagnosing the column-integrated moist static energy budget associated with the northward-propagating boreal summer intraseasonal oscillation. *Climate Dynamics*, 54(11-12):4711–4732.

Wang, Z., Lin, L., Yang, M., Xu, Y., and Li, J. (2017). Disentangling fast and slow responses of the East Asian summer monsoon to reflecting and absorbing aerosol forcings. *Atmospheric Chemistry and Physics*, 17(18):11075–11088.

Watanabe, M., Kamae, Y., Shiogama, H., DeAngelis, A. M., and Suzuki, K. (2018). Low clouds link equilibrium climate sensitivity to hydrological sensitivity. *Nature Climate Change*, 8(October).

Watanabe, M., Shiogama, H., Tatebe, H., Hayashi, M., Ishii, M., and Kimoto, M. (2014). Contribution of natural decadal variability to global warming acceleration and hiatus. *Nature Climate Change*, 4(10):893–897.

Watanabe, M., Suzuki, T., O'Ishi, R., Komuro, Y., Watanabe, S., Emori, S., Takemura, T., Chikira, M., Ogura, T., Sekiguchi, M., Takata, K., Yamazaki, D., Yokohata, T., Nozawa, T., Hasumi, H., Tatebe, H., and Kimoto, M. (2010). Improved climate simulation by MIROC5: Mean states, variability, and climate sensitivity. *Journal of Climate*, 23(23).

Watanabe, M. and Tatebe, H. (2019). Reconciling roles of sulphate aerosol forcing and internal variability in Atlantic multidecadal climate changes. *Climate Dynamics*, 53(7-8):4651–4665.

Watanabe, S., Hajima, T., Sudo, K., Nagashima, T., Takemura, T., Okajima, H., Nozawa, T., Kawase, H., Abe, M., Yokohata, T., Ise, T., Sato, H., Kato, E., Takata, K., Emori, S., and Kawamiya, M. (2011). MIROC-ESM 2010: Model description and basic results of CMIP5-20c3m experiments. *Geoscientific Model Development*, 4(4).

Wen, G., Marshak, A., Cahalan, R. F., Remer, L. A., and Kleidman, R. G. (2007). 3-D aerosol-cloud radiative interaction observed in collocated MODIS and ASTER images of cumulus cloud fields. *Journal of Geophysical Research Atmospheres*, 112(13).

Wentz, F. J., Ricciardulli, L., Hilburn, K., and Mears, C. (2007). How much more rain will global warming bring? *Science*, 317(5835).

Wentz, F. J. and Schabel, M. (2000). Precise climate monitoring using complementary satellite data sets. *Nature*, 403(6768).

Wentz, F. J. and Spencer, R. W. (1998). SSM/I rain retrievals within a unified all-weather ocean algorithm. *Journal of the Atmospheric Sciences*, 55(9).

White, B., Gryspeerdt, E., Stier, P., Morrison, H., Thompson, G., and Kipling, Z. (2017). Uncertainty from the choice of microphysics scheme in convection-permitting models significantly exceeds aerosol effects. *Atmospheric Chemistry and Physics*, 17(19):12145–12175.

Wild, M. (2009). Global dimming and brightening: A review. *Journal of Geophysical Research*, 114(12):D00D16.

Wild, M., Hakuba, M. Z., Folini, D., Dörig-Ott, P., Schär, C., Kato, S., and Long, C. N. (2019). The cloud-free global energy balance and inferred cloud radiative effects: an assessment based on direct observations and climate models. *Climate Dynamics*, 52(7-8).

Williams, A. I. L., Stier, P., Dagan, G., and Watson-Parris, D. (2022). Strong control of effective radiative forcing by the spatial pattern of absorbing aerosol. *Nature Climate Change*, 12(8):735–742.

Wood, R. (2012). Stratocumulus Clouds. *Monthly Weather Review*, 140(8):2373–2423.

Wood, R. (2015). Clouds and Fog: Stratus and Stratocumulus. In *Encyclopedia of Atmospheric Sciences*, pages 196–200. Elsevier press.

Wood, R. and Bretherton, C. S. (2006). On the Relationship between Stratiform Low Cloud Cover and Lower-Tropospheric Stability. *Journal of Climate*, 19(24):6425–6432.

Wu, P., Wood, R., Ridley, J., and Lowe, J. (2010). Temporary acceleration of the hydrological cycle in response to a CO 2 rampdown. *Geophysical Research Letters*, 37(12).

Wu, T., Lu, Y., Fang, Y., Xin, X., Li, L., Li, W., Jie, W., Zhang, J., Liu, Y., Zhang, L., Zhang, F., Zhang, Y., Wu, F., Li, J., Chu, M., Wang, Z., Shi, X., Liu, X., Wei, M., Huang, A., Zhang, Y., and Liu, X. (2019). The Beijing Climate Center Climate System Model (BCC-CSM): The main progress from CMIP5 to CMIP6. *Geoscientific Model Development*, 12(4).

Wu, T., Song, L., Li, W., Wang, Z., Zhang, H., Xin, X., Zhang, Y., Zhang, L., Li, J., Wu, F., Liu, Y., Zhang, F., Shi, X., Chu, M., Zhang, J., Fang, Y., Wang, F., Lu, Y., Liu, X., Wei, M., Liu, Q., Zhou, W., Dong, M., Zhao, Q., Ji, J., Li, L., and Zhou, M. (2014). An overview of BCC climate system model development and application for climate change studies. *Journal of Meteorological Research*, 28(1).

Xie, P. and Arkin, P. A. (1998). Global monthly precipitation estimates from satellite-observed outgoing longwave radiation. *Journal of Climate*, 11(2):137–164.

Xie, P., Janowiak, J. E., Arkin, P. A., Adler, R., Gruber, A., Ferraro, R., Huffman, G. J., and Curtis, S. (2003). GPCP pentad precipitation analyses: An experimental dataset based on gauge observations and satellite estimates. *Journal of Climate*, 16(13).

Xie, S.-P., Deser, C., Vecchi, G. A., Ma, J., Teng, H., and Wittenberg, A. T. (2010). Global Warming Pattern Formation: Sea Surface Temperature and Rainfall. *Journal of Climate*, 23(4):966–986.

Xie, S.-P., Kosaka, Y., and Okumura, Y. M. (2016). Distinct energy budgets for anthropogenic and natural changes during global warming hiatus. *Nature Geoscience*, 9(1):29–33.

Yang, F., Kumar, A., Schlesinger, M. E., and Wang, W. (2003). Intensity of Hydrological Cycles in Warmer Climates. *Journal of Climate*, 16(14):2419–2423.

Yang, J., He, S., and Bao, Q. (2021). Convective/Large-scale Rainfall Partitions of Tropical Heavy Precipitation in CMIP6 Atmospheric Models. *Advances in Atmospheric Sciences*, 38(6):1020–1027.

Yang, S. and Smith, E. A. (2008). Convective-stratiform precipitation variability ar seasonal scale from 8 yr of TRMM observations: Implications for multiple modes of diurnal variability. *Journal of Climate*, 21(16).

Yeager, S. G., Danabasoglu, G., Rosenbloom, N. A., Strand, W., Bates, S. C., Meehl, G. A., Karspeck, A. R., Lindsay, K., Long, M. C., Teng, H., and Lovenduski, N. S. (2018). Predicting Near-Term Changes in the Earth System: A Large Ensemble of Initialized Decadal Prediction Simulations Using the Community Earth System Model. *Bulletin of the American Meteorological Society*, 99(9):1867–1886.

Yin, X., Gruber, A., and Arkin, P. (2004). Comparison of the GPCP and CMAP merged gauge-satellite monthly precipitation products for the period 1979-2001. *Journal of Hydrometeorology*, 5(6).

Yukimoto, S., Adachi, Y., Hosaka, M., Sakami, T., Yoshimura, H., Hirabara, M., Tanaka, T. Y., Shindo, E., Tsujino, H., Deushi, M., Mizuta, R., Yabu, S., Obata, A., Nakano, H., Koshiro, T., Ose, T., and Kitoh, A. (2012). A new global climate model of the Meteorological Research Institute: MRI-CGCM3: -Model description and basic performance-. *Journal of the Meteorological Society of Japan*, 90(A).

Yukimoto, S., Koshiro, T., Kawai, H., Oshima, N., Yoshida, K., Urakawa, S., Tsujino, H., Deushi, M., Tanaka, T., Hosaka, M., Yoshimura, H., Shindo, E., Mizuta, R., Ishii, M., Obata, A., and Adachi, Y. (2019). MRI MRI-ESM2.0 model output prepared for CMIP6 CMIP.

Zanis, P., Akritidis, D., Georgoulias, A. K., Allen, R. J., Bauer, S. E., Boucher, O., Cole, J., Johnson, B., Deushi, M., Michou, M., Mulcahy, J., Nabat, P., Olivié, D., Oshima, N., Sima, A., Schulz, M., Takemura, T., and Tsigaridis, K. (2020). Fast responses on pre-industrial climate from present-day aerosols in a CMIP6 multi-model study. *Atmospheric Chemistry and Physics*, 20(14):8381–8404.

Zelinka, M. D., Myers, T. A., McCoy, D. T., Po-Chedley, S., Caldwell, P. M., Ceppi, P., Klein, S. A., and Taylor, K. E. (2020). Causes of Higher Climate Sensitivity in CMIP6 Models. *Geophysical Research Letters*, 47(1):1–12.

Zhang, K., O'Donnell, D., Kazil, J., Stier, P., Kinne, S., Lohmann, U., Ferrachat, S., Croft, B., Quaas, J., Wan, H., Rast, S., and Feichter, J. (2012). The global aerosol-climate model ECHAM-HAM, version 2: sensitivity to improvements in process representations. *Atmospheric Chemistry and Physics*, 12(19):8911–8949.

Zhang, R. and Delworth, T. L. (2006). Impact of Atlantic multidecadal oscillations on India/Sahel rainfall and Atlantic hurricanes. *Geophysical Research Letters*, 33(17):L17712.

Zhang, S., Stier, P., and Watson-Parris, D. (2021). On the contribution of fast and slow responses to precipitation changes caused by aerosol perturbations. *Atmospheric Chemistry and Physics*, 21(13):10179–10197.

Zhang, S., Wang, M., Ghan, S. J., Ding, A., Wang, H., Zhang, K., Neubauer, D., Lohmann, U., Ferrachat, S., Takeamura, T., Gettelman, A., Morrison, H., Lee, Y., Shindell, D. T., Partridge, D. G., Stier, P., Kipling, Z., and Fu, C. (2016). On the characteristics of aerosol indirect effect based on dynamic regimes in global climate models. *Atmospheric Chemistry and Physics*, 16(5):2765–2783.

Zhao, M., Golaz, J. C., Held, I. M., Guo, H., Balaji, V., Benson, R., Chen, J. H., Chen, X., Donner, L. J., Dunne, J. P., Dunne, K., Durachta, J., Fan, S. M., Freidenreich, S. M., Garner, S. T., Ginoux, P., Harris, L. M., Horowitz, L. W., Krasting, J. P., Langenhorst, A. R., Liang, Z., Lin, P., Lin, S. J., Malyshev, S. L., Mason, E., Milly, P. C., Ming, Y., Naik, V., Paulot, F., Paynter, D., Phillipps,

P., Radhakrishnan, A., Ramaswamy, V., Robinson, T., Schwarzkopf, D., Seman, C. J., Shevliakova, E., Shen, Z., Shin, H., Silvers, L. G., Wilson, J. R., Winton, M., Wittenberg, A. T., Wyman, B., and Xiang, B. (2018). The GFDL Global Atmosphere and Land Model AM4.0/LM4.0: 1. Simulation Characteristics With Prescribed SSTs. *Journal of Advances in Modeling Earth Systems*, 10(3).

Zhao, S. and Suzuki, K. (2019). Differing Impacts of Black Carbon and Sulfate Aerosols on Global Precipitation and the ITCZ Location via Atmosphere and Ocean Energy Perturbations. *Journal of Climate*, 32(17):5567–5582.

Zheng, B., Tong, D., Li, M., Liu, F., Hong, C., Geng, G., Li, H., Li, X., Peng, L., Qi, J., Yan, L., Zhang, Y., Zhao, H., Zheng, Y., He, K., and Zhang, Q. (2018). Trends in China's anthropogenic emissions since 2010 as the consequence of clean air actions. *Atmospheric Chemistry and Physics*, 18(19):14095–14111.

Zhou, C., Lu, J., Hu, Y., and Zelinka, M. D. (2020a). Responses of the Hadley Circulation to Regional Sea Surface Temperature Changes. *Journal of Climate*, 33(2):429–441.

Zhou, C. and Penner, J. E. (2016). Why do GCMs overestimate the aerosol cloud lifetime effect? A comparison of CAM5 and a CRM. *Atmospheric Chemistry and Physics Discussions*, (July):1–16.

Zhou, C., Zelinka, M. D., Dessler, A. E., and Wang, M. (2021). Greater committed warming after accounting for the pattern effect. *Nature Climate Change*, 11(2):132–136.

Zhou, C., Zelinka, M. D., and Klein, S. A. (2017). Analyzing the dependence of global cloud feedback on the spatial pattern of sea surface temperature change with a Green's function approach. *Journal of Advances in Modeling Earth Systems*, 9(5):2174–2189.

Zhou, T., Zhang, W., Zhang, L., Zhang, X., Qian, Y., Peng, D., Ma, S., and Dong, B. (2020b). The dynamic and thermodynamic processes dominating the reduction of global land monsoon precipitation driven by anthropogenic aerosols emission. *Science China Earth Sciences*, 63(7):919–933.